UNIVERSITEIT VAN PRETORIA
UNIVERSITY OF PRETORIA
YUNIBESITHI YA PRETORIA

AERODYNAMIC LOSSES AND ENDWALL HEAT TRANSFER IN A LINEAR VANE CASCADE WITH ENDWALL FILM-COOLING AND ENDWALL-LEADING EDGE CONTOURING

by

ADEOLA SUHUD SHOTE

Submitted in partial fulfilment of the requirements for the degree of

DOCTOR OF PHILOSOPHY IN ENGINEERING

Department of Mechanical and Aeronautical Engineering
University of Pretoria

January, 2019

Supervisor: Dr. G.I. Mahmood
Co-supervisor: Prof. J.P. Meyer

ABSTRACT

Title : Aerodynamic Losses and Endwall Heat Transfer in a Linear Vane Cascade With Endwall Film-cooling and Endwall-Leading Edge Contouring
Author : Adeola Suhud Shote
Supervisors : Dr. G.I. Mahmood
: Prof. J.P. Meyer
Department : Mechanical and Aeronautical Engineering
University : University of Pretoria
Degree : Doctor of Philosophy in Engineering (Mechanical)

Elevated inlet temperature is desirable in turbine passages. This is not without a whole lot of aerodynamic loss, endwall thermal stresses consequences and pressure loss penalties most especially downstream of the turbine passage. Film cooling and endwall modification are needed to increase the efficiency and prolong the material life of the turbine endwall and components. The main objective of this work is to investigate the heat transfer influence at the near endwall region by employing the leading edge contouring and film-cooling at the endwall.

The hub-side blade profile and passage geometry of the 1st stage nozzle guide vane of a GE-E^3 *turbine engine are scaled up and employed in a linear cascade for the experimentation at a Reynolds number of 2.1E+05 based on turbine vane-blade chord and reference velocity. The hot endwall of the turbine engine was replicated experimentally by supplying constant heat flux at the endwall. A numerical model of the cascade is employed in a commercial computational fluid dynamics (CFD) code STAR CCM+*^{TM} *to optimize fillet shape. CFD is employed to predict the baseline case (no film-cooling, no endwall modification) and Fillet-1 endwall modification case (no film-cooling). Experimentally, the efficacy of four unique upstream film-cooling schemes and geometries are investigated with two linear fillets employed at the endwall-blade junction. The film-cooling is employed at five different inlet blowing ratios (M=1.0, 1.4, 1.8, 2.2 and 2.8). The interaction of the film-cooling jets with the main flow inside the cascade are captured and analyzed. The leading-edge film cooling schemes tested include the flush slots, the slot-discrete holes combination, the discrete holes and the linear inlet beveled/curved holes. The distance travelled and spread of the film cooling along the endwall are assessed with respect to the effectiveness and non-dimensional temperature. Two linear contoured endwall geometries known as the fillets were employed at the blade-endwall junction along with the film-cooling configuration at the endwall for the experimental measurement.*

The computational results of static pressure on the vane blade surface at the mid-span of the baseline and Fillet-1 cases (M = 0) shows good agreement with the experimental cases. The simulation also captures appropriately the passage vortex as presented by the experimental result of the coefficient of the total pressure loss. The location and the magnitude of the total pressure loss distribution of the computational result are comparable with that of the experiment. The linear variations of Fillet-1 in the axial and spanwise directions have significant effect on the approaching endwall boundary layer of the horse shoe vortex. The optimized contoured endwall reduces the size and magnitude of the horse shoe vortex at the near endwall of the vane-blade.

High Nusselt number (Nu) is recorded at the throat region of the endwall for the baseline without fillet case in the experiment. This is attributed to the flow acceleration effect. However, with the installation of Fillet-1 and Fillet-2, the magnitude of the Nusselt number at the throat region reduced by (20 – 40)% from that of the baseline case. Fillet-2 has the lowest reduction effect on the Nu at the throat region of the endwall. The non-dimensional temperature of the flow field near the endwall shows that Fillet-1 and Fillet-2 improve the endwall film cooling coverage in both pitchwise and axil directions. In general, high film cooling jet flux, provides better cooling and endwall coverage as the momentum of jet reduces the pitchwise cross flow that is responsible for high heat transfer and aerodynamic loss. With the injection of the high momentum film cooling flow (M = 2.8), the result shows excellent improvement in the adiabatic effectiveness for all the leading-edge film cooling configurations. The curved holes produced the best effectiveness distributions at the endwall. However, the slot-discrete hole configuration with the fillet or without the fillet are having the best reduction influence on the passage vortex at the exit plane of the turbine cascade passage. Therefore, the magnitude and size of the passage vortex are reduced significantly. At blowing ratio ≤ 2.2, with the fillet and without the fillet, the main flow has more influence on the film-cooling jets thereby reducing the adiabatic effectiveness coverage of the endwall. Generally, Mass fractions are found to increase as the blowing ratio increases and decrease with enwall modification. Fillet-1 recorded the least mass fraction for all blowing ratios investigated.

Keywords: *Endwall, film cooling, Fillet, total Pressure loss, adiabatic effectiveness, Nusselt number*

ACKNOWLEDGEMENTS

I feel very humbled in the presence of the Supreme Being (Allah), making this remarkable research a reality. All Praises and adorations go to Allah, the Lord of the worlds! I cannot but thank Him for His mercies in the number of times of His creatures for making this research possible.

I also want to show my gratitude to my supervisors, Dr. Gazi Mahmood and Prof. Josua Meyer for their technical input, sincere advice and financial support to make this research a reality.

I cannot forget to gratify the unflinching helps of Chris Govinder and Donald Keetse in the Wind Tunnel Lab. At any point in time, they are always ready to assist. I also appreciate the contributions of my colleagues who stood by me throughout this work. I cannot thank you enough but the memories will never be forgotten.

The material and financial supports of CSIR, Armscor and University of Pretoria are highly appreciated.

The foundational roles played by my parents cannot go unmentioned. My acknowledgment goes to my parents for their parental tutelage form childhood.

Lastly, the unflinching supports of my wife and children (Muizzah, Muklisoh and Muqoddas) are highly appreciated.

TABLE OF CONTENTS

LIST OF FIGURES

LIST OF TABLES

NOMENCLATURE

a	Area vector
C	True chord
C_{ax}	Axial chord
C_d	Coefficient of discharge
C_p	Specific heat capacity at constant pressure
$\dot{m}$	Mass flow rate
D	Diameter
G	Grid flux
I	current
IR	infrared
k	Thermal conductivity
M, M_{in}	Blowing ratio
n	Number of variables/Number of data points
Nu	Nusselt number
P	Pitch/Pressure
PS/SS	Pass side/Suction side
Pr	Prandtl number
Q	Quantity of heat
q	Rate of heat transfer
r	Radius
r_c	Apparent radius of particle clusters
R	Resistance
Re	Reynolds number
S	Span/vector between cell face & centroid
s	blade surface distance from leading edge
T	Temperature
LE/TE	Leading edge/Trailing edge
Tu	Turbulent intensity
t	Time
U	Free stream velocity

V	Volume/voltage
u, v, w	Local velocities
x	thickness
X_G, Y_G, Z_G	Global coordinates
x, y, z	Local coordinates

Greek symbols

β	Orifice diameters ratio
∂	Partial derivative
η	Adiabatic effectiveness
Δ	Difference
Γ	diffusivity
δ	Boundary layer/uncertainty
∇	Gradient operator
μ	Dynamic viscosity
ρ	Density
τ	Shear stress
θ	Non-dimensional temperature
ϕ	Scalar quantity
χ	Porosity
ω	vorticity

Subscripts

ax	Axial
b,x	Local blade quantity related to ‘*X*’
$cool$	Cooling
$cond$	Conduction
$conv$	Convection
e,x	Local endwall quantity
ew	Endwall
fc	Film cooling
g	Grid

id	Ideal
in	inlet
h	Hot
loc	Local
ref	Reference
$mass - av$	Mass average
max	Maximum
p	Quantity relating to constant pressure
$pass$	passage
$p, blade$	Pressure on blade
plm	plenum
$pt, loss$	Total plenum loss
s, ref	Static reference
T	Thermal
th	Thickness/thermal
t, ref	Total reference
t, x	Local total
x	Quantity relating to 'X' direction
w	wall

PUBLICATIONS IN JOURNALS AND CONFERENCE PROCEEDINGS

The following articles and conference papers were produced during this research.

Journal articles

Adeola S. Shote, Gazi I. Mahmood and Josua P. Meyer (2019) Influences of large fillets on endwall flows in a vane cascade with upstream slot film-cooling, *Experimental thermal and Fluid Science Journal*, ETFS_2019.

. (Under review)

Adeola Shote, Barbara Huyssen, Gazi Mahmood and Josua Meyer (2019) Endwall Heat Transfer and Bleed Film-Cooling in a Filleted Vane Cascade, *Experimental thermal and Fluid Science Journal*, ETFS_2019.

. (Under review)

Conference papers

A.S. Shote, K. Arnachellan, G.I. Mahmood and J.P. Meyer (2016) Total Pressure Losses and Endwall Region Temperature Field in a Linear Vane Cascade with Slot Film Cooling Flow, *Proceedings of the International Aerospace Symposium of South Africa*, Pretoria, South Africa.

B. Huyssen, **A.S. Shote** and G.I. Mahmood (2016) Computational Investigation of Flow Structure in a Linear Vane Blade Cascade with Filleted Endwall*, Proceedings of the International Aerospace Symposium of South Africa, Pretoria*, South Africa.

1. CHAPTER 1: INTRODUCTION

1.1 Background

A typical turbine engine generates astonishing amount of energy with a lot of associated thermal stresses aerodynamic losses propagating along the turbine components and passages. These associated problems such as secondary flows, heat transfer at the passage resulting in thermal load and a significant reduction in the life span of the turbo-machinery components and parts. Gas turbines play key role in driving modern day activities primarily in power generation and aircraft and industrial flow transfer. Gas turbines are also used to drive pumps, compressors and turbochargers in the industrial applications where electricity from the power grid is not available. Besides, increase in gas turbine thermal efficiency is highly desirable for sustainability of turbine operation as energy demand keeps increasing across the nations of the world. Therefore due to the work load of gas turbines to drive daily activities, the vanes and components are under severe thermal penalties and turbulence effects. The turbulent flow is termed secondary flow which is responsible for significant increase in aerodynamics losses increasing the pressure losses across the stator and rotor passages and reducing the turbine overall efficiency. Secondary flows, increases mixing between the main flow and endwall flow, lifting of the film cooling flow exposing the endwall to hot gas. We cannot be complacent with the present day design of turbine as demand for energy keeps increasing. One of the contemporary ways of reducing thermal stresses is through the use of film cooling schemes. The interaction of the complex flow structure at the endwall region makes it difficult to predict accurately the heat transfer at the endwall regions and secondary pressure losses across the turbine passage. Therefore, designers are striving to come up with turbine passage designs that will match modern day increasing energy demand and efficiency with respect to material selection and thrust to weight ratio. The structural modifications in the passage design are primarily concentrated at the endwall region so as to not affect the main flow, throat design, and blade loading. However, accurate prediction of the endwall coolant flow behaviour of film cooling geometry scheme is also important.

Film cooled jet can play a leading role in the reduction of the vortical flows that is responsible for the high heat transfer in the near end wall region. The design of complex cooling scheme and assessment of the coolant jet behavior at the endwall combined with a contoured endwall near the leading edge region are of interest in this research. The contour endwall near the leading edge in the form of three-dimensional fillet is known to reduce the effects of endwall region secondary flows and heat transfer. However, the configuration and schemes of the film cooling and endwall contouring must be carefully examined for effectiveness. Linear cascade testing and full rotation rig have been used by recent designers to carry out predictions of the operating conditions in a turbine and turbo-machinery systems. The test rig employed in this research is a linear turbine cascade housing seven GE-E^3 vane-blade profile. This research also employs numerical predictions of the cascade flows using the $k-\omega$ turbulence model of the Reynolds-averaged Navier-Stokes (RANS) solver in STAR-CCM+^{TM}. The stationary cascade test facility and the numerical model of the cascade used in the present research are atmospheric employing the incompressible flow at ambient conditions. However, the basic flow dynamics in the atmospheric cascade caused by the boundary layer, pitchwise pressure gradient, stagnation region separation, and the resulting secondary flows at the endwall are also present in the real turbine passages. The results of the present investigations are thus very relevant and important for the gas turbine design.

High inlet temperature is desired while the resulting flows also cause wide variations in temperature gradient in the passage. This research describes in detail the heat transfer and the film cooling predictions at the passage endwall region of the boundary layer. The film cooling geometries employed in this research include four unique leading-edge film cooling hole designs: combination of slots and discreet cylindrical holes, flush slots, curved/beveled holes. Flow measurements of the film-cooling are also obtained with discrete cylindrical holes located in the endwall inside the blade passage. This work also aims to understand the baseline and filleted cases of the endwall heat transfer. Computational fluid dynamics

(CFD) predictions are employed to show the effects of the geometric variations of one of the fillets employed in the experiments on the endwall region flow field.

1.2 Specific Objectives

The linear GE-E^3 vane cascade was designed to facilitate probe traverse within the passage and the reference plane for measurement. The test section is the part of an open atmospheric wind tunnel. All works were performed base on constant primary flow with a Reynolds no of 250,000. The objectives of the research were to influence the endwall region flow and heat transfer by employing: (i) the leading edge contouring in the form of fillets, (ii) the film cooling flow at endwall, and (iii) the fillets in conjunction with the film cooling flow. By influencing the endwall flow field the total pressure losses and endwall heat transfer across the cascade passage can be controlled and the film cooling effectiveness on the endwall can be enhanced. The endwall region flow field and boundary layer separation are the primary causes of the secondary flow losses and adverse effects on the film cooling effectiveness and endwall heat transfer in the blade passage of the stator. The effects of fillet on the film-cooling performance were investigated to show if additional advantages can be gained in the reduction of the secondary flows and endwall heat transfer. The following activities were performed to quantify the performances of fillets and film cooling flows and therefore, to achieve the objectives:

i) determine the detailed thermal flow field near the near-endwall-region and the heat transfer on endwall inside the blade passage with and without the fillets.
ii) compare the various film cooling scheme in terms of the adiabatic effectiveness on the endwall, depth of penetration of the film jet into the boundary layer, and the pitchwise coverage of the film-cooling flow on the endwall in the cascade passage.
iii) carry out the computational prediction of the flow structure within the passage using CD Adapco's STAR-CCM+^{TM} and quantify the effects of fillet geometry.
iv) examine the combined effects of both the film-cooling schemes and the fillet(s) and quantify the effects of fillet geometry.

1.3 Organisation of the dissertation

The main text consists of six chapters which are further subdivided into appropriate sub headings to highlight all the specifics covered in the research and easy referencing.

Chapter 2 includes the relevant literature survey relating to the work that has been done in the past.

Chapter 3 consists of the test rig description of the seven blades linear cascade. It also has the film cooling circuit by the side to supply the secondary flow in to the cascade.

In Chapter 4, computational fluid dynamics model of a periodic passage is also modelled using CD Adapco's STAR-CCM+^{TM} (8.06 version). The results are validated with the experimental flow structures. A discretization independence study is carried, checking for convergence and results disparities are compared with benchmark results.

Chapter 5 presents the various film cooling results and the heat transfer result at the near endwall and endwall regions of the blade passage. The experimental and numerical analyses are presented and discussed.

Chapter 6 summarizes the overall results obtained in the study and presents conclusions and recommendations from the study.

2. CHAPTER 2: RELEVANT REVIEW OF LITERATURE

In the last two decades, new studies have been presented in the literature focusing on the improvement of the operation of the combustor. The relevant overviews of literatures are presented here.

2.1 Heat Transfer and Film-Cooling Literatures

Past literatures have established that contoured end-wall reduces heat transfer and the flow structures of the secondary flow near the end-wall region. Figure 2.1 shows the leading edge fillet geometries employed by (Mahmood and Acharya, 2007) to attempt to attenuate the heat transfer near the end-wall region. It was therefore established that the end-wall Nusselt number is smaller near the upstream of the throat region. According to (Mahmood and Acharya, 2007), this means that the leading edge fillet reduced the heat transfer at the end-wall and near the end-wall regions. Heat transfer measurements (Kang et al., 1999, Lynch et al., 2011a, Thole and Knost, 2005) are performed near the endwall region with modifications. Two distinct Reynolds numbers are used by (Kang et al., 1999). Flow at higher Reynolds number are found to enhance the heat transfer at the trailing-edge of the endwall. But, in (Lynch et al., 2011a), the use of 3-dimentional contoured endwall are found to reduce the heat transfer at the endwall by about 20%. However, in (Thole and Knost, 2005) the combined effects of film-cooling and the slot-flow on the endwall heat transfer are investigated. The outcome shows that the film-cooling and slot-flow had significant cooling on the mid-passage region of the endwall. Highly resolved heat transfer measurement are performed by (Laveau et al., 2015) on a cylindrical, three dimensional endwall of a nozzle guide vane passage at two different Reynolds Numbers (Re). The experimental results are also compared with Reynolds Averaged Navier-Stoke’s predictions. The results (Laveau et al., 2015) show the origin of the heat transfer at the inlet of the passage. The region of the high Nusselt Number corresponds to the migration and activities of the vortex domain. The study of the mechanism of the formation of the pressure loss on a highly loaded gas turbine blade using stereoscopic particle image velocimetry is presented by (Bear et al., 2018). The trailing edge vortex, the corner vortex and the passage vortex are affirmed to generate high total pressure loses. In (Bear et al., 2018), total pressure transport prediction is found to corresponds with total pressure loss downstream of the passage.

Performance of leakage flow (Figure 2.2) as a means of cooling the turbine endwall in a cascade system was done experimentally and numerically by (Ranson et al., 2005). This study employs a backward facing upstream slot, mid-passage gap and a downstream gap at different leakage flow rates. Thermal flow fields are also captured and presented. The results (Ranson et al., 2005) shows that at all flow rates, little benefit of cooling are derived from the leakage flow through the mid-passage. However, leakage injection from the upstream showed better cooling coverage of the endwall than the mid-passage jet. Computational cooling results match the experimental one (Ranson et al., 2005). Thermal field and flow structure measurements in a turbine passage for a combustor exit flow are captured experimentally and presented by (Colban et al., 2003). The combustor simulator is placed up stream of the leading edge of the vane passage. In (Colban et al., 2003), the combustor turbine liner shows significant effect on the leading edge horse shoe vortex as the horse shoe vortex disappears compared to the typical baseline case without combustor liner. However, the interaction of the slot coolant results in lifting of bulk of the coolants from the endwall towards the mid-span. This is not a favourable condition in terms of the expected temperature reduction from film cooling. Conjugate heat transfer technique is deployed (Mensch and Thole, 2015b) to account for the internal and external cooling of turbine components. Included in the numerical and experimental geometrical configurations are the impingement and the film cooling holes. The impingement is varied and the numerical and experimental results (Mensch and Thole, 2015b) show good agreement between area-averaged film cooling effectiveness and impingement temperature coefficient. Also, changes in height have resultant effects on the heat transfer coefficient. However, performance of thermal barrier coating on the conjugate heat transfer in turbine parts is examined in (Mensch et al., 2014). Internal impingement jet cooling and film cooling at different blowing

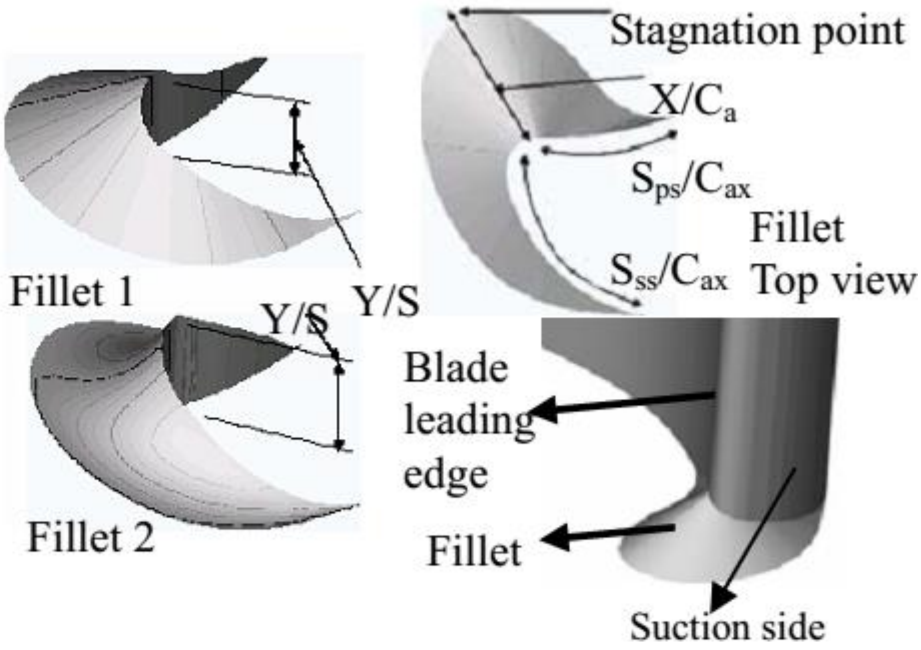

Figure 2-1: Leading edge fillet geometry (Mahmood and Acharya, 2007)

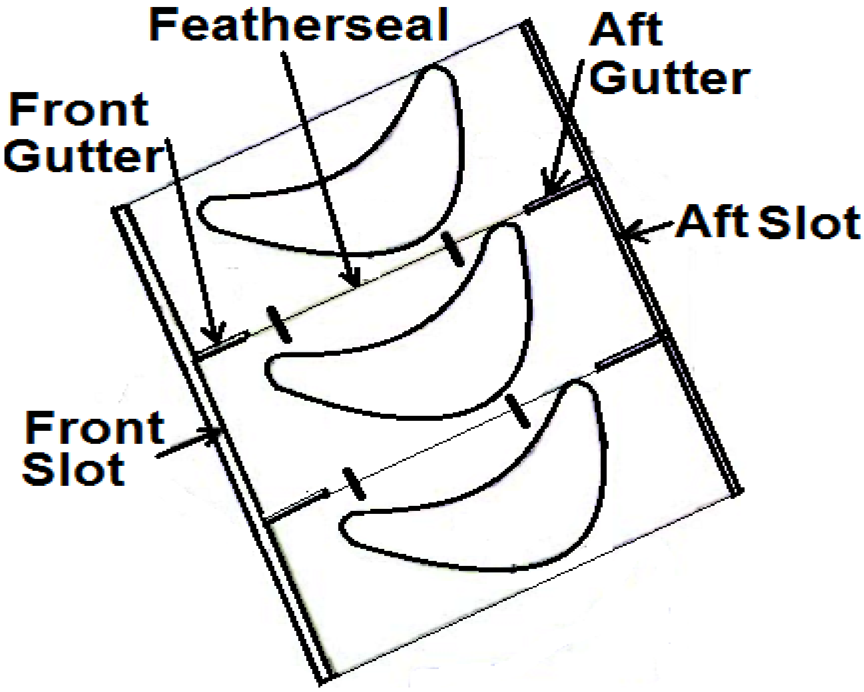

Figure 2-2: Schematics of leakage slots and gutters (Ranson et al., 2005)

ratios with and without thermal barrier coatings are tested and computed numerically. Thermal barrier coating is found (Mensch et al., 2014) to improve the overall effectiveness more than increasing the blowing ratio of the film cooler. Film cooling coverage on the endwall is enhanced with thermal barrier coating.

Computational results (Mensch et al., 2014) show that there is wide variation in the temperature gradient within the impingement passage at the endwall. Radomsky and Thole (Radomsky and Thole, 2002) studied high free stream turbulence level as it affects the heat transfer in a turbine passage. The mean and fluctuating velocities are captured at low (0.6%) and high turbulence (19.5%) intensities. At low turbulence level, the velocity profile indicates a linear behaviour with distance from the wall while at high turbulence level, the mean velocity profile indicates fully developed turbulent profile. In (Lynch and Thole, 2008, Lynch and Thole, 2011), adiabatic effectiveness and heat transfer of the endwall with the flush slot upstream of the leading edge and mid-passage gap on the endwall are presented experimentally and numerically. This work (Lynch and Thole, 2008) also considered the leakage flow and the thermal expansion of the endwall as a result of high temperature. Findings (Lynch and Thole, 2008) show that better coolant coverage, lower heat transfer and higher cooling effectiveness are achieved with reduction in the slot width at constant blowing ratio. Effectiveness level lowers as the axial distance of the slot moves downstream and the trajectory of the coolant flow is influenced by the trajectory of the complex secondary flows at the endwall(Lynch and Thole, 2008). In (Lynch and Thole, 2011), heat transfer coefficient around the throat region are higher for the endwall with a mid-passage gap than for endwall without the gap. However, heat transfer increases at the throat region from the coolant jet coming from the mid-passage gap. Adiabatic effectiveness and convective heat transfer are measured by (Thrift et al., 2011a, Thrift et al., 2011b)on an axisymmetric contoured endwall. Planar endwall passage measurement is compared with contoured endwall passage. Two dimensional leakage slot normal to the endwall is placed upstream of the leading edge of the vane cascade. In addition to this, film cooling holes are placed at the end wall passage(Thrift et al., 2011a). Results (Thrift et al., 2011a) indicate that contoured endwall assisted in the axial spreading of the leakage coolant jet over the endwall compared to the plane endwall whereas flat endwall provides better film cooling coverage. In general, increase leakage and film cooling mass flow rates in (Thrift et al., 2011a) increase the film cooling effectiveness and consequently better cooling coverage. In (Thrift et al., 2011b), there is reduction of heat transfer on the contoured endwall relative to planar passage. However, increase in the leakage flow jet leads to increase in the adiabatic film cooling effectiveness close to the suction side. The effect of free stream turbulence intensity, turbulence length scale and exit Reynolds number on the surface heat transfer are tested by (Carullo et al., 2011, Nasir et al., 2009) at realistic engine Mach number conditions. In,(Carullo et al., 2011) free stream turbulence are generated by passive grid at 2%, 12% and 14% at the cascade inlet and the exit Mach numbers used are 0.55, 0.78 and 1.03. High inlet turbulence are shown by (Carullo et al., 2011, Nasir et al., 2009) to augment the heat transfer on the pressure and suction sides of the blade near the endwall. The numerical computations of the heat transfer conformed to experimental results in (Carullo et al., 2011, Nasir et al., 2009) except where TEXSTAN in (Carullo et al., 2011) are found to over predict the heat transfer level at high free stream turbulence level. Convective heat transfer due to free stream turbulence is reported (Thole et al., 2002). The regions studied include the endwall, mid span and the stagnation area of the turbine vane. The results show that the available correlations (flat plate and the simple cylinders-in-cross-flow) are not accurate in predicting heat transfer augmentation for a turbine vane. At the stagnation region (Thole et al., 2002), the fluctuating velocities are anisotropic in form.

Discreet film cooling holes and leakage flow slots are place at the endwall according to(Thrift et al., 2012). The orientation and position of an upstream leakage slot on the cooling of low pressure turbine blade are researched. Two upstream slots geometries (45° and 90°) and several leakage mass flux ratios are employed. The findings (Thrift et al., 2012) are shown to have effect on the endwall cooling performance and the flow field at the stagnation plane. The 45° upstream slot geometry is shown to have better improvement in the endwall cooling coverage compared with 90° slot. Coolant jet injections at 90° also resulted in the formation of large leading edge vortex. The effect of leakage flow rates; expansion and contraction of combustor-turbine interface on endwall cooling performance are done by (Cardwell et al., 2007). Increase in mass flow rate of the slot leakage flow between combustor and turbine leads to increase in the local adiabatic effectiveness level. However, increasing the width of the interface in (Cardwell et al., 2007) reduces the coolant coverage at the endwall.

A high lift and high stagger angle front loaded blade profile is contoured close to the endwall and is studied experimentally and numerically (Sangston et al., 2014). The contoured blade surface at the endwall gives a fillet. Total pressure loss measurement downstream of the blade gives a mixed out mass average endwall and passage reduction of about 23% and 10% respectively. The endwall fillet reduces the turbulent kinetic energy and the Reynolds shear stress magnitudes throughout the passage. In summary (Sangston et al., 2014), stagger angle has significant effect on the high lift front loaded low pressure turbine endwall loss.

Experimental effect of the combustor exit profile by non-reacting simulator on the turbine research facility is carried out by (Barringer et al., 2007, Barringer et al., 2009a). Annular turbine ring is modeled for the experiment to provide a combustor exit pressure and temperature profiles with the associated turbulence level. According to the results in (Barringer et al., 2007), several inlet flow physics profiles to the turbine are generated representative of the actual engine conditions which have varying significant influences on the local aerodynamics and heat transfer. Besides, results (Barringer et al., 2009a) show that with an increase in the heat transfer near the mid-pitch with increasing distance into the passage occurred closer to the inlet of the passage. Inlet pressure profile have significant varying size, strength and path effects on the secondary flows near the endwall (Barringer et al., 2009a) which resulted in the wide variation in the Nusselt number distribution on the endwall. Thermal and flow field associated with turbine aero-engine are previously reported by (Vakil and Thole, 2005, Barringer et al., 2002). Combustor simulator is used (Vakil and Thole, 2005) to generate a representative of the aero-engine flow-thermal condition. In the measurement (Vakil and Thole, 2005), high penetration of the dilution jets on the flow and thermal fields resulted in high turbulence flow fields. The dilution jet and the main stream interaction essential produces what is called ‘kidney-shaped’ thermal field due to counter rotating vortices(Vakil and Thole, 2005). However, the flow field simulation was presented with no downstream turbine section in (Barringer et al., 2002). The dilution jet turbulence level is found by (Barringer et al., 2002) to be in the range of 15-18% at the exit of the combustor with a length scale corresponding to the dilution hole diameter. According to (Barringer et al., 2002), the total pressure exhibits a profile different from a uniform/turbulent boundary layer. A study of migration of different inlet radial flow physics profiles of combustor exit is examined by(Barringer et al., 2009b). Several inlet and exit radial profiles of temperature and pressure were tested. A reduction in temperature is observed (Barringer et al., 2009b) near the outside diameter for all the inlet profile studied. The profile of the total pressure near the endwall affects the redistribution of stagnation enthalpy though the turbine passage(Barringer et al., 2009b).

Experimental investigation of the flow structure with the use of the leading edge fillet is conducted by (Mahmood and Acharya, 2007, Mahmood et al., 2005). Mahmood *et al.* (Mahmood et al., 2005) investigated the flow structure and heat transfer in a linear blade cascade with and without leading edge fillets. Four different profiles are developed and tested in succession (Mahmood et al., 2005) by putting each of the fillet at the endwall-leading edge junction. Results (Mahmood and Acharya, 2007, Mahmood et al., 2005) show that the use of the fillets reduce the size of the vortex structure and with associated pressure loss coefficient reduction at the leading edge. In (Mahmood et al., 2005) concave fillet also shows a promising reduction in the Nusselt number distribution at the endwall when compared with the baseline. There is also reduction in the pitch angle of local flow at the leading and trailing edges of the turbine blade passage (Mahmood and Acharya, 2007). Measurement of endwall heat transfer are reported (Lynch et al., 2011a) with nonaxisymmetric endwall contouring and flat endwall without contouring in a low pressure turbine. The effect of varying the inlet Reynolds number for both baseline without contouring and contoured endwall is reported (Lynch et al., 2011a). Contoured endwall is found to reduce the strength of the passage vortex and heat transfer is found to reduce by about 20% in the region of high heat transfer. It is shown by (Lynch et al., 2011a) that the effect of endwall contouring heat transfer is not dependent on the cascade exit Reynolds number.

The possibility of using the leakage slot between the combustor and the turbine blade for cooling is investigated (Thrift et al., 2013, Thrift et al., 2012). Four different angles (90°, 65°, 45° and 30°) of combustor-turbine slot interface orientations located at 0.17Cax upstream of the linear turbine cascade are employed to see the effect on the net heat transfer. Reducing the slot angle to 45° provides as much as 137% reduction in the averaged heat load at the endwall(Thrift et al., 2013). High slot angles (90° and 65°) lead to the formation of large leading edge horse shoe vortex(Thrift et al., 2013). At all inlet angle (Thrift and Thole, 2012), a vortex turning into the endwall is found for low momentum injection.

2.2 Turbine Film-cooling Schemes

Computational and Experimental measurements are carried out by (Knost and Thole, 2005) on two end wall film cooling hole structures combined with cooling from flush slot (Fig. 2.2). Included in the second cooling hole scheme is the gutter having the potential of coolant leakage. The coolant is injected at angle 30 deg from the end wall hole cooling schemes systematically arranged along iso-velocity lines at the end wall. In (Knost and Thole, 2005), two difficult regions (leading edge and pressure side end wall junction) to be cooled are presented. At the upstream of the pressure side, the jets are seen to separate from the surface and also at the downstream portion of the passage, the jets are also observed to impact effectively on this region. Thermal barrier coating is another way of insulating the turbine from hot gases. Thermal barrier coatings blockages on cylindrical and shaped film cooling holes in a turbine system is simulated by Whitfield et al.(Whitfield et al., 2015). At high blowing ratios, the effectiveness of the cylindrical and shaped holes decreases by about 75% from blockage. However, shaped holes are found by (Whitfield et al., 2015) to performed better than cylindrical holes in all cases studied. The region of study focus by (Sundaram and Thole, 2008) is the vane end wall junction close to the vane stagnation point where film cooling is a challenge because of the development and swiping action of the horse shoe vortices. Bumps and trenches configuration holes are placed at four cooling hole diameters from the stagnation and upstream slot is also placed at seventeen cooling hole diameters from the leading edge. Trench placed along the row of film-cooling holes enhances adiabatic effectiveness level better than individual hole trenches and bumps for various blowing ratios. Experimental and computational studies (Colban et al., 2008, Colban et al., 2007, Colban and Thole, 2007) are carried out on cylindrical and fan-shaped film cooling holes at the end wall, vane surface at varying freestream turbulence intensities. In (Colban et al., 2008), two staggered rows of cylindrical and shaped film cooling holes are placed upstream of a vane passage each. Fan-shaped holes are found to increase film cooling effectiveness by 75% over cylindrical holes. Increase in the blowing ratio also shows promising result for fan-shaped holes over that of the cylinder holes. Also in (Colban et al., 2007), the renormalization group (RNG) k-ε turbulence model gave a better prediction of the average film cooling effectiveness and v2-f turbulence model accounted for a more accurate flow physics representation. Film cooling benefit and the inherent consequent of total pressure loss is studied by (Colban and Thole, 2007). According to (Colban and Thole, 2007), shaped film cooling holes generated less total pressure loss compared to cylindrical holes and shaped holes also provided better cooling to the end wall region. However, both shaped hole and cylindrical hole increased the aerodynamic loss through the turbine blade passage. Computational predictions of film cooling and heat transfer at the end wall are carried out by (Hada and Thole, 2011, Lynch et al., 2011b). The geometry involved in (Lynch et al., 2011b) included nonaxisymmetric end wall contouring. Comparisons are made with experiment as regards exit flow structure, end wall heat transfer and end wall film cooling. In terms of film cooling, simulation agreed closely with experiment. There is also clear indication by both computation and experimentation that the nonaxisymmetric end wall inhibits the spread of the film cooling flow at the end wall. However, in (Hada and Thole, 2011), combustor turbine junction and the mid-passage slot are considered. Results show that by raising the combustor slightly higher than the downstream part of the end wall, coolant coverage is found to be more effective. The effect of well-sealed mid-passage gap that is aligned or misaligned and roughness on end wall film cooling are investigated by (Cardwell et al., 2006). Mis-aligned mid passage gap (suction side of the end wall higher than pressure side of the end wall) leads to acute reduction in the film cooling effectiveness. A thicker boundary layer has a significant effect on the jet separation from the end wall as regards the high blowing ratio. Sundaram et al. (Sundaram et al., 2008) investigated the effects of contaminant deposits on the film cooling along pressure side (PS) of the vane end wall;. The film cooling hole arrays were placed along the end wall of the PS of the vane passage. The study (Sundaram et al., 2008) is based on semi-elliptical shaped holes placed along the PS to simulate the various row depositions of the film cooling holes. It is discovered that the deposits hindered the mean adiabatic effectiveness level downstream of the film cooling hole arrays by diverting the coolant jet towards the vane end wall junction on the PS. According to (Sundaram and Thole, 2007), the effect of partial film cooling hole blockage by deposits and the effect of spallation thermal barrier coatings are carried out. Film cooling holes at the end wall are blocked at the exit by 25% conforming to the required geometrical dimensions. The results (Sundaram and Thole, 2007) show that deposits near the film cooling hole exit sometimes increase the cooling effectiveness particularly at the leading edge. Also spalled end wall and increase in the hole blockage led to deterioration in the cooling effectiveness with increase in blowing ratio.

Film cooling flow field measurement are evaluated by (Sundaram and Thole, 2009). An array of two dimensional film cooling holes in a trench with an interface slot is placed upstream of a vane leading edge. Results show that the trench produced better overall cooling when compared with the case of no trench arrangement since the coolant are found to attached to the end wall. The use of the trench (Sundaram and Thole, 2009) also gives rise to flow reversal at the leading edge and therefore resulting in high vorticity, hence, adiabatic effectiveness is enhanced. Thole and Knost (Thole and Knost, 2005) studied the effects of injecting coolant at different flow rates through a combustor turbine interface and compare the effect of the leakage flow has on the downstream film cooling injection. Upstream slot and some arrays of film cooling holes are placed at the end wall of a vane passage. The duo of film cooling and slot flow cases are sufficient for significantly cooling the end wall. At constant slot flow with increased film cooling flow rate, measured thermal fields show a change in the passage vortex. The slot flow is entrained in the passage vortex and transported towards the suction side (SS).

The effect of blocking within impingement or sand-laden film cooling stream is investigated (Cardwell et al., 2010). The turbine configuration used is a double wall liners commonly used for cooling of internal and external parts. Four different geometries of the impingement and film cooling hole liners are experimented. The quantum of blocking increases as temperature is increasing in all cases tested. The study (Cardwell et al., 2010) also shows that impingement can be used to break up larger particles so that the tendency of film cooling hole blocking can be reduced.

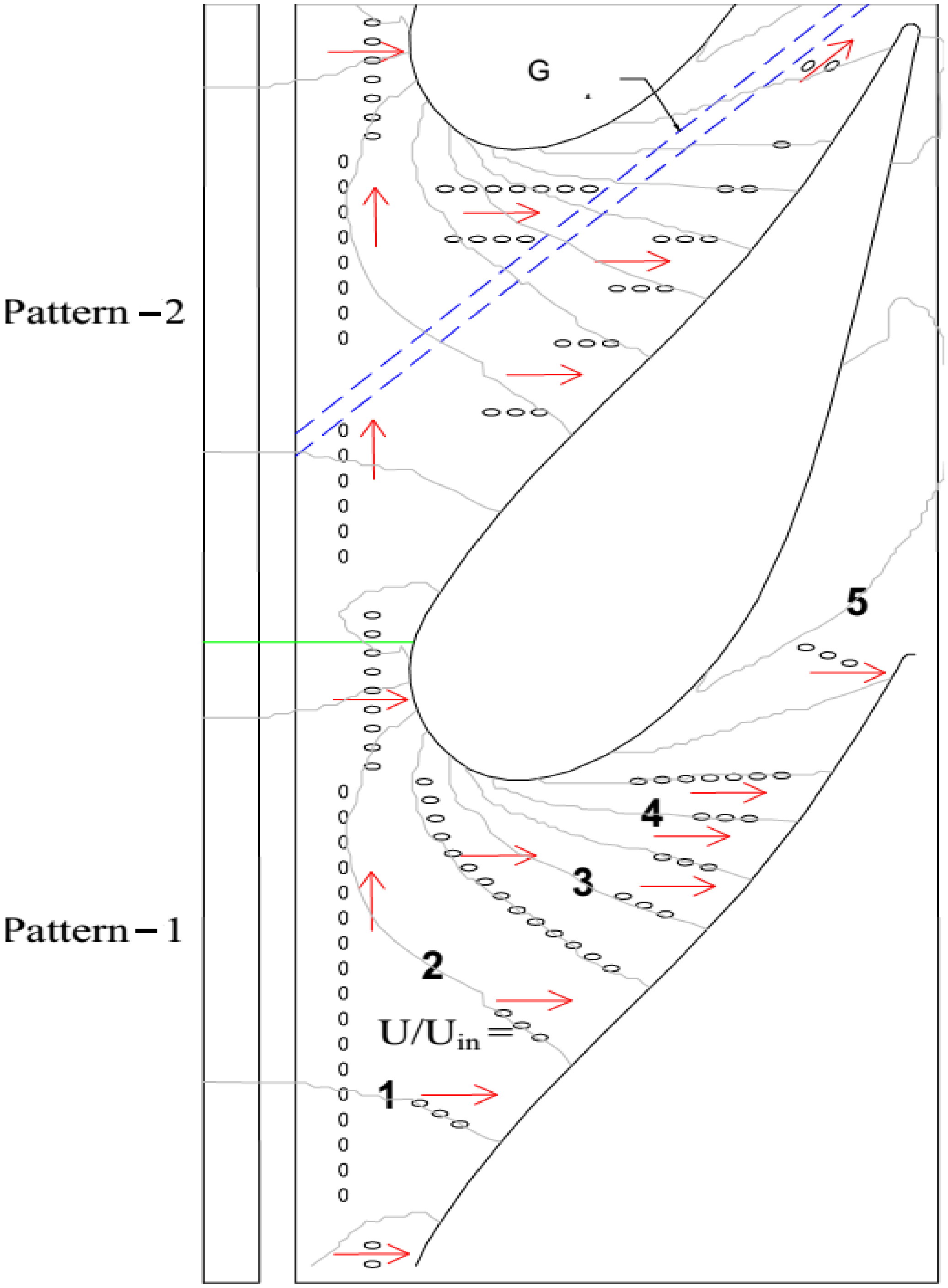

Figure 2-3: Two film-cooling patterns with iso-velocity contours and injection directions (Knost and Thole 2005)

Staggered film cooling and impingement hole liners is found to attract lesser deposit.

Experimental and computational studies of flat plate film cooling geometries have been researched by(Eberly and Thole, 2014, Harrington et al., 2001). Time resolved particle image velocimetry data for a film cooled flow at low and high density ratios is studied(Eberly and Thole, 2014). Cylindrical laterally spaced film cooling holes with axial geometric configuration is employed in(Eberly and Thole, 2014). Time resolved flow field data of the shear layer vortices are consistent with momentum flux ratio. The adiabatic effectiveness shows increased spreading at high density for the same mass flux ratio. Increase in momentum leads to jet separation. However, in (Harrington et al., 2001), results show that at blowing ratio of 0.65, there is separation of the coolant jet downstream of the hole. The high free stream turbulence produces a larger effect for lower blowing ratios.

A number of recent researches have been carried out on multiphase particle decomposition in gas turbine components; on end wall film cooling holes in transverse trenches (Lawson and Thole, 2012b), on end wall film cooling (Lawson and Thole, 2012a), on showered head with staggered film cooling holes (Lawson and Thole, 2012a) on a nonaxisymmetric contoured end wall with film cooling (Lawson et al., 2013) and on a gas turbine end wall with impingement and film cooling (Mensch and Thole, 2015a). Results show that: 0.8D trench performed better than other configurations with and without decomposition on the surface(Lawson and Thole, 2012b), about 30% reduction in the adiabatic effectiveness is recorded(Lawson and Thole, 2012a), deposition decreases with increase in coolant blowing ratio and effectiveness reduction increases with an increase in particle temperature(Lawson et al., 2012), contouring reduces decomposition around film cooling holes and decomposition reduces cooling effectiveness by 50% on a flat end wall and 40% on a cooled contoured end wall (Lawson et al., 2013) and the roughness effects of the decomposition neutralizes the insulating effect on the end wall.

2.3 Flow Structure and Computational Predictions in Past Studies

Past studies by (Kang and Thole, 2000), (Hermanson and Thole, 2002), (Radomsky and Thole, 2000), and (Harmanson et al., 2002) have shown the evolution of the pressure side-leg vortex and suction side-leg vortex around the leading edge of a vane cascade. The effects of the turbulence and boundary conditions at the cascade inlet contributed to the passage vortex formed in the vane passage downstream. The endwall boundary layer and cross flow caused by the pressure difference between the pressure side and suction side are responsible for the development of the passage vortex (Acharya and Mahmood, 2007).

Employing the blade/vane-endwall junction fillet and endwall contouring to reduce the strength and effects of the endwall region secondary vortices has been investigated by (Lynch et al., 2011a, Mahmood and Acharya, 2007, Mahmood et al., 2005, Saha and Acharya, 2008, Shih and Lin, 2003, Stitzel and Thole, 2004, Thrift et al., 2011b, Zess and Thole, 2002) . Computational studies of heat transfer at the endwall are performed at different Reynolds number on flat and non-axisymmetric three dimensional contoured endwall with upstream slots for film cooling (Lynch et al., 2011a, Saha and Acharya, 2008, Stitzel and Thole, 2004, Thrift et al., 2011b). Their findings show that heat transfer is affected by secondary flow fields, variation in upstream slots geometry and cooling schemes. The deployment of three dimensional contoured endwall is also found to reduce heat transfer and total pressure loss (Saha and Acharya, 2008). The effects of using leading-edge fillets on the secondary flow fields, axial vorticity, pressure loss coefficient and yaw and pitch angles in a turbine passage are investigated experimentally by these researchers (Mahmood and Acharya, 2007, Mahmood et al., 2005, Zess and Thole, 2002). Two dimensional linear blade cascade is setup to investigate the role of these leading-edge fillets at the end wall junction. These investigators demonstrated and found out that the leading-edge fillet changes the location and interaction of these secondary flows which are responsible for reduction in the surface heat transfer and aerodynamic loss in a turbine passage. Leading-edge fillet reduces axial vorticity, turbulent intensity and Nusselt number distribution upstream of the throat. According to the computational study of Shih and Lin (Shih and Lin, 2003), introduction of the inlet swirl to a vane passage and leading edge fillet on the vane-endwall reduces aerodynamic losses and heat transfer in the turbine vane passage. The investigations are based on two leading-edge fillet geometries whose thicknesses fade on the vane surface and endwall respectively. Inlet swirl angle between (+30 to -30)deg and vice versa were invoked for each fillet configurations. Comparison are made with baseline and the results show that both leading-edge fillet and inlet swirl have significant reduction potential in surface heat transfer and aerodynamic loss. In all cases studied by (Shih and Lin, 2003), a reduction of about 40% in the stagnation pressure differential from the nozzle’s inlet to the exit was recorded. Leading-edge contour geometries are also studied by (Becz et al., 2003, Becz et al., 2004) to provide information on the average total pressure loss coefficient of the secondary flows in a high turning linear blade cascade. Bulbs and parabolic fillet configurations are used at the leading-edge of the turbine profile. Results (Becz et al., 2003, Becz et al., 2004) show that reduction achieved by the use of the bulb/fillet differs and that the best features of each geometry can be combined to achieve maximum reduction in the pressure loss coefficient. Numerical and experimental investigations by Sangston et al. (Sangston et al., 2014) in a low speed linear turbine cascade employ alteration of the airfoil profile at the endwall region. The results of (Sangston et al., 2014) show a change in the strength and location of the horseshoe and passage vortices compared to the case without any airfoil profile modification. There are reduction in total pressure loss, turbulent kinetic energy and magnitude of Reynolds normal stress throughout the passage. Flow visualization techniques are employed by (Aunapu et al., 2000) to capture the secondary flows in a large-scale two half-blade cascade (Fig.2.3). The research in (Aunapu et al., 2000) is primarily on the installation of end-wall jets to reroute the passage vortex path and essentially reduce the ‘hot spots’ effect on the suction side of the blade. Torre et al.(Torre et al., 2010) use a new design approach for the blade cascade endwall. This approach (Torre et al., 2010) is based on the use of contoured endwall to control the formation of horseshoe vortices so that the formation of secondary vortices at the suction side passage can be effectively reduced. The numerical and experimental study (Torre et al., 2010) indicate attenuation of the secondary flows, 72% reduction in the secondary kinetic energy helicity and 20% reduction in the mixed-out endwall losses in the turbine passage.

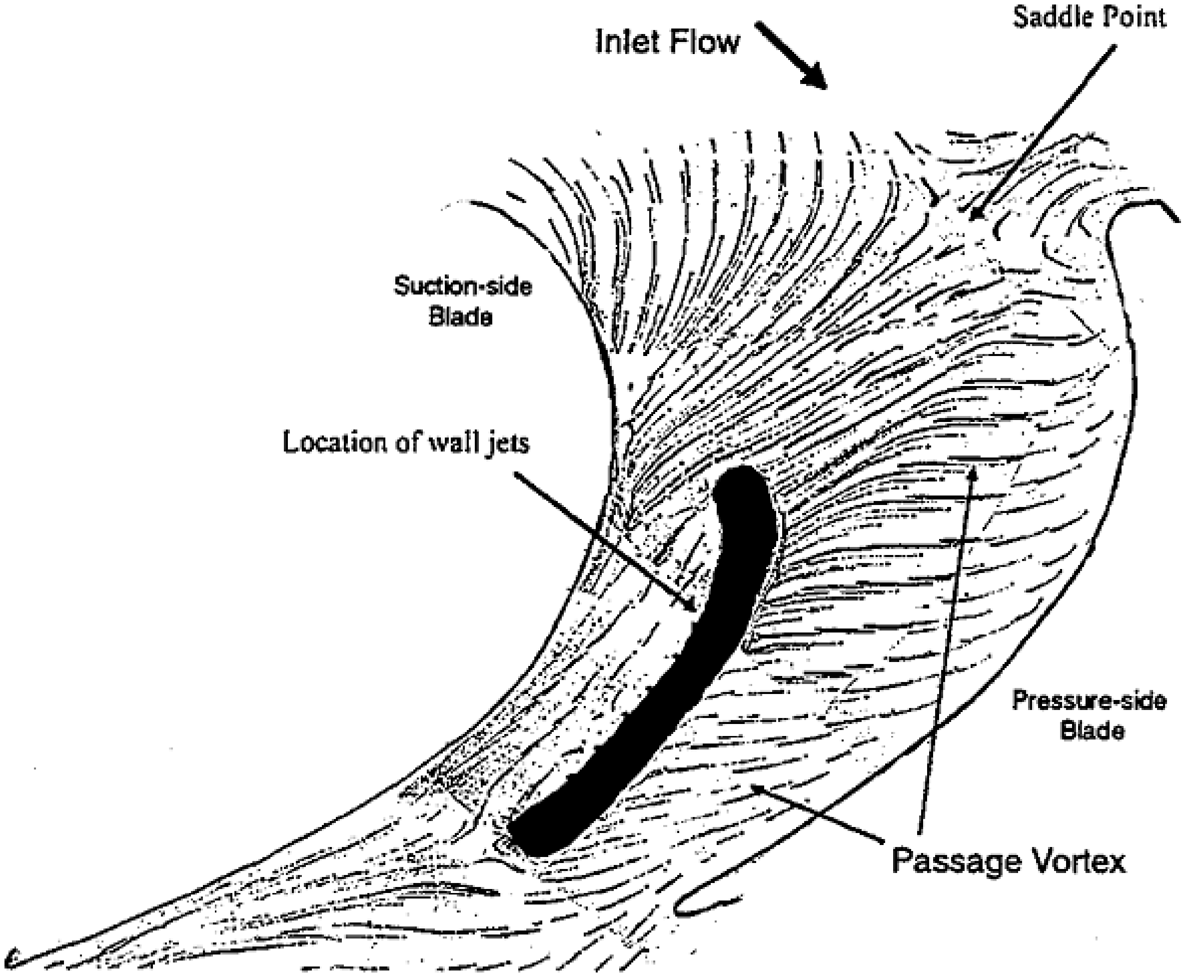

Figure 2-4: Ink-dot flow visualisation on endwall; center line wall jets (Aunapu et al., 2000)

3. CHAPTER 3: EXPERIMENTAL METHODOLOGY, INSTRUMENTATION AND UNCERTAINTIES

3.1 Test section and instrumentation description

The Test Facility was designed and constructed along with my colleague (K. Arnachellan) a master student on the same Test-rig. The cascade test section is part of an atmospheric low-speed wind tunnel where the flow density and temperature remain the same as the laboratory air. The flow in the open-circuit wind tunnel is generated by the suction of two duct-fans (axial-flow) connected in series at the end of the wind-tunnel.

The cascade geometry and vane-blade profile are obtained from the 1st stage nozzle guide-vane (NGV) passage geometry and vane profile, respectively, of the GEE^3 engine turbine (Timko, 1990). The test section houses seven two-dimensional blades and some measurement instrumentations (Figure 3.1). The test vane-blades are 6 times the actual size of a GEE^3 vane profile. The vane profile is just extruded along the span to create a two-dimensional vane-blade. The pitch-spacing between the blades is also six times the pitch of the vane passage at the hub-side in the actual $GE\text{-}E^3$ engine. The scaled-up geometry in the cascade then provides a Re at the exit of the vane passage close to that in the real engine. However, because of atmospheric wind tunnel, the compressibility, Mach number, temperature, and buoyancy effects are not matched with the real engine conditions. On the other hand, the large geometry of the cascade passage is beneficial for the measurements of the secondary flows with the conventional intrusive probes as the flow features are then also scaled up in the similar order of magnitudes. The geometric parameters of the vane-blade are shown in Table 3.1. The blades are fabricated from polycarbonate, coated with polyurethane to provide a smooth surface. The yellow region of Fig. 3.1 is the measurement area between the blades 3, 4 and 5. Seven blades are chosen to provide the periodic flow conditions between the blade passages without the need of tailboards. By-passes are introduced to bleeds the flow through the outer sides of blades 1 and 7 so that a periodic flow condition will sufficiently be produced. Twenty one pressure tapes are distributed along the profiles of blades 3, 4, and 5 at the mid-span (0.5s) to capture the static pressure and to confirm the periodicity of the blade. Hollow cores inside blades (3, 4, 5) as shown in Fig. 3.1(c) and cut-out section at the top side of the endwall of the measuring blades are used to route-out plastic tubes from the blade profile pressure taps to a manual multi-scanner valve. The scanner is then connected to a pressure transducer through a plastic tube. Arnachellan (Arnachellan, 2017) provides details of the multi-port manual scanner. Various slots are machined at the top endwall according to Plane-1 to Plane-4 of Fig. 3.1(b) for the insertion and traveling of probes that scan the flow-field in the planes. The slots are masked with overlapping taped to reduce leakage during data acquisition. The yaw orientations, global and the local coordinate systems employed for the measurement are shown in Figure 3.1b. Reference properties are measured at 2.5C_{ax} upstream of the leading edges of the blades (Figure 3.1a). The measured reference properties outside the boundary layer are spatially averaged to be reported and used to normalize other measured properties. A Passive turbulence grid of 6mm cylindrical rods equi-spaced is placed at 6.5C_{ax} from the leading edge to generate isotropic turbulence for the flow upstream of the cascade passages. Two dimensional contraction fitted with honeycomb are installed at the tunnel entrance to straighten and accelerate the flow smoothly towards the turbulence grid along the rectangular cross-section passage. At the test section area (endwall), film cooling system is installed to provide cooled or uncooled flows into the cascade as per the need. Various designs of the film cooling hole geometries are examined for effectiveness and coverage at the endwall region. Here-dimensional fillets are also designed and employed at the junction of the blade-endwall to the effects on the heat transfer and the flow structure at the near endwall region. The inlets of two duct-fans (7.5 kW and 15 kW) are connected downstream of the cascade far away to minimize the noise of fan rotation in the cascade flow. The fans provide enough flow rate for the Re to be about Re250, 000 at the cascade inlet.

A five-hole total-static pressure probe of tip diameter 1.6 mm is employed for the flow measurements in Planes-1 to 4 of Fig. 3.1(b). The five-hole probe is mounted on a two-axis traverse system which is driven by a Velmex^{TM} motor controller. The global coordinate system (X_G, Y_G, Z_G) originates from the leading-edge at the bottom endwall. The various local coordinate systems originate from the pressure or suction side of the blades and are shown in Figure 3.1b. Five pressure transduces are employed to capture the analog pressure signals simultaneously at the five ports of the five-hole pressure probe. Appropriate excitation voltages are supplied by the DC power supply sources (30V-10A) to power all the pressure transducers used in the experiments. The pressure signals from the probe are transferred through silicon tubes to the transducers. The voltage signals from all the pressure transducers are digitized by the National Instrument™ data acquisition system. An in-house built LabVIEW™ computer programme is configured to communicate with the data acquisition system and control the traverse movement through the motor controller. The LabVIEW™ programme records the voltage signals at a frequency of 100Hz for 2 seconds from each transducer and time-averages the signals. The traverse movement in a measurement plane is controlled with a location grid (computer file with spatial locations) that has finer spatial locations close to the endwall. The appropriate calibration curves are then applied to the time-averaged data of the various transducers. Fig. 3.2 shows a sample calibration for one of the transducers used for the data acquisition. The rest transducers calibrations are in (Appendix A). Calibration and data reduction and calibration for the five-hole probe followed (Ligrani et al., 1989b, Ligrani et al., 1989a). Therefore, the local velocities (u, v, w), total and static pressures are obtained from the measured data and calibrations. The reduced data from the five-hole probe measurements accounted for the spatial distances between the probe ports and streamline curvature at the probe tip according to (Ligrani et al., 1989a).Details of the calibration procedure and graphs are in Appendix B. A Pitot-static tube of 1.7mm tip diameter is used to measure the reference properties at the reference plane. The Pitot tube is connected to separate transducers for appropriate data capturing and digitization. A Constant Temperature Anemometer (Hot wire) is also used to measure the turbulent intensity (Tu) of the free stream (U) at the reference plane. However, the present hot wire is not suitable to measure the flow inside the cascade passage, thus, is only used to measure the streamwise (x) velocity (U) at the reference plane. The zero-offset voltages of the pressure transducers at the no-flow condition were accounted for during the voltage to pressure-unit conversions in the calibrations. The bias errors of the pressure transducers were thus accounted for in the calibrations.

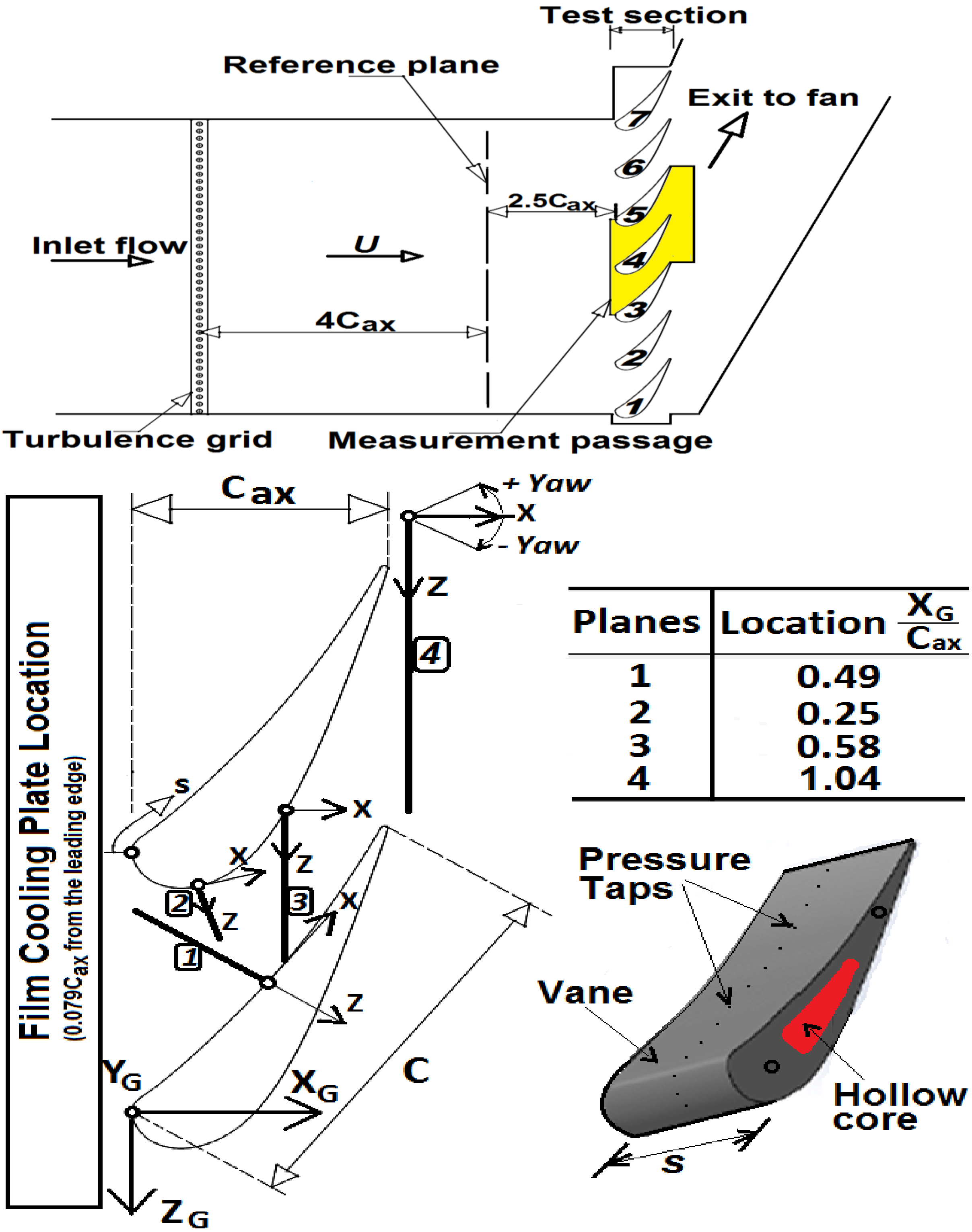

Planes	Location $\frac{X_G}{C_{ax}}$
1	0.49
2	0.25
3	0.58
4	1.04

Figure 3-1: Schematic representation of the wind tunnel test section

Table 3-1: Geometric parameters of the vane cascade

Scale factor	C_{ax} (m)	C(m)	C/S	C/P	Incidence
6	0.203	0.355	1.477	1.328	0°

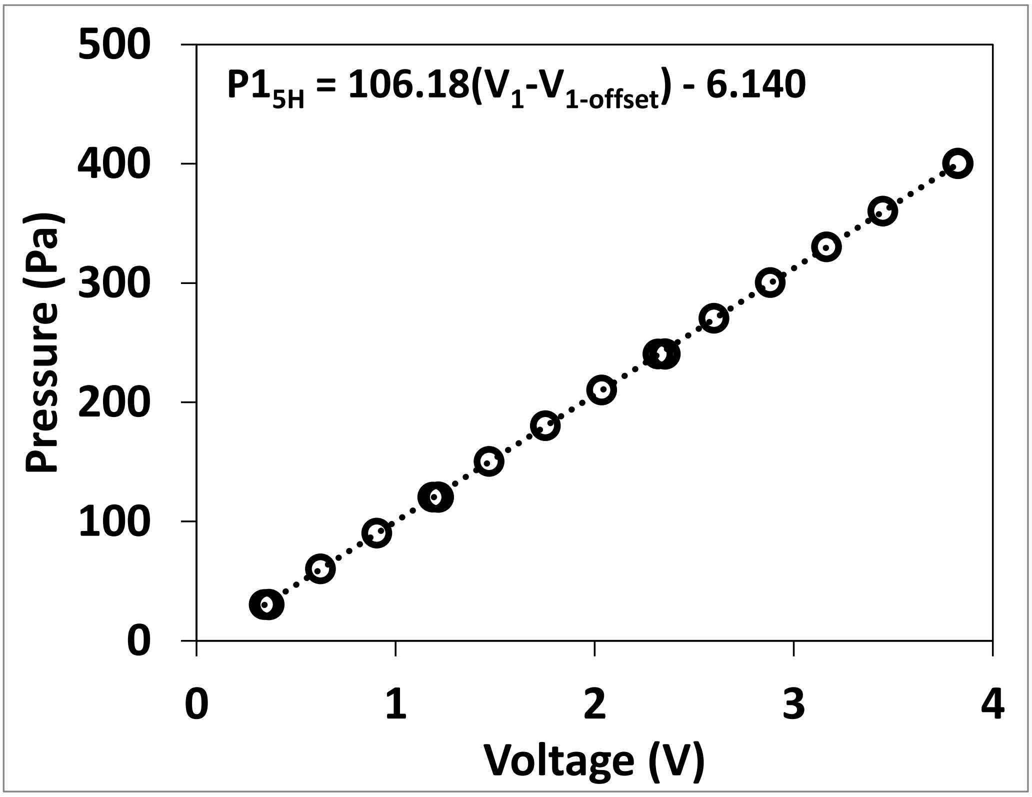

Figure 3-2: Siemens transducer calibration for five hole probe port-1(P15H)

3.2 The film cooling geometries and schemes

The film-cooling flow is supplied to the test section through various designs of cooling hole configurations in a plate located at the bottom endwall $0.079C_{ax}$ upstream of the blade leading edge as shown in Fig. 3.1(b). The secondary flow circuit employed to supply the film-cooling flow to the film cooling plate is shown in Fig. 3.3. As shown in Fig. 3.3, the film cooling flow through the channel delivered by a 1.0kW blower and an 800W blower and metered with an orifice (β = 0.7, based on ASME standards for orifice, pipes, flanges and fittings). The beta (β) ratio is the ratio of the orifice diameter to that of the internal diameter of the pipe. A pressure transducer connected to the National Instrument™ data acquisition system is used to measure the differential pressure across the orifice plate. The signal from the differential voltage is recorded in voltage and appropriate calibration is applied to convert it to the pressure unit. The ducting of the film cooling circuit includes the evaporators (H.E.) of two chilling units, a large plenum box just underneath the film cooling plate. The H.E. controls the temperature of the film-cooling flow. Figure 3.3 shows a baffle is installed in the plenum box to ensure a smooth flow of the coolant into the cooling holes. The film cooling mass flow rate are varied for different experiments by changing the fan speed and diameter of the metered pipe section. The pipes used for the film cooling include 5.08cm, 10.16cm and 15.24cm of nominal diameter as the beta ratio (ß = 0.7). The PVC flanges are used to position securely and centrally the orifice plate in the pipe. Figure 3.4 shows a picture of the film-cooling flow circuit partially. Various combinations and/or arrangements of the three available pipes, the orifices and the blower speed can be used to achieve the desired blowing ratios (M) and coolant temperature. Five blowing ratios (M = 1.0, 1.4, 1.8, 2.2 and 2.8) are used for the film cooling experiments. The ducting, film cooling plenum box and the endwall are sufficiently insulated to minimize heat transfer to the coolant flow from the outside environment. The upstream evaporator (H.E.) cools the incoming air and the downstream evaporator (H.E.) further brings the temperature down to the desired film cooling inlet temperature. This is ensured by adjusting the refrigerant flow rate in the chiller systems. With a value of 0.6 as the discharge coefficient (C_d) for the orifice plate, the mass flow rate of film-cooling flow is obtained from Eqn. 3.1. The inlet Blowing ratio (M) and the Mass fraction of the film-cooling flow can be computed using Eqns. 3.2 and 3.3, respectively. Figure 3.5 shows four configurations of the film-cooling holes in the film-cooling plate. The slot, slot-hole and hole arrays are located $0.079C_{ax}$ upstream of the blade leading-edge of the cascade. All the slots and holes are inclined at 30^o to the endwall of the cascade as shown in Figure 3.5(e). The slots and holes of Figure 3.4 (a-c) are machined into three acrylic plates of thickness 20mm, while Figure 3.4d is produced in a 3-D printing machine with zero porosity. The distinct feature of Figure 3.5(d) is that all the film cooling holes are bevelled/curved towards the cascade flow direction. Figure 3.6 shows the test section area and the instrumentation.

$$\dot{m}_{cool} = \rho C_d \left(\frac{\Pi}{4} D_{orifice}^{2}\right) \left(\frac{2\Delta P_{orifice}}{\rho\left(1-\beta^{4}\right)}\right)^{\frac{1}{2}} \tag{3.1}$$

$$M = \left(\frac{P_{plm} - P_{s,ref}}{P_{t,ref} - P_{s,ref}}\right)^{\frac{1}{2}} \tag{3.2}$$

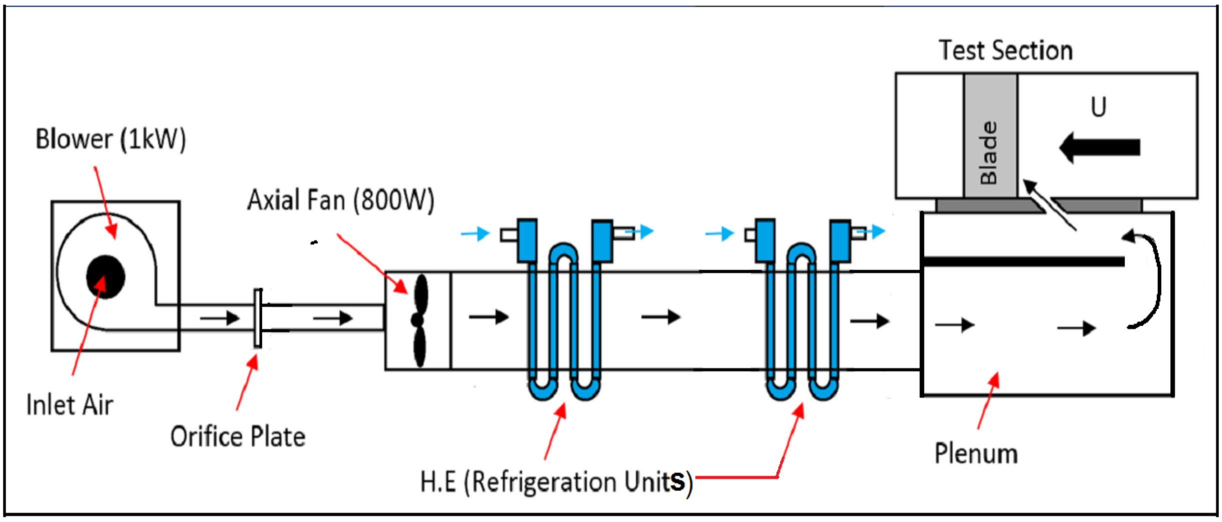

Figure 3-3: Film cooling loop and geometry

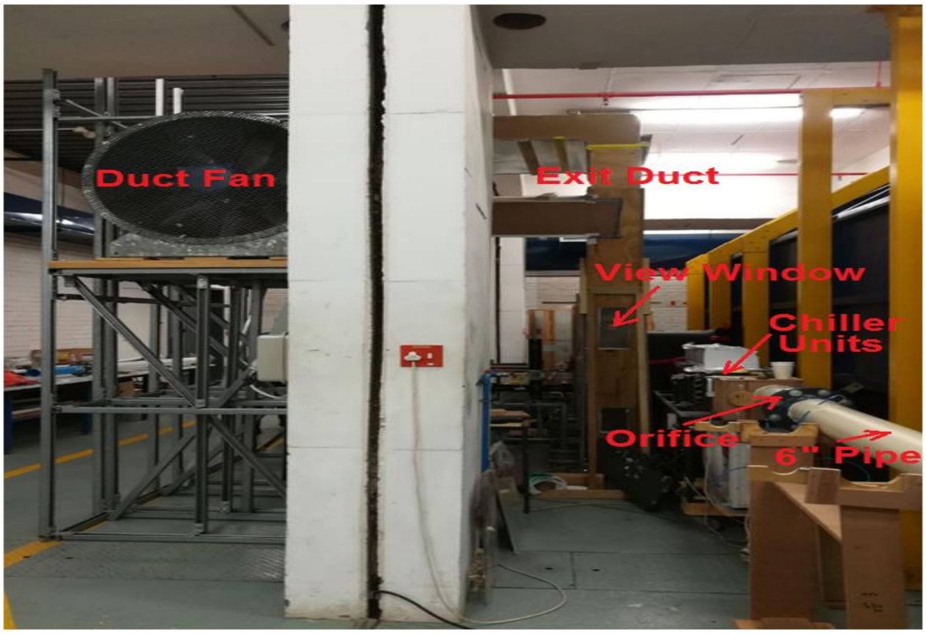

Figure 3-4: Film cooling system and the main channel blower

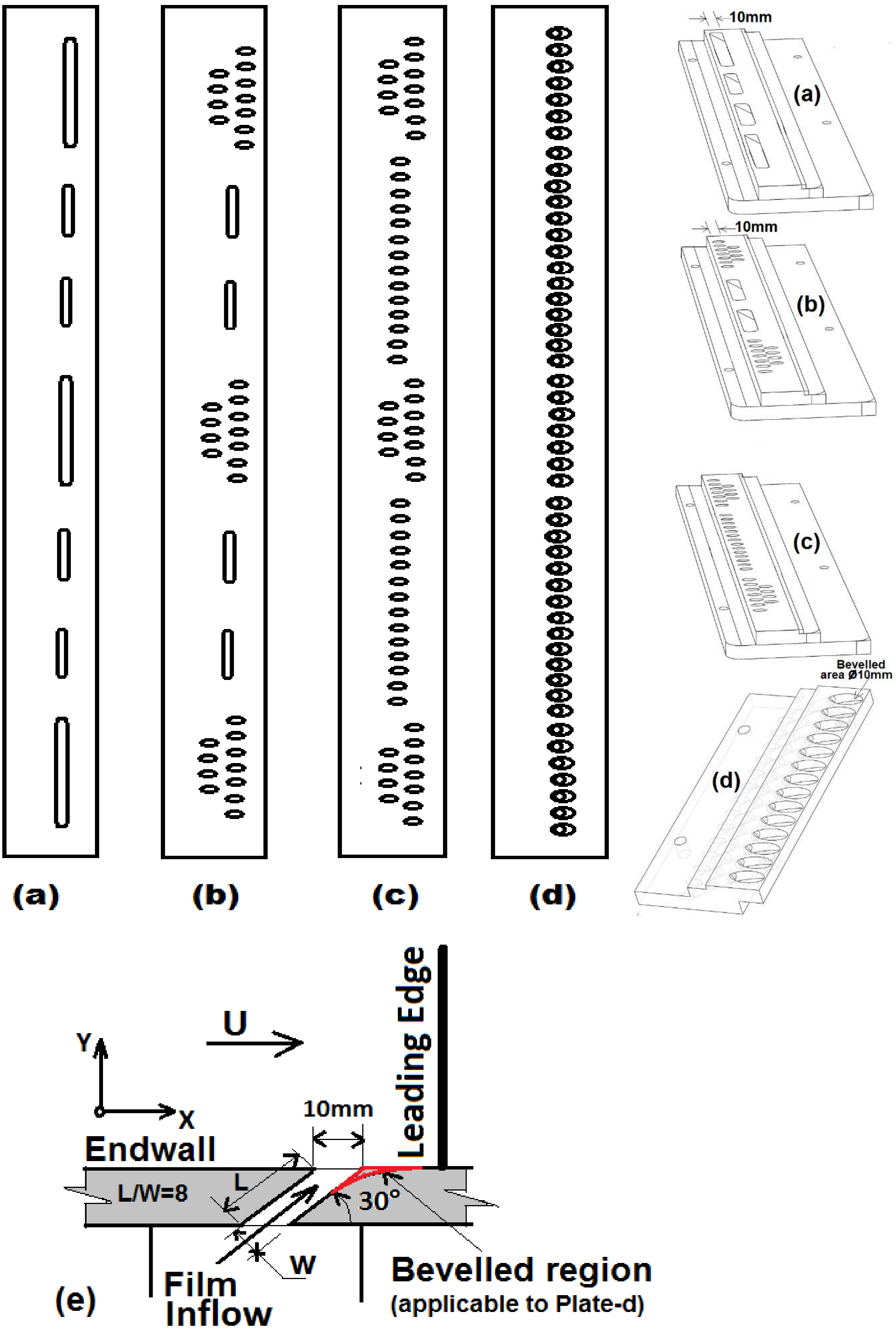

Figure 3-5: Leading edge (LE) Film cooling plates

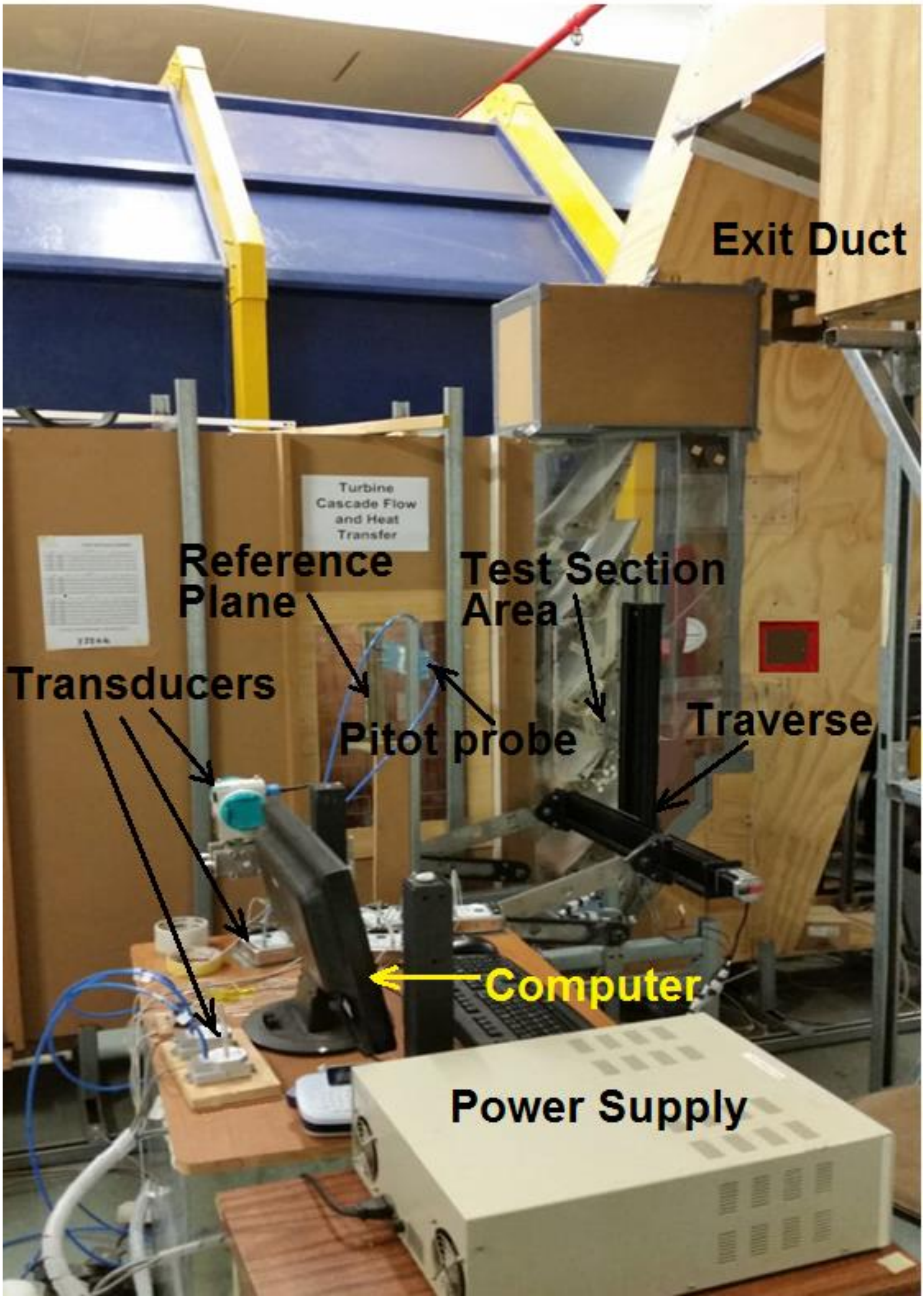

Figure 3-6: Test section area and the instrumentation

$$M_{fraction} = \frac{M_{cool}}{M_{pass}} \tag{3.3}$$

3.3 Thermocouples, Endwall Heater, Infra-red Camera locations and Descriptions

Forty five T-type thermocouples (0.25mm-gage wire) manufactured from Omega are butt welded and calibrated from 20°C to 58°C in a water bath calibrator of accuracy ±0.1°C. The tip size of the thermocouple after the welding is typically 0.5 mm. Figure 3.7 shows the calibration curves for thermocouples 34, 36, 40 and 42. These thermocouples are carefully installed at known locations on the bottom endwall. The thermocouples are numbered as shown in Figure 3.8. To install the thermocouples in the bottom endwall, thermocouples are inserted in the through-holes drilled at the known locations. The thermocouple tips are placed adjacent to the Kapton^{TM} tape (thickness 0.065mm) covering the endwall on the flow side. The Kapton^{TM} layer is covered by a layer of self-adhesive copper tape (thickness 0.035mm, width 25mm). The thermocouples are held in place in the holes with silicon glue away from the tip region. The tip region of the thermocouple in the hole is then filled in with a thermal conductive epoxy. The measuring passage is between blade-3 and blade-4. The passage is painted black (emissivity, $\varepsilon = 0.96$) for heat transfer and film cooling flow. Thus, the copper strips covering the first Kapton^{TM} layer are laid 0.5mm apart in parallel to each other along the blade pitch and soldered at the ends in serpentine pattern to convert them into one single continuous-strip electrically. A DC power source is then connected across the ends of the continuous copper strip to supply current. As the individual copper strips have uniform cross-sections and resistivity, the current density through the strips can be assumed constant. Constant heat flux can be supplied on the endwall. The heater extends upstream of the leading edge ($7C_{ax}$) and to the two neighbouring passages to ensure appropriate inlet thermal boundary layer ($(\delta/S)_T = 0.1$) and possible error elimination due to conduction. The endwall is appropriately foam insulated to reduce the heat loss by conduction. The endwall thermocouples are routed out and connected to the National Instrument data acquisition (DAQ) system controlled by LabVIEW^{TM} computer programme. The DAQ system time averages the temperature data from the thermocouples at a frequency of 60Hz for 2 sec from each thermocouple. Thereafter, appropriate thermocouple calibrations are applied. Thermocouples are also placed across the insulation layer of the bottom endwall to measure temperature difference and estimate the one-dimensional conduction losses through the endwall. For the heat transfer measurements, the conduction losses are about 2%-3% of the gross electric power input to the copper strip. The convective power from the endwall heater to the passage flow in heat transfer measurements is estimated after subtracting the conduction losses from the total heater power as shown in Eqns (3.1 & 3.2). Equations (3.2 – 3.5) also show the estimations of *Nu* and *St* based on the average convective heat flux and adiabatic film-cooling effectiveness (ε), respectively, from the measured endwall temperatures.

$$Q_{cond} = \frac{k_{insulation} * A_{Heat}\left(T_{av\_1} - T_{av\_2}\right)_{insulation}}{\left(\Delta x_{th}\right)_{insulation}} \tag{3.1}$$

$$Q_{conv} = (IV)_{pass} - Q_{cond} \tag{3.2}$$

$$q_{flux} = \frac{Q_{conv}}{A_{Heat}} \tag{3.3}$$

$$Nu = \frac{\left(q_{flux} C_{actual}\right)}{\left(T_{loc} - T_{ref}\right) k_{air}} \tag{3.4}$$

$$St = \frac{q_{flux}}{\left(T_{loc} - T_{ref}\right) C_p U_{ref} \rho_{air}} \tag{3.5}$$

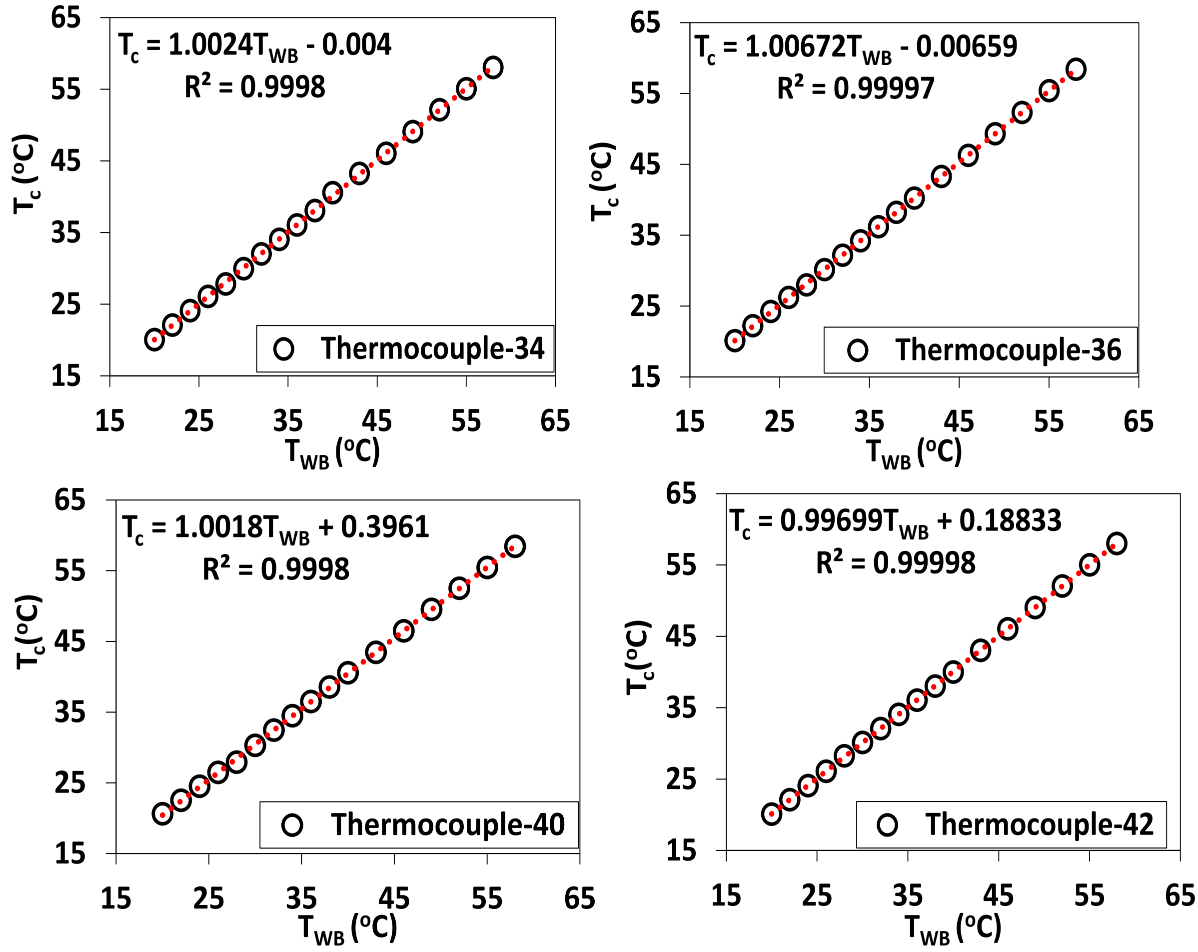

Figure 3-7: Sample thermocouple calibrations

3.3.1 Thermal probe

A suitable temperature probe is constructed in-house to obtain the temperature field of the flow close to the endwall region of the heated cascade passage between blades 3 and 4. The thermal field measurement are only limited in planes-1, 2, and 3 (refer to Fig. 3.1) upstream of the passage. The schematic construction of the temperature probe is shown in Figure 3.9. The K-type insulated thermocouple wires are butt-welded at the end to form the junction as recommended by (Han and Goldstein, 2008). The junction end of the K-type thermocouple is suspended at the end of a long rod by two hypodermic needles which are about 10mm apart. The thermocouple wires run through the hollow steel rod (5mm dia.). The thermocouple ends are connected to the DAQ system. The same water bath calibrator as for the endwall thermocouples is used to calibrate the probe. To scan the measurement planes, the temperature probe assembly is installed on the two-axis traverse system driven by a Velmex™ motor controller. . The signals from the probe are time averaged at 60 Hz over 2 sec. This probe is also used to measure the thickness of the reference thermal boundary layer. An in-house coded LabVIEW™ computer programme is employed to record the time averaged temperature data from all the thermocouples and to communicate with the motor controller. The non-dimensional temperature, Θ of the flow field is computed from the Eqn. 3.6.

3.3.2 Infrared camera

An infrared thermal-imaging camera (FLIR™ A35sc) of pixel resolution 320 by 256 pixels is employed to obtain the thermal images of the endwall during the heat transfer and film-cooling effectiveness measurements. The depth of image –pixel is 14 bit. It operates at a frame rate of 60Hz with a 48° lens. The camera is calibrated between -40°C to +550°C. Figure 3.10 shows four specific window locations to ensure that the entire endwall is completely covered by the camera images. An anti-reflection coated Zinc-Selenide (Zn-Se) window covers one cut-out hole at a time as the camera views the bottom endwall through the Zn-Se window. The IR camera is positioned upright at the centre of a window for capturing image of the bottom endwall. Blank window covers close the other three cut-out windows. The field width of the camera image covers about 12.5 cm x 12.5 cm of the endwall at each window location giving a pixel size of 0.4 mm x 0.5 mm. The camera image is calibrated based on the in-situ calibration technique in (Sargent et al., 1998) against the temperatures at the endwall thermocouples located in the image. A typical image calibration curve for the IR measurements is shown in Figure 3.11. The curve is fit to a second order polynomial as prescribed by (Sangston et al., 2014). Using the known locations of the thermocouples and pixel size, the spatial positions of the image pixel are determined. Twenty (20) instantaneous image samples at the quasi-steady thermal conditions of the endwall are time averaged at each window location. Four time-averaged images from the four window locations (1-4) in Figure 3.10 are then combined for full coverage of the entire passage endwall between blades 3 and 4. Pixel values in overlapping region of the images are averaged after appropriate thermocouple temperature vs. pixel temperature calibrations have been applied. For filleted cases, some of the thermocouples are completely covered when fillet is installed. Such thermocouples are not taken as part of the calibration for film cooling and heat transfer measurements. The adiabatic effectiveness of the film cooling at the endwall is computed using Eqns. 3.7.

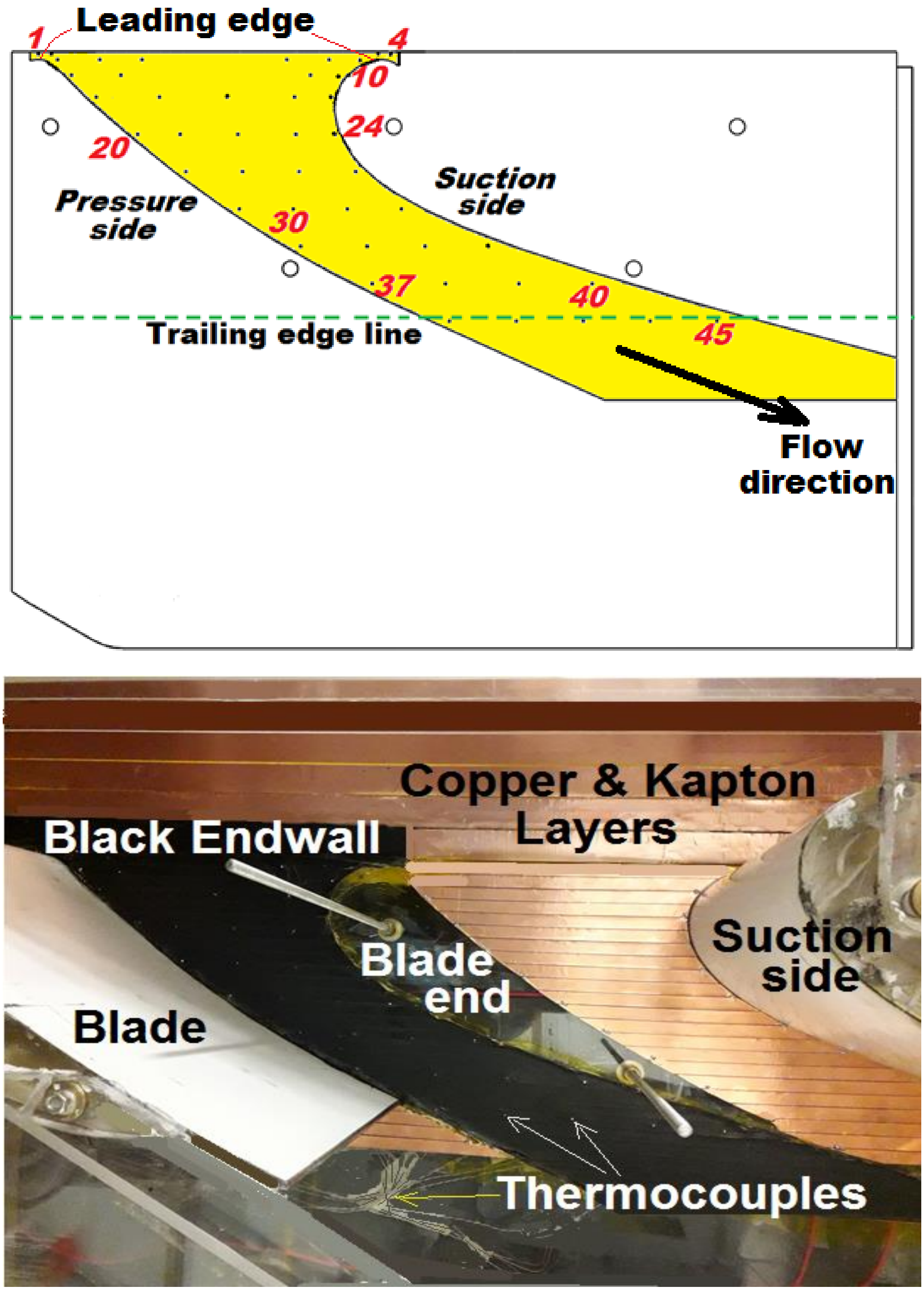

Figure 3-8: Thermocouple locations on the endwall

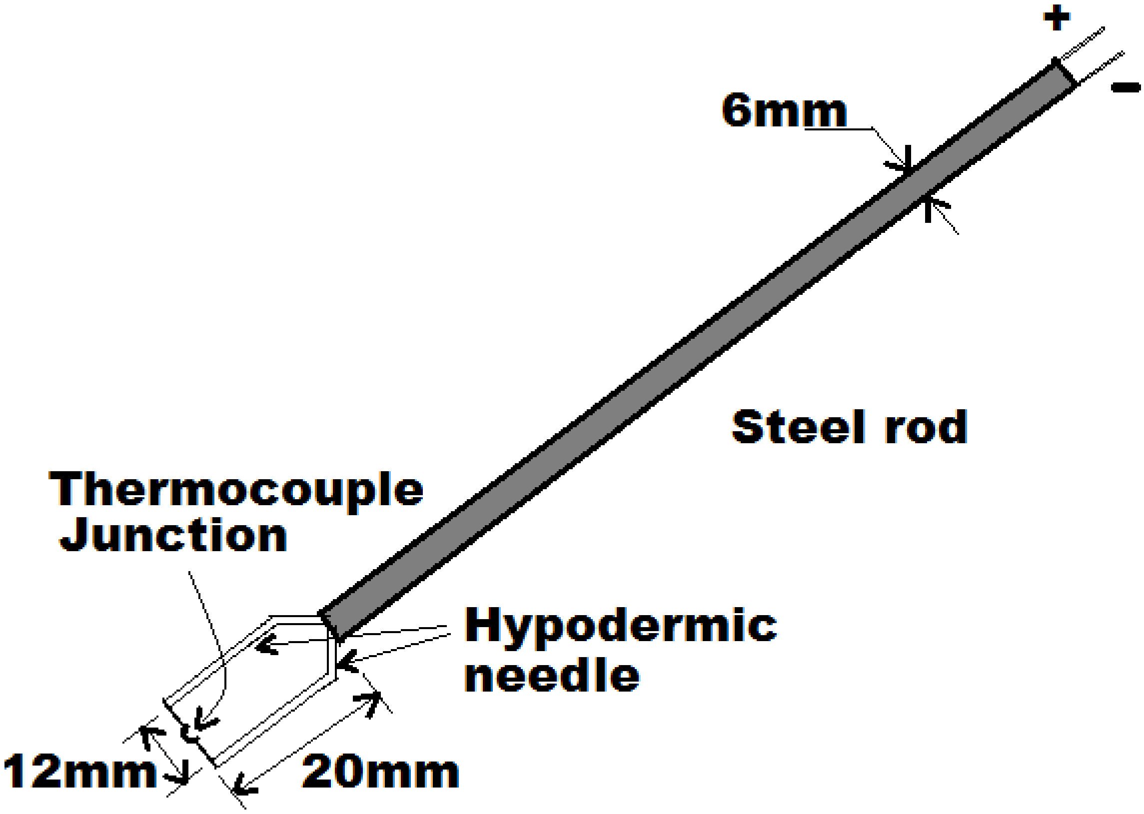

Figure 3-9: Temperature probe construction with insulated thermocouple

Non-dimensional temperature, $\theta = \frac{\left(T_{loc} - T_{plm}\right)}{\left(T_{ref} - T_{plm}\right)}$ (3.6)

Adiabatic effectiveness is computed with the notation:

$$\eta = \frac{\left(T_{ref} - T_{ew}\right)}{\left(T_{ref} - T_{fc}\right)} \tag{3.7}$$

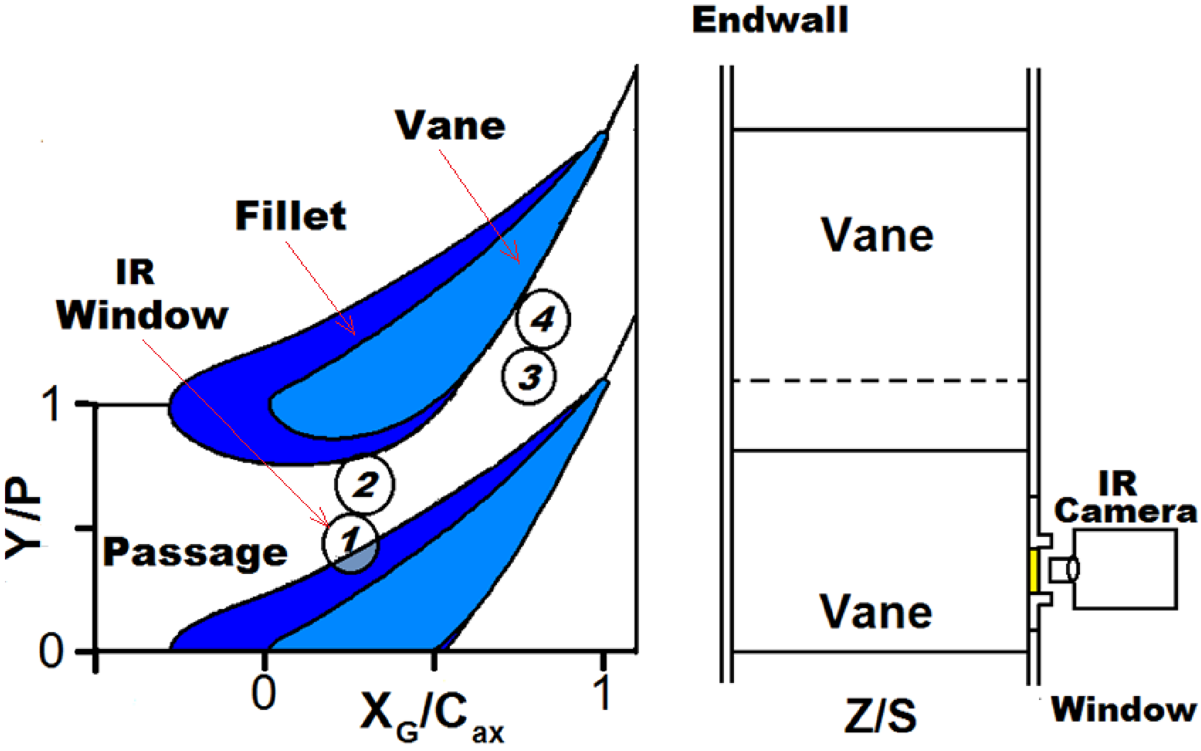

Figure 3-10: Infrared (IR) imaging window locations in the top endwall

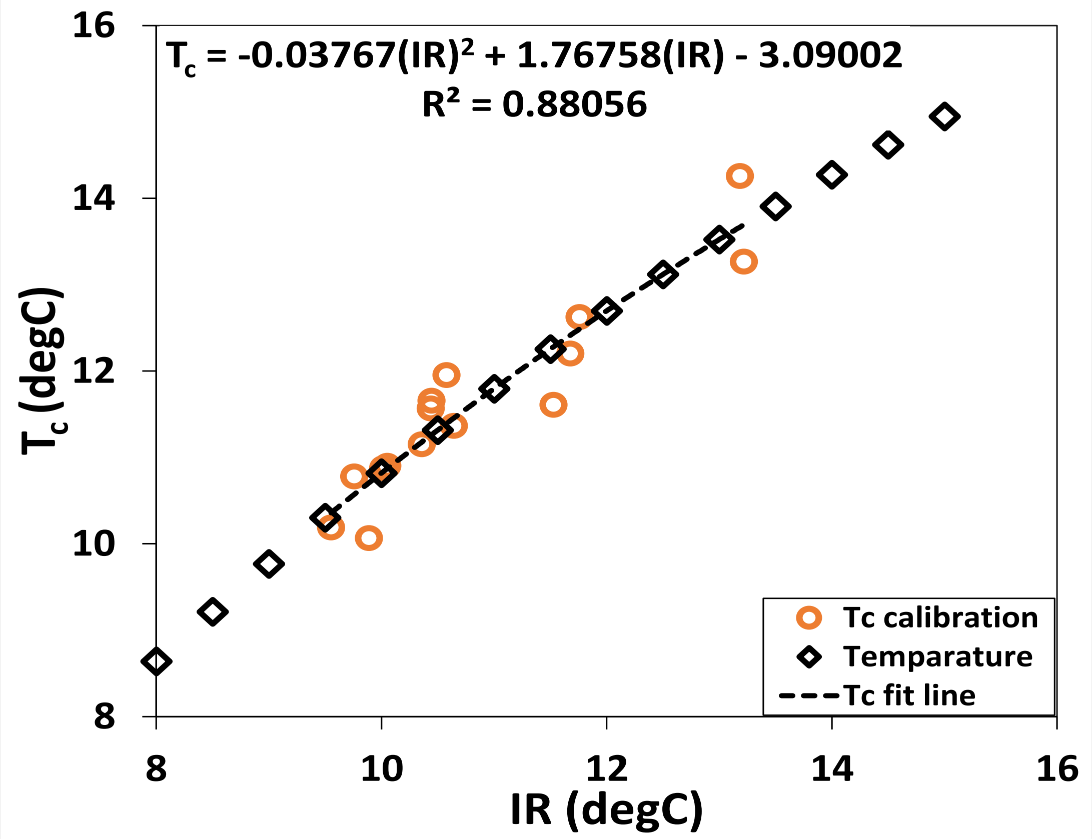

Figure 3-11: Sample thermocouple and pixel temperature calibration for Window-1, baseline curved holes film cooling (Br = 2.8)

3.4 The fillets geometries

Both of the two endwall fillets experimented (Fillet-1 and Fillet-2) have linear profile as the height varies linearly from the blade profile to the endwall. The maximum height of each fillet is located at the leading edge as shown in Figure 3.12. The fillet height also varies linearly from the leading edge towards the trailing edge on both sides of the blade profile. The trailing edges of the fillets thus blend smoothly with the blade profile and endwall simultaneously. The fillets are designed based on previous investigations (Becz et al., 2003, Mahmood et al., 2005, Zess and Thole, 2002) and some preliminary CFD simulations in the STAR-CCM+^{TM}. The profiles and the equations that form part of the fillet curves are shown in Fig. 3.13 and Appendix C. The coordinates in parentheses for Fillet-1, a (-7.493, -24.178), b (-10.784, -31.575), c (-20.962, -35.458), d (-26.022, -28.971), e (-21.735, -23.856), f (-16.067, -9.389), g (-1.1455, -0.271) and for Fillet-2, b (-7.450, -24.083), b (-24.109, -29.397), c (-24.109, -29.397) denote the end or beginning points through which the successive equations in Appendix C form smooth curves. Location d (-26.022, -28.971) denotes the leading-point on Fillet-1, the profile is tangent to the blade surface at point g (-1.1455, -0.271) on the PS (trailing edge), however, it blends smoothly at a (-7.493, -24.178) on the SS (throat region). Fillet-2 has three coordinates with location b (-24.109, -29.397) representing the leading-point on the fillet, the other two locations [a (-7.493, -24.178) on the PS and point c (-7.450, -13.084) on the SS] are the termini points on the throat area of the blade profile.

Both fillet geometries follow the pressure and suction sides of the vane. However, the height $(Y/S)_{Max}$ differs and the leading extent $(X/C_{ax})_{Max}$ upstream of the blade leading edge also differs between the two fillets as shown in Fig. 3.12. Fillet-1 has ($Y/S_{max} = 0.3$) at the leading-edge, equivalent to the reference velocity boundary layer of $\delta/S=0.10$. Fillet-1 extends $0.3C_{ax}$ upstream while Fillet-2 only extends for 20% of the axial chord. On the suction side, the trailing edges of both fillets are located at the passage throat. On the pressure surface, the trailing edge of Fillet-2 also is located at the throat region. However, Fillet-1 extends all the way to the trailing edge of the blade.

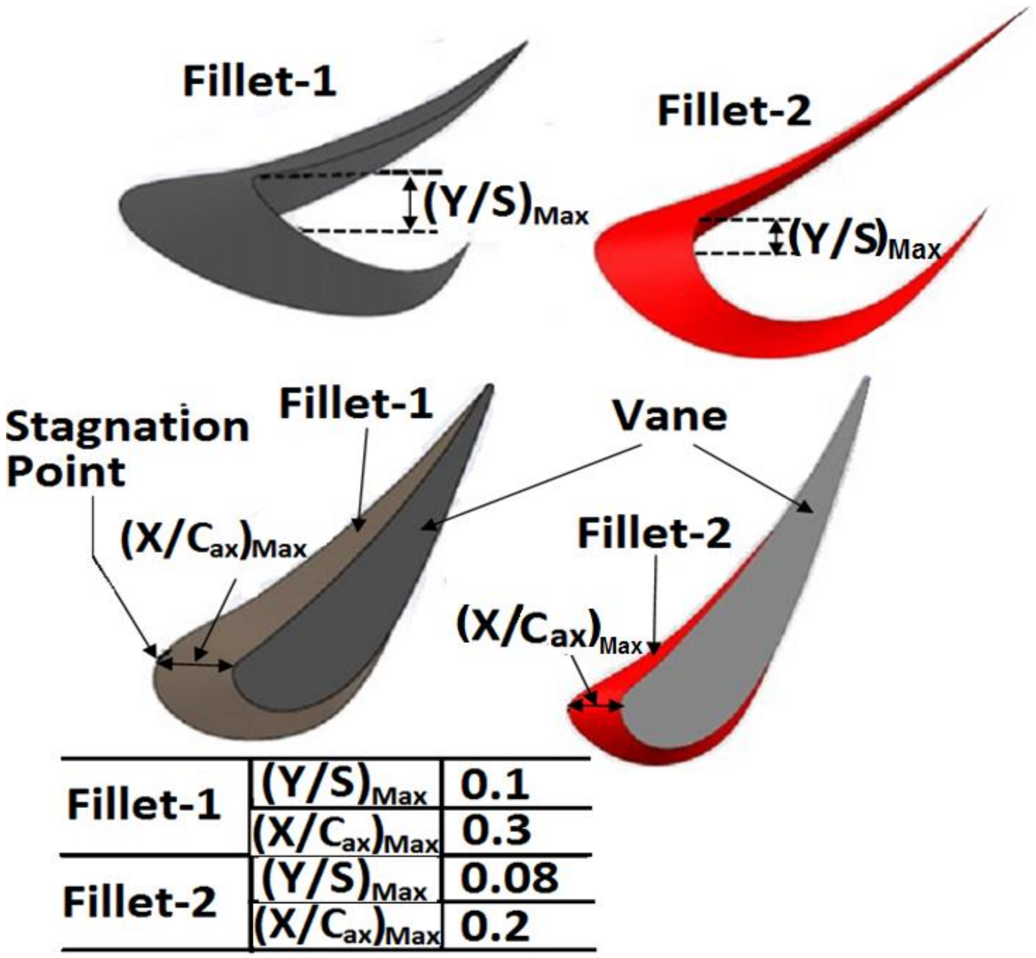

Fillet-1	$(Y/S)_{Max}$	0.1
	$(X/C_{ax})_{Max}$	0.3
Fillet-2	$(Y/S)_{Max}$	0.08
	$(X/C_{ax})_{Max}$	0.2

Figure 3-12: Fillets design and geometries

3.5 Experimental Uncertainties

The degree of error in a set of experimental or measured data is termed uncertainty. It is the probability or the certainty that the error does occurred in an experimental measurement. It is also an interval or range in which a measured value is expected to lie.

(a)

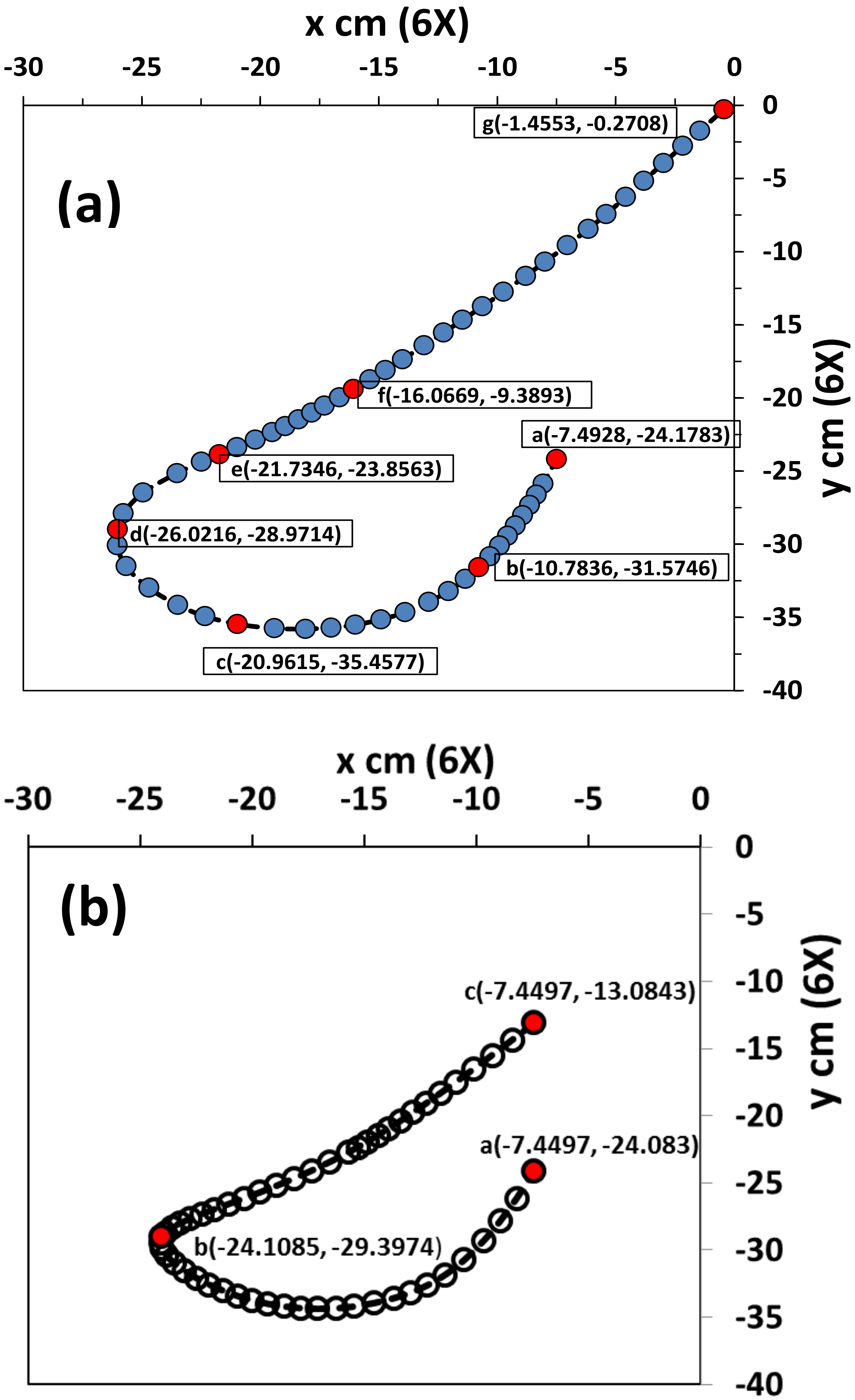

Figure 3-13: Profiles of the fillets (a) Fillet-1 and (b) Fillet-2

The uncertainty analyses of these experimental data are thus very important to validate the results of the experimental investigation. In (Moffat, 1988), the uncertainty analysis is calculated as the magnitude of the bias and precision errors at 95% confidence interval (Eqn. 3.8). Appendix D gives the detail of sample calculations and the overall uncertainty computations.

3.5.1 Pressure transducers' uncertainties

The precision component of the uncertainty for the pressure transducer is obtained by linear regression and the bias component is the combination of the accuracy or sensitivity of the transducer from the manufacturer and the accuracy of the calibrator. The summary of all the uncertainties from the pressure transducers are presented in Table 3.2.

Table 3-2: Uncertainties of calibrated Pressure transducers

S/N	Transducer Name	Measurement Location	Bias Error (Pa)	Precision Error (Pa)	Overall Uncertainty (Pa)	Overall Uncertainty (%)
1	Siemens SITRANS	Five hole probe: Port-1	1.0	2.67	2.690	1.375
2	Omega PX653	Five hole probe: Port-2	3.105	1.08	3.524	0.661
3	Omega PX653	Five hole probe: Port-3	3.105	1.69	3.525	0.661
4	Omega PX653	Five hole probe: Port-4	3.105	0.867	3.526	0.658
5	Omega PX653	Five hole probe: Port-5	3.105	0.66	3.525	0.660
6	Omega PX2650	Pitot probe: Total Port	0.31	1.279	1.867	4.719
7	Omega PX2650	Pitot probe: Static Port	1.24	0.506	2.838	1.669
8	Omega PX2650	Film cooling plenum pressure	3.1	2.57	4.400	1.550
9	Omega PX2650	Orifice differential pressure	3.0	4.77	4.270	1.471

$$\delta = \sqrt{B_i^2 + P_i^2} \tag{3.8}$$

3.5.2 Film cooling measurement uncertainties

The uncertainties of the pressure data from the five hole probe is determined by taking four measurements at three distinct regions in measuring Plane-4, blowing ratio M = 2.8. New location file is generated and invoked by the LabVIEW programme to provide spatial data at regions close to the trailing edge, inviscid region of the exit area and the pressure side close to the end wall at Plane-4. The procedure and computation of the uncertainty follows that of the (Moffat, 1988). The uncertainties at the trailing edge region are relatively high due to the chaotic flow of the secondary flow at that region. The overall uncertainties for measured pressures (P-1: P-5) in the five hole probe are presented in Table 3.3. The uncertainties in the calculated results such as local velocity components (u, v, w), pitch angle, yaw angle, total pressure and static pressure from the programme are then obtained and tabulated as shown in Table 3.4. The local velocity components (u, v, w) are then used to obtain the axial vorticity which then provides a means to obtain its uncertainties as presented in Table 3.4. The coefficient of total pressure loss is also computed and the resulting uncertainties are obtained and presented as shown in Table 3.4.

Table 3-3: Uncertainties of Pressure transducers as percentage

Measurement Port	Pressure side Uncertainty (%)	Inviscid region Uncertainty (%)	Suction side Uncertainty (%)
P-1	3.408 – 16.256	1.846 – 11.551	2.494 – 14.412
P-2	3.800 – 8.327	0.857 – 6.321	5.358 – 16.818
P-3	4.523 – 11.563	1.106 – 7.980	4.127 – 11.710
P-4	4.537 – 9.996	1.107 – 4.581	3.853 – 10.554
P-5	3.696 – 15.730	1.030 – 5.775	2.909 – 19.662

The uncertainties in the reference static and total pressure obtained from the Pitot - static tube are 2.653% and 9.573%. Free stream velocity component is then computed from the static and total pressures obtained from the Pitot - static probe. The uncertainty of the free stream velocity component is obtained as δU_o = 2.612%. The film cooling plenum pressure uncertainty and that of the pressure drop across the orifice plate for M = 2.8 are 1.087% and 5.822%. Also the uncertainty for the blowing ratio (M = 2.8) and that of the film cooling mass flow rate are δM = 4.66 and $\delta \dot{M}_{cool}$ = 3.718% of the nominal values of the data respectively.

Table 3-4: Uncertainties of Five hole Probe Results

Computed Result	Pressure side Uncertainty (%)	Inviscid region Uncertainty (%)	Suction side Uncertainty (%)
u	0.873 – 11.337	0.812 – 5.695	3.187 – 18.508
v	1.850 – 13.452	0.705 – 7.626	1.242 – 9.321
w	2.054 - 8.555	1.396 – 8.114	1.750 – 12.600
P_{tot_5hole}	2.903 – 13.784	1.291 – 3.146	4.458 - 18.814
P_{Stat_5hole}	1.173 – 3.040	1.660 – 4.113	1.680 – 5.039
Pitch (°)	4.694 – 12.619	1.969 – 12.840	4.159 – 14.824
Yaw (°)	3.249 – 8.369	2.062 – 9.852	3.503 – 10.054
$C_{pt, loss}$	2.288 – 14.320	5.63 – 12.210	5.715 - 18.850
$\omega_x C/U$	5.676 - 9.595	4.660 – 11.118	5.998 – 17.622

The calculated uncertainties are shown to be relatively higher compare to the measured data as shown in Tables 3.3 and 3.4. The very small diameter of the five hole ports (0.5mm) and the increase length of the tube for traverse (35 – 50 cm) have contributed to the increase in the uncertainties due to the delay in the pressure sensing of the transducers uncertainty estimations. The uncertainty estimation at the pressure and suction sides are higher than the inviscid region due to the unsteadiness of the secondary flow close to the blade profile. The interaction of the film cooling flow and the main flow also contributes to the increase in the uncertainties values. The flow yaw and the pitch angles also contributed to the rise in the uncertainties particularly at the boundary layer region close to the end wall where the turning is very high

3.5.3 Static pressure uncertainties at the mid-span of the blade

Twenty one pressure taps are created at the mid-span and routed out through the hub side of the blade as shown in Figure 3.1. The overall uncertainties of the coefficient of static pressures at the mid-span ($Y_G/S = 0.5$) of instrumented Blade are obtained from 11 sample data from each port and presented in Table 3.5. The maximum uncertainty occur close to the leading-edge stagnation region ($x/C = 0$) towards the pressure side. The maximum uncertainty in this result is obtained as $C_{p,\ blade} = 8.350\%$.

Table 3-5: Uncertainties of the blade pressure at the mid-span

Port	x/C	Blade Profile Pressure Uncertainty (%)
1	-0.56587	0.965
2	-0.53117	1.193
3	-0.47729	1.130
4	-0.40987	1.513
5	-0.35487	2.643
6	-0.30748	2.858
7	-0.25529	1.225
8	-0.18702	1.952
9	-0.10776	2.630
10	-0.04795	2.373
11	-0.01354	11.759
12	-0.00254	12.705
13	0	2.818
14	0.006488	1.796
15	0.028491	3.107
16	0.083498	4.478
17	0.163611	21.929
18	0.253315	3.316
19	0.365867	0.626
20	0.45811	0.965
21	0.540197	1.192

3.5.4 Temperature and Nusselt number uncertainties

The heat transfer measurements are obtained by thermocouples (T_c) and IR camera (T_{IR}). Thereafter, Nu and effectiveness (η) are obtained from the data. The overall uncertainty are estimated for each window location data and presented as shown in Table 3.6. The highest film cooling effectiveness in Windows 1 and 2 is < 9%. The uncertainty values are relatively high at Windows 3 and 4 when compared with Windows 1 and 2. This is attributed to the effect of the secondary flows. This complex flow close to the endwall, towards the downstream of the passage affect the uncertainties because of the high flow acceleration towards he passage.

Table 3-6: Uncertainties of heat transfer measurements

Computed Result	Window-1 Uncertainty (%)	Window-2 Uncertainty (%)	Window-3 Uncertainty (%)	Window-4 Uncertainty (%)
T_c	4.005	7.039	5.526	3.978
T_{IR}	6.097	6.345	7.459	5.267
Nu	2.796	6.956	9.297	14.661
η	4.244	8.364	15.505	16.671

The overall uncertainty in the non-dimensional temperature is $\delta\Theta = 7.15\%$ (see Appendix D for detail). The turbulent intensity (Tu) uncertainty obtained from the hot-wire data is $\delta Tu = 4.8\%$ of the nominal measured value.

3.6 Computational domain

Computational fluid dynamics (CFD) of the representation of a passage through the vanes is modelled using Solidworks^{TM} and CD adapco STAR-CCM+^{TM}. The essence of this is to predict some effects of fillet on the flow field which are otherwise difficult to capture in the measurements.

The blade geometry used for the computations is the same profile as that of the experiment. A passage geometry is modelled such that the inlet is placed at one C_{ax} upstream of the leading edge and the exit is also placed at one C_{ax} downstream in the streamwise direction from the trailing edge. The computational domain is shown in Fig. 3.14. The domain is, however, taken up to the mid-span of the vane to implement the flow and geometric symmetry about the mid-span to save the computational time. Periodic boundary condition is placed at the leading edge planes as shown in Figure 3.14. A defined velocity profile is place at the inlet to ensure the 0.1S thickness of the velocity boundary layer as the flow approaches the vane leading edge. The other walls are set as adiabatic walls (SS, PS and the endwall). The coordinate system adopted in the simulation is also shown in Figure 3.14.

With air as the working fluid, the Reynolds Averaged Navier-Stokes (RANS) model of CFD is used to achieve the solution of the discretised flow domain. Finite volume polyhedral mesh with fifteen refined prism layer mesh at the walls is used to completely resolve the flow at the walls and the near endwall regions. The model employs the *K-omega* (k-ω) turbulent model. The total volume of the discretised cells is 1.6E+6 to ensure $y^+<1$ at the walls. Normalised residuals are resolved below 10^{-4} for continuity, momentum, turbulent kinetic energy, and shear-stress dissipation rate equations. Convergence is achieved after about 900 iterations. Grid independence of the discretized volume is checked by increasing the grid size by 10E+4 cells which result in only a 2% change in the total pressure losses at the exit plane of the vane. The discretization of domain and k-ω model of the RANS computational scheme remain the same when the adiabatic fillet-1 is added in the computational model. The governing equations employed by the STAR-CCM+™ (CD-adapco, 2013) for the solution of the finite volume discretization are the incompressible Navier-Stokes equations in the continuous integral form as in Eqn. (3.9). The integral form of this RANS equation is represented in the discrete form for the cell-centred control volume in Eqn. (3.10). The total numbers of equations correspond to the total number of cells in the grid volume.

The detail of the second order upwinding scheme equations for the finite volume solution is provided in Appendix E.

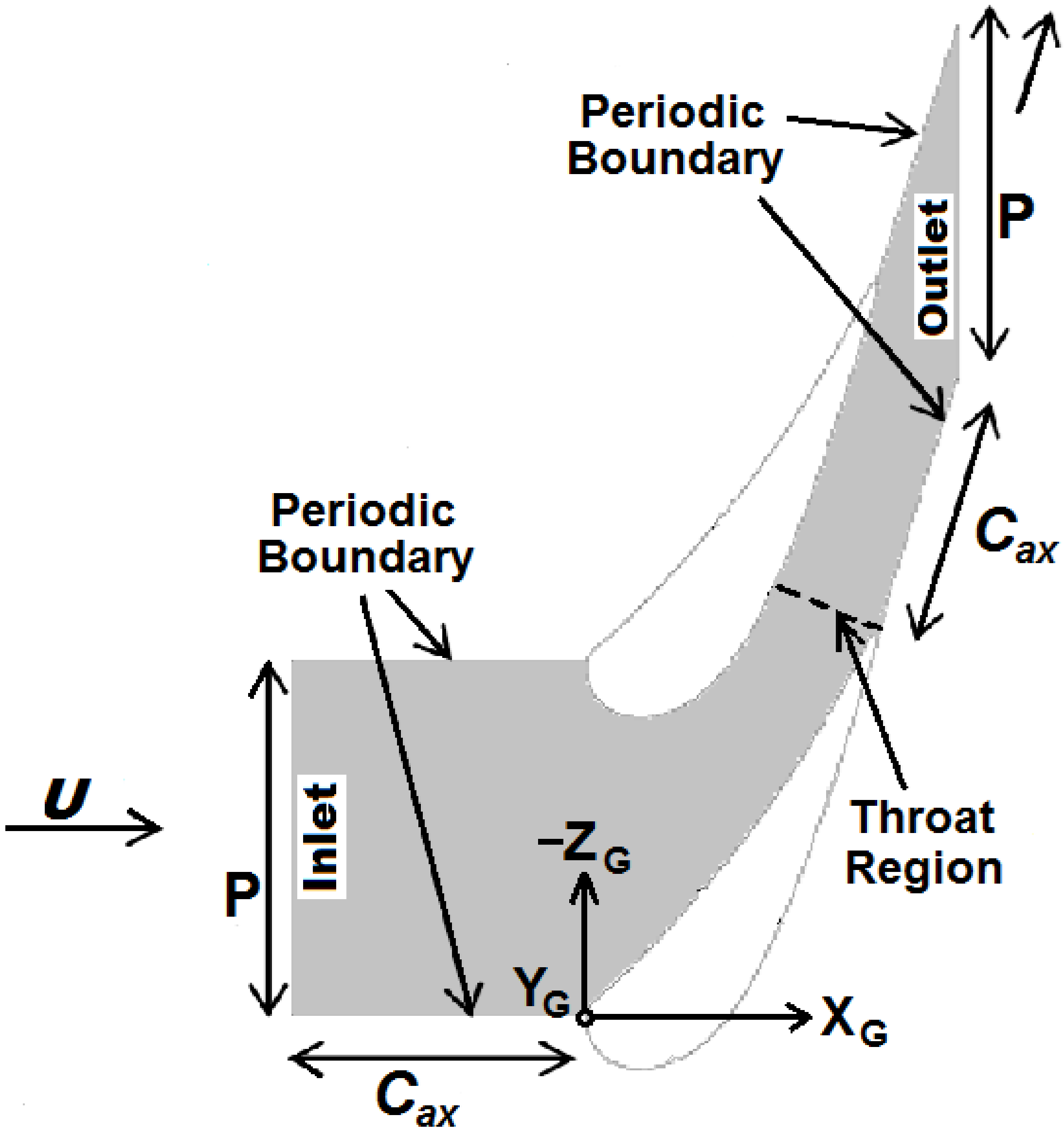

Figure 3-14: Computational domain

$$\underbrace{\frac{d}{dt}\int_V \rho\chi\phi\, dV}_{\text{transient term}} + \underbrace{\oint_A \rho\phi(v - v_g)\,.\,da}_{\text{convective flux}} = \underbrace{\oint_A \Gamma\nabla\phi\,.\,da}_{\text{diffusive flux}} \quad + \quad \underbrace{\int_V S_\phi\, dV}_{\text{volumetric source term}} \tag{3.9}$$

$$\frac{d}{dt}(\rho\chi\phi V)_0 + \sum_f [\rho\phi(v.a - G)]_f = \sum_f (\Gamma\nabla\phi.a)_f + (S_\phi V)_0 \tag{3.10}$$

4. CHAPTER 4: FLOW STRUCTURE RESULTS FOR EXPERIMENTATION AND COMPUTATION

4.1 Experimentation: Velocity Boundary Layer

The reference properties for the experimentation and computation are presented in Table 4.1. The flow in the cascade tunnel is treated as incompressible as the pressure drop and temperature change are small across the cascade section. The density of air flow thus remains the same as the atmospheric density in the laboratory. These properties are measured at $2.5C_{ax}$ upstream of the cascade stagnation point as shown in Figure 3.1. The wind tunnel operates as a suction facility and the gauge pressures are considered negative in the computations and conversion processes. The reference boundary layer Thickness for velocity is measured with a 1.7mm tip-diameter pitot-static tube. The streamwise turbulence intensity is obtained with constant temperature anemometer (hot wire) probe. The probe measured the properties at 5 kHz for 10 seconds. However, this hot wire was not used for scanning of data from the endwall to a region just above the mid-span because of it design limitations. Therefore, 1.6mm tip-diameter five-hole probe was used to take measurement within the vane passage Unlike the hot-wire probe, the five-hole pressure probe provides the information on the three velocity components as well as the local pressures. Unlike the hot-wire probe, the five-hole pressure probe provides the information on the three velocity components as well as the local pressures. Transducer calibrations are presented in Section 3.5.1.

The main objective of taking the reference velocity boundary layer measurement (Figure 4.1) is to use it to bench mark the reference properties for the STAR-CCM+^{TM} computations. This reference velocity boundary layer is used for the computations. The Pitot - static tube to measure the boundary layer is mounted on a traverse system. The traverse is being controlled by an in-house LabVIEW^{TM} program that also records signals from the on the DAQ–system connected to the pressure probe. Location grid is read-in by the LabVIEW^{TM} program for the appropriate scanning resolutions. The experimental results from the reference plane shows that the boundary is about 10% of the span of the blade as shown in Figure 4.1. The maximum inlet velocity is approximately 11 m/s while static pressure is constant throughout reference plane. At Y/S > 0.15, the average velocity is equal to the free stream velocity.

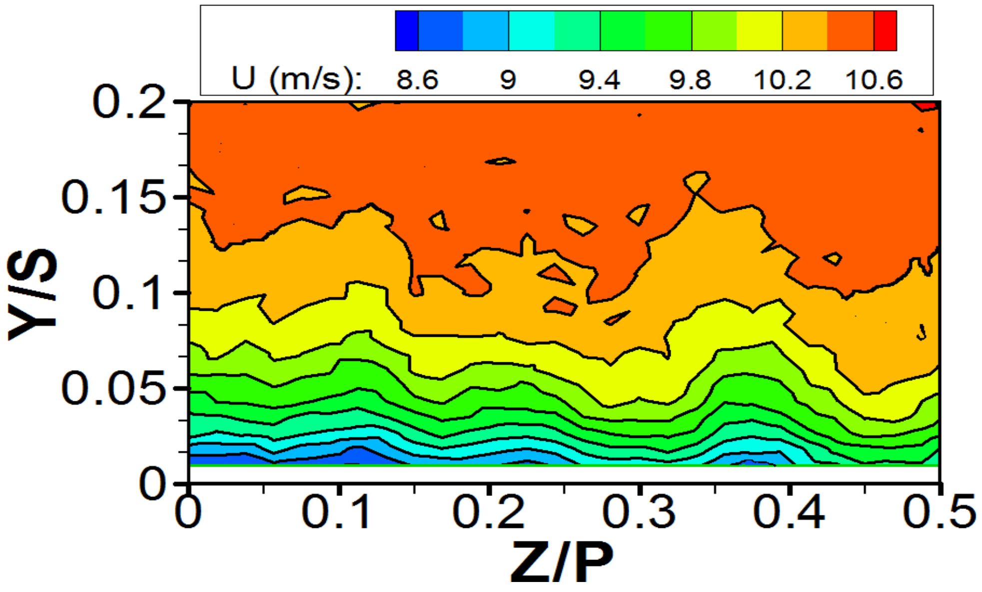

Figure 4-1: Streamwise velocity, U in the Reference plane

4.2 Computational Validation: Static Pressure Distribution at Mid-Span

The computation is only limited to baseline and Fillet-1 using STAR-CCM+^{TM} while the computational simulations of another fillet geometry (Fillet-2) are investigated by my PhD colleague (Barbieri Barbara) working on the same test section. Ansys-Fluent^{TM} is employed to do the simulations of Fillet-2 case while STAR-CCM+ is used to do the computations of Fillet-1 case.

Measured results and computational predictions of the static pressure distributions at the mid-span ($Z_G/S=0.5$) along the vane surface are presented in Figure 4.2. The static pressure is normalized as in Eq. 4.1 and presented as the coefficient of static pressure ($C_{p,blade}$) on curvature distance, s/C along the blade surface shown in Figure 3.1b. Location s/C = 0 0 corresponds to the stagnation region where the global coordinate takes its origin. The static pressures presented include the computational results with the Fillet-1 and without fillet. The zero location for the global coordinate system is located at the leading-edge of the vane profile and on the endwall. This stagnation position corresponds to the location where the coefficient of static pressure is highest as shown in Figure 4.2 (a). The flow accelerates within the blade passage as the static pressure and $C_{p,blade}$ decrease both on the suction side (SS) and pressure side (PS) of the vane. The lowest coefficient of static pressure, at s/C=-0.26 on the SS corresponds the throat region within the passage. Immediately after the throat downstream, there is a rapid increase in pressure thereby causing deceleration towards the passage exit. The transition from laminar to turbulent boundary layer on the vane surface at SS occurs between -0.26<s/C<0. The numerical results accurately predict the static pressure coefficient on the blade passage. The distribution of static pressure coefficient for Fillet-1 is very similar to the baseline experimental $C_{p,blae}$ and shows that the fillet is not affecting the blade loading in the inviscid region. This simply means the fillet design is okay for experimentation because the design is expected not to change the blade loading. The reasonable similarities between the computations and experimental $C_{p,blade}$ data validate the modifications and the numerical simulations.

Table 4-1: Reference flow parameters 2.5C_{ax} upstream of cascade inlet

	Experiment	Computations
Freestream velocity, U (m/s)	11.0	11.0
$P_{s,r}$ (kPa), absolute	88	101.9
Boundary layer thickness	0.10S	0.10S
Streamwise turbulence intensity	2.5 %	2 %
Air temperature (K)	298	300
Air density, ρ (kg/m^3)	1.02	1.02
Reynolds Number, Re (=$\rho U_{ref} C/\mu$)	2.1E+05	2.1E+05

Equation 4.2 is used to compute the mass average of total pressure loss coefficient in the baseline numerical model (no fillet) at five pitchwise planes at different axial locations (X_G/C_{ax}) through the entire passage. These are being computed for the various computational grids to show grid independence of the results. In Figure 4.2b, the mass-average $(C_{pt,loss})_{mass\text{-}av}$ shows less than 2% deviation at each locations when the computational volume domain cells is being reduced or increased by 4.0 E05 cells. Table 4.2 presents the overall mass average of $C_{pt,loss}$ for experimental and computation. The mass averaged increases across the passage and reduces with the use of Fillet-1. This show that the fillet is reducing the effect of the secondary flows close to the endwall. In general, the baseline experimental $(C_{pt,loss})_{mass\text{-}av}$ is comparable with baseline computation.

$$C_{p,blade} = \frac{\left(p_{b,x} - p_{s,ref}\right)}{0.5\rho U^2} \tag{4.1}$$

$$\left(C_{pt,loss}\right)_{mass-av} = \frac{1}{m_{in}} \iint \left[\frac{P_{t,ref} - P_{t,x}}{0.5\rho U^2}\right] (\rho u_x) dA \tag{4.2}$$

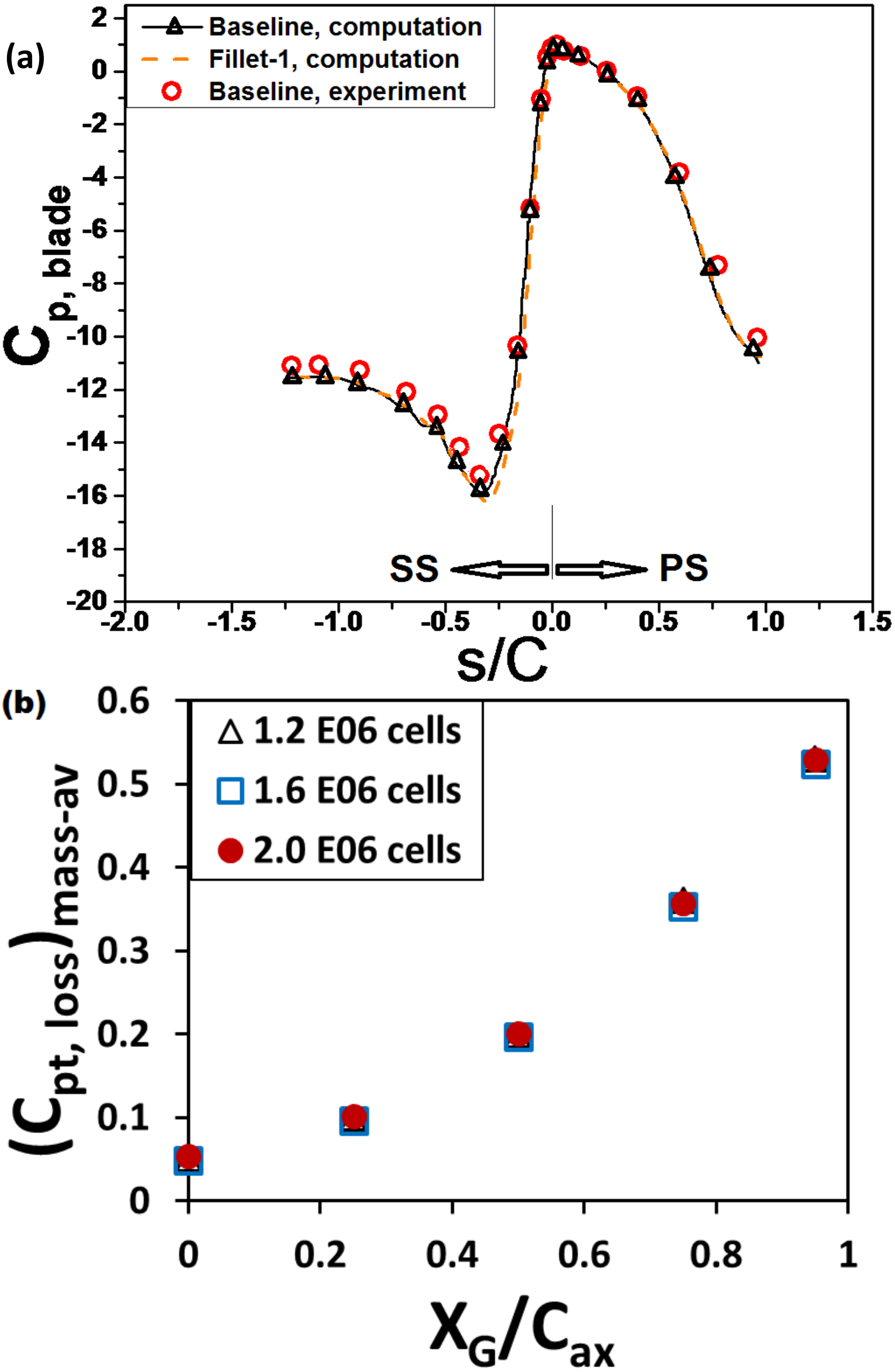

Figure 4-2: a) Cp,blade along blade profile at mid-span, and b) Grid sensitivity of mass-averaged coefficients, (Cpt,loss)mass-av

Table 4-2: Overall mass-averaged $C_{pt,loss}$ coefficients in Plane-3 and Plane-4

Overall $(C_{pt,loss})_{mass\text{-}av}$	Plane-4 (X_G/C_{ax} = 1.04)	Plane-3 (X_G/C_{ax} =0.58)
Experiment, Baseline	0.870	0.294
Computation, Baseline	0.700	0.202
Computation, Fillet-1	0.634	0.170

4.3 Validation: Endwall Static Pressure

The validation of the baseline computational model (no fillet, no film-cooling) is also presented by comparing the normalized static pressure coefficient, $C_{p,static}$ distributions on the cascade passage endwall in Fig. 4.3(a & b). The $C_{p,static}$ data in the figure are computed from the endwall static pressures, $p_{e,x}$ along the passage from Eqn 4.3 and are presented in the form of contour plots in Fig. 4.3.

$$C_{p,static}=\frac{\left(p_{s,r}-p_{e,x}\right)}{0.5\rho U^{2}} \tag{4.3}$$

The contour values of $C_{p,static}$ in Fig. 4.3(a & b) increase, in general, from the leading edge region to trailing edge region as the flow accelerates due to the decrease in the static pressure along the passage. The $C_{p,static}$ values are then the highest (between 10 and 13) at the passage throat area. As shown in the figure, the distributions of $C_{p,static}$ contours between the experimental case and computations differ little from each other. Appendix F shows the comparisons of $\Delta C_{p,static}$, the pitchwise difference of $C_{p,static}$, between the baseline and Fillet-1 cases.

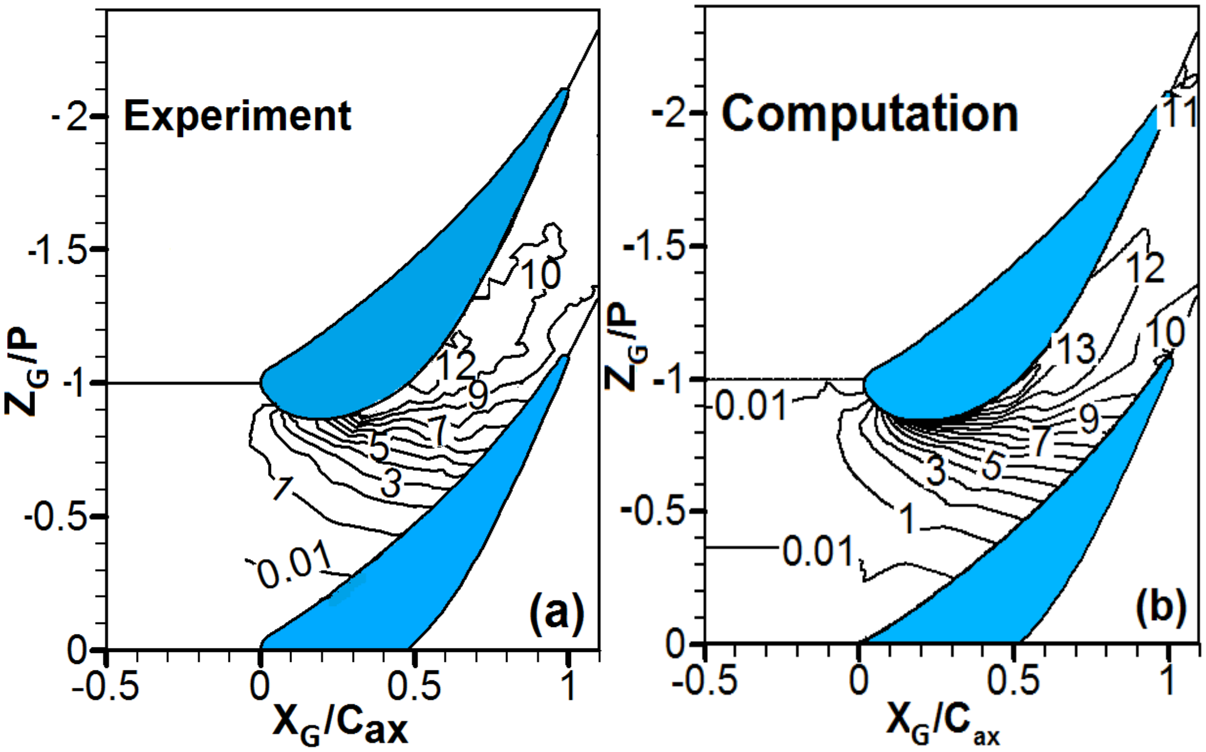

Figure 4-3: Baseline endwall static pressure ($C_{p,static}$) for (a) experiment and (b) computation

4.4 Validation: Total Pressure Loss

The distributions of baseline total pressure loss coefficients in Plane-4 (Figure 3.1) are presented in Figure 4.4 for the computation and the experiment. The vane trailing edge (TE) is located just upstream of Y/P = 1.1 in the figures and the axial direction is coming out of the plane of paper. The right side of TE always refers the pressure side (PS) and the left side of TE refers to suction side (SS) of the vane. The high $C_{pt,loss}$ $1.25<Y/P<0.65$ and $0.225<Z/S<0.075$ are clearly apparent from the experimental and computational results as shown in Figure 4.4. The $C_{pt,loss}$ is computed from the local total-pressure values, $p_{t,x}$ as in Eqn. 4.4. The $C_{pt,loss}$ is an indication of the secondary flow losses along the vane passage because of the entropy generation and total pressure drop in the vortex motion. This passage vortices are substantially responsible for high aerodynamic loss in the passage of the turbine blade (Kang et al., 1999). Higher $C_{pt,loss}$ implies higher total pressure losses in the vane passage. The vertical contour lines of very high $C_{pt,loss}$ in the region between Y/P = 1 and TE are caused by the TE wake vortices. The experimental data and numerical model in the TE vortex region do not represent the actual physics accurately because of the limitations on the probe and present turbulence modelling. The magnitudes of the contour lines in the passage vortex region for the experiment are almost matching those of the computation in the corresponding locations, with some slight difference in the location of the vortex core (the highest $C_{pt,loss}$). In General, measurement agrees with simulation prediction when the size, apparent location, and contour magnitudes of the passage vortex outside the TE wake region are compared.

.

$$C_{pt,loss} = \frac{\left(p_{t,ref} - p_{t,x}\right)}{0.5\rho U_{ref}^{\;2}} \qquad 4.4$$

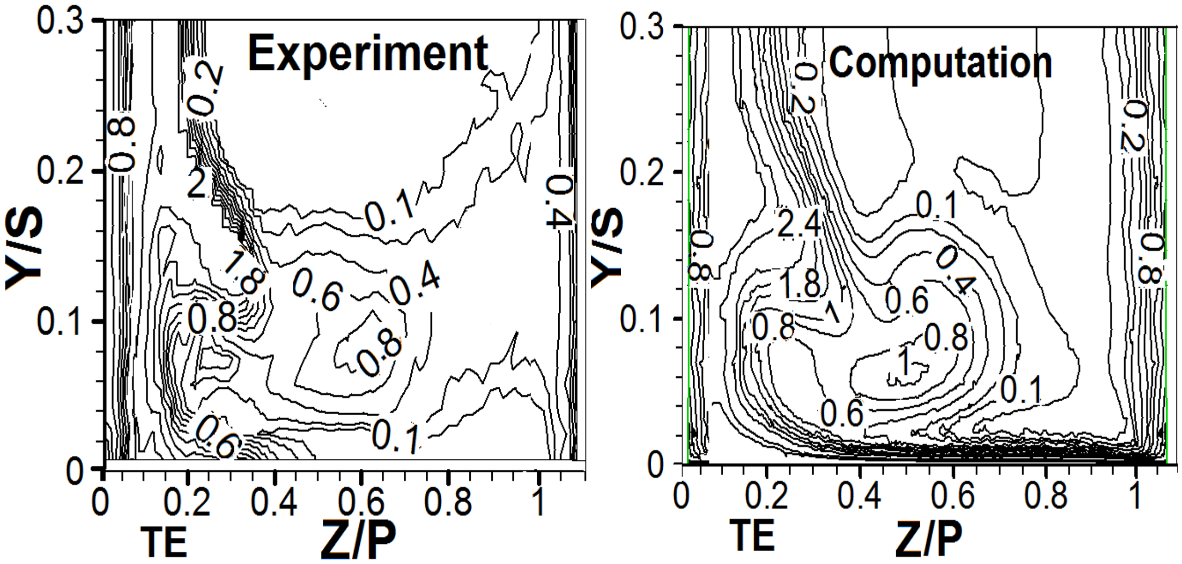

Figure 4-4: Baseline total pressure loss coefficient ($C_{pt,loss}$) for experiment and computation in Plane-4 at X_G/C_{ax} = 1.04

.

4.5 Computations: Streamlines and Yaw Angles near the Endwall

Figure 4.5 and Figure 4.6 present the computational results for the baseline and Fillet-1 cases at plane $Y_G/S = 0.002$, parallel and close to the endwall. The development of horse shoe vortices is observed just upstream of the stagnation point, somewhere around the saddle point ($Z_G/P = 0.12$; $X_G/C_{ax} = -0.3$). In both cases, the streamlines turn towards the suction sides. The region of very high cluster of streamlines depicts where the PS and SS horse shoe vortices meet to form the passage vortex. Some of these streamlines takes their origin from another spanwise plane. These lead to the formation of the re-attachment and separation lines starting upstream of the stagnation point of the leading edge of the blade. However, the heavy turning especially around the separation and re-attachment lines in Figure 4.6a (baseline case) have been substantially reduced with the use of a Fillet-1 in Figure 4.6b. This provides a very suitable situation for the film cooling of the endwall region.

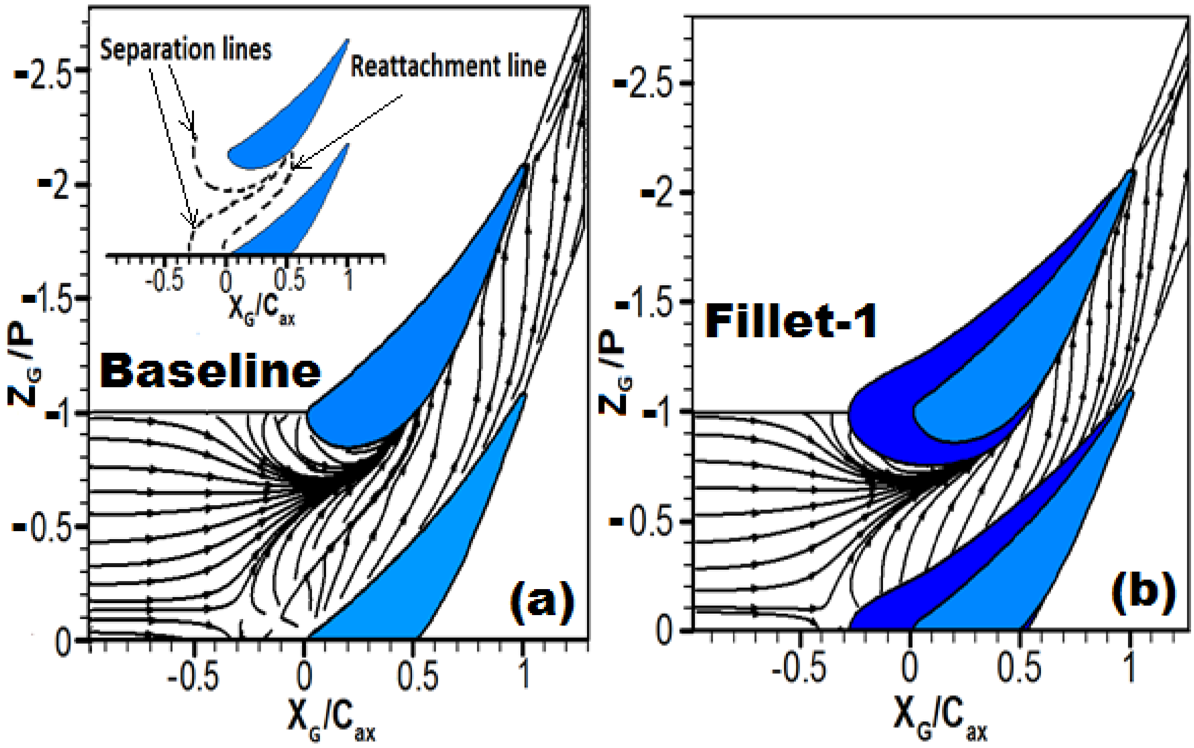

Figure 4-5: Streamlines for (a) Baseline and (b) Fillet-1 (computations) in $Y_G/S = 0.002$ plane parallel to endwall

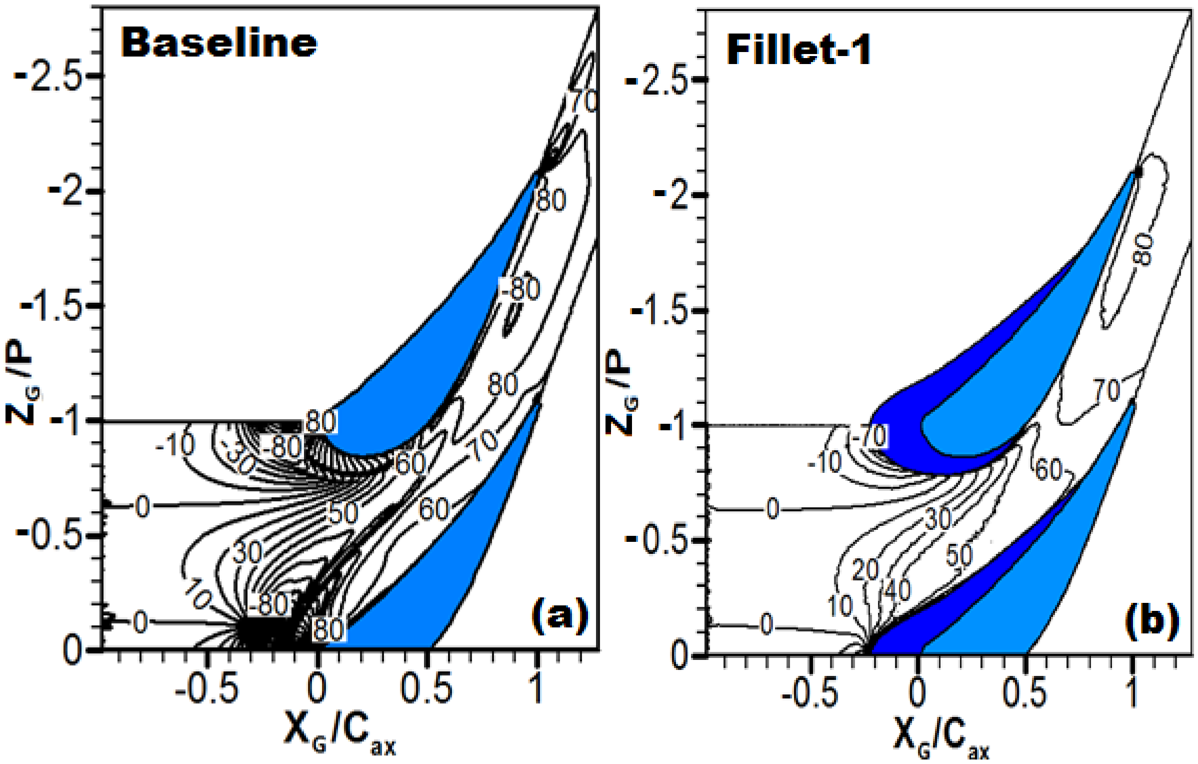

Figure 4-6: Flow yaw angles for (a) Baseline and (b) Fillet-1 (computations) in Y_G/S = 0.002 plane parallel to endwall.

4.6 Computation: Normalized Endwall Shear Stress: $\tau_x/(0.5\rho U^2)$

The x-component of shear stress (τ_x) on the endwall from computations are normalized by the dynamic pressure ($0.5\rho U^2$) of reference plane. The normalized results are then plotted in Figure 4.7 along the pitchwise (Z_G/P) direction at three axial (X_G/C_{ax}) locations for the baseline and Fillet-1. The fillet is present both on the pressure side and suction side of the passage in the three X_G/C_{ax} locations where the data are presented in Fig. 4.7. However, data are not presented on the fillet surface as the fillet is considered as part of the vane-endwall junction. At a given X_G/C_{ax} location, the lowest and highest values of Z_G/P indicate the pressure side and suction side, respectively. For the fillet case, the pressure side and suction side are considered where the fillet profile intersects the endwall. The values of $\tau_x/(0.5\rho U^2)$ in Figure 4.7 vary according to the local flow direction, velocity, and location of boundary layer separation from endwall. The values of $\tau_x/(0.5\rho U^2)\leq 0$ are then the results of flow separation and reverse flow. The high values of $\tau_x/(0.5\rho U^2)$ are caused by the local flow accelerations near the suction side. As shown in Figure 4.7, the $\tau_x/(0.5\rho U^2)$ values are comparable between the fillet and baseline cases at the Z_G/P locations away from the pressure side and suction side of the passage at all the axial locations. Then, near the pressure side at the three X_G/C_{ax} locations the $\tau_x/(0.5\rho U^2)$ values are higher for the fillet than for the baseline because of the higher streamwise flow accelerations and smaller yaw angle for the fillet near the endwall.

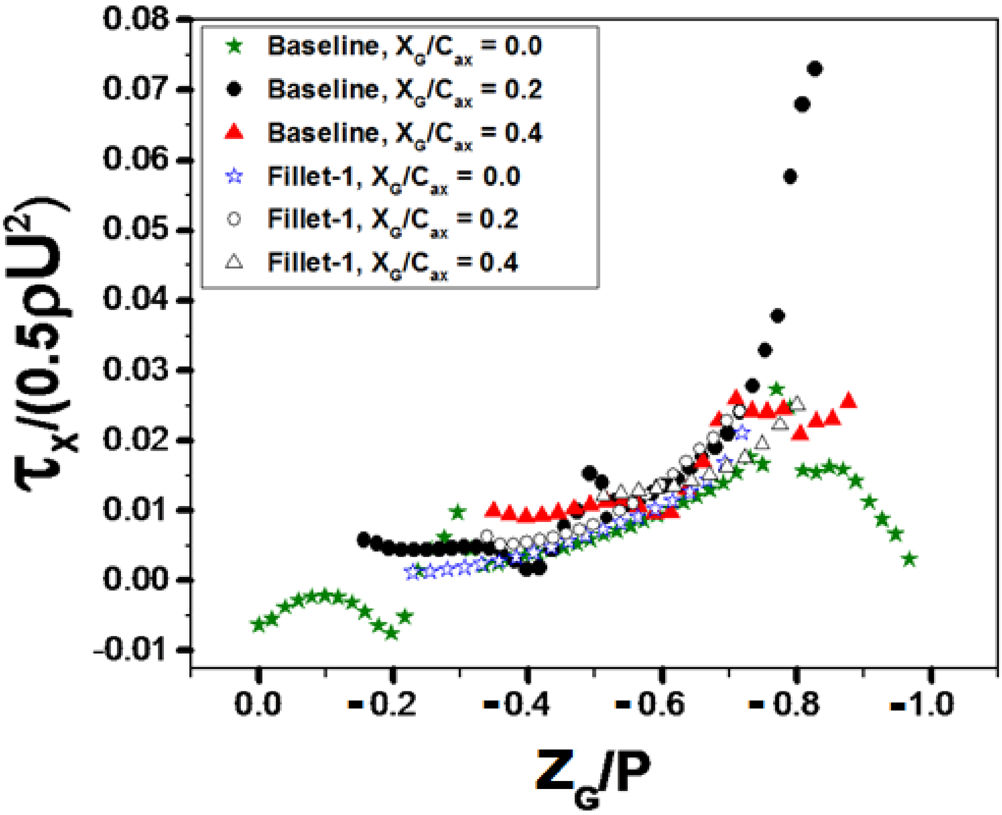

Figure 4-7: Shear stress at the endwall for Baseline and Fillet-1 (computations)

4.7 Distribution of Total Pressure Vorticity and Yaw Angle in Plane-4 at X_G/C_{ax} = 1.04

Here, attention is given to the exit plane (Plane-4) to determine the overall effects and penetration of the film cooling flow into the main stream with and without the endwall modifications (fillets). In this section, only the flush slots will be considered for all blowing ratios (M = 1.0 – 2.8). This leading edge slot film cooling geometry is considered in it entity. Total pressure loss coefficient ($C_{pt\text{-}loss}$) is for computed using Eqn 4.4 while the axial vorticity is computed using Eqn. 4.5.

The data for $C_{pt\text{-}loss}$ are presented in Figures 4.8 to 4.12 and for normalized vorticity, ($\omega_x C/U$) are presented in Figures 4.13 to 4.17. Figure 4.8a is considered alongside with Figure 3.4a which show the geometry and location of the flush slot upstream of the stagnation point of the vane-blade. In Figure 4.8a, the shaded areas of the film cooling plate are the area covered by the Fillet-2 while the entire 82 mm slot-holes directly upstream of the leading-edge are covered by Fillet-1. These areas are fully sealed for Baseline-2 and partially sealed for Fillet-2 during experimental data acquisitions respectively. Here, Baseline-1 then refers to configurations where all the slots are opened for full film cooling flow. The same contour levels shown in the single legend for all the plots in Figure 4.8a are used for convenience and proportional comparison. Data are presented from 2 mm from the endwall up to the region slightly above the mid-span in Plane-4 at all blowing ratios. The local coordinate system (X, Y, Z) originates from the suction side of Vane-4 profile (as shown in Figure 3.1) at the endwall. The trailing-edge (TE) is located just upstream at Z/P = 0.2 (Figures 4.8 – 4.17). The effect of the $C_{pt\text{-}loss}$ is the maximum about Z/P = 0.2 as shown in Figures 4.8 to 4.12. The exit wakes from the TE are responsible for these high values of $C_{pt\text{-}loss}$ in that region. In Figure 4.8a, the fully developed passage vortex is located at Z/P = 0.1 to 0.5, Y/S = 0.1 to 0.25. The suction side of vane is on the right side of TE while the pressure side is located on the left side of TE location of Z/P = 0.2. In Baseline-1, the size of the passage vortex is bigger than other cases, however, for Fillet-1 case, there is apparent second bump as some high loss region due to the mixing losses film flow with the boundary layer flow that is swept toward suction side by the endwall streamlines. In the Fillet-1 case, the mixing loss is lifted up from the endwall to show the distinctive loss region making two distinct passage vortex bumps located at Y/S 0.1 and Y/S = 0.25. This is not desirable as high $C_{pt\text{-}loss}$ is responsible for aerodynamic losses in turbine passage (Mahmood et al., 2005). This suggest that the interaction of the film cooling flow with the cross flow is giving rise to the positive axial vorticity. Baseline-2 and Fillet-2 are showing weaker passage vorticity with reduced sizes. The passage vortex has moved towards the endwall at location Y/S = 0.1 for Baseline-2 and Fillet-2 cases. Further reduction of the passage vortex is shown in Figure 4.9 as the blowing ratio increases to M = 1.4. This means that there seems to be influence of the film cooling flow on the cross-flow. However, Fillet-1 still has two distinct bumps with reduction in size when compared with Fillet-1 of Figure 4.8. Also Baseline-2 and Fillet-2 show weaker passage vortex when compared with M=1.0 respectively. At higher blowing ratios (M=1.8, 2.2 and 2.8), weaker passage vortex are seen (Figures 4.10 to 4.12). In Baseline-2 and Fillet-2 of M = 1.8, the passage vortex continue to move closer to the endwall and smaller in size when compared with M = 1.4 of Figure 4.9. This means that increase in the mass flux of the cooling jets gives rise to the reduction in the strength and size of the passage vortex as the location moves close to the endwall. The area covered by (Z/P>0.4, Y/S>0.25) refers to the free stream region as $C_{pt\text{-}loss}$ is the lowest. In all cases and blowing ratios, the trailing-edge wakes is seen at location about Z/P = 0.2 with varying degree of $C_{pt\text{-}loss}$ magnitudes. In general, high blowing ratio seems best in terms of potential for the total pressure reduction.

The axial vorticities causing the total pressure loss coefficients are presented in Figure 4.13 – 4.17. As expected, the negative vortices are close to the endwall which is responsible for the passage boundary layer and film cooling flow. These figures complement what the total pressure loss presented for all the blowing ratios. With endwall modification, vorticity magnitudes also reduce as the film cooling jet momentum flux increases i.e. M increases, thereby increasing the local film cooling effectiveness. In general, the positive and negative vorticities are due to the yaw orientations in the positive and negative directions (Figures 4.13 to 4.17).

$$\text{Axial vorticity} = \frac{\omega_x C}{U_{ref}} \qquad 4.5$$

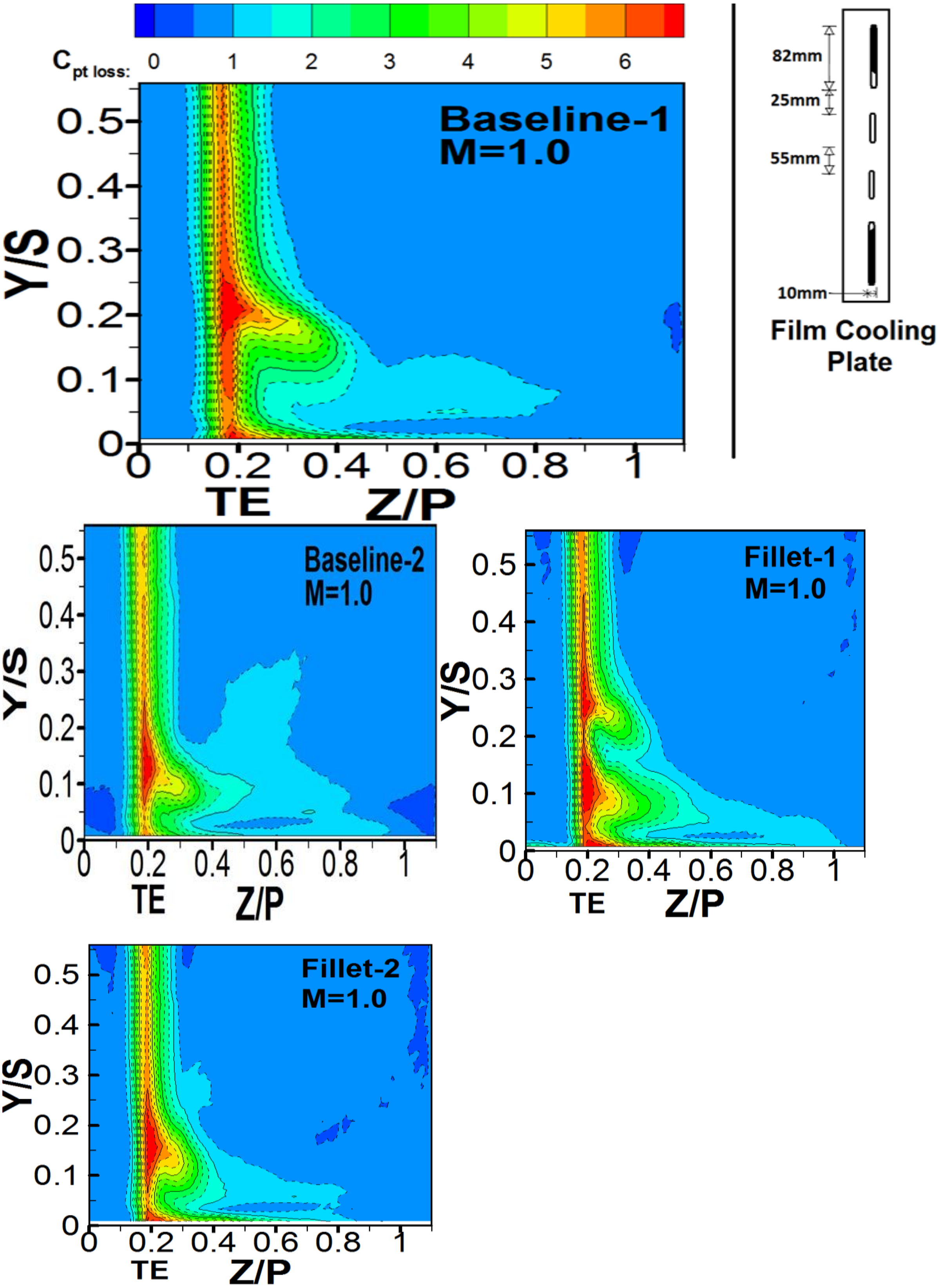

Figure 4-8: Distributions of total pressure loss coefficient, $C_{pt,loss}$ in Plane-4 at X_G/C_{ax} = 1.04 for M = 1.0 with and without fillets

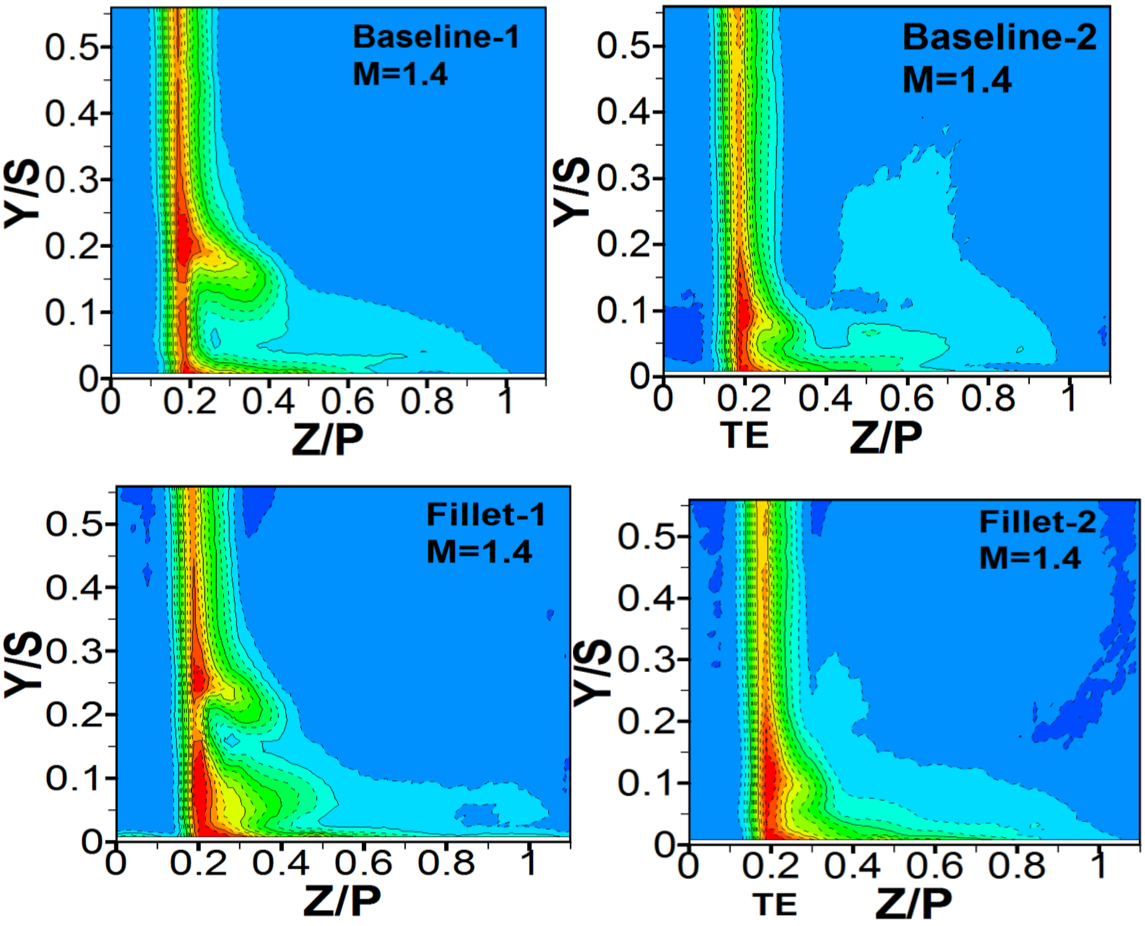

Figure 4-9: Distributions of total pressure loss coefficient, $C_{pt,loss}$ in Plane-4 at X_G/C_{ax} = 1.04 for M = 1.4 with and without fillets

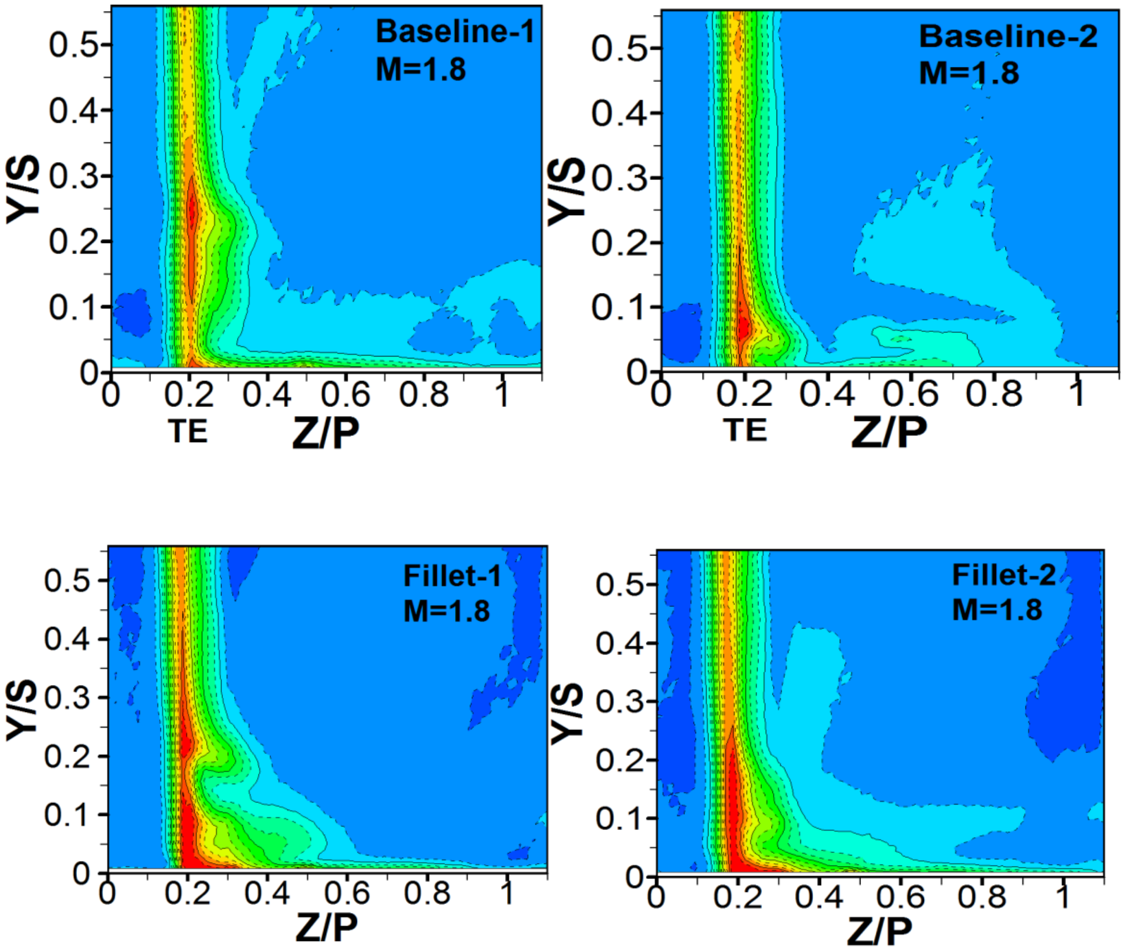

Figure 4-10: Distributions of total pressure loss coefficient, $C_{pt,loss}$ in Plane-4 at X_G/C_{ax} = 1.04 for M = 1.8 with and without fillets

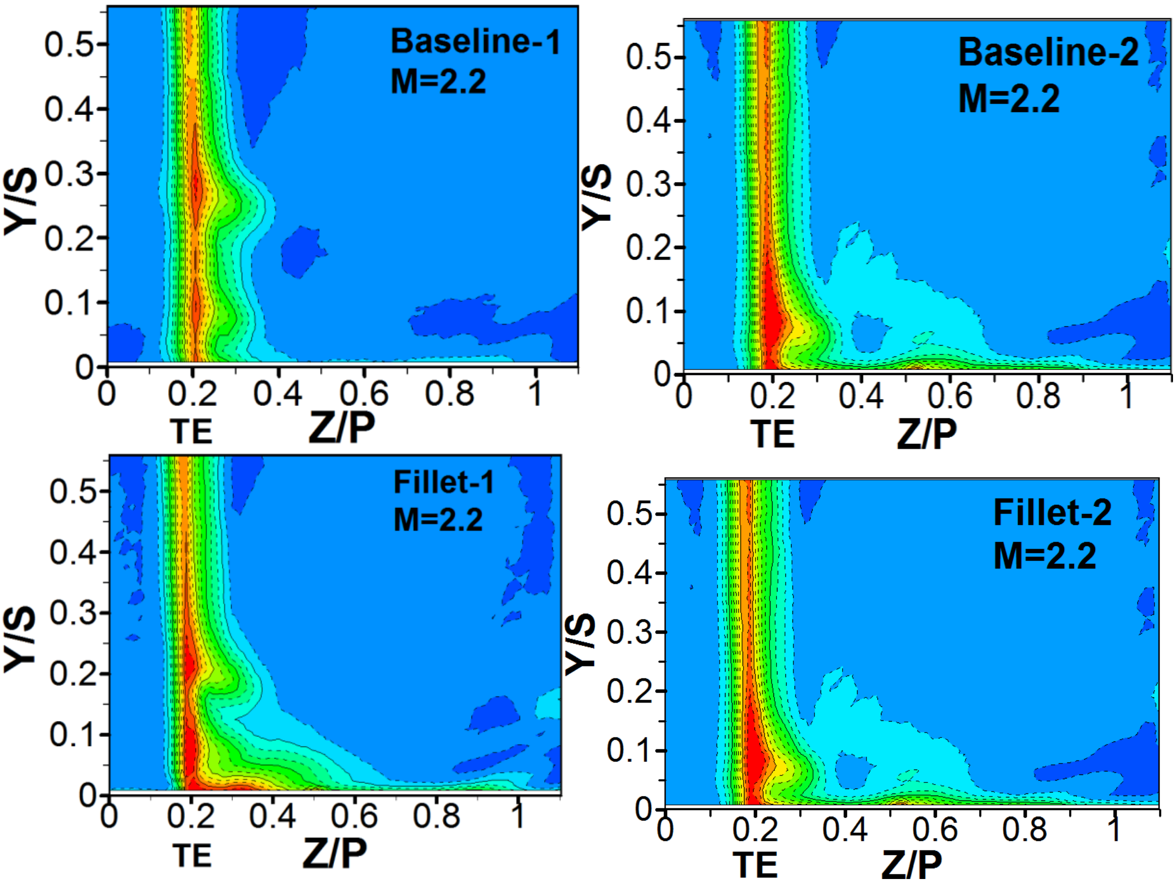

Figure 4-11: Distributions of total pressure loss coefficient, $C_{pt,loss}$ in Plane-4 at X_G/C_{ax} = 1.04 for M = 2.2 with and without fillets

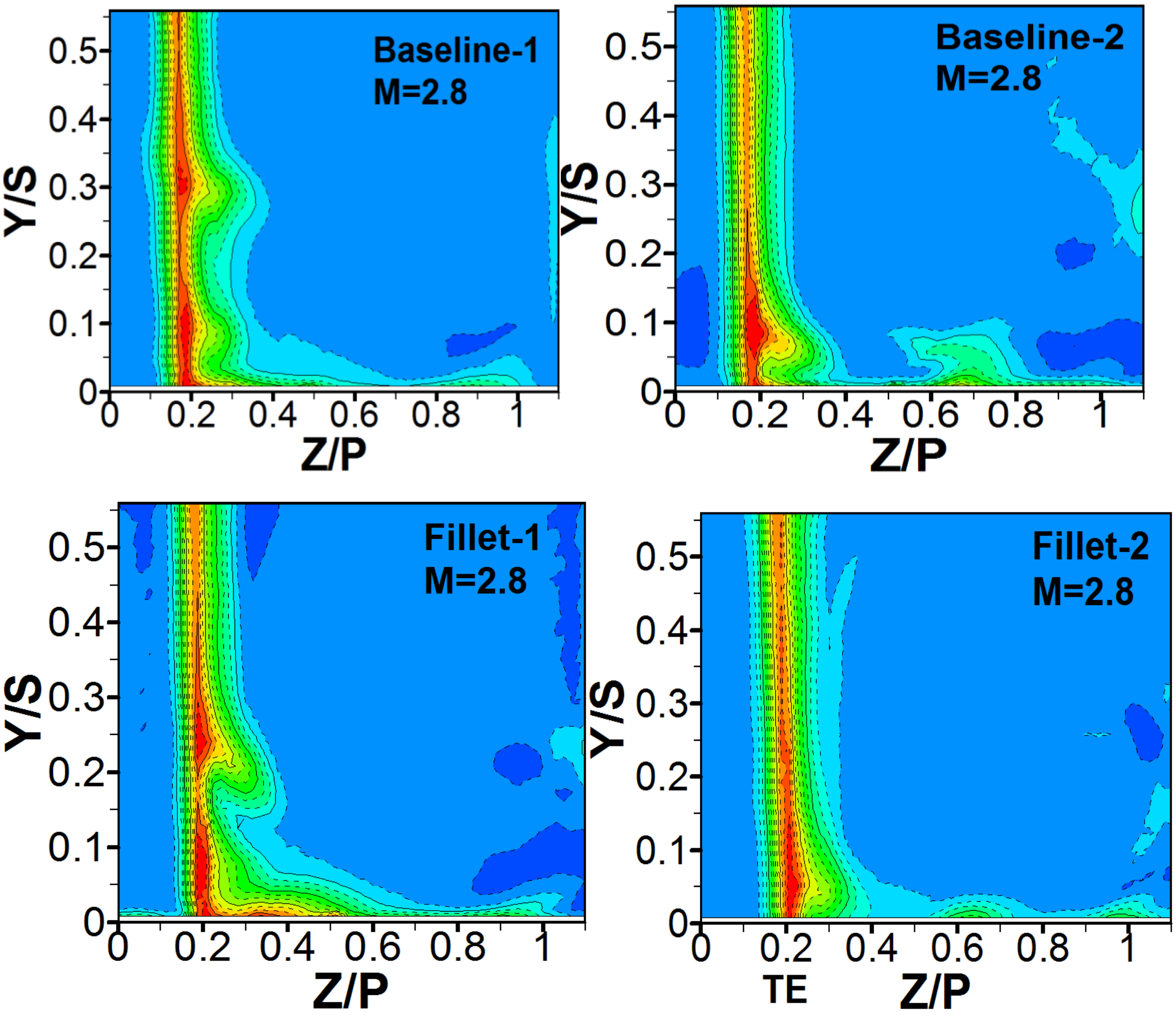

Figure 4-12: Distributions of total pressure loss coefficient, $C_{pt,loss}$ in Plane-4 at X_G/C_{ax} = 1.04 for M = 2.8 with and without fillets

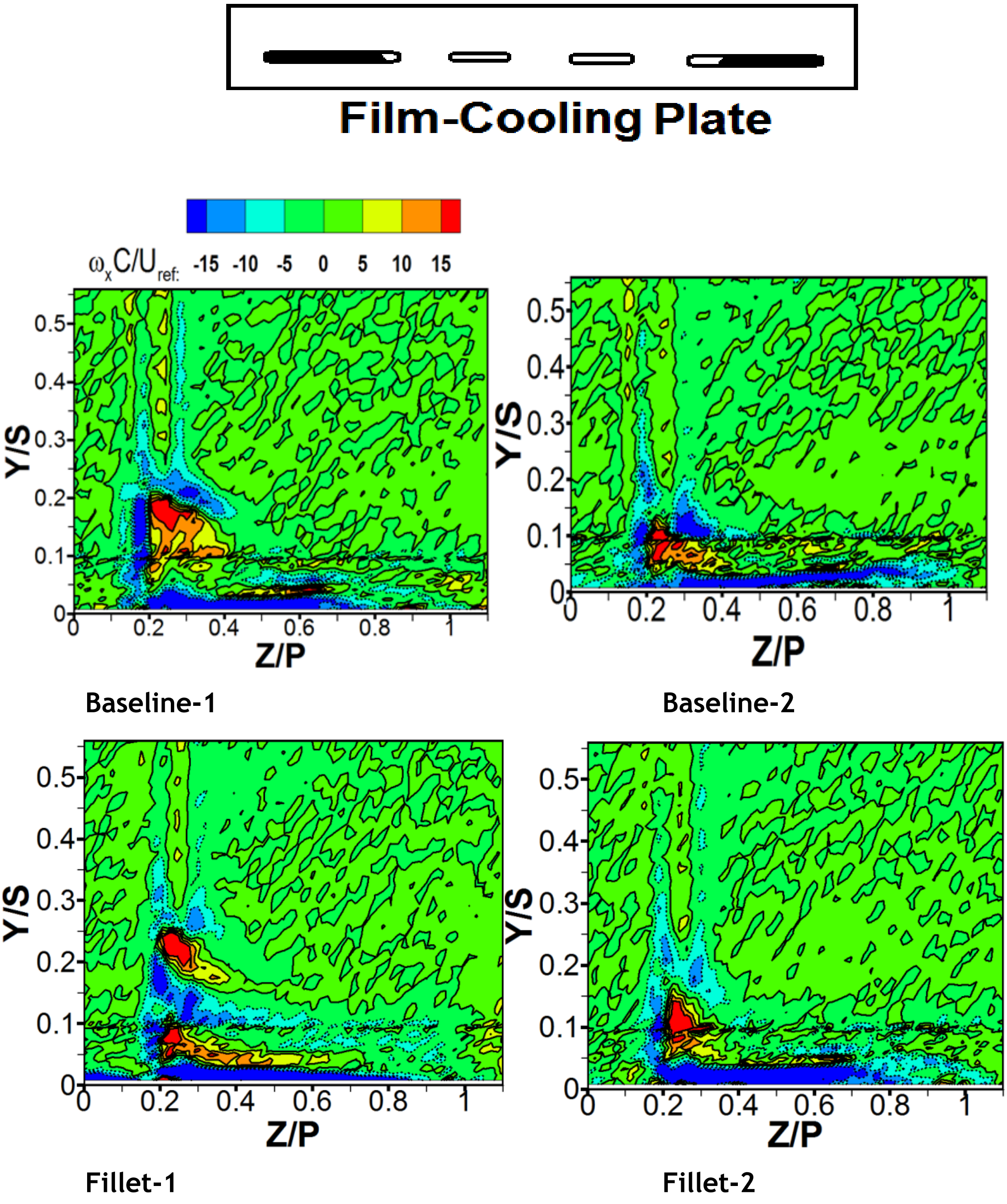

Figure 4-13: Contour plots of $\omega_x C/U_{ref}$ in Plane-4 at X_G/C_{ax} = 1.04 for M = 1.0 with and without fillets

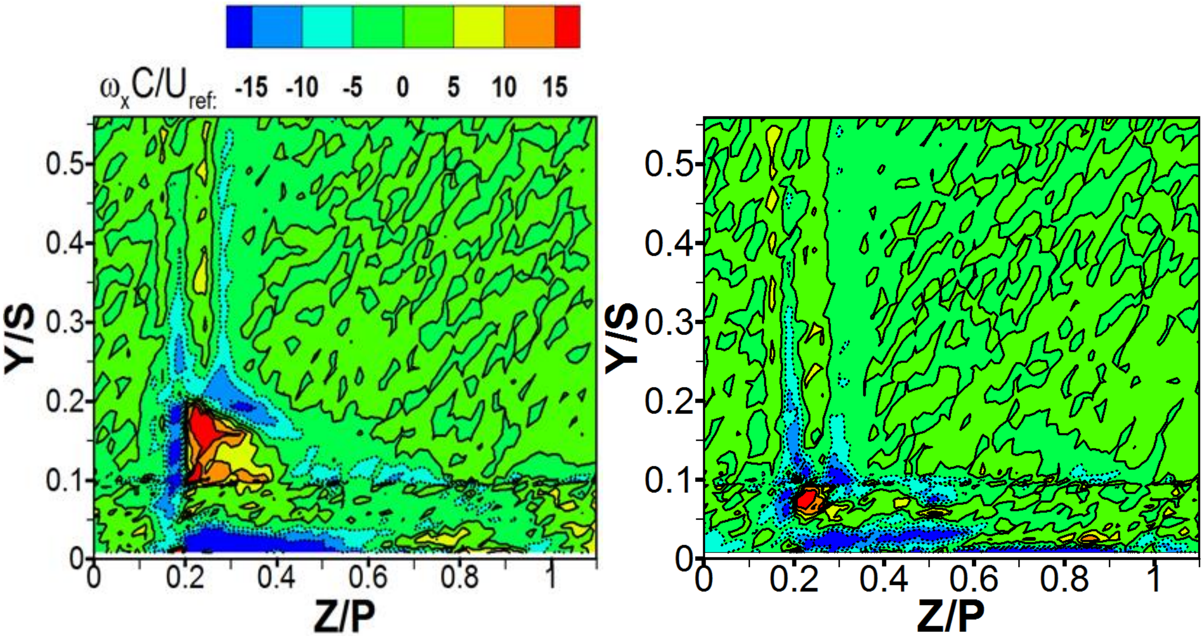

Baseline-1

Baseline-2

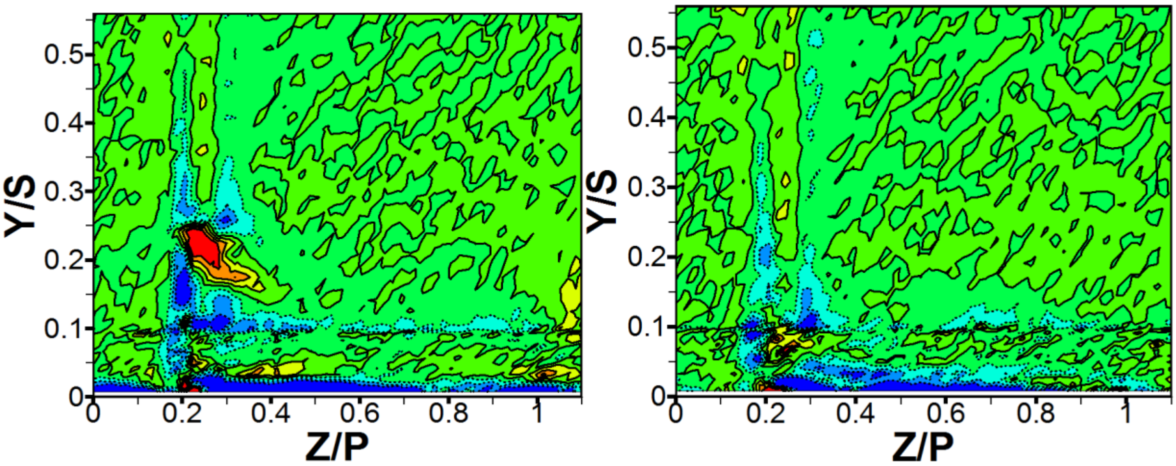

Fillet-1

Fillet-2

Figure 4-14: Contour plots of $\omega_x C/U_{ref}$ in Plane-4 at X_G/C_{ax} = 1.04 for M = 1.4 with and without fillets

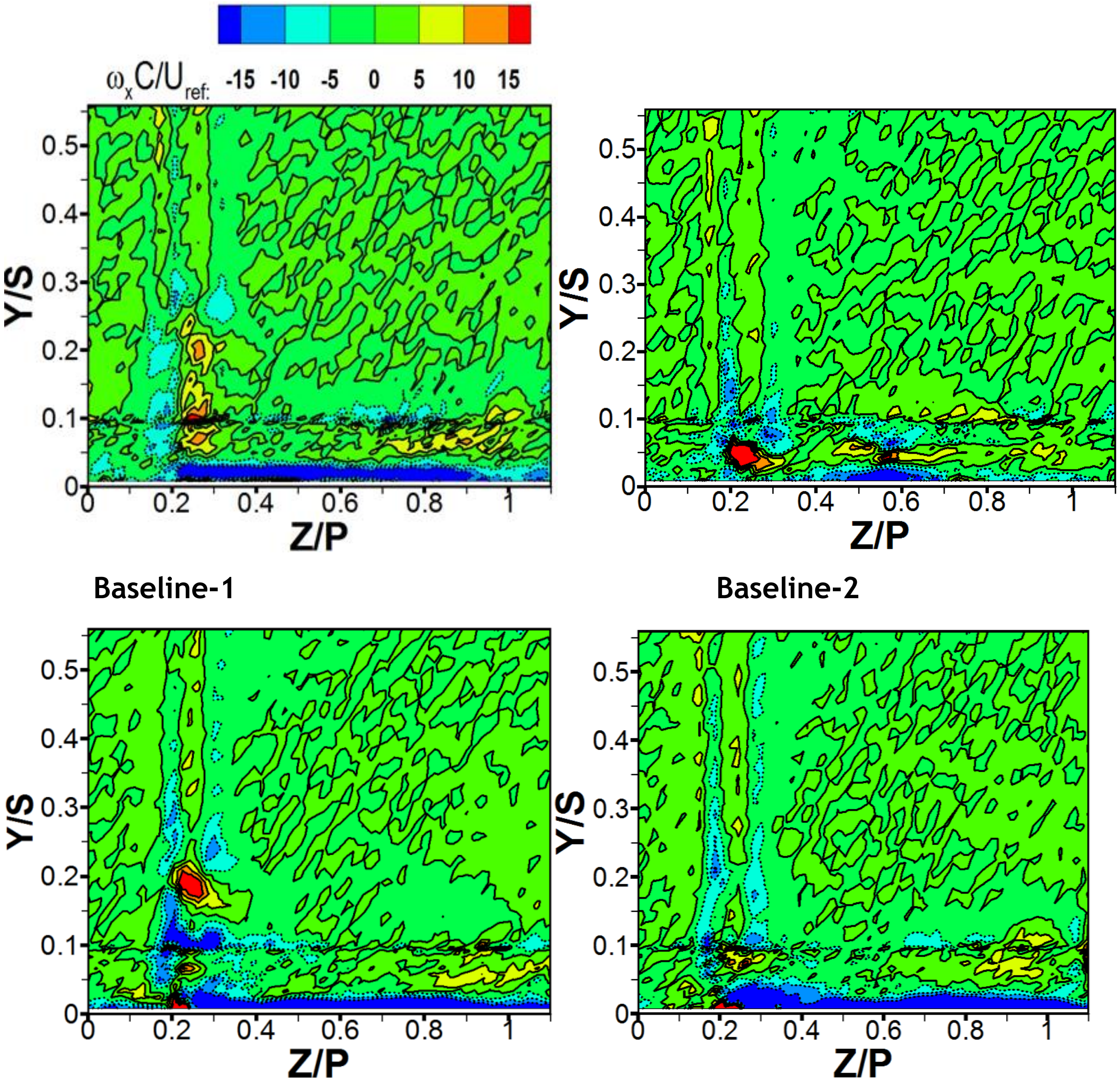

Baseline-1

Baseline-2

Fillet-1

Fillet-2

Figure 4-15: Contour plots of $\omega_x C/U_{ref}$ in Plane-4 at X_G/C_{ax} = 1.04 for M = 1.8 with and without fillets

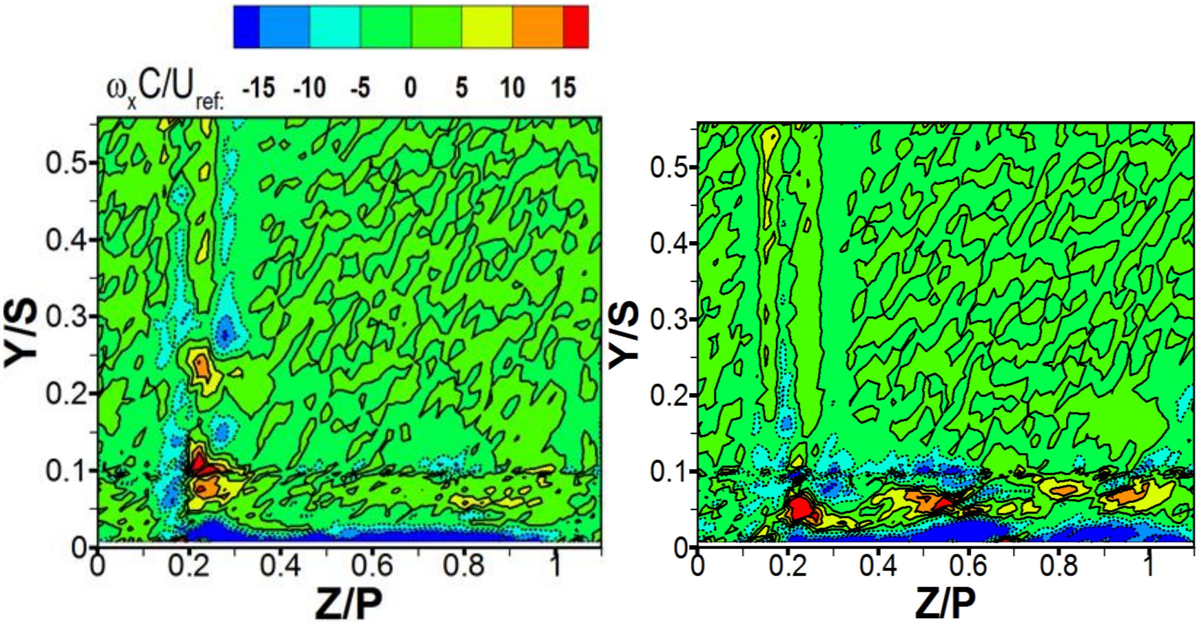

Baseline-1 **Baseline-2**

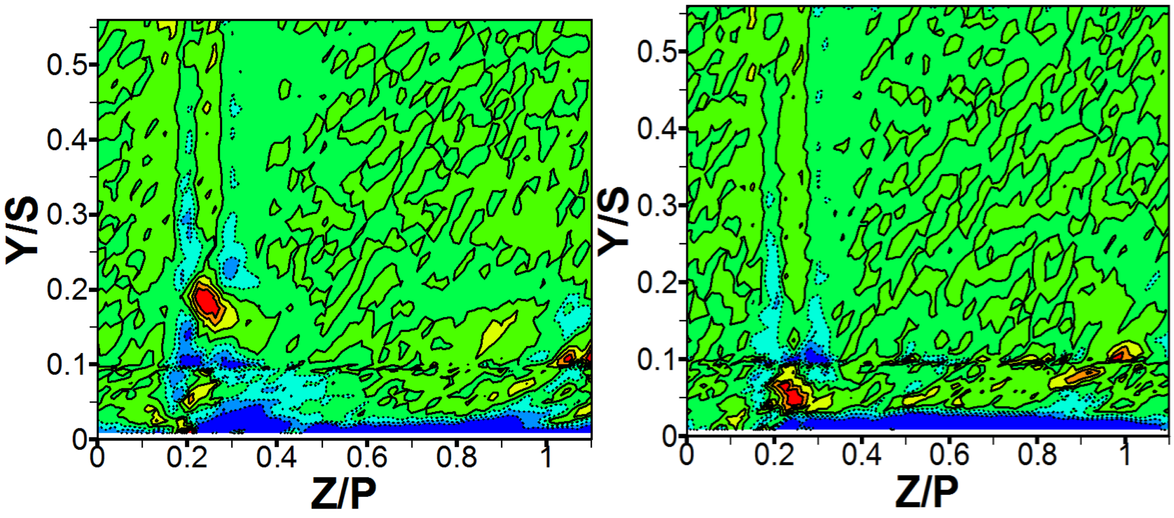

Fillet-1 **Fillet-2**

Figure 4-16: Contour plots of $\omega_x C/U_{ref}$ in Plane-4 at X_G/C_{ax} = 1.04 for M = 2.2 with and without fillets

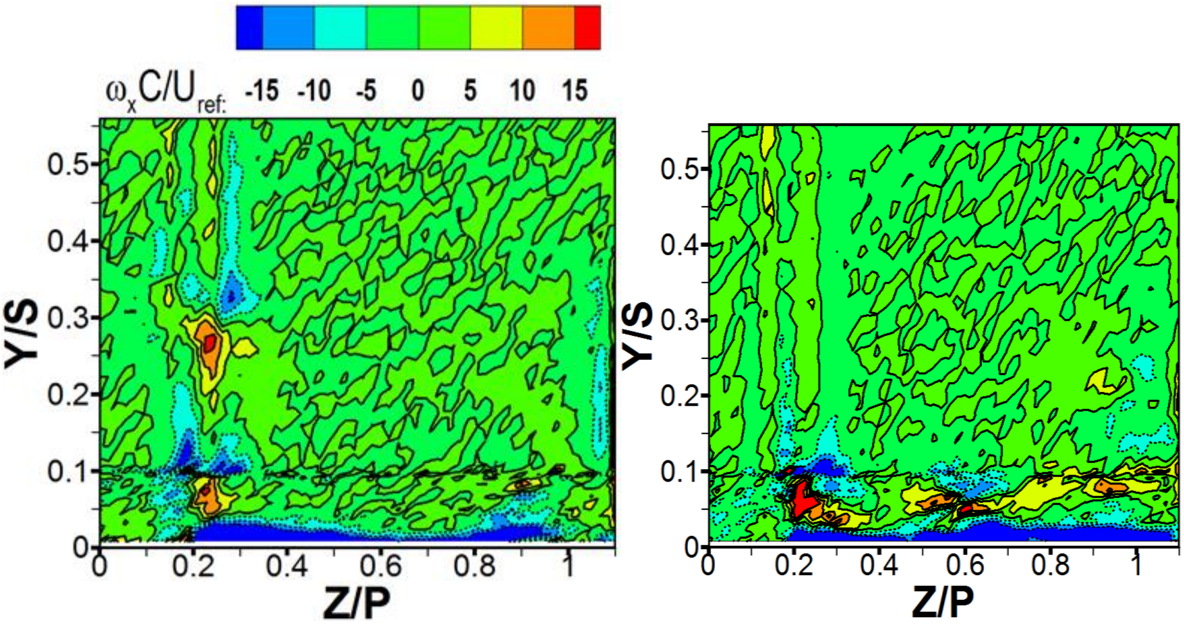

Baseline-1

Baseline-2

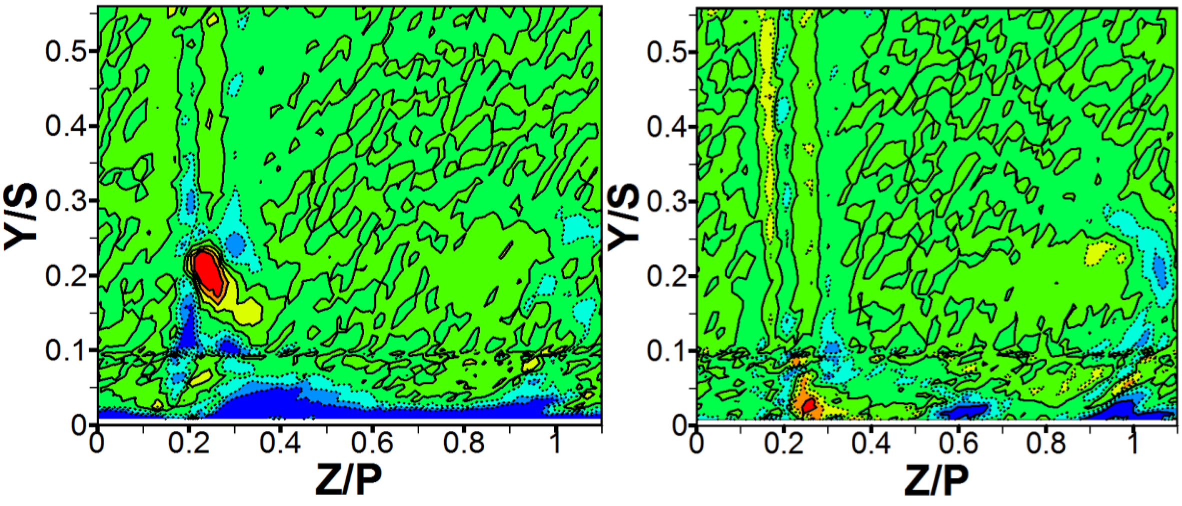

Fillet-1

Fillet-2

Figure 4-17: Contour plots of $\omega_x C/U_{ref}$ in Plane-4 at X_G/C_{ax} = 1.04 for M = 2.8 with and without fillets

Figures 4.18 to 4.20 provide the flow turning (yaw) from the inviscid flow direction that is exiting the turbine passage. It also provides the turning angle of the flow near the endwall due to secondary flows. The magnitude of the yaw angles are expected to be low for flow uniformity at the exit as the flow enters the next row of turbine blades in a gas turbine engine. Large values of the flow yaw angles are recorded at the near end wall ($Y/S < 0.1$) towards the SS for $M = 1.0$ (Figure 4.18). However, as the blowing ratio increases, there is reduction in the magnitude of the yaw angle value. The combined effect of the fillet and the blowing ratio is evident as the turning (yaw) is reduced along the endwall region. This implies that the passage vortex is weaken as previously shown in the $C_{pt,\ loss}$ values of Figure 4.12 near the endwall. The effect of the cross flow has apparently reduced with the employment of the fillet. High values of yaw angles are recorded at the trailing edge regions of Figures 4.18 to 4.20. This is a region of very high $C_{pt,\ loss}$ values (refer to Figures 4.8 to 4.12). The trailing edge wakes are responsible for these high values.

4.7.1 Mass Averaged $C_{pt\ loss}$ in the pitchwise plane at $X_G/C_{ax} = 1.04$ (Experimental)

Further analyses are carried out on the results in Figures 4.8 to 4.12 by estimating the mass-averaged of $C_{pt\text{-}loss}$ in the Plane-4 at all blowing ratios. The pitchwise mass-averaged is computed by numerically integrating Eqn 4.2 pitchwise line along Z/P at each Y/S measured location. The dA and m_{in} in the integrand of Eq. 4.2 is then determined based on the spatial (Y, Z) resolutions between the measurement grid locations and local axial velocity. The results are presented in Figure 4.21 and Figure 4.22. In Figure 4.21 and Figure 4.22, the higher $(C_{pt\text{-}loss})_{mass\text{-}av}$ near Y/S =0 0 is caused by the boundary layer effect close to the endwall. High $C_{pt,loss}$ near endwall is caused by viscous effects, wall turbulence, and entropy generation due to mixing of coolant flow with boundary layer flow. This is coming from the high momentum film cooling gets interacting with the free stream flow.

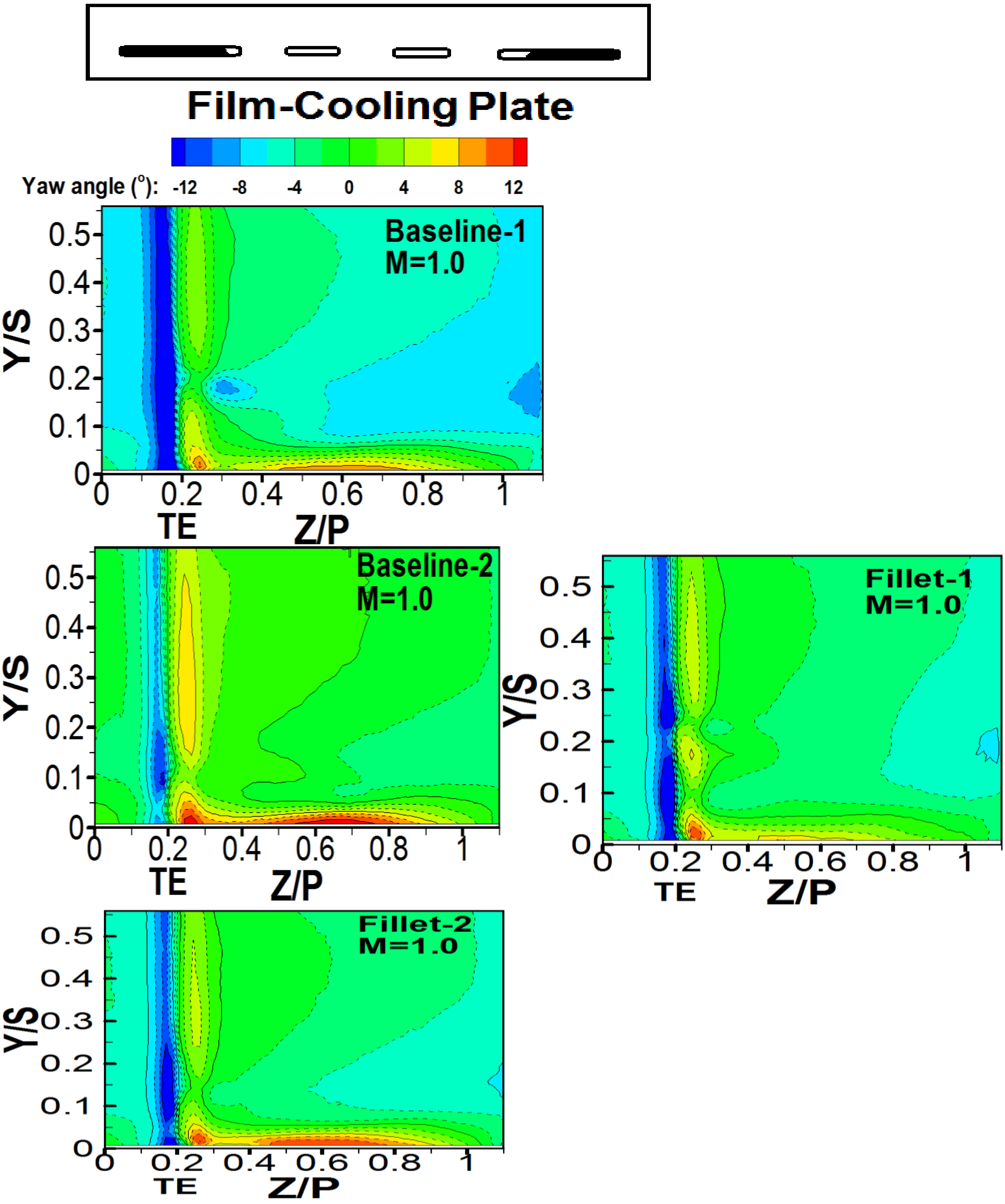

Figure 4-18: Contour plots of yaw angle in Plane-4 at X_G/C_{ax} = 1.04 for M = 1.0 with and without fillets

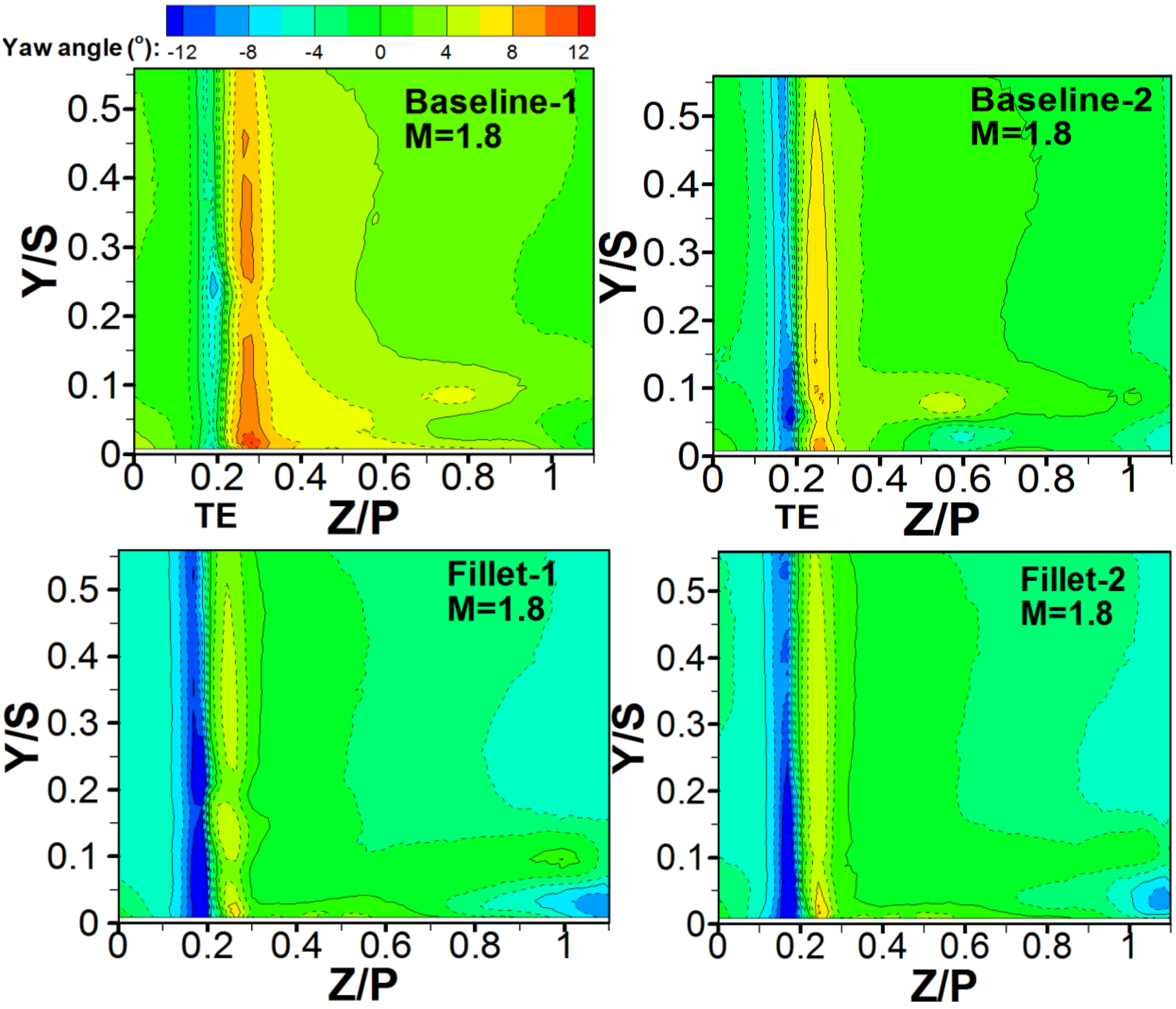

Figure 4-19: Contour plots of yaw angle in Plane-4 at X_G/C_{ax} = 1.04 for M = 1.8 with and without fillets

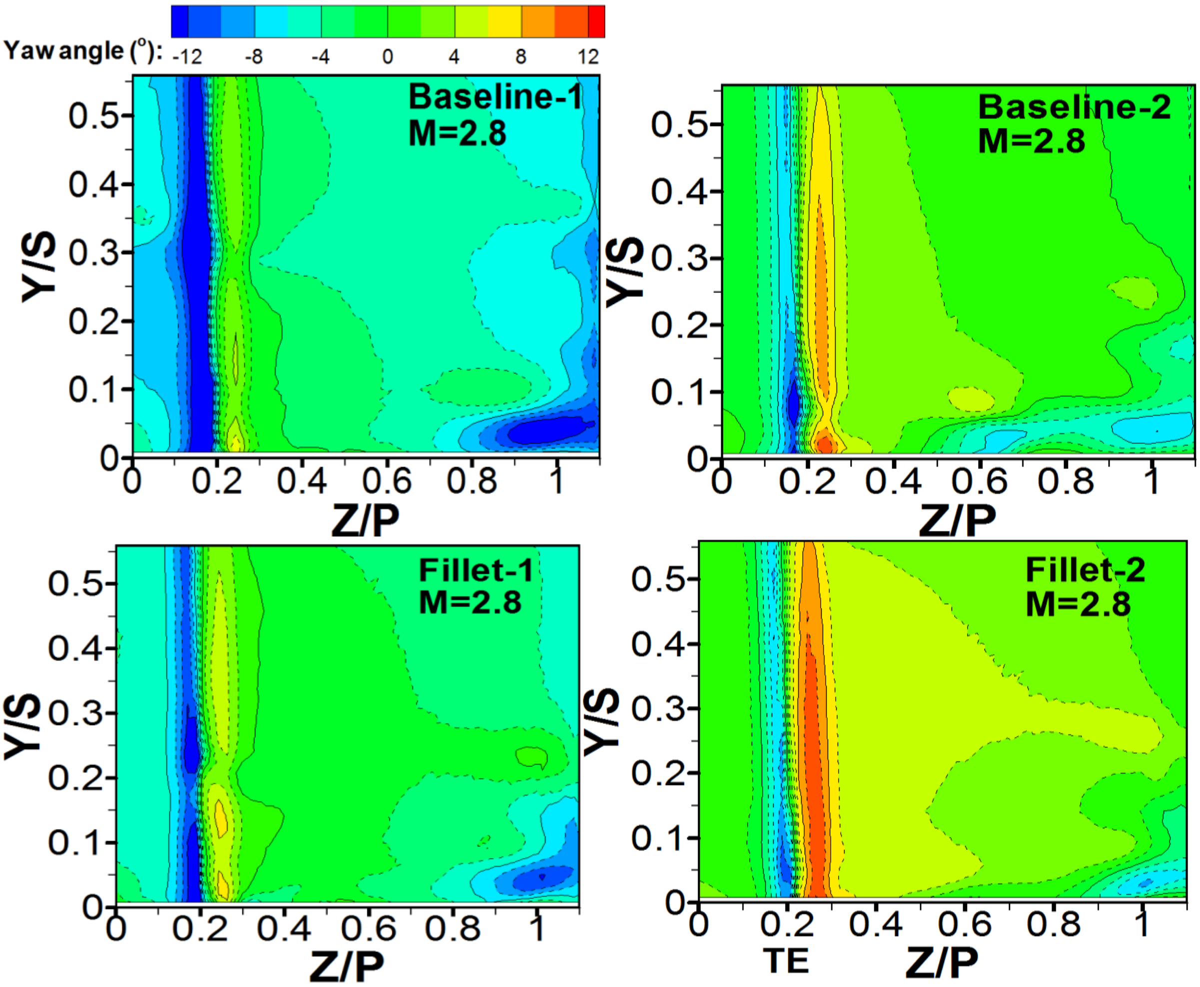

Figure 4-20: Contour plots of yaw angle in Plane-4 at X_G/C_{ax} = 1.04 for M = 1.8 with and without fillets

However, for each configuration (Baseline-1, Baseline-2, Fillet-1 and Fillet-2) in Figure 4.21 and Figure 4.22, high (M=2.8) gives lower mass-averaged $C_{pt\text{-}loss}$ which are favourable results as total pressure loss is reduced at the exit. The introduction of the fillets is contributing to the reduction of the total pressure loss due to the favourable interaction of the film flow with the fillet profiles. In Baseline-1 (Figure 4.21a) at M=2.2, the mass averaged is also showing the two bumps located at Y/S = 0.08 and Y/S = 0.23. The sudden rise in the mass-averaged at Y/S = 0.08 for M= 2.2 in Basline-1 is due to high entropy generation as a result of the chaotic mixing at that region. This rise (Y/S = 0.08) for Baseline-2 is also so slightly noticeable for M=2.8 with lesser magnitude due to the fluctuations in the turbulent TKE of the film cooling jet with the main flow. Besides, the second rise in the mass-averaged $C_{pt\text{-}loss}$ at Y/S = 0.23, M = 2.2 (Baseline-1) is due to the reduced passage vortex strength and size.

In general, region Y/S>0.4 up to the mid-span is having an approximate value of unity mass averaged $C_{pt\text{-}loss}$. This shows that total pressure loss is not significant there. The high magnitude of the exit wakes shown previously in Figure 4.8a is also partly responsible for the sudden rise (Y/P=0.07) in Figure 4.21.

The mass fraction of coolant flow relative to the passage mass flow (in a single passage) is computed with the Equation 4.6 and tabulated in Table 4.3. The coolant mass flow, M_{cool} is obtained from the orifice plate in the film-cooling flow circuit. The passage mass flow, M_{pass} is obtained from the reference velocity, U and passage inlet area (P*S) at the vane leading edge. It is apparent from the table that Fillet-1 is having the lowest mass fraction. As expected, as the blowing ratio increases, the mass fraction increases.

Table 4-3: Mass fraction of coolant

	1.0	1.4	1.8	2.2	2.8
Baseline-1	0.005800	0.026612	0.06555	0.08111	0.111819
Baseline-2	0.005755	0.022721	0.044563	0.060214	0.094777
Fillet-1	0.005229	0.017106	0.043968	0.060214	0.094091
Fillet-2	0.005755	0.022903	0.059169	0.073501	0.094296

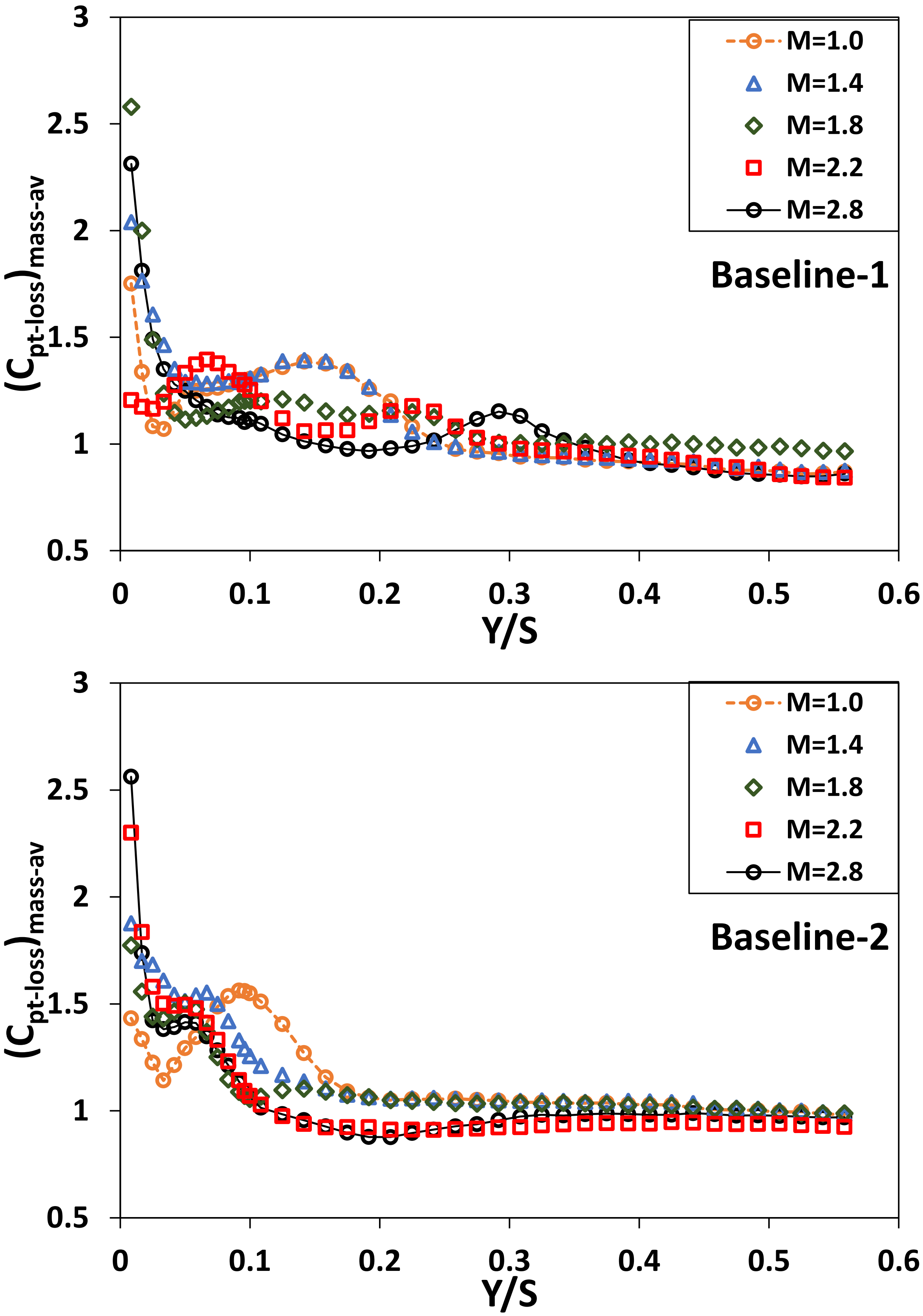

Figure 4-21: Mass-averaged ($C_{pt,loss}$)mass-av Line plot of total pressure loss coefficient, $C_{pt,loss}$ in the pitchwise planes at X_G/C_{ax} = 1.04 for for (a) Baseline-1 & (b) Baseline-2

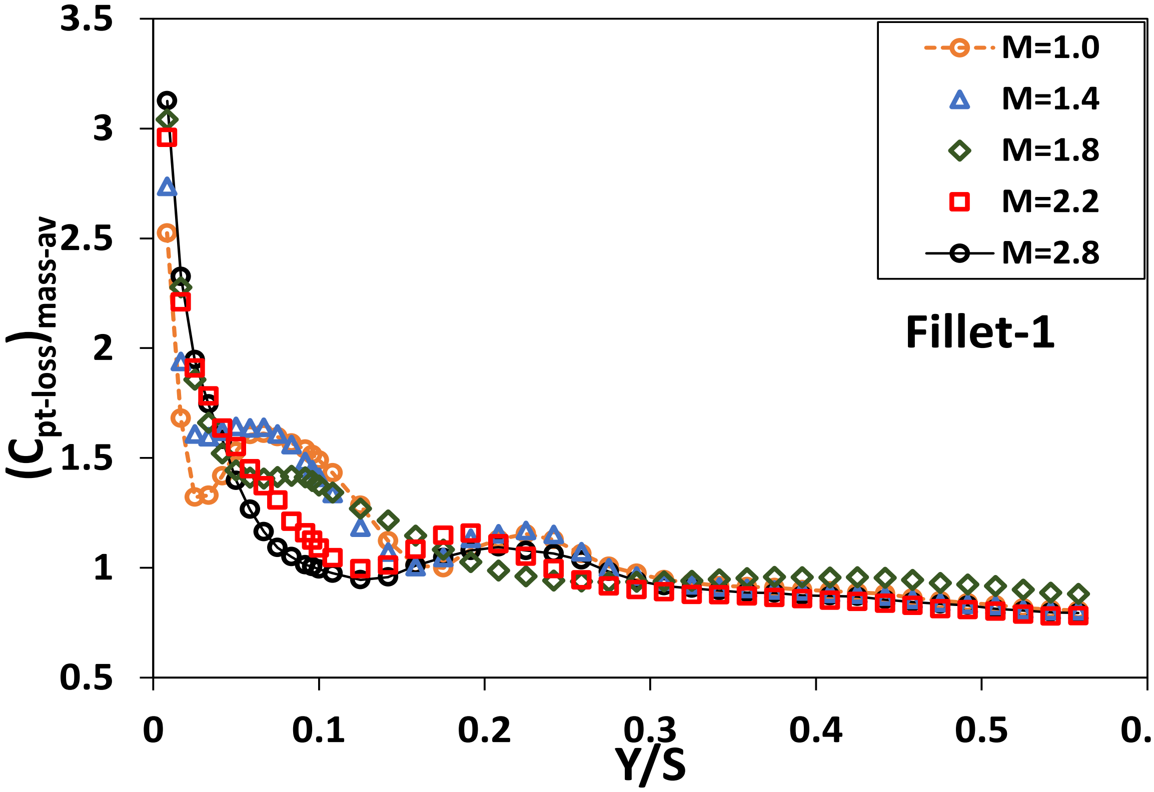

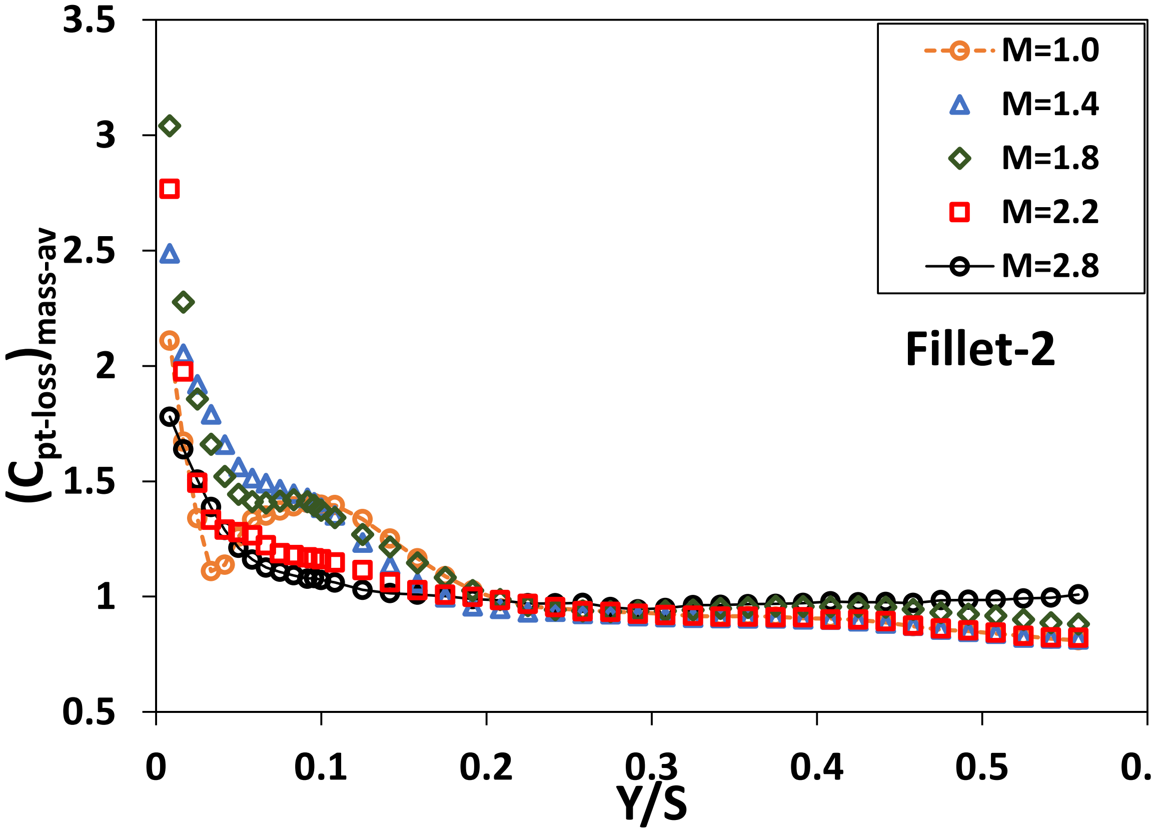

Figure 4-22: Mass-averaged ($C_{pt,loss}$)mass-av Line plot of total pressure loss coefficient, $C_{pt,loss}$ in the pitchwise planes at X_G/C_{ax} = 1.04 for for (a) Fillet-1 & (b) Fillet-2

$$M_{fraction} = \frac{M_{cool}}{M_{pass}} \tag{4.6}$$

4.7.2 Global Mass Averaged $C_{pt\ loss}$ in the pitchwise plane at $X_G/C_{ax} = 1.04$ (Experiments)

The overall mass-averaged C_{ptloss} of all the blowing ratios in Plane-4 are presented (Figure 4.23a) at different M values to determine the aerodynamic effect on the exit flow structures. Equation 4.2 is again numerically integrated to compute the overall loss coefficients in Figure 4.23 with the m_{in} now referring to the vane passage mass flow (M_{pass} in a single passage). The ratio of the overall mass-averaged C_{ptloss} to that of the mass fraction is also presented in Figure 4.23b. At blowing ratio M >1.8, there is gradual reduction in the total pressure loss. This is attributed to the reduction of the pressure and suction side leg vortices by the film cooling jets and the end wall modification. Figure 4.23a shows that at the highest blowing ratio, the various configurations of endwall and combinations of film-cooling arrangements perform almost the same way. At blowing ratio M=2.2, the Baseline-1 records the highest overall mass-averaged of $C_{pt\text{-}loss}$ due to the interactions of the film cooling jet with ~~and~~ the passage vortex and endwall boundary layer, thereby increasing the passage pressure more than the other configurations. In summary, at high blowing ratios, the high momentum jets is traveling all the way to the exit and is having a favourable effect on the cross-flow and the passage vortex by reducing the flow circulation within the passage region. This may afford better coverage of endwall by the film cooling with appreciable increase in the film-cooling effectiveness on the endwall thereby prolonging the turbine endwall component against early failure from high pressure fluctuations and high temperature.

However, the ratio of the overall mass averaged and the mass fraction decrease as the film cooling blowing ratio increases for all cases and configurations considered (Figure 4.23b). This is simply in agreement with the conclusion of (Friedrichs et al., 1997). At M<1=1.8, Fillet-1 is showing higher pressure loss per mass fraction. This means that Fillet-2 performs better with the film cooling flow at lower blowing ratios. Refer to Section 3.5.1 and Appendix D for the detail uncertainties associated with all the experimental data.

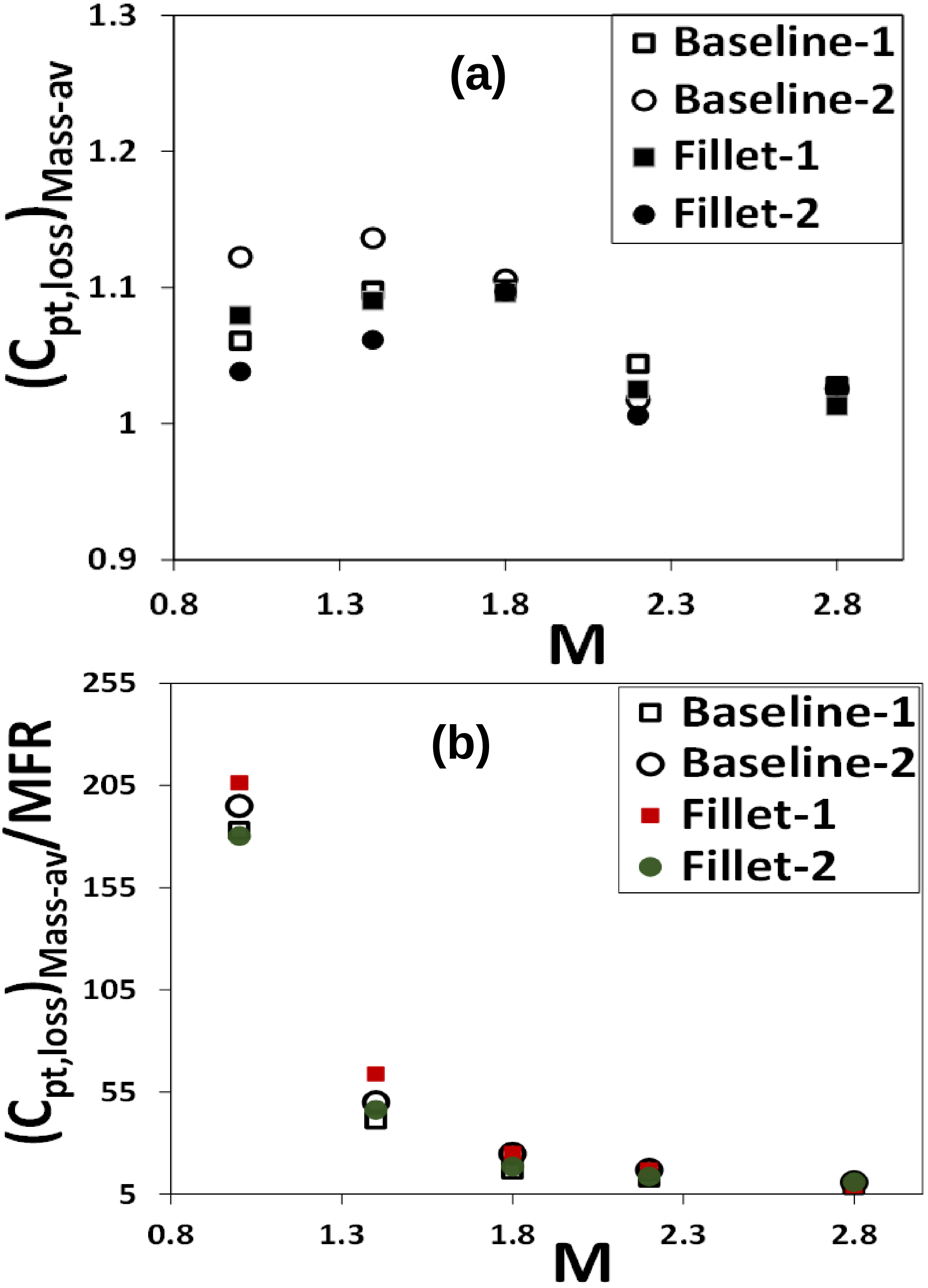

Figure 4-23: ***(a) Mass-averaged ($C_{pt,loss}$)$_{mass\text{-}av}$ and (b) mass-averaged $C_{pt,loss}$ per mass fraction** ratio **(MFR) of film flow in Plane-4 with and without fillet***

5. CHAPTER 5: HEAT TRANSFER AND FILM COOLING RESULTS

5.1 Experimental: Thermal boundary layer

Periodic flow condition is ensured (Figure 5.1) from time to time during different measurements are taken on the turbine-vane test rig. This is done in the test section to ensure that the experimental condition of the cascade is a representative of the turbine vane passages. Adiabatic endwall is also ensured at the film-cooling side of the vane-blades as shown in Figure 3.1 during the film-cooling measurements. The ambient conditions like temperature and density are assumed to be constant for the measurement at a given test condition. The coefficient of static pressure taken along the blade profile at mid-span, $Y_G = 0.5S$ is computed using the measured static pressures and Equation 4.1. Figure 5.1 shows that there is no significant change in the pressure loading on Blades 3, 4 and 5. This implies that the blades are periodic according to (Kang and Thole, 2000). Installation of Fillet-1 and Fillet-2 separately also shows that the employed fillets are not adding extra load on the blade since the static loadings on the blade remain approximately the same through the flow regime (Figure 5.2).

The thickness of thermal boundary layer is measured in the reference plane just like the velocity boundary layer at the streamwise free-stream turbulence intensity (*Tu*) of 2.5%. During the temperature flow-field measurements of incoming air to the cascade, the endwall both inside cascade and upstream of cascade (up to 1.4 m upstream from the leading edge) is heated with the copper tape heater providing a constant heat flux into the flow. The thermal boundary layer (Figure 5.3) is about 8% of the blade span. The ratio of the velocity boundary layer to the thermal boundary layer gives a Prandtl number (Pr) of about 0.7 – 1.0.

5.2 Nusselt Number distribution at the Endwall

The secondary flows along the endwall formed by the strong vortical flows advect heat from the leading-edge horseshoe vortices and augment the local heat transfer at the endwall region. Figure 5.4 is presented for the local heat transfer distributions in the form of Nu along the endwall. Baseline in this case refers to configuration with no fillet and no film flow ($M = 0$) and Fillet-1 and Fillet-2 refer to the blade-endwall junction modifications without film cooling.

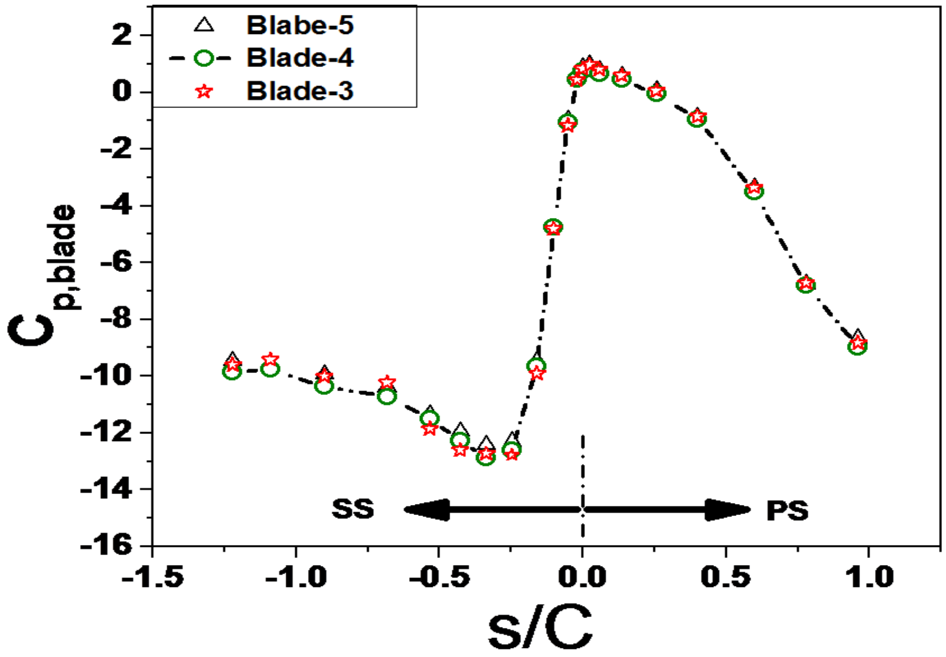

Figure 5-1: Static pressure coefficients on the measurement blades

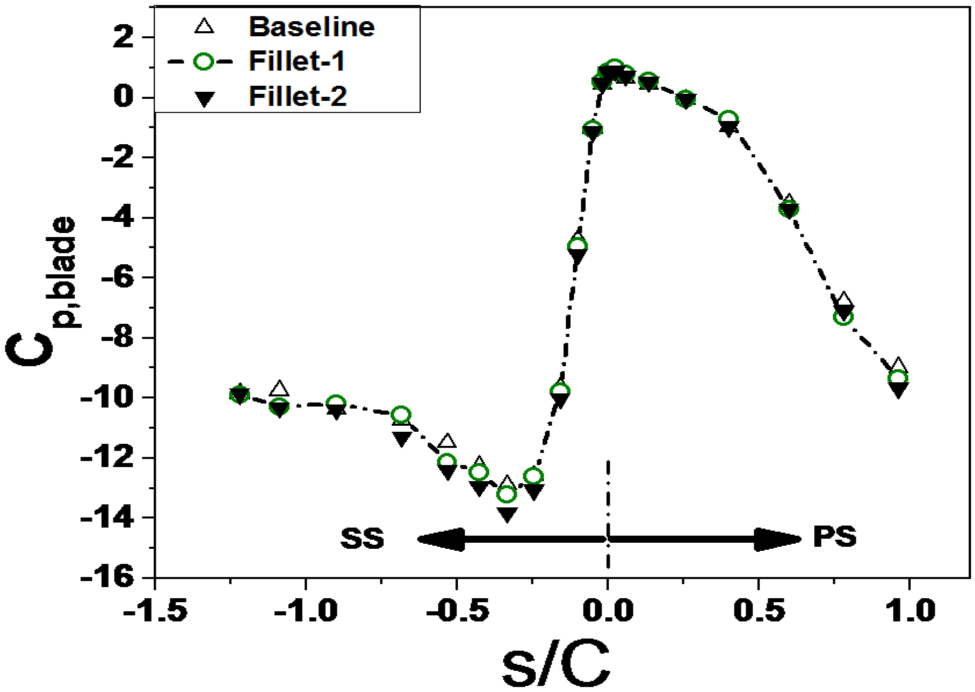

Figure 5-2: Static pressure coefficients on the blade

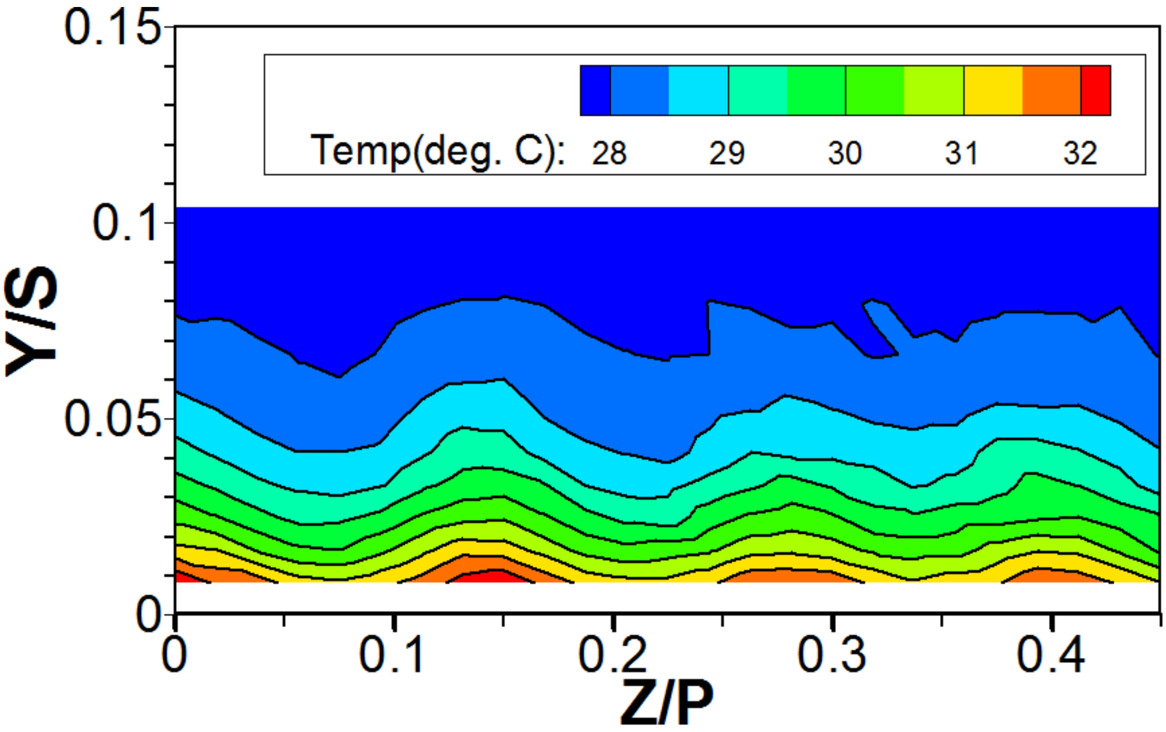

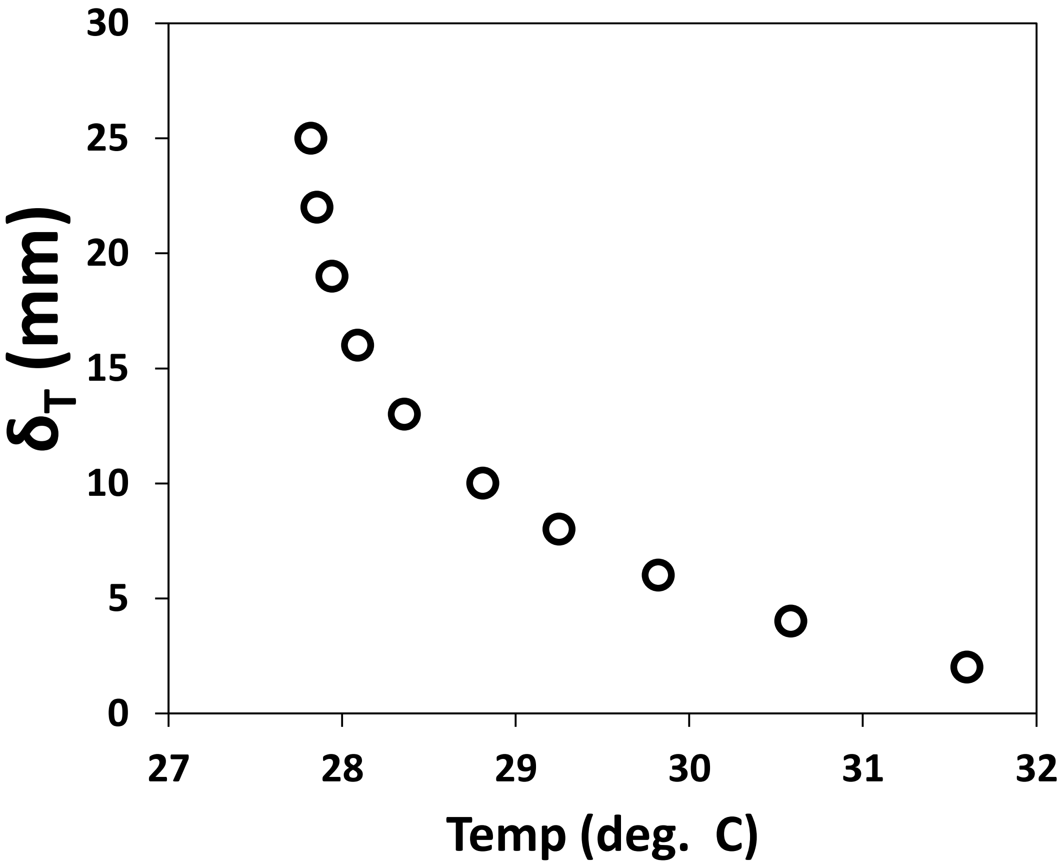

Figure 5-3: Reference thermal boundary layer (a) surface plot (b) line plot

The heat transfer is being presented in terms of the Nusselt number (Nu). Appendix G also gives the Stanton number representations of the heat transfer coefficients. Thermocouples are embedded in the endwall and make contact with the heater foil while the blade surface is considered to be adiabatic. As the bottom side of the blade is not heated, conduction heat loss through the blade is not considered. However, the bottom sides of the fillets are heated where no thermocouples are present. Consequently, heat transfer data are not presented on the fillet(s) surface. The outer side of endwall is insulated to reduce heat loss by conduction through the acrylic polycarbonate plate. A constant heat flux is provided to the flow from the endwall copper strip heaters employing a suitable bottom endwall shown in Figure 3.8 starting just upstream of the leading-edge all the way to the exit Plane-4 location at 1.04C_{ax}. In the upper endwall, four windows (Figure 3.10) provide optical access to the heated bottom endwall for infrared (IR) imaging at the steady state temperatures. The images from four windows are combined to give a complete coverage of the cascade passage bottom endwall. A Zn-Se window with anti-reflection coating, that passes the infra-red (IR) wavelength (between 5 μm and 95 μm) is used at the upper wall windows. The thermocouple coordinate locations (Figure 3.6) are used for the calibration of images from the infer-red (IR) camera. Details of the in-situ calibration of the IR-images are described in the 3.3.2 Section of Chapter 3 of this thesis. Six thermocouples are placed at the boundary between the acrylic endwall and insulation material. Six thermocouples are also placed at the other side of the insulation layer. The temperature differences across the insulation layer then provide estimation of the one-dimensional conduction loss through the endwall from the heater side to outside ambient air. As the heaters are placed on the flow side of the endwall and the most of the heater power is convected to the air flow, the conduction loss is usually about 3% of the total heating power which is also found by (Mahmood et al., 2005). The reference air temperature is also taken simultaneously with the endwall temperatures. The Eqns. (5.1-5.5) along with the energy balance are used to determine the conduction power loss, convection power to the flow, local Nusselt numbers, and local Stanton numbers. Note that the Nu and St in Eqns. (5.4) and (5.5) are calculated based on the average convective heat flux at the endwall. As indicated earlier, the St distributions on the endwall are provided in Appendix G.

“Baseline” condition in this chapter refers to a condition of no film flow (M = 0) and no fillet installed. The reference velocity and thermal boundary conditions are kept the same in the cascade for all the test conditions. Fillet-1 and Fillet-2 also refers to the situations of no film cooling flow (M = 0) with only the fillets installed. The global coordinate system is located at (0, 0, 0) at the junction of endwall and leading-edge of Vane-3.

The resulting Nu distributions are presented in Figure 5.4 with the fillets and without the fillet. For all three cases, the region $X_G /C_{ax} > 0.6$ has high and gradual increase of Nu because of the acceleration of the passage flow in the throat region. Higher Nu near the PS and SS leading edge at $X_G/C_{ax} < 0.2$ are caused by the PS leg and SS leg vortices for all three cases. For the baseline case, the region is larger because of the stronger passage vortex. However with the installation of Fillet-1 and Fillet-2, the mid-regions of the passages to the suction side are having lower Nu coverage areas compared to those with the baseline case.

The lowest Nu region for Fillet-2 is larger in size Compared to the baseline and Fillet-1 cases in Fig. 5.4, particularly in the mid-passage region ($0.25 < X_G/C_{ax} < 0.6$). The reattachment line downstream of the passage vortex moves upstream as the fillet is employed and causes the boundary layers (both velocity and temperature) to be thicker along the mid-passage region. The low Nu value region is thus larger for the fillets than the baseline in the mid-passage ($0.25 < X_G/C_{ax} < 0.6$). Besides, further downstream along the endwall, the Nu are smaller for the fillets than for the baseline case. This shows that by repositioning the reattachment line the fillets reduce the accelerations in the boundary layer at and downstream of the throat ($X_G/C_{ax} > 0.6$). The local Nu distributions in $X_G/C_{ax} > 0.6$ thus do not increase for the fillet in the same way as for the baseline (Kang and Thole, 2000).

$$Q_{cond} = \frac{k_{insulation} * A_{Heat}\left(T_{av\_1} - T_{av\_2}\right)_{insulation}}{\left(\Delta x_{th}\right)_{insulation}} \qquad (5.1)$$

$$Q_{conv} = (IV)_{pass} - Q_{cond} \qquad (5.2)$$

$$q_{flux} = \frac{Q_{conv}}{A_{Heat}} \qquad (5.3)$$

$$Nu = \frac{\left(q_{flux} C_{actual}\right)}{\left(T_{loc} - T_{ref}\right) k_{air}} \qquad (5.4)$$

$$St = \frac{q_{flux}}{\left(T_{loc} - T_{ref}\right) C_p U_{ref} \rho_{air}} \qquad (5.5)$$

5.3 Temperature Field with Endwall Heating

Further analysis of the influences of passage vortex on the convection of heat from the endwall is carried out at the pitchwise plane (X_G/C_{ax} = 0.58) where the pressure side-leg and suction side-leg vortices combine to form the passage vortex (refer to the Fig. 4.5). Temperature scans of the flow-field are taken with a K-type thermocouple probe as illustrated in Section 3.3.1 of Chapter 3. The measurements provide the depth of penetration of the heat in the spanwise direction from the heated endwall. The data are presented in Figures 5.4. The suction side is located on the left side while the pressure side is located on the right side of the figure. The free-stream temperature is about 24 °C. The solid lines in the contour plots indicate the temperature levels of 24.5°C, 27°C, 29.5°C, 32°C, and 34.5°C. The triangular regions at the bottom corners for Fillet-1 have no data because of the presence of the fillet volume. The region of $Z/P < 0.3$ and $Y/S < 0.1$ is experiencing high temperatures due to the mixing by vortical flows in the passage vortex structures. This region also corresponds to the region of high acceleration towards the passage throat (refer to Fig. 5.5). The heat is being propagated in the spanwise direction up to about 10% of the span in the baseline case. The magnitude of the heat in the fillet cases are reduced as shown in Fillet-1 and Fillet-2. This shows the favourable effect of the leading-edge modification on the endwall heat convection. The local high temperature between $0.05 < Y/S < 0.1$ at the suction side (SS) for the Fillet-1 in Figure 5.4 in caused by the suction side-leg vortex. The high temperature region suggests a link between the endwall flow-temperatures and positive axial vorticity from the endwall modification.

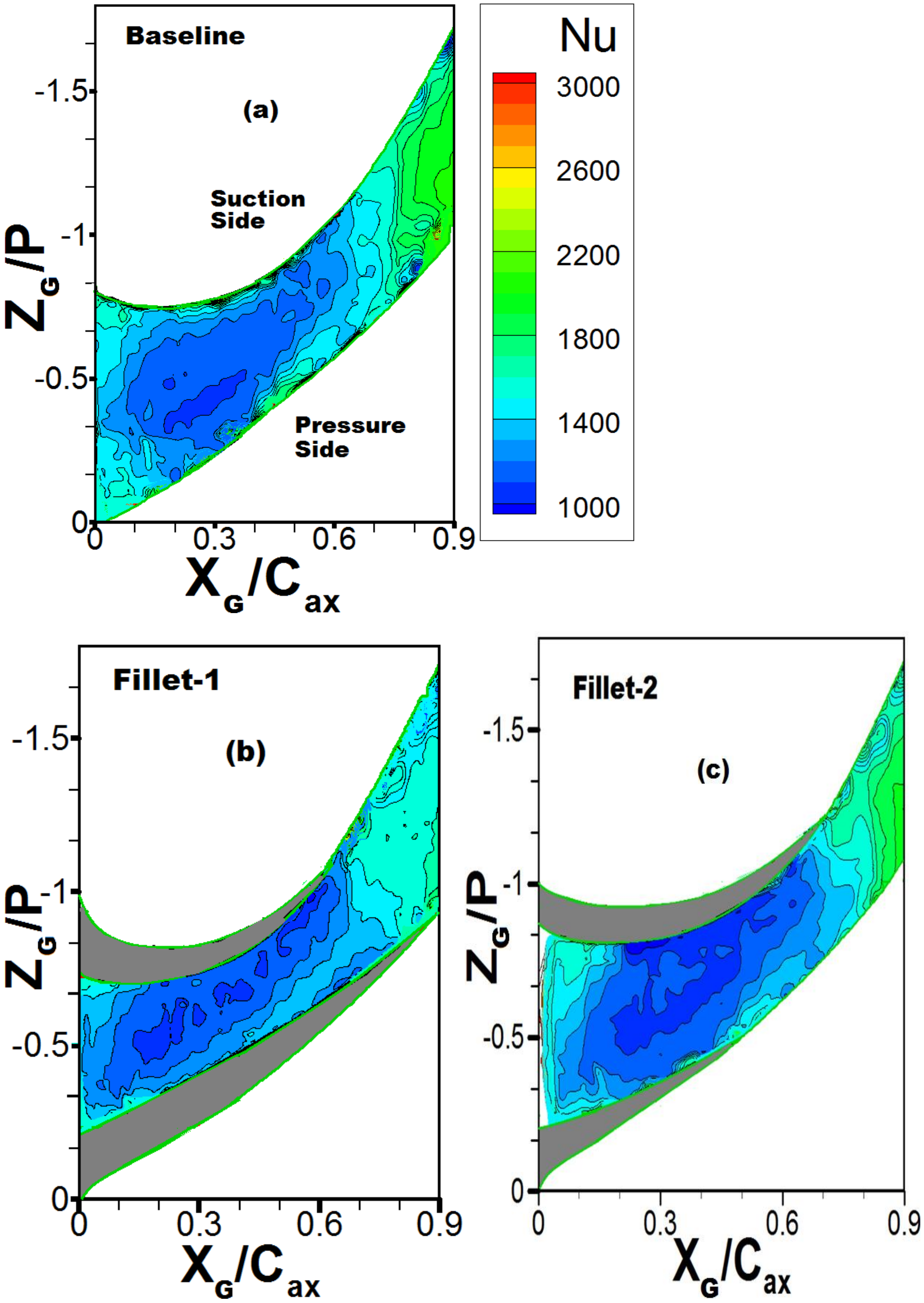

Figure 5-4: Nusselt number distribution at the endwall for M = 0 with and without fillets (a) Baseline (b) Fillet-1 and (c) Fillet-2

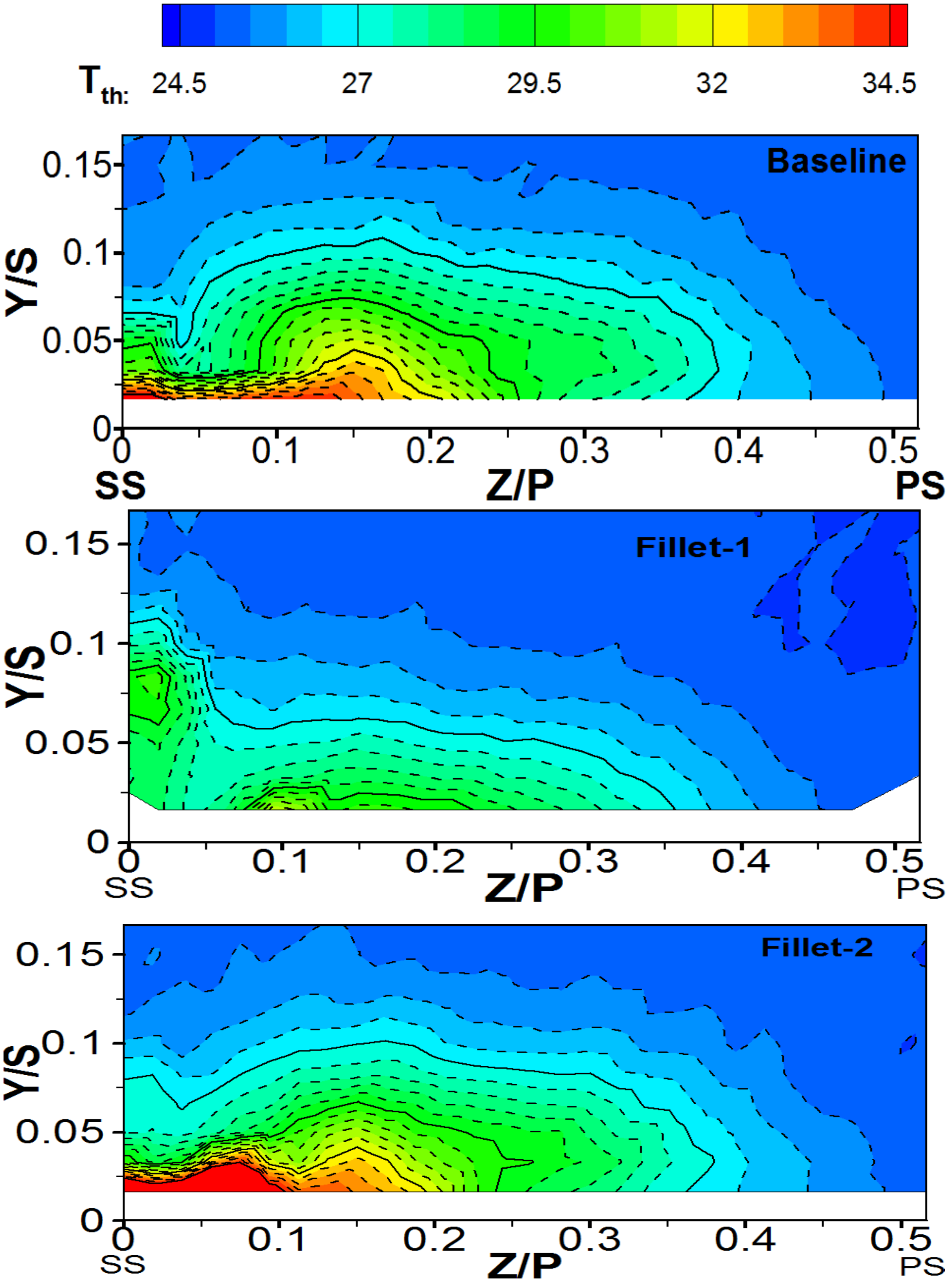

Figure 5-5: Temperature distribution in Plane-3 at XG/Cax = 0.58 without film cooling (M = 0)

5.4 Nondimensional Temperature Fields with Film Cooling

Nondimensional temparature field (ϴ) of the flow near the endwall is computed using the Equation 5.6. The temperature data are obtained with the film cooling flow and when the endwall is adiabatic. The contour are presented in Plane-1, Plane-2 (upstream) and Plane-3 (throat region) in Figs. 5.6 to 5.17. All the contour plot varies between $0.3 \leq \Theta \leq 0.9$. At $\Theta \geq 0.9$, the temparature is approximately the same as the free stream temparature. Therefore, the lower the magnitutude of ϴ, the better the cooling. This means that lower ϴ is desired for effective cooling of the endwall. Plane-1 and Plane-2 are parpendicular to the curvature of the blade profile as shown in Figure 3.1 and Plane-3 are papendicular to the axial-chord direction of the blade. The local coodinate systems take their origins from the pressure or sudction sides of the blade. The results are presented for the leading-edge slots film cooling plate at blowing ratios M = 1.0, 1.4, 1.8 and 2.2 with and without the fillets. The slot could be partially blocked or fully opened depending on the fillet profile extention upstream of the leading-edge. The shaded triangular regions in the bottom corners in Figs. 5.6 to 5.17 reprent then fillets. Also, the dark shaded regions in the slot geometry of Fig. 5.6 are the regions where the slot opennings are partially covered by the Fillet-2 and are therefore, are sealed accordingly for the Baseline-2 data acquisitions. With the installation of Fillet-1, the 82 mm slots upstream are completely blocked by the fillet for the film cooling flow. For the Baseline-1, the two 82 mm slots are thus covered completely for film cooling flow. This means that only the two middle film cooling slots are opened for the film cooling flow. Baseline then refers to a configuration where all the film cooling holes are opened.

$$\theta = \frac{\left(T_{loc} - T_{plm}\right)}{\left(T_{ref} - T_{plm}\right)} \tag{5.6}$$

Nondimensional temperature in Plane-1 are presented in Figures 5.6 to 5.9. The pressure side is located on the right side as shown in the figures in accordance with the local coordinate system. The blade-endwall juction is sufficiently cooled as the cooling spreads up the blade to about Y/S = 0.15 for blowing ratio of M=2.2. However, as the blowing ratio decreases, the cooling effectiveness reduces. At the lowest blowing ratio (M=1.0), the coolant is not reaching the pressure surface of the blade. This means that the temparature at the pressure surface is approximately equal to free stream temparature. Also the magnitude of ϴ close to the endwall (Figures 5.6 to 5.9) for Fillet-1 is higher than the other configurations. Baseline seems to be showing better cooling spread and coverage of the endwall as the ϴ values are smaller than for the other configurations. The coolant coverage along pitchwise direction is better because of the pitchwise opening of film cooling, film cooling flow momentum and cooling flow rate increase with M enabling some coolant flow to escape the lift-off by the pressure side-leg vortex and flow under the boundary layer and vortex. Also, the coolant flow turns toward the suction side because of the pitchwise pressure gradient and high streamline turnings upstream of separation region (refer to Fig. 4.5). The above factors cause less coolant flow and higher ϴ values near the PS in plane 1 of Figs. 5.6 to 5.9.

Increase in the mass flow rate of the cooling jet increases the positive axial vorticity (Sundaram and Thole, 2009) which counters the formation of the passage vortex that is responsoble for high aerodynamics loss in turbine systems and passages. With the installation of Fillet-1, there is a sight reduction in the spread of the film cooling jet at the endwall. This is as a result of the fillet interaction with the cross-flow and the film cooling jet. The use of Fillet-1 or Fillet-2 shows a reduction in the film cooling coverage (Figures 5.6 - 5.9).

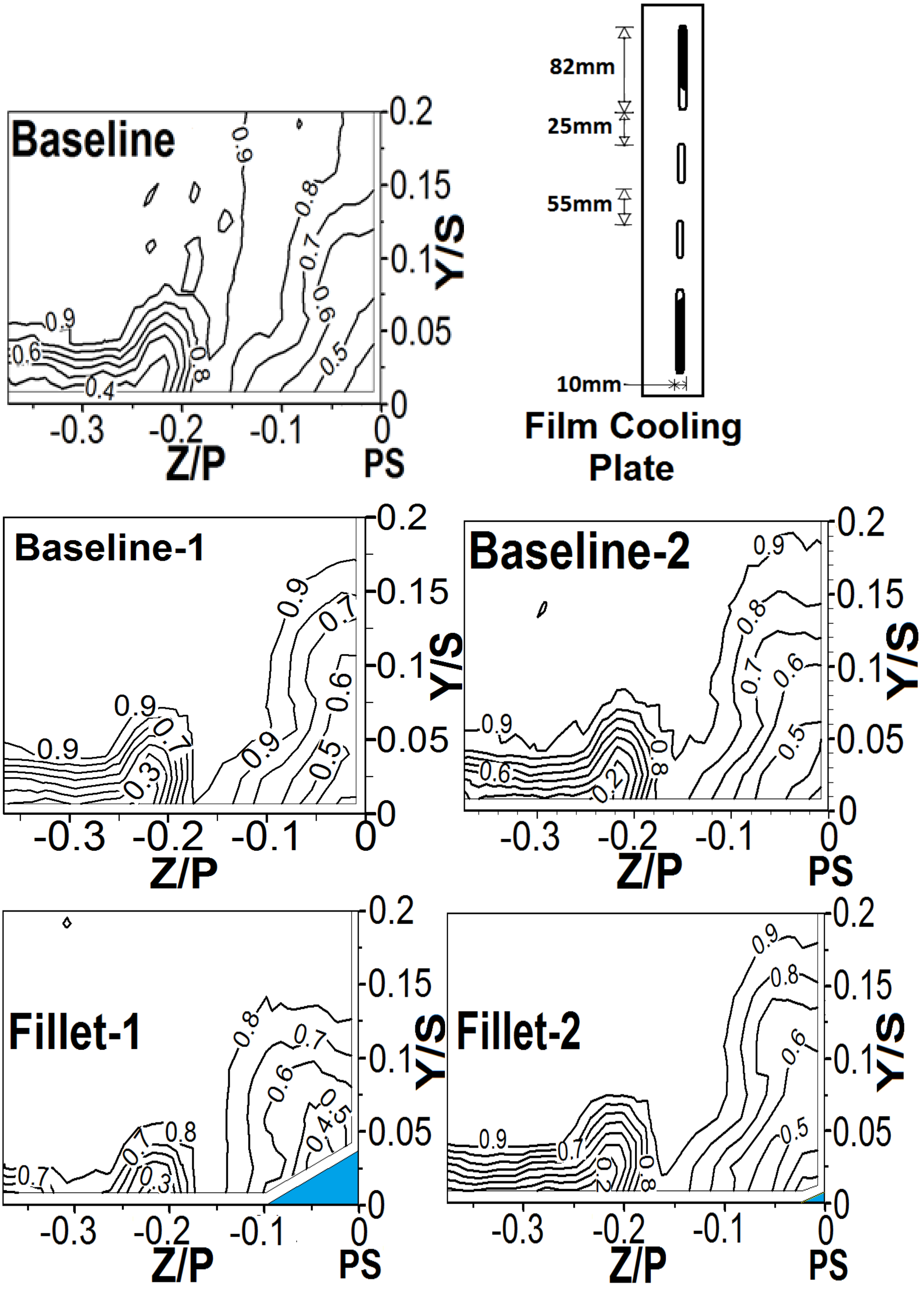
Baseline
82mm
25mm
55mm
10mm
Film Cooling Plate
Baseline-1
Baseline-2
Fillet-1
Fillet-2
Z/P
Y/S
PS
-0.3
-0.2
-0.1
0
0.05
0.1
0.15
0.2
0.9
0.8
0.7
0.6
0.5
0.4
0.3
0.2

Figure 5-6: Contours of non-dimensional temperature (θ) distribution in Plane-1 at X_G/C_{ax} = 0.49 for M=2.2

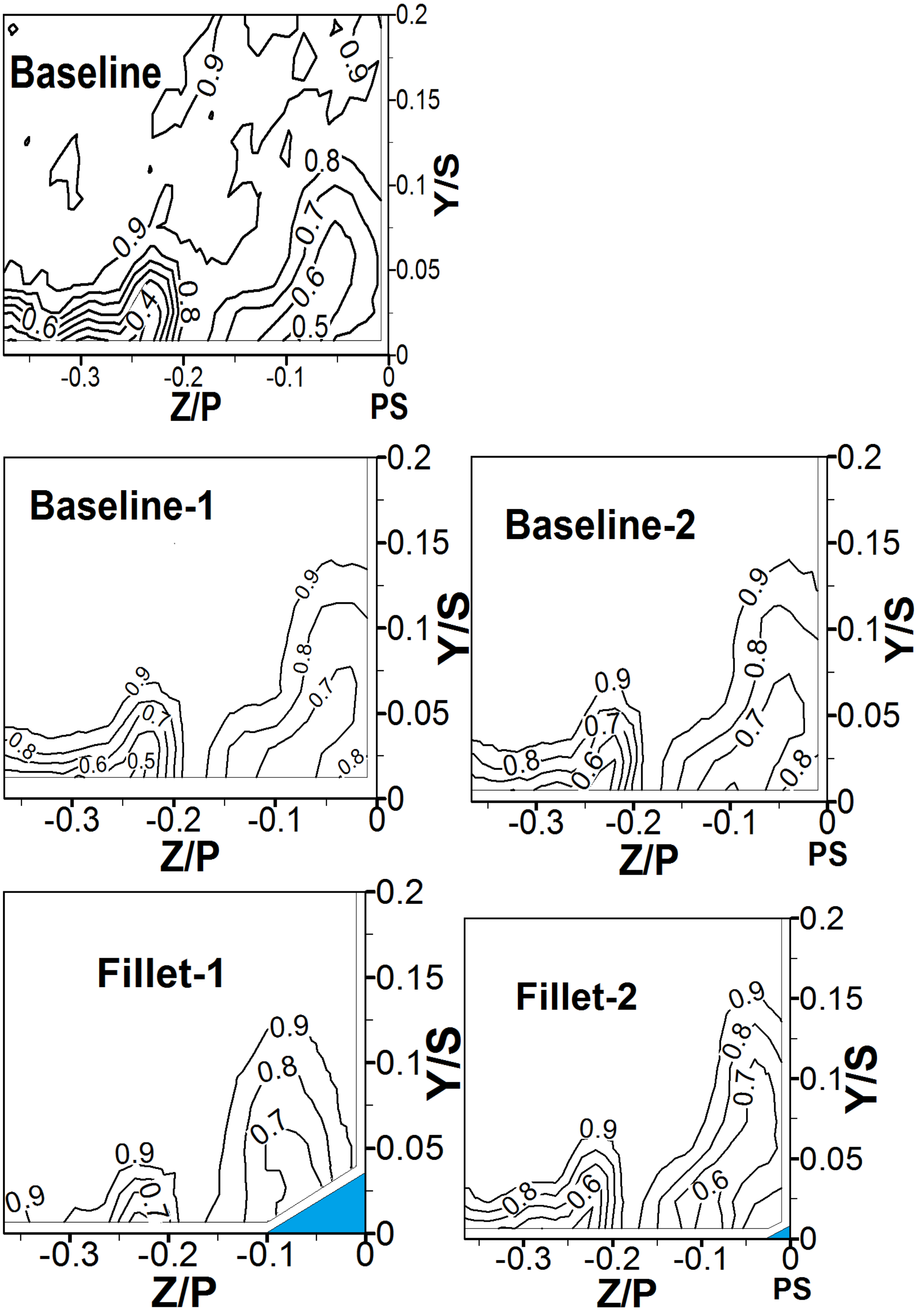

Figure 5-7: Contours of non-dimensional temperature (θ) distribution in Plane-1 at X_G/C_{ax} = 0.49 for M=1.8

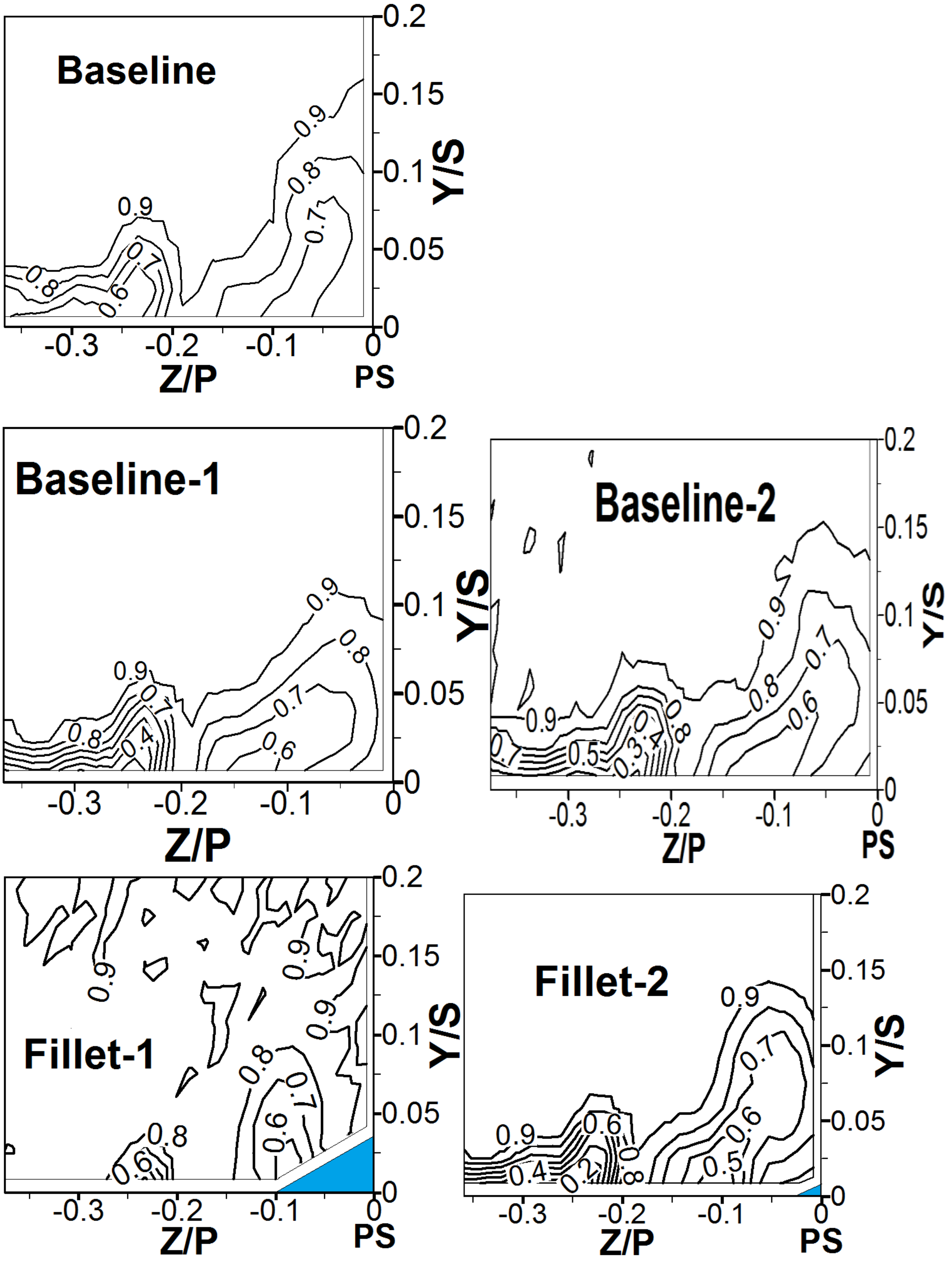

Figure 5-8: Contours of non-dimensional temperature (θ) distribution in Plane-1 at X_G/C_{ax} = 0.49 for M=1.4

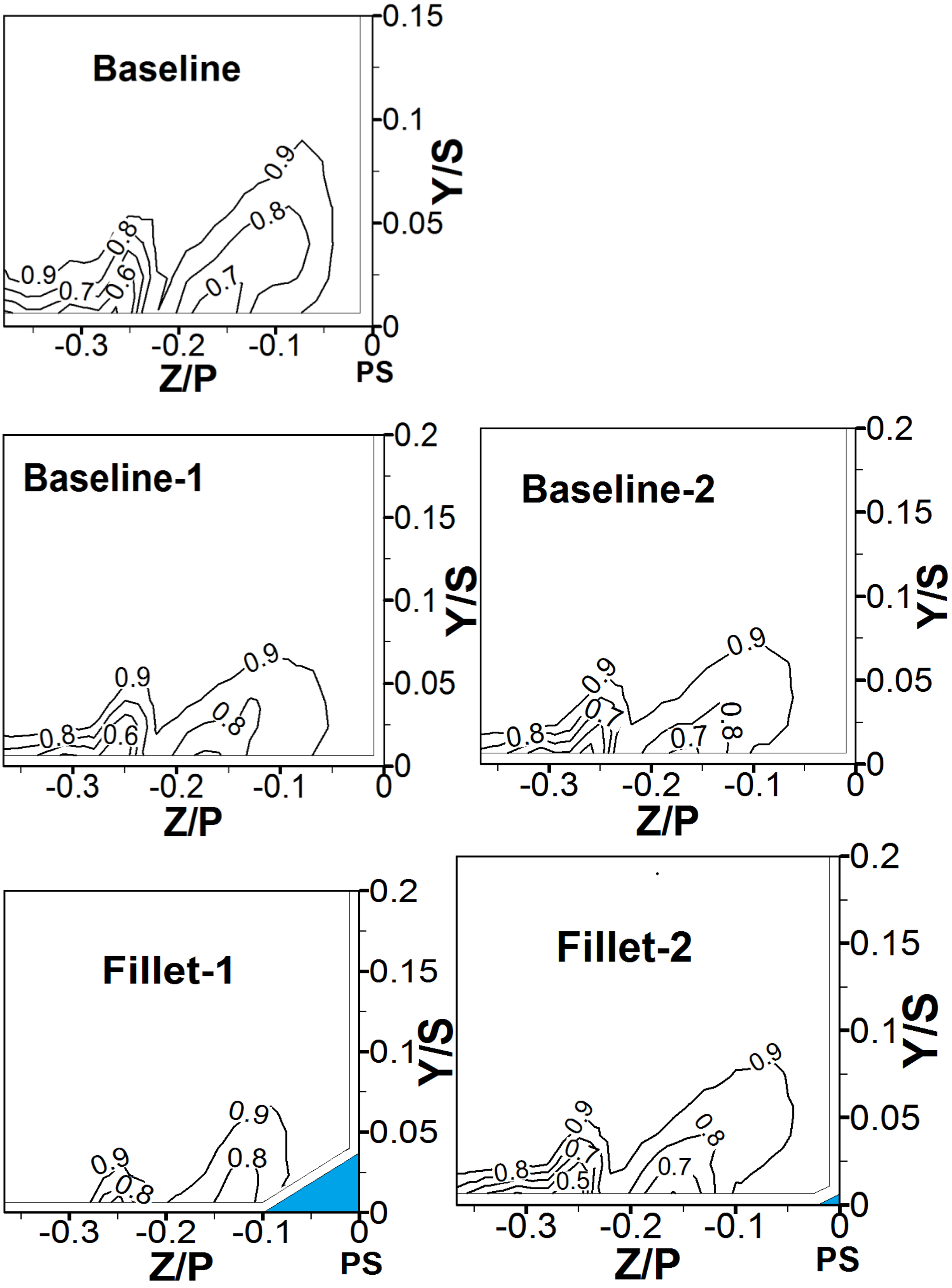

Figure 5-9: Contours of non-dimensional temperature (θ) distribution in Plane-1 at X_G/C_{ax} = 0.49 for M=1.0

Temperature fields are also measured in Plnae-2 at $X_G/C_{ax} = 0.25$ in Figs. 5.10 to 5.13. The local coordinate system originates from the endwall where the suction-surface intersects with the plane. Therefore, the suction side is located on the left side. Non-dimensional temperature field, Θ in Plne-2 contours are presented in Figures 5.10 to 5.13. As expected, Baseline-1 and Fillet-1 are also showing less coverage and less magnitudes at the endwall and suction side compared with the others. In other words, the region $Z/P \leq 0.1$ at the suction side of the blade endwall junction is generally uncooled. This is as a result of the blockage of the film cooling slots upstream. The magnitudes and the pitchwise coverage reduce as the blowing ratio reduces. There is a formation of a cooling effectiveness core located at $Y/S = 0.05$ and $Z/P = 0.05$ for Baseline-2 and Fillet-2. These suggest the interactions of the film cooling flow with the suction side-leg of horse shoe vortex cause some lift-off of the cold fluid. In general, the Baseline, Baseline-2 and Fillet-2 are performing better than the other two configurations for all the blowing ratios. The effect of the cooling in Baseline-1 and Fillet-1 is only felt at region $Z/P \geq 0.1$ on the endwall because of the coolant flow mostly from the 55 mm slots.

The nondimensional temparature fields, Θ are being compared for the filleted and unfilleted configurations in Plane-3 as shown in Figures 5.14 to 5.17. The pressure and the suction sides are shown on the right and left sides of the figures. The origin of the local coordinate system is located at the vane suction side endwall junction. The orientation of the local coordinate system is show in Figure 3.1. The lower the value of Θ, the better the cooling at the endwall area. The Fillet-1 and Baseline-1 are showing very low coolant coverage along pitchwise, Z/P direction as shown previously in Figures 5.6 to 5.13. In Fillet-1 and Baseline-1 cases, the region $Z/P \leq 0.15$ is not adequately cooled due to the covering of the film cooling slot. The effectiveness is proportional to the blowing ratio. However, the film cooling coverage is sufficiently reaching the entire pitch distance of the vane-blade for Baseline case ($M = 2.2$, 1.8 and 1.4) with the exception of $M=1.0$ when the film cooling is not reaching the pressure side (Figure 5.15). Figures 5.14 to 5.17 show that the film cooling effectiveness is spreading from the leading-edge all the way to region $X_G/C_{ax} > 0.5$ in the axial direction. This means that the film cooling jets will interact positively with the cross-flow and can escape the lift-off by the passage vortex structures. Other non dimensional tempareture schemes and $C_{pt\ loss}$ at XG/Cax = 0.58 (M = 2.8) are provided in Appendix H.

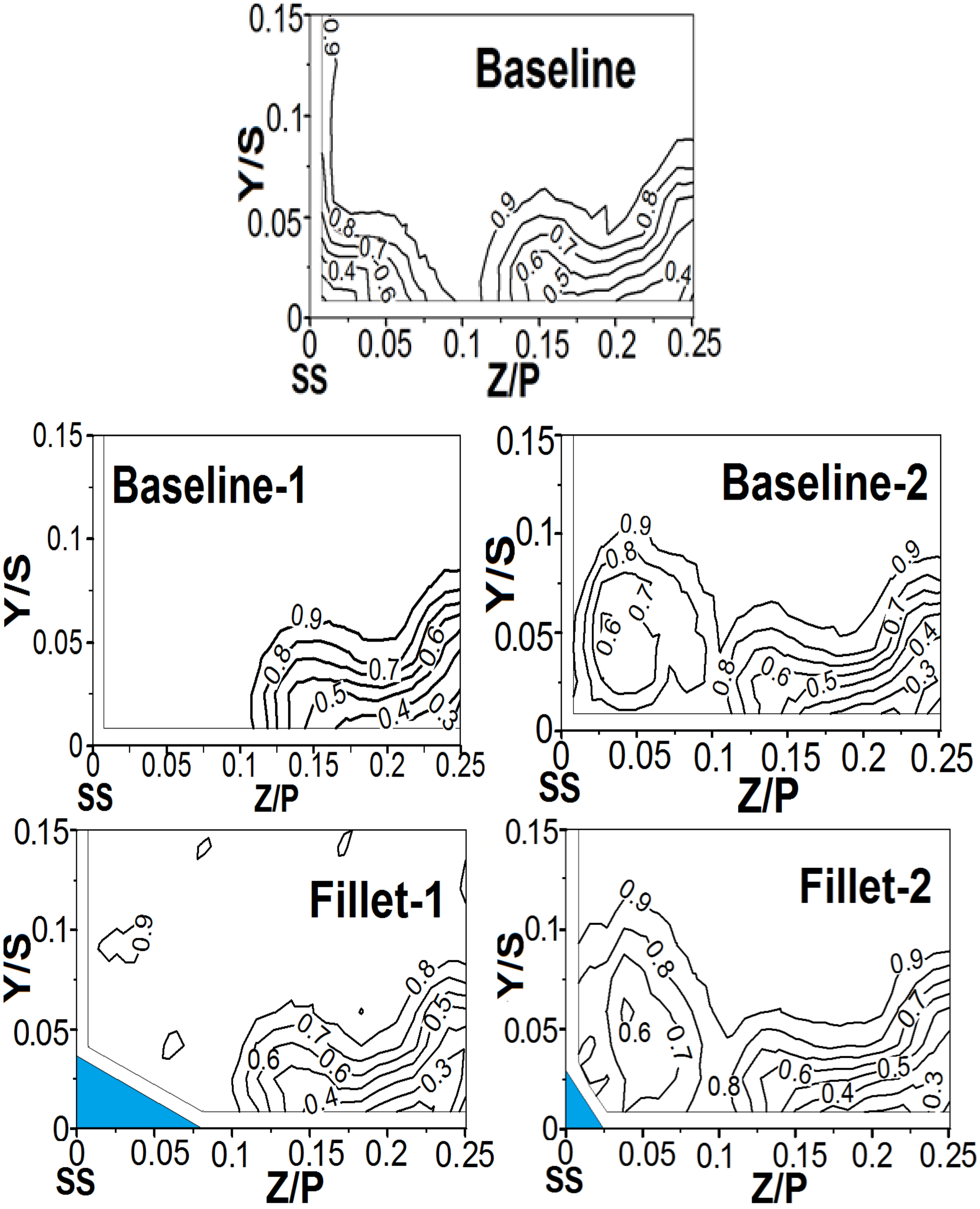

Figure 5-10:   Figure 5.10: Contours of non-dimensional temperature (θ) distribution in Plane-2 at X_G/C_{ax} = 0.25 for M=2.2

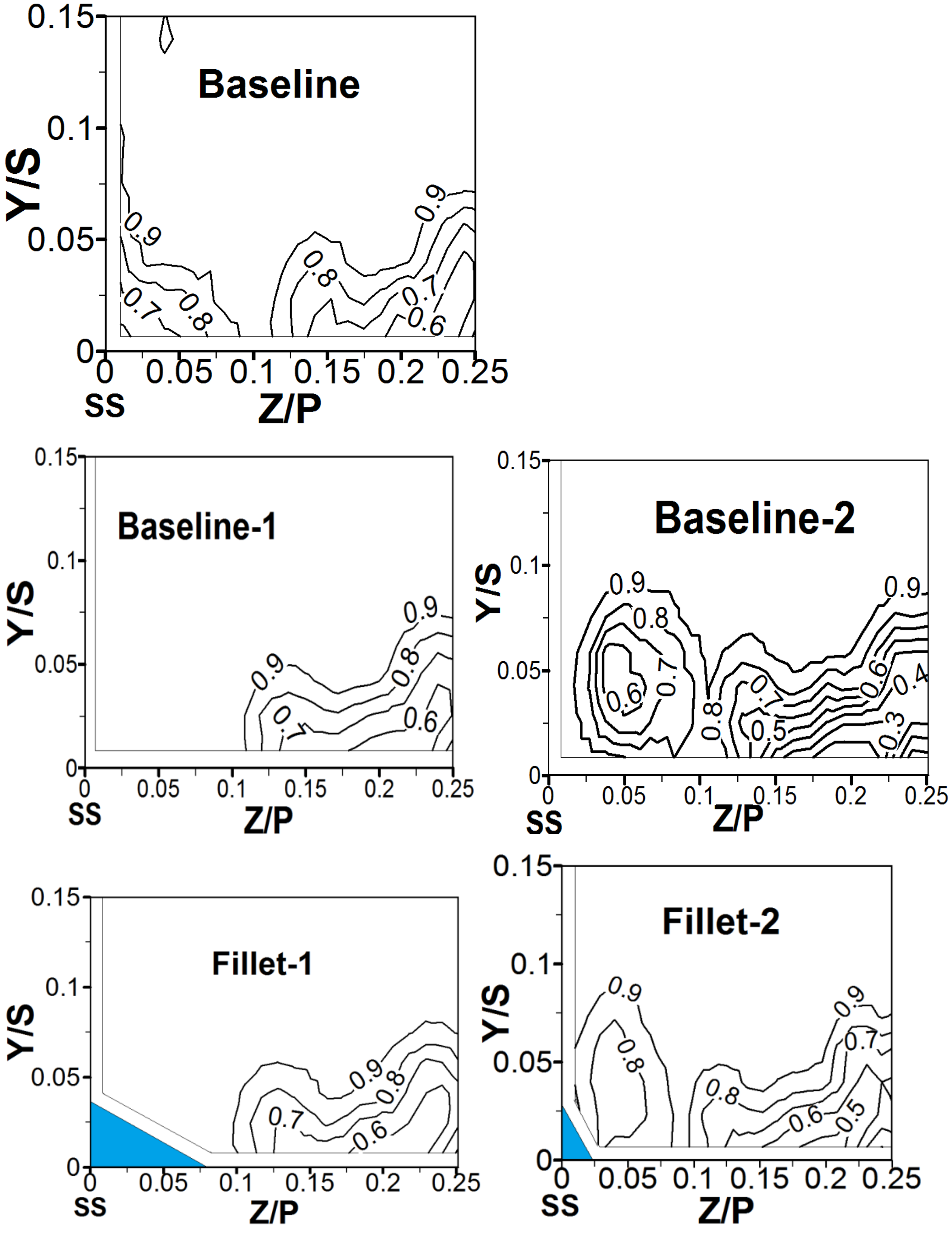

Figure 5-11: Contours of non-dimensional temperature (θ) distribution in Plane-2 at X_G/C_{ax} = 0.25 for M=1.8

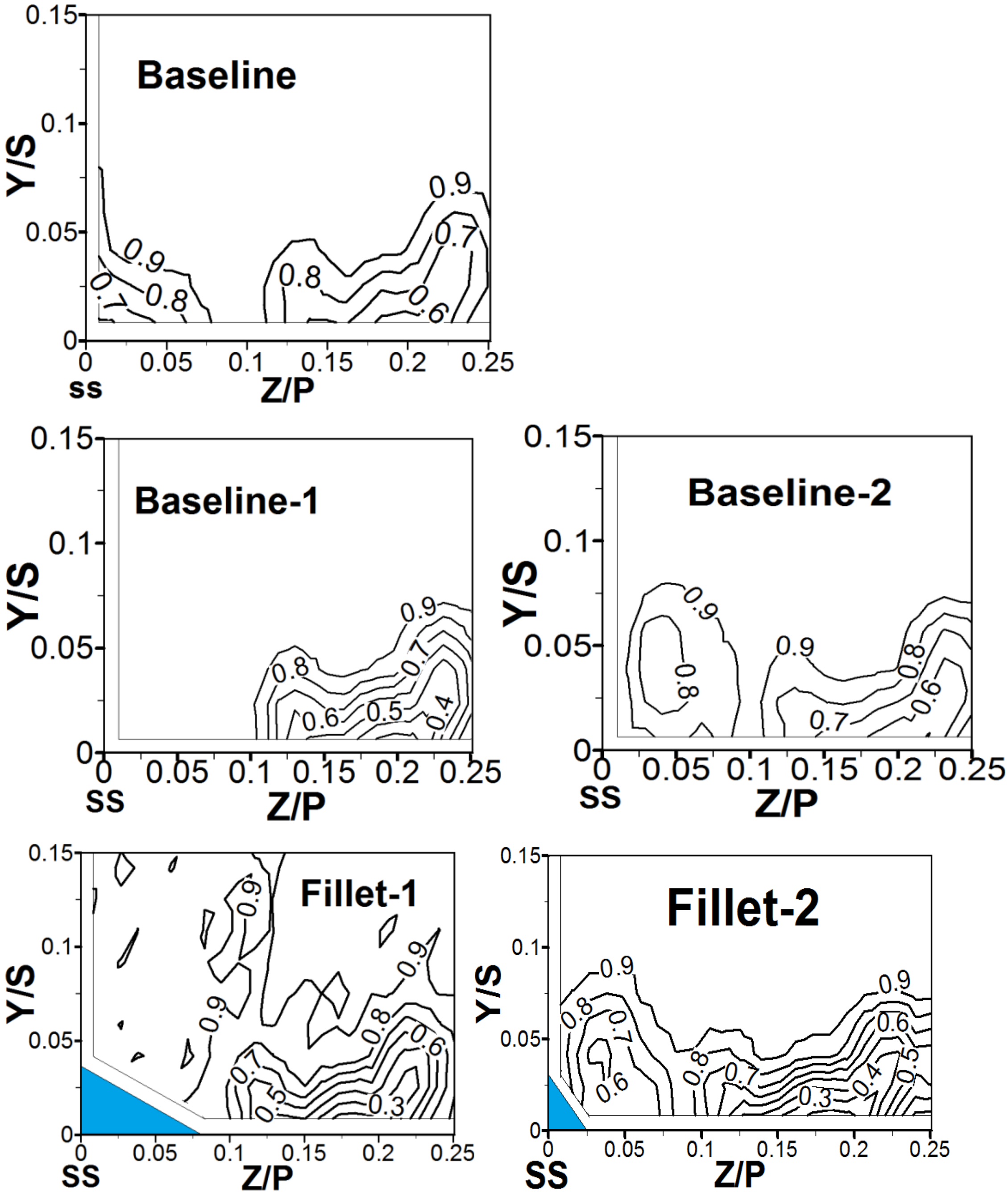

Figure 5-12: Contours of non-dimensional temperature (θ) distribution in Plane-2 at X_G/C_{ax} = 0.25 for M=1.4

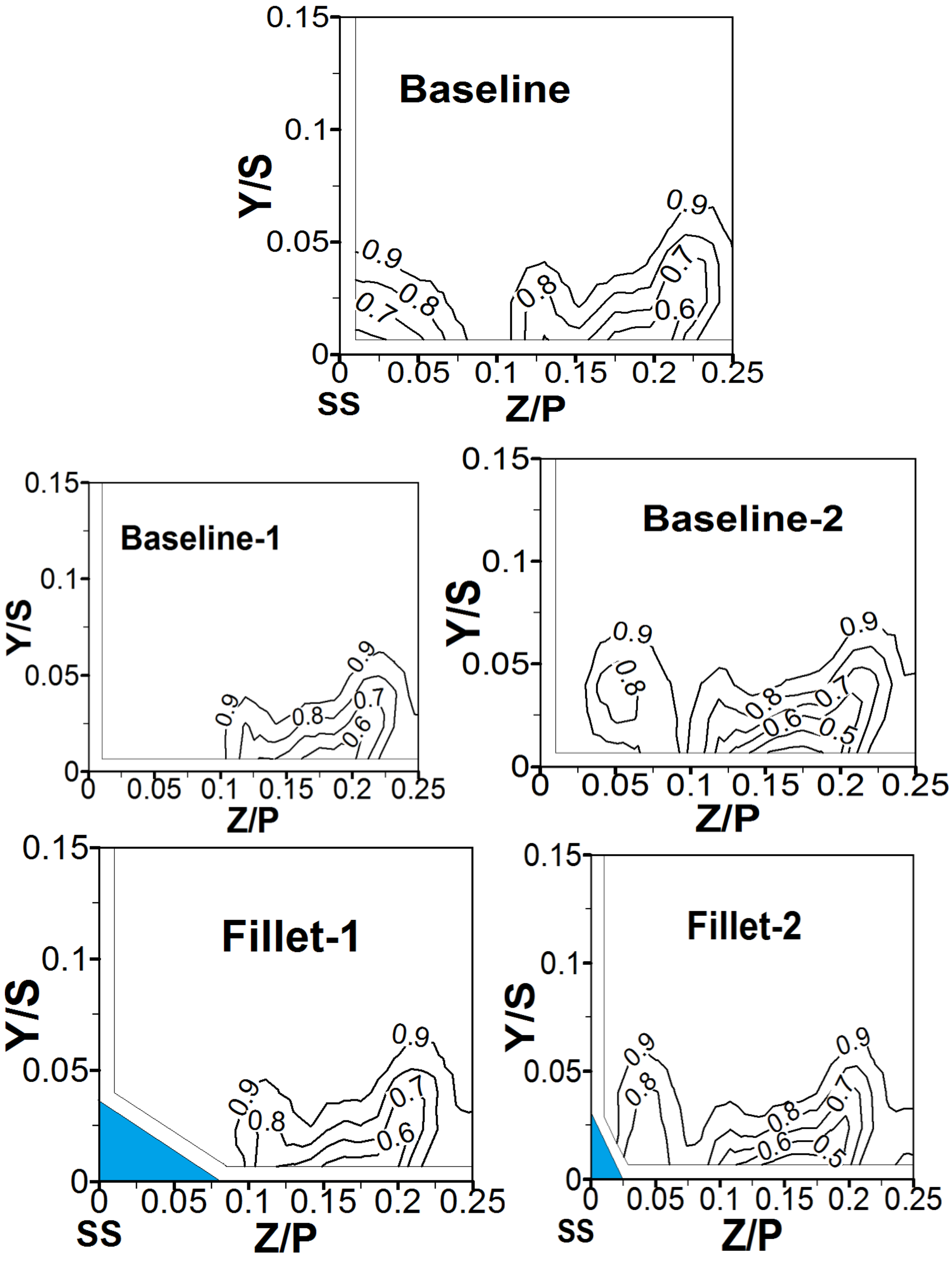

Figure 5-13: Contours of non-dimensional temperature (θ) distribution in Plane-2 at X_G/C_{ax} = 0.25 for M=1.0

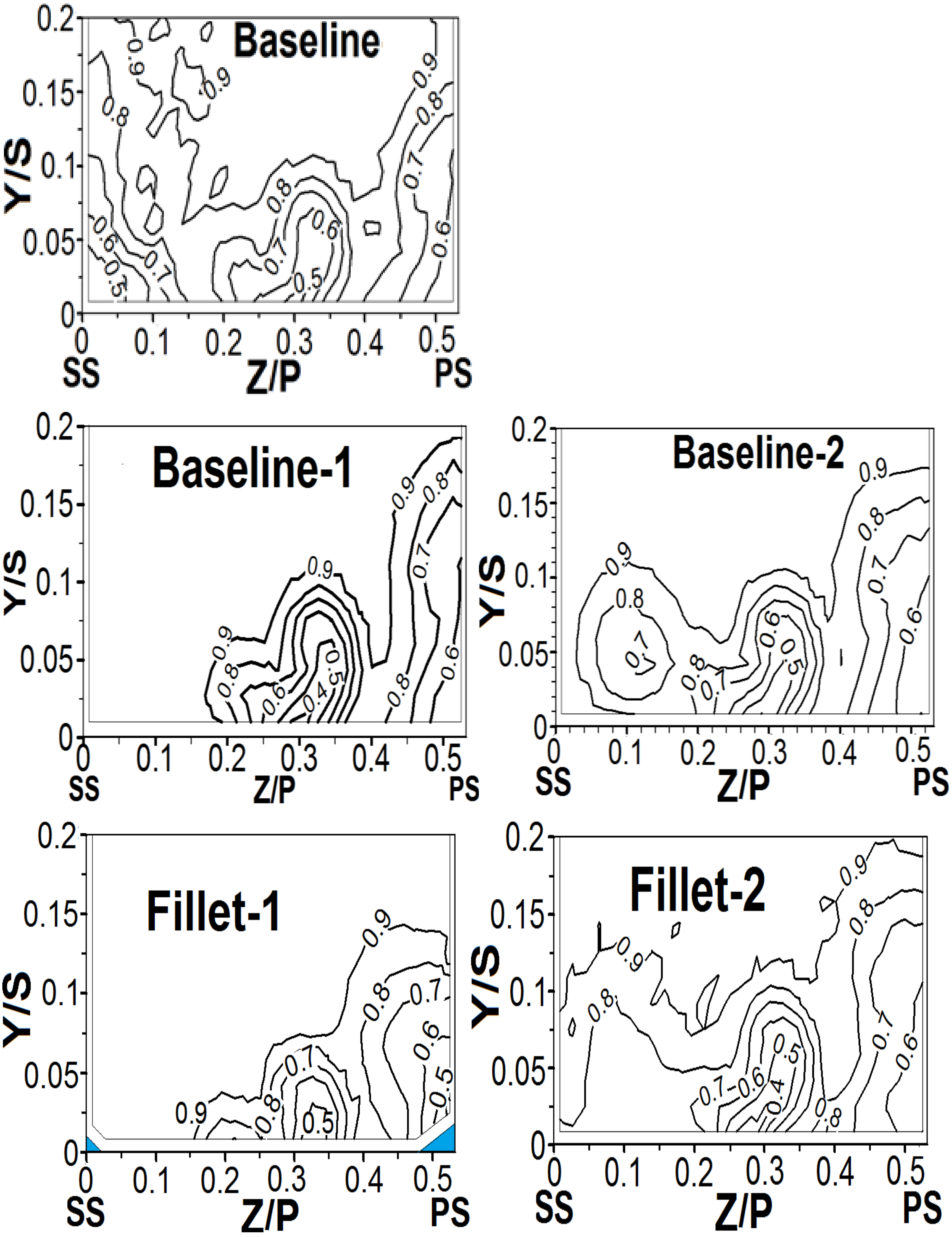

Figure 5-14: Contours of non-dimensional temperature (θ) distribution in Plane-3 at X_G/C_{ax} = 0.58 for M=2.2

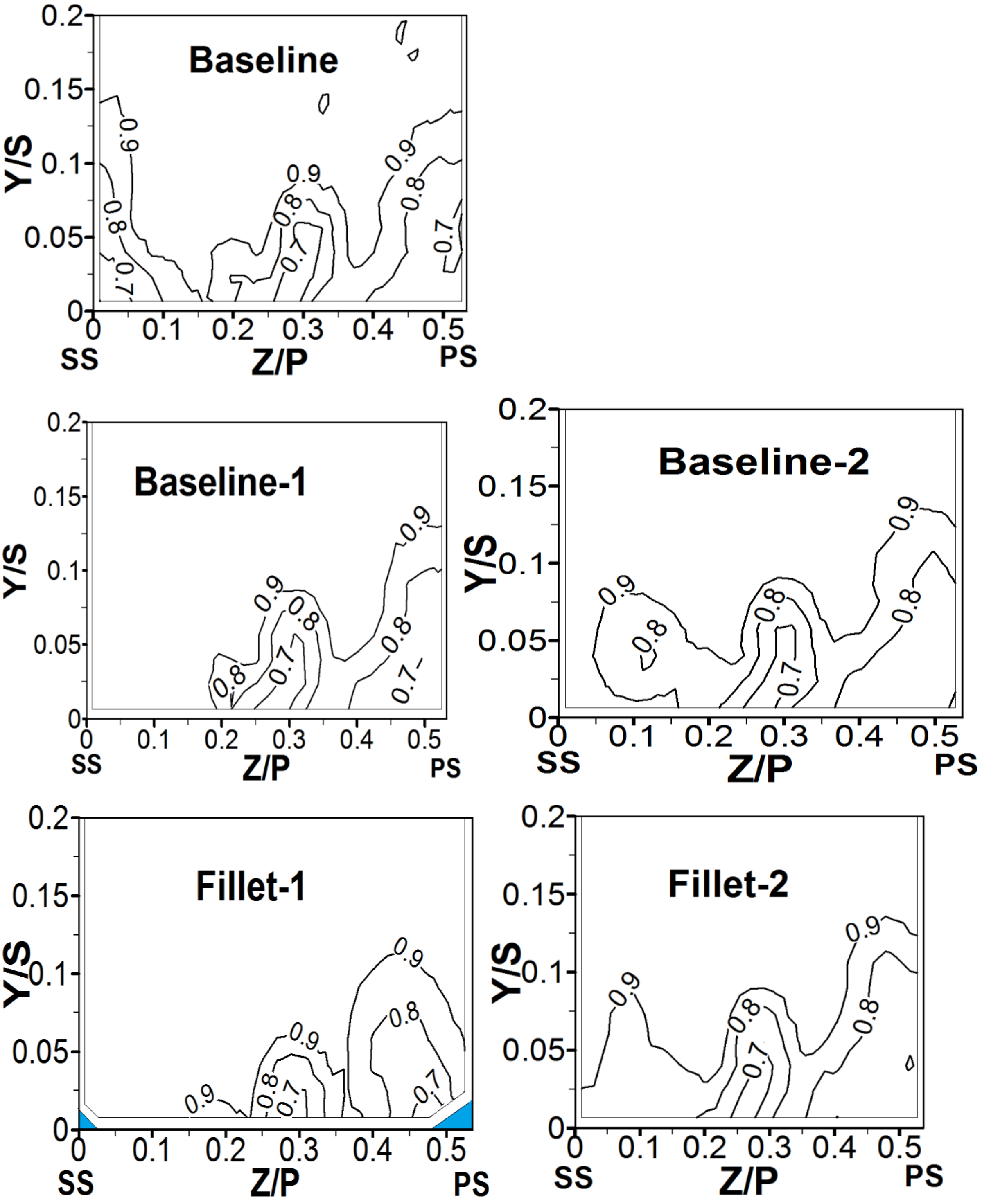

Figure 5-15: Contours of non-dimensional temperature (θ) distribution in Plane-3 at X_G/C_{ax} = 0.58 for M=1.8

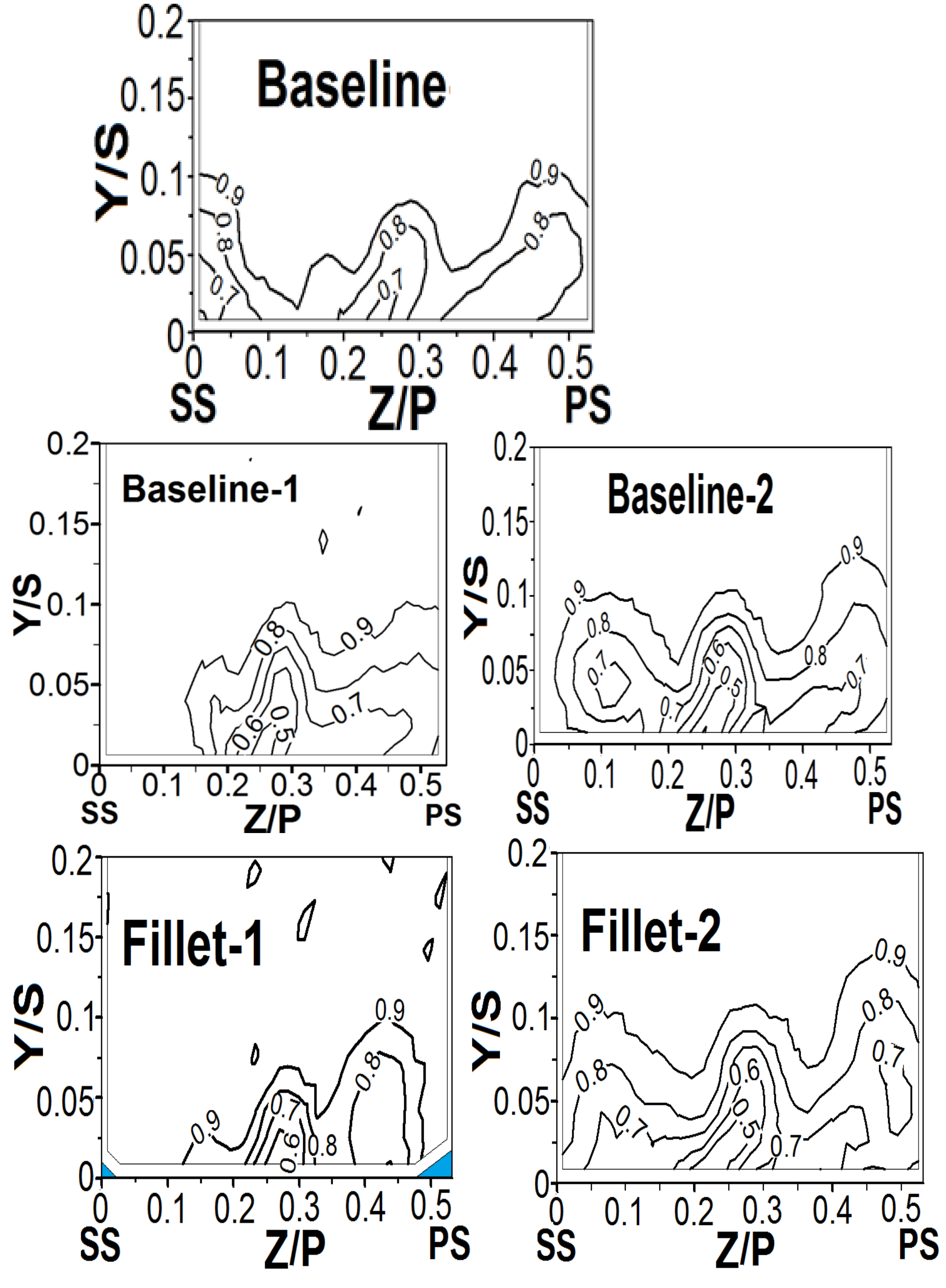

Figure 5-16: Contours of non-dimensional temperature (θ) distribution in Plane-3 at X_G/C_{ax} = 0.58 for M=1.4

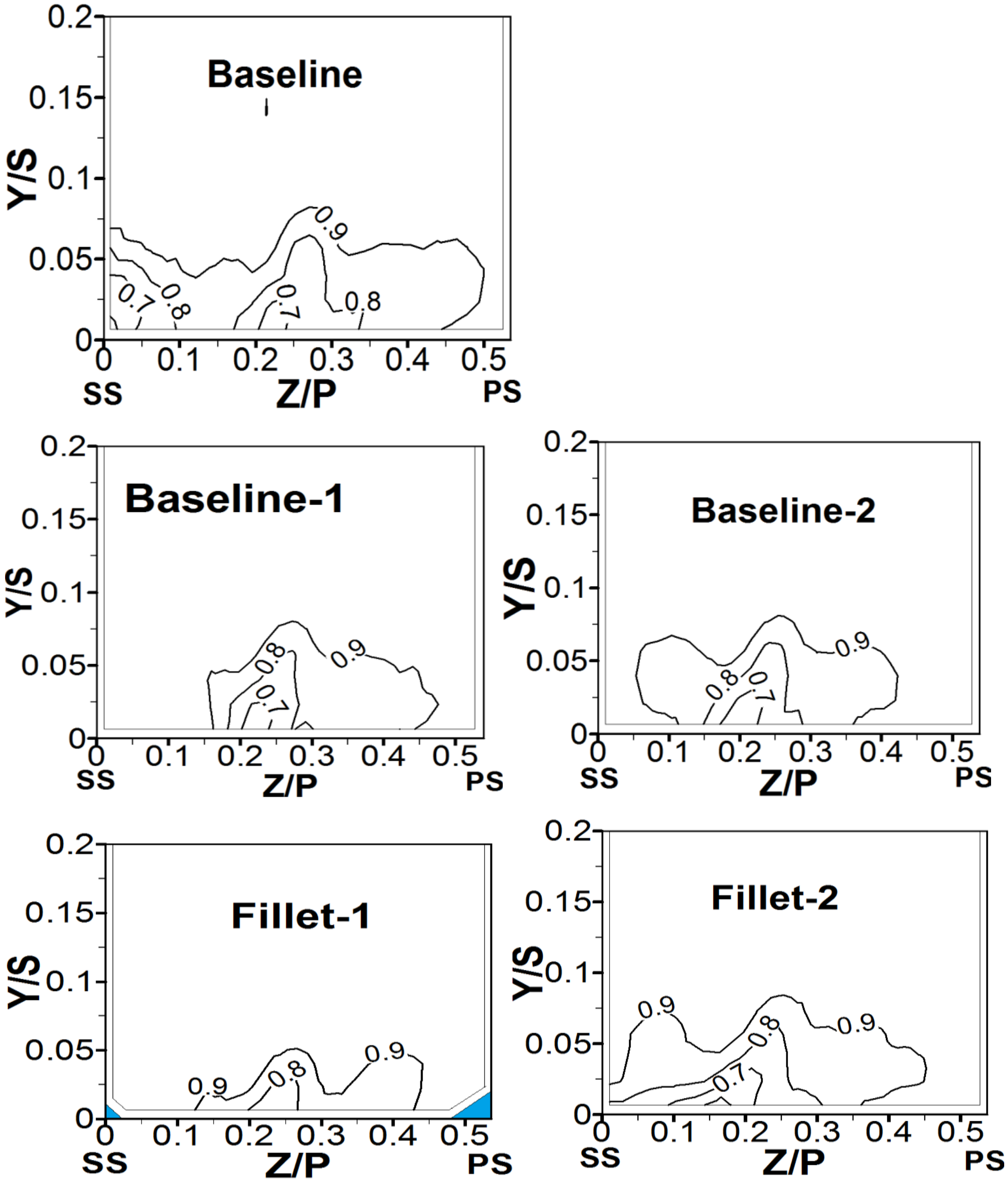

Figure 5-17: Contours of non-dimensional temperature (θ) distribution in Plane-3 at X_G/C_{ax} = 0.58 for M=1.0

5.5 Averaged Value of Nondimensional Temperature Distribution

In order to discern the performance differences between the configurations for the leading-edge slot film cooling, Figures 5.18 to 5.20 are presented for comparisons. The figures are presented for the data in Planes-1, 2, 3. The pitchwise averaged values of the non-dimensional temperature, Θ are plotted which are computed at a given Y/S location by averaging arithmetically the pitchwise local data along Z/P. Locations Y/S = 0.0 on the plots are the endwall local origins according to the local coordinate system. The lower the value of Θ near the Y/S = 0 location, the better the cooling. Since the endwall film cooling flow design and configuration are of paramount importance, therefore, the region Y/S < 0.1 is more focused on in the following discussions. Figure 5.18 shows that the average Θ in Plane-3 is increasing from endwall location to a spanwise height of about 10% of the span. Fillet-1 shows the highest average Θ values followed by Baseline-1 in Plane-3 for all the M tested except for M =1.4. This implies that the Fillet-1 case cannot cool the endwall as good as the other cases at $X_G/C_{ax} \geq 0.58$. The average Θ values for all the cases and blowing ratios beyond Y/S > 0.1 is approximately the same as the freestream Θ approaching the unity. Higher Θ values are desirable at Y/S > 0.1 as the coolant should not be penetrating high above the endwall into the freestream.

The difference in the performance of Fillet-1 and Fillet-2 cases in Figure 5.19 in the region Y/S < 0.1 is not significant as both are seen to be cooling the endwall more than the other configurations with lower Θ values at all the blowing ratios. Three factors may contribute to lower the average Θ values in Y/S < 0.1 for the fillets: (i) Plane-2 of Fig. 5.19 is located nearest to the film-cooling slot locations, (ii) the blocked holes with the fillets cause higher film-cooling flow rate through the 55 mm slots than the case when all the slots are open, and (iii) the fillets reduce the suction side-leg vortex (refer to Fig. 4.5) responsible for scooping up the coolant flow near the suction side. In Figure 5.20 for the Plane-1, Fillet-1 is showing weakest cooling as the values of Θ in the region Y/S < 0.05 is the highest for all the blowing ratios, M. The coolant coverage of endwall near the pressure side for the Fillet-1 case is the weakest as previously shown in Figures 5.6 to 5.9.

5.6 Film Cooling Adiabatic Effectiveness of the Endwall

For effective cooling of the turbine endwall, the geometry and film cooling scheme play key role as stated by (Friedrichs et al., 1999). Though effectively cooled endwall is desirable, it can only be achieved with careful and innovative design of the film-cooling configurations. In Chapter 3, Figure 3.1 and Figure 3.5 show the location and design of the film cooling plate. Figure 5.21 also shows the film cooling plate and the endwall film cooling for slots and discrete holes combination. The leading-edge film cooling holes and slots are located 0.079C$_{ax}$ upstream of the stagnation-edge of the blade (Figure 3.1). Appendix H also shows other information on the LE film cooling plates. Figures 5.21 to 5.25 will be considered for appropriate comparisons of the adiabatic effectiveness vis-à-vis with the various other endwall film-cooling configurations. Film-cooling effectiveness data with all the slot open for the Baseline case (different vane-blade profile) are presented by (Thole and Knost, 2005). Similar measurements in the present cascade are not obtained. Instead, the 82 mm film cooling slots just upstream of the leading edge are replaced by the discrete cylindrical holes configured in small spacing to simulate the slot cooling.

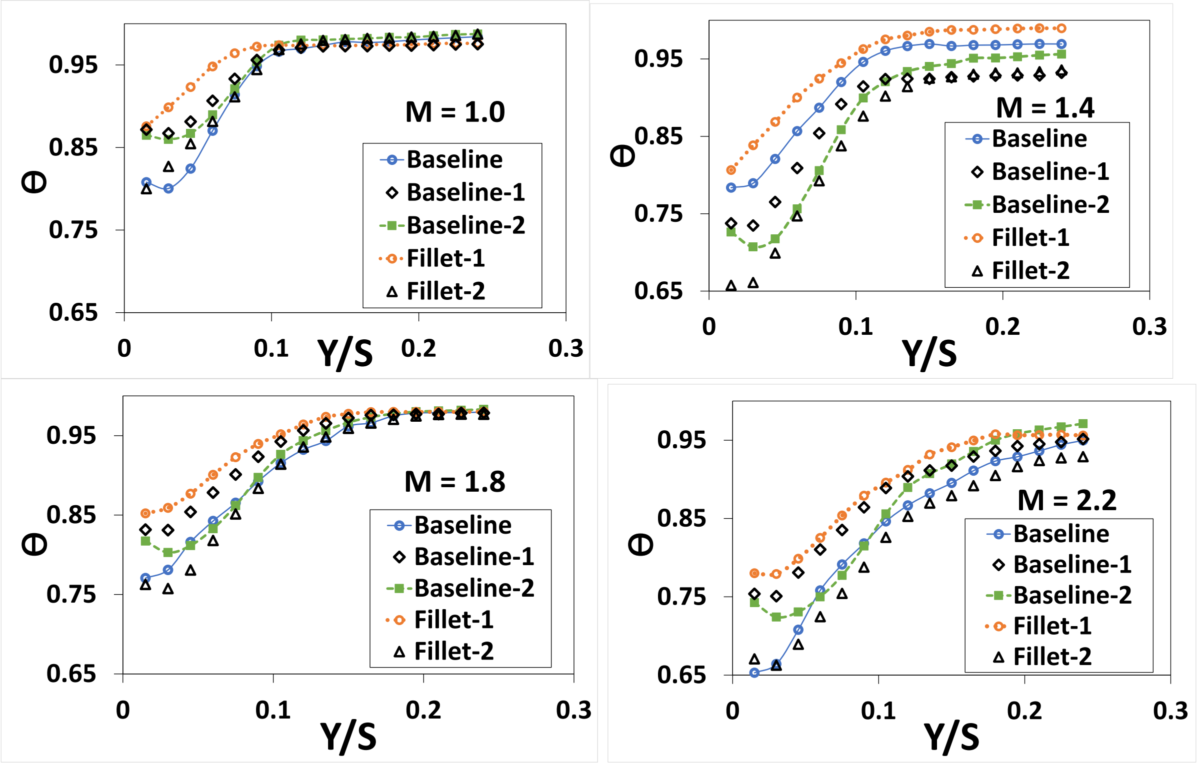

Figure 5-18: Pitchwise averaged of Non-dimensional temperature (θ) distribution in Plane-3 at X_G/C_{ax} = 0.58 for M=1.0, 1.4, 1.8 and 2.2

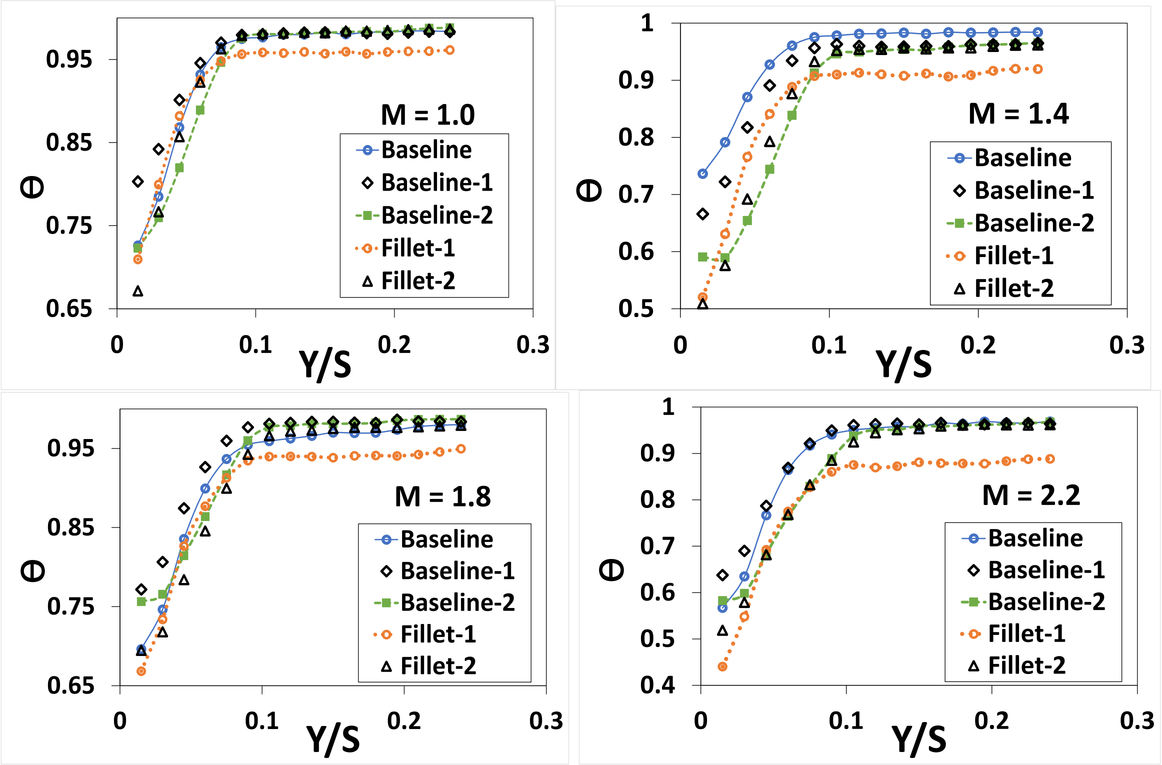

Figure 5-19: Pitchwise averaged of Non-dimensional temperature (θ) distribution in Plane-2 at X_G/C_{ax} = 0.25 for M=1.0, 1.4, 1.8 and 2.2

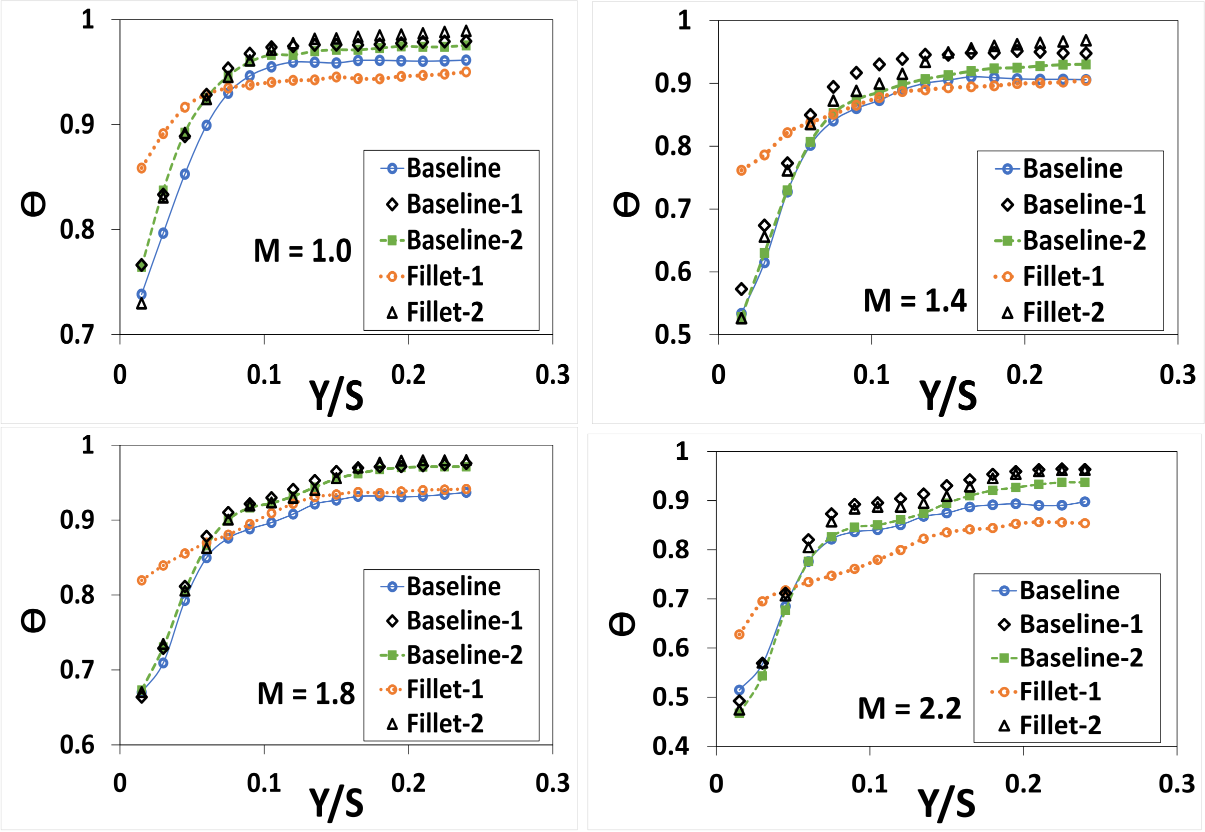

Figure 5-20: Pitchwise averaged of Non-dimensional temperature (θ) distribution in Plane-1 at X_G/C_{ax} = 0.49 for M=1.0, 1.4, 1.8 and 2.2

The flooded contours of the endwall are kept at the same legend range for comparison for all slot-hole combination with fillets and without fillets. The results are presented in terms of adiabatic effectiveness (***η***) which is defined and computed by Equation 5.7. Figure 5.21a also shows the pressure and the suction sides of the blade. The ambient temperature remain relatively constant for the endwall temperature measurements. The higher the adiabatic effectiveness, the chiller the endwall. Eleven discrete holes are strategically arranged just upstream of the leading edge by placing four holes slightly upstream of the other seven holes as shown in Figures 3.1, 3.3, 3.4, 3.5 and 5.21. The introduction of Fillet-1 or Fillet-2 (Figure 3.12) brings about the partial covering of some or all of the discreet holes at the leading-edge. Figure 5.21a shows the entire leading-edge film cooling plate configuration. The shaded holes are covered by the introduction of Fillet-2 while the entire discreet holes (the shaded and the red holes) are covered by the installation of Fillet-1. Thus Baseline-1 and Baseline-2 are also obtained to see the combined effect of the use of the fillet and the film cooling jets. However, Baseline here refers to configuration where all the holes (slots and discreet) are opened for full film cooling flow. For Baseline-1 and Baseline-2, the fillet covered holes are covered with a masking tape accordingly. Therefore, Baseline-1 and Fillet-1 only have the two slots opened for film cooling mass flux. Local distributions of the η values are presented in Figs. 5.21 to 5.35. At the highest blowing ratio (M=2.8), the film cooling seems to be reaching the pressure side region thereby providing sufficient cooling to that area. The past works in the literatures indicate that the endwall region near the pressure side of the cascades is the hardest to cool (very low η values). This happens because of high turning of the coolant streams toward the suction side and the lift-off of the coolant flows by the passage vortex structures along the boundary layer separation region between the separation lines and reattachment lines (refer to Fig. 4.5). High value of cooling effectiveness is concentrated at the slot injection regions and the effectiveness dissipates downstream. As the blowing ratio reduces, the effectiveness also reduces with reduction in the axial and pitchwise spread along the passage. Streamlines close to the endwall is directing the trajectory of the film cooling jets towards the suctions side at lower blowing ratios (M<2.8). This means that reduction in the coolant mass flux leads to reduction in cooling effectiveness on the endwall. At lowest blowing ratio (M = 1.0), high effectiveness is seen at the upstream without sufficient spread over the area. This means that at M = 1.0, the main flow sweeps off the coolant flow thereby reducing the adiabatic effectiveness. In general, the highest blowing ratio (M=2.8) provides the most effective and cooling coverage of the endwall. The adiabatic effectiveness is lower for Fillet-1 and Fillet-2 because the leading-edge discrete holes are totally or partially blocked thereby reducing the mass flux of the film cooling flow into the cascade. All the film cooling cases reduce the $C_{pt\text{-}loss}$ as shown previously indicating weaker passage vortex.

$$\eta = \frac{\left(T_{ref} - T_w\right)}{\left(T_{loc} - T_{plm}\right)} \qquad 5.7$$

Two other new modifications (the discrete holes and the curved/bevelled holes configurations) to the leading-edge film cooling holes in endwall are presented at all blowing ratios (M=1.0, 1.4, 1.8, 2.2 & 2.8) to evaluate their effects on the adiabatic effectiveness (η). The two middle slots in Figure 5.21a are replaced by a set of fourteen discrete holes equi-spaced (10 mm) upstream of the cascade leading-edge. Each hole is 10 mm in diameter as stated previously in Figure 3.5. These geometries are also tested to see the effects of the curved holes with the fillets. The results of local η distributions are presented in Figures 5.26 – 5.35. Just as observed earlier, effectiveness, η reduces as the blowing ratio, M reduces. The effectiveness also reduces when some holes are sealed according to where the fillet is present. Similar to Figures 5.21 to 5.25, the highest blowing ratio is providing much desired endwall cooling near the pressure endwall. Blowing ratio (M=2.8), is expected to have strong counter-effect on the cross-flow and the leading-edge vortices. At highest blowing ratio, the adiabatic effectiveness tend to be much higher towards the pressure side. The pressure side is more cooled for blowing ratio of 2.8 as compared with blowing ratio <= 2.2, in which cases higher effectiveness values are present towards the suction side.

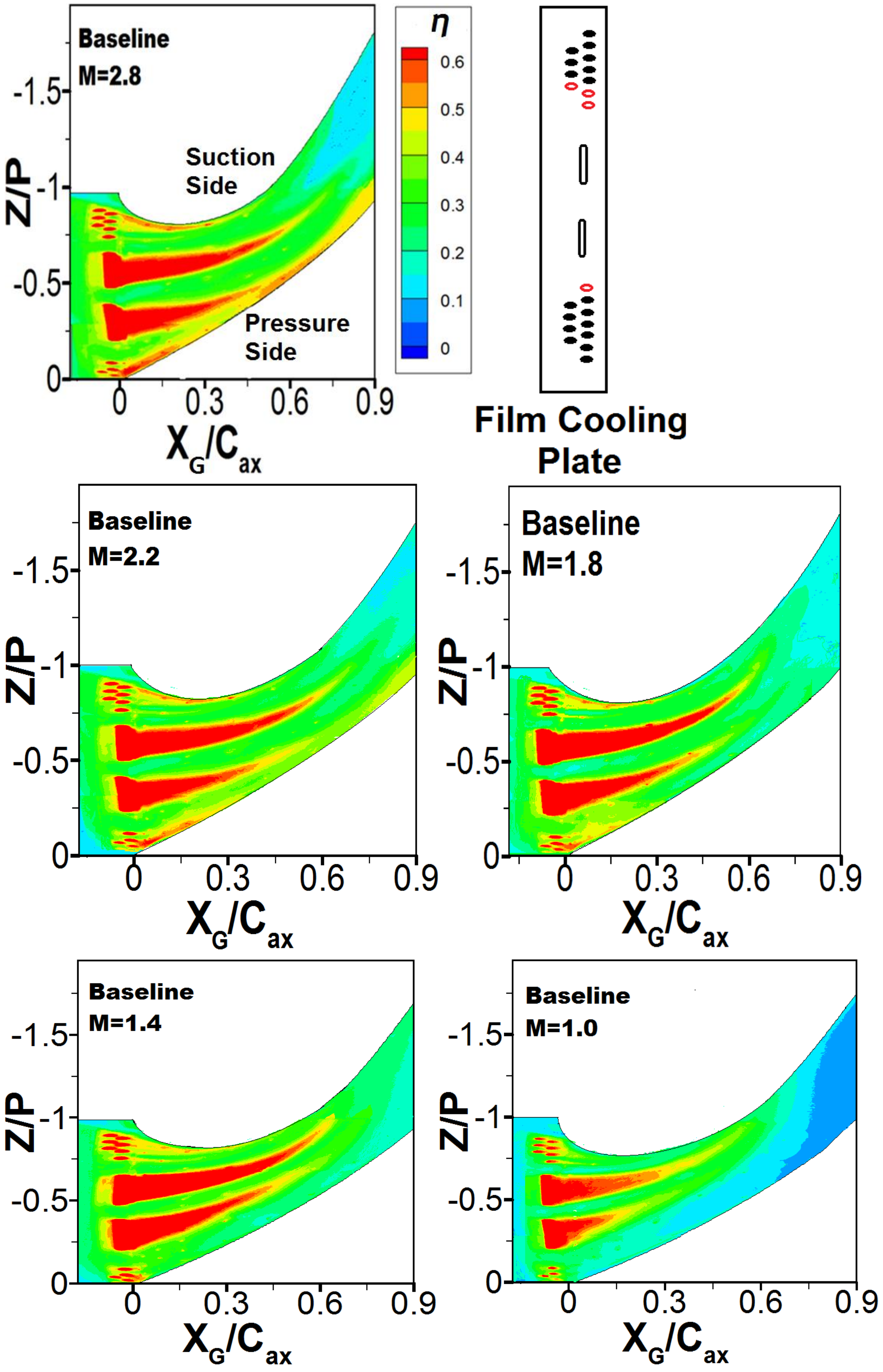

Figure 5-21: Endwall film cooling with slot and discrete holes geometry for Baseline

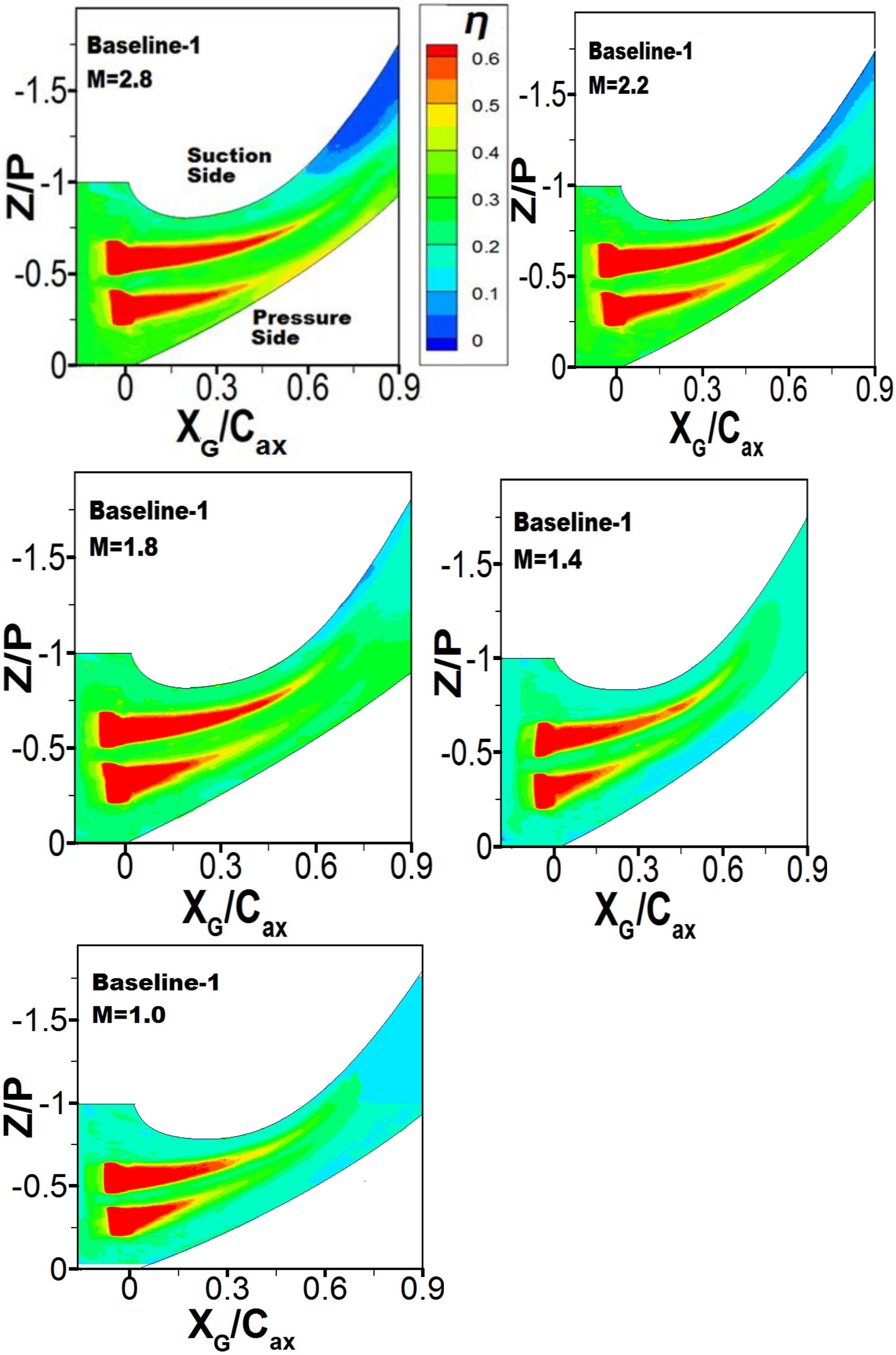

Figure 5-22: Endwall film cooling with slot and discrete holes geometry for Baseline-1

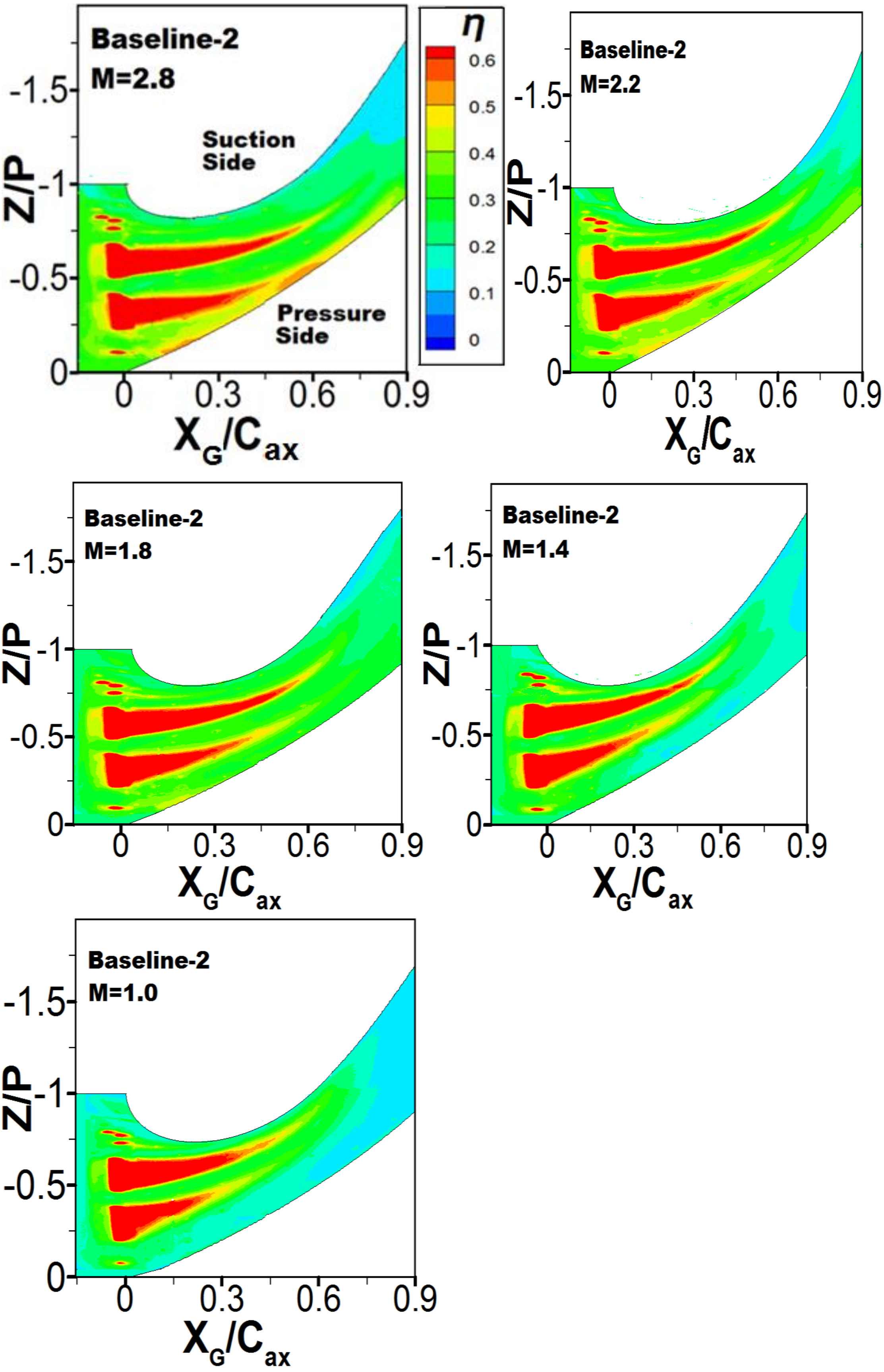

Figure 5-23: Endwall film cooling with slot and discrete holes geometry for Baseline-2

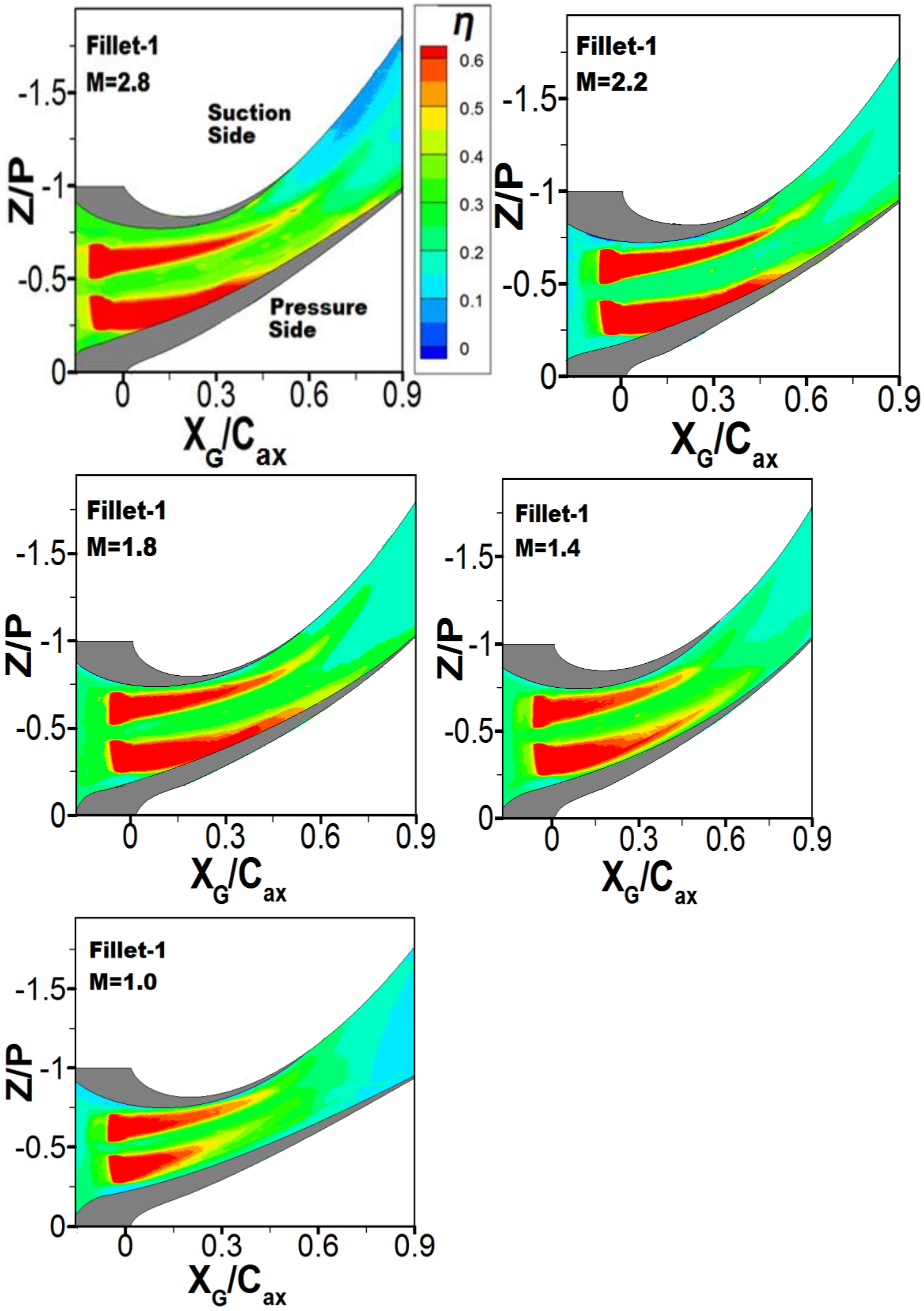

Figure 5-24: Endwall film cooling with slot and discrete holes geometry for Fillet-1

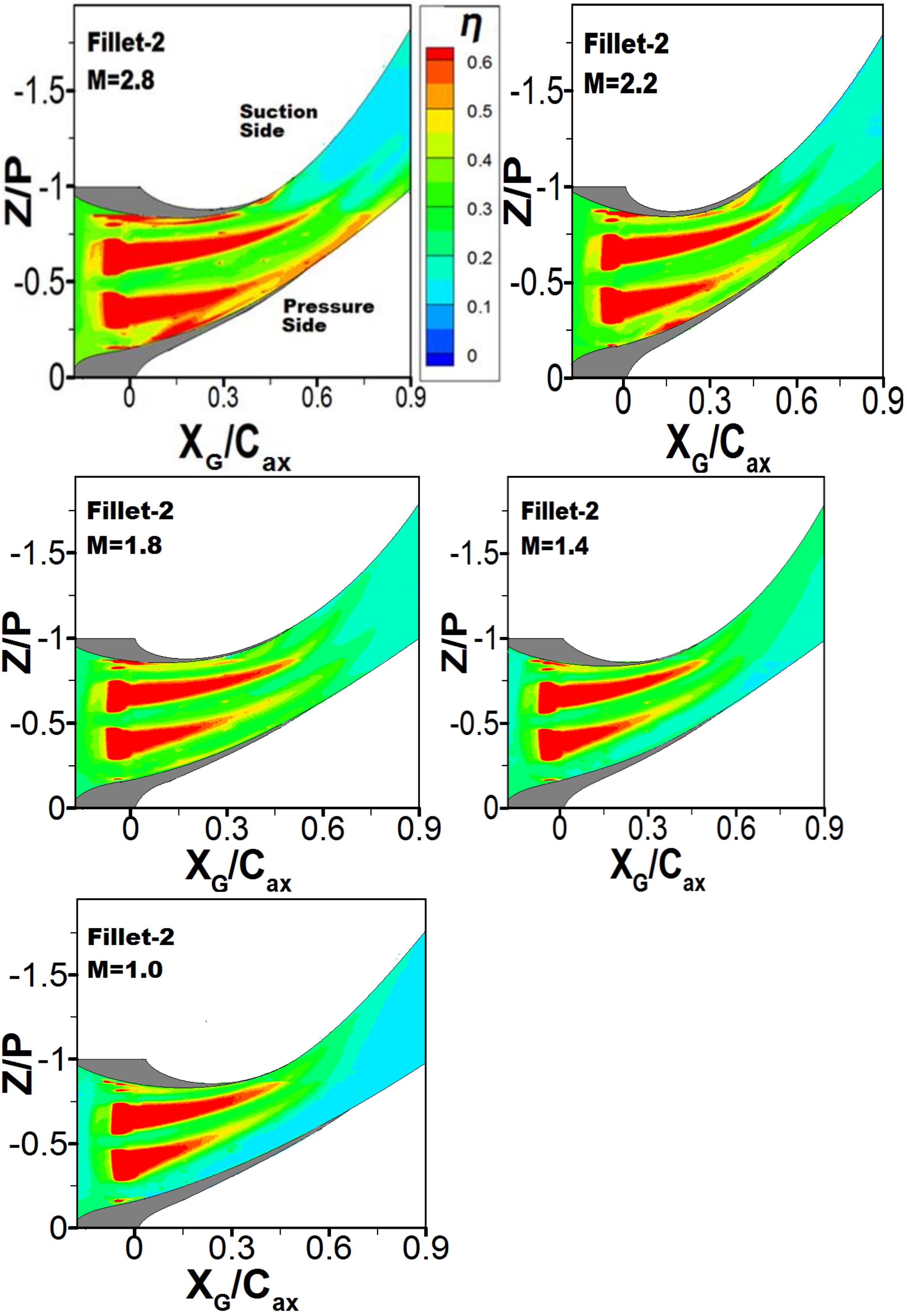

Figure 5-25: Endwall film cooling with slot and discrete holes geometry for Fillet-2

Since Baseline-1 and Baseline-2 is having fewer number of holes to discharge film-cooling jets, when compared with Baseline, the η is higher for Baseline than Baseline-1 and Baseline-2. The curved holes perform better than the discrete holes upstream of the throat area in terms of the higher lateral and axial spread of the effectiveness on the endwall. Fillet-2 seems to be having higher *η* when compared with Fillet-1. This is because Fillet-1 is having fewer number of discharge holes upstream, thereby limiting the mass flux of the cooling jet in Fillet-1. With the use of the curved holes (Figures 5.31 – 5.35), there is tremendous improvement in the film cooling effectiveness when compared with the discrete hole configurations (Figures 5.26 – 5.30). The lateral and axial spreads are much uniform at the endwall when Figures 5.26 to 5.35 are compared with Figures 5.21 to 5.25 at respective blowing ratios. In general, the best film-cooling performance in terms of the coverage and adiabatic effectiveness values is obtained with the use of curved (bevelled) holes.

The pitchwise averaged of the endwall effectiveness for all the configurations are also plotted to further compare the performance of each configuration and scheme. These are presented in Figure 5.36 to 5.39. This is computed by averaging the Z/P constant locations along the axial direction starting from the global coordinate origin (X_G,Y_G,Z_G). As shown previously in Figs. 5.21 to 5.35, the adiabatic effectiveness increases as the mass flux of the film cooling increases and reduces along the axial direction of the passage. The averaged effectiveness values for the discrete hole configuration (in Figure 36) show that Fillet-2 is apparently performing better than Fillet-1. This is evident as Filet-2 is having higher effectiveness magnitude than all the other configurations. In Figure 5.37 as stated earlier, the effectiveness also reduces with reduction in mass flux of the coolant. For slot-discrete hole configuration, Fillet-2 performs better than other configurations at $M<2.8$ (Figure 5.38).

In general, Effectiveness reduces with: (i) reduction in mass flux of the film cooling flow and (ii) increase in the axial distance along the passage. The curved (bevelled hole) and slot-discrete hole configurations performed better than the discrete hole configuration in terms of the axial and lateral spread of the effectiveness on the endwall.

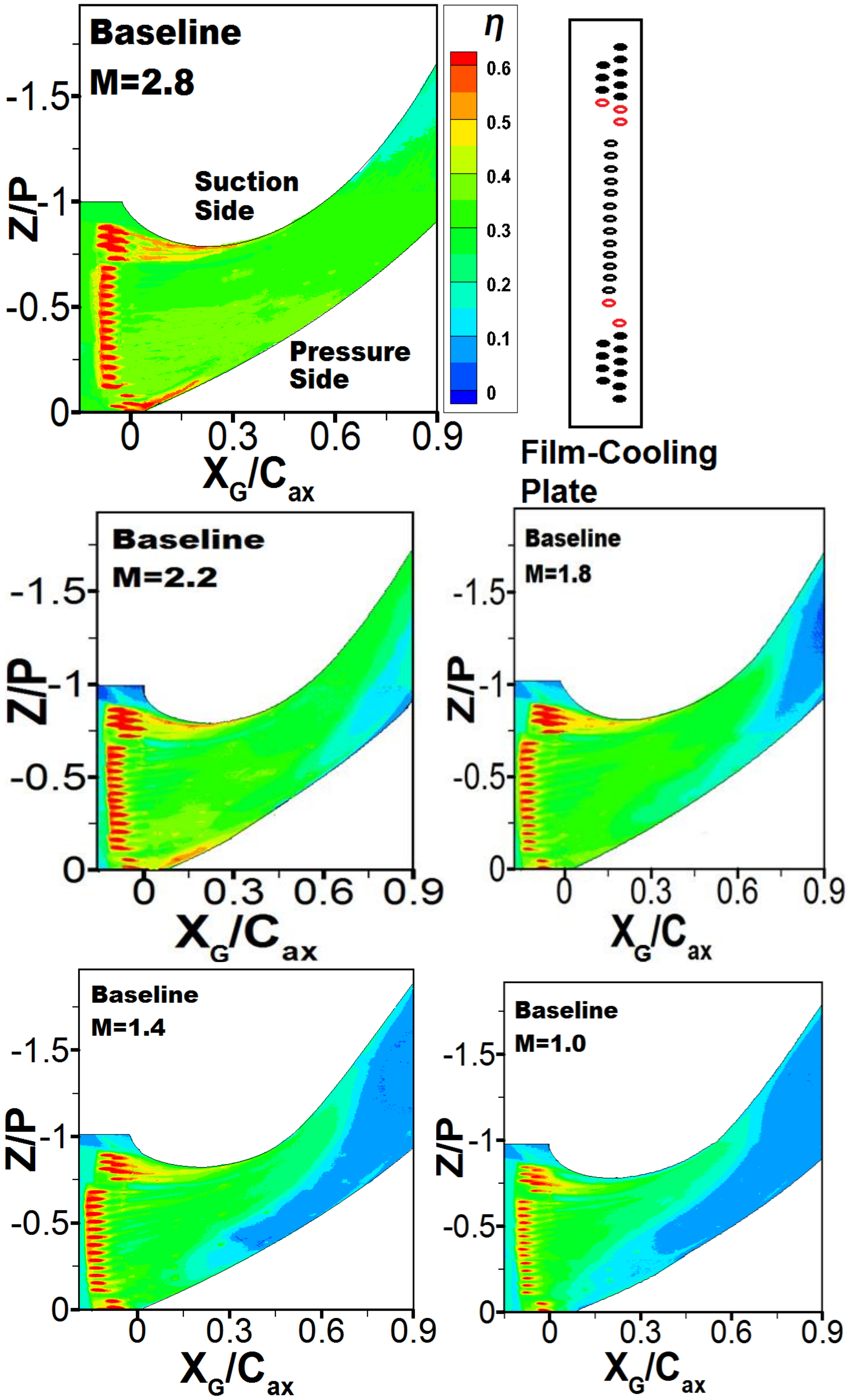

Figure 5-26: Endwall film cooling with discrete holes geometry for Baseline

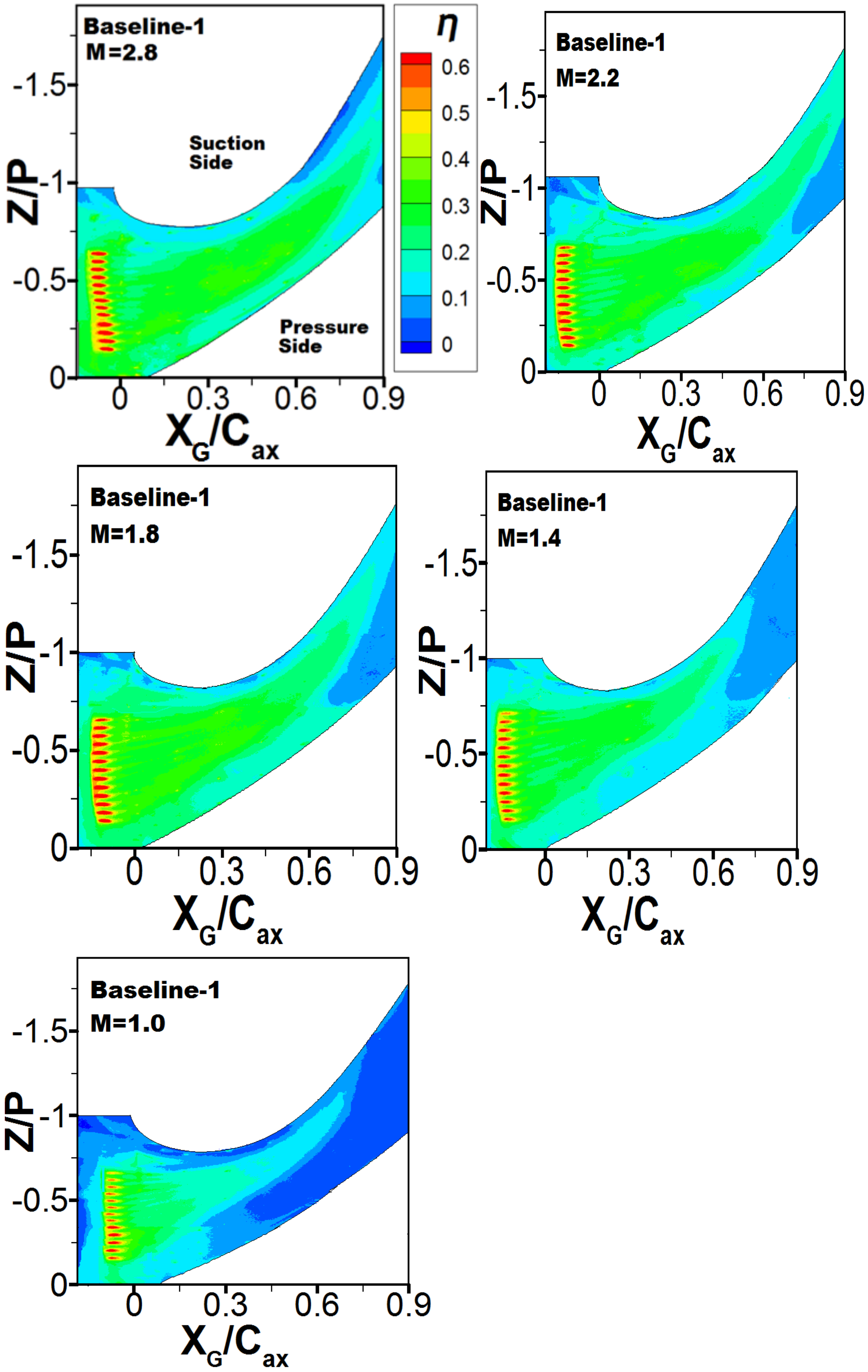

Figure 5-27: Endwall film cooling with discrete holes geometry for Baseline-1

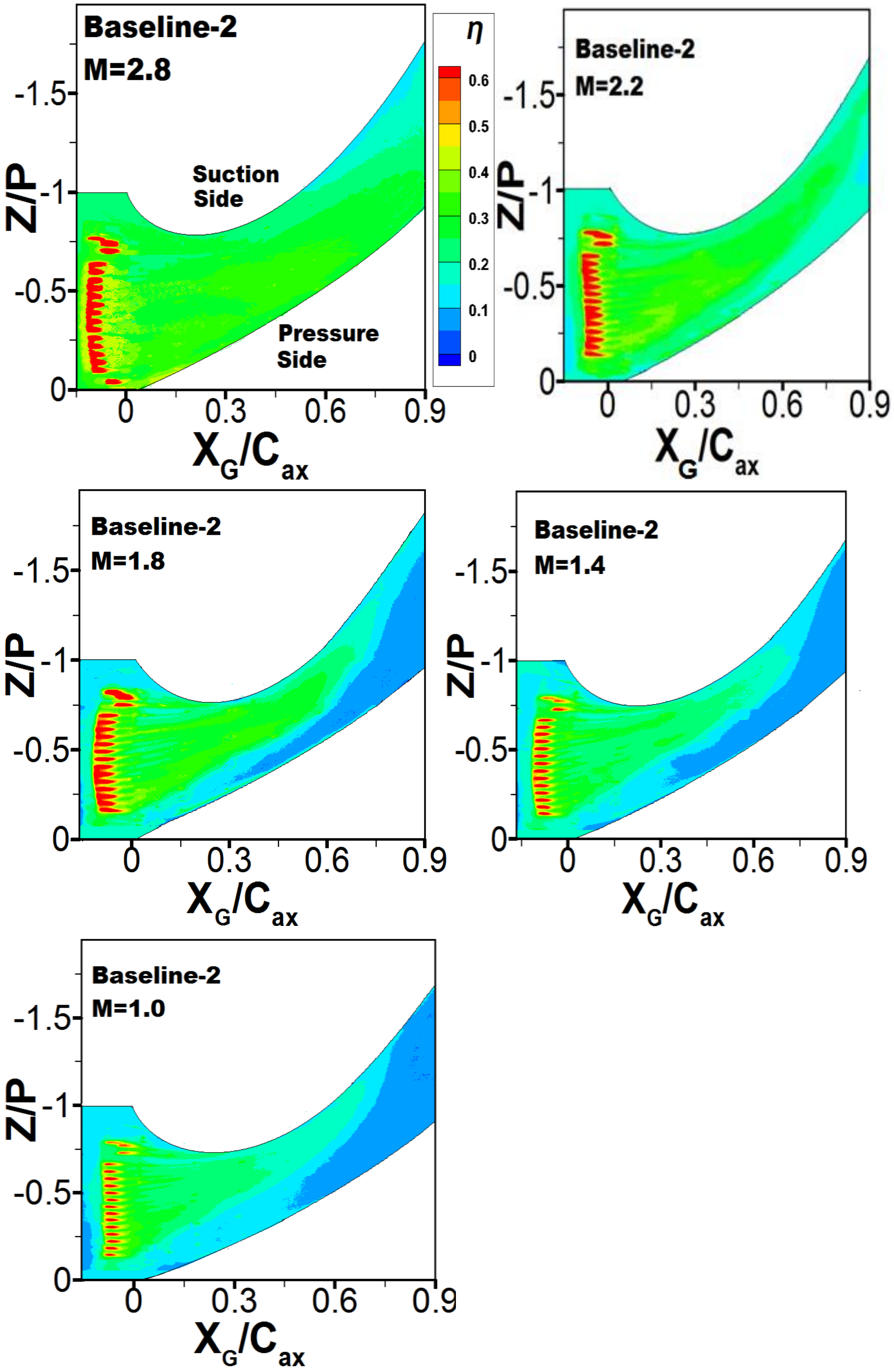

Figure 5-28: Endwall film cooling with discrete holes geometry for Baseline-2

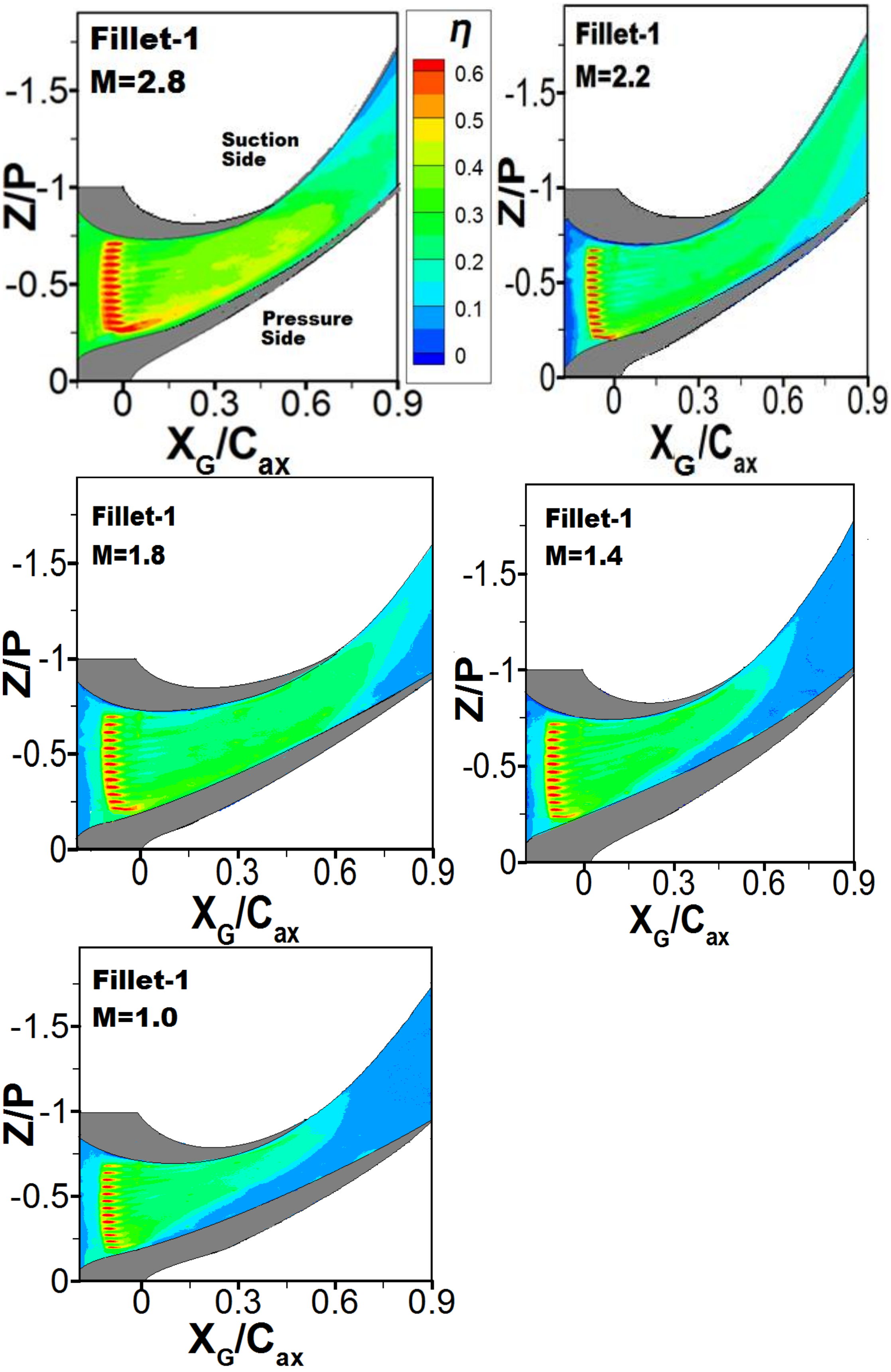

Figure 5-29: Endwall film cooling with discrete holes geometry for Fillet-1

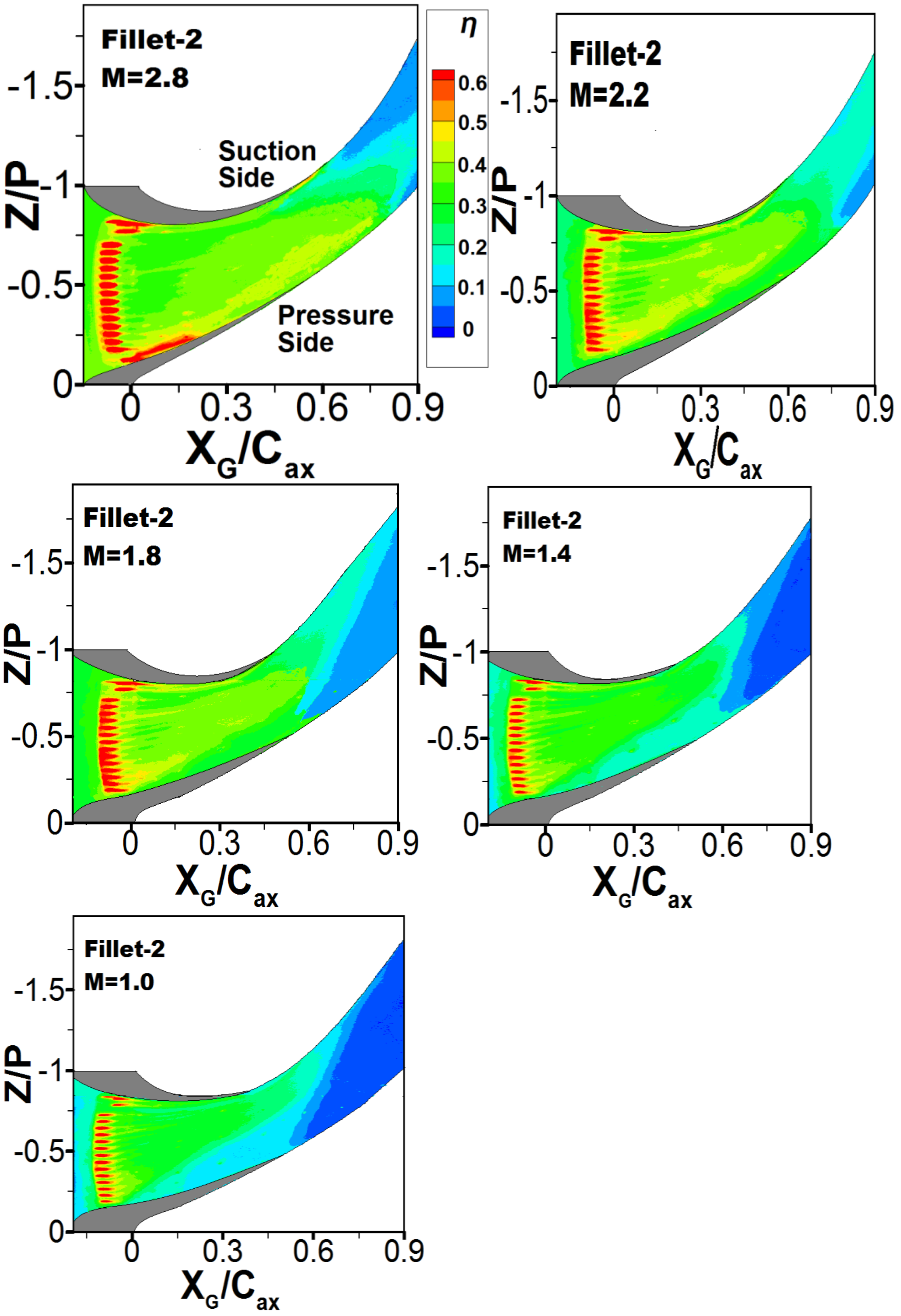

Figure 5-30: Endwall film cooling with discrete holes geometry for Fillet-2

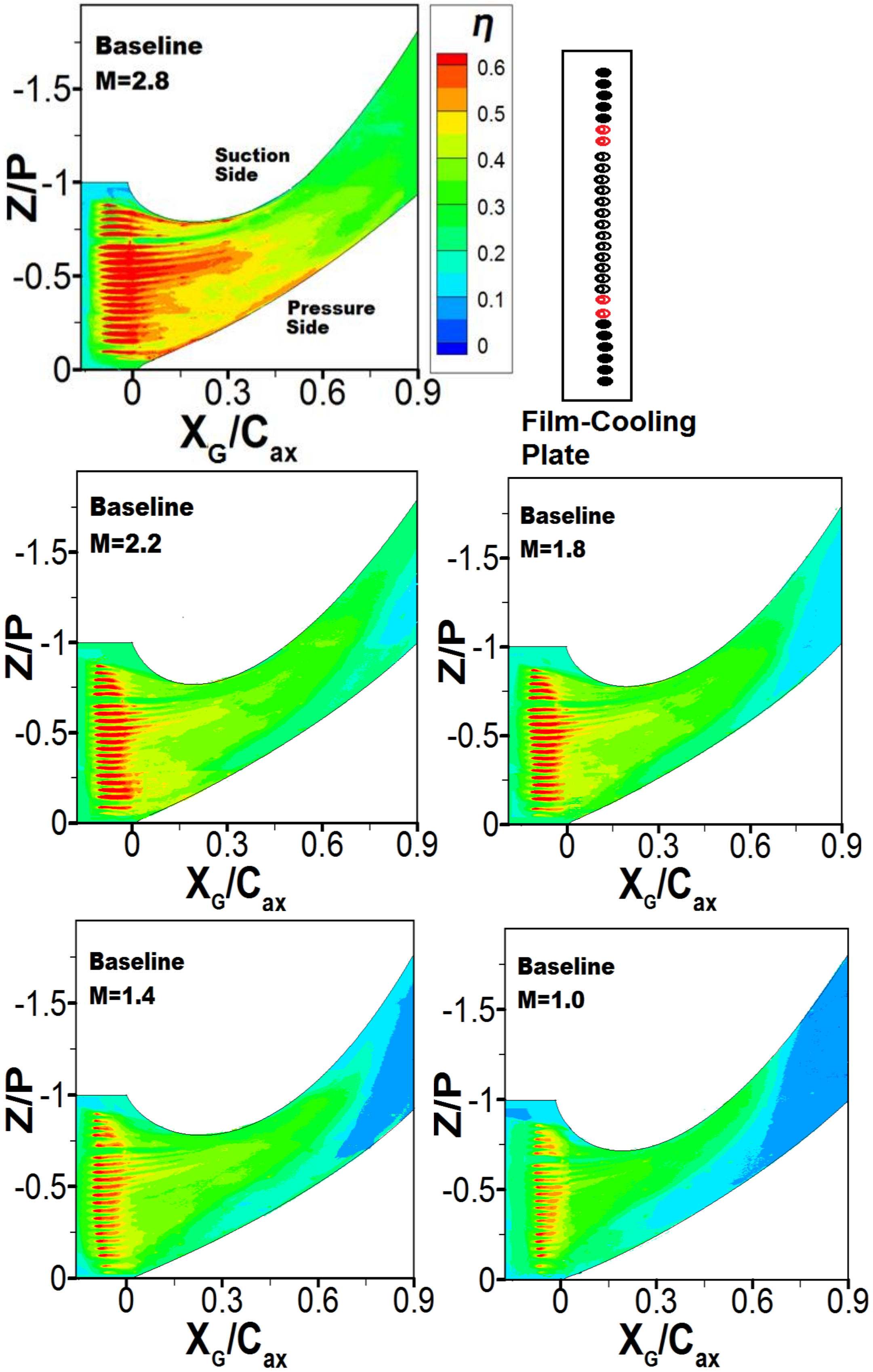

Figure 5-31: Endwall film cooling with bevelled holes geometry for Baseline

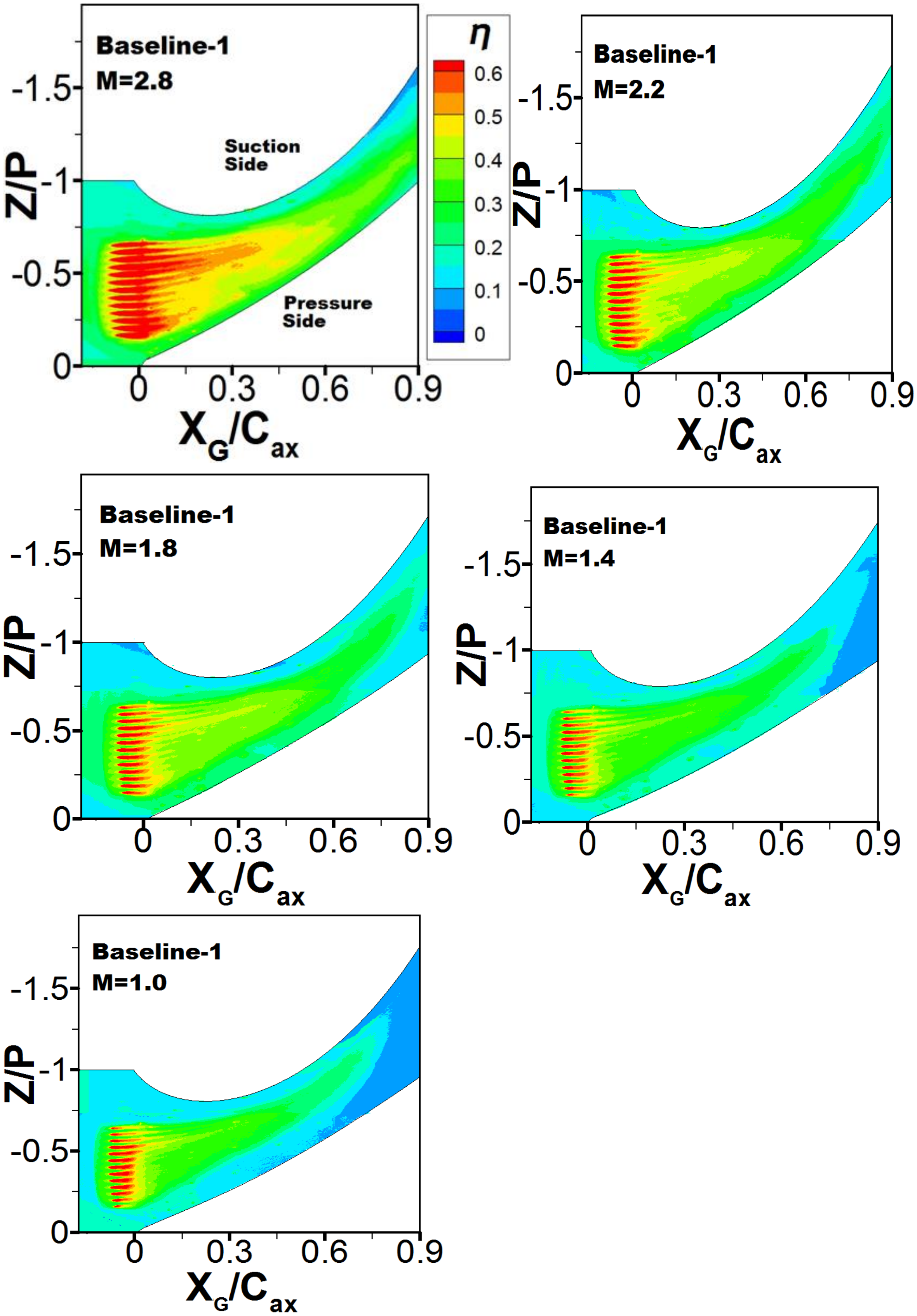

Figure 5-32: Endwall film cooling with bevelled holes geometry for Baseline-1

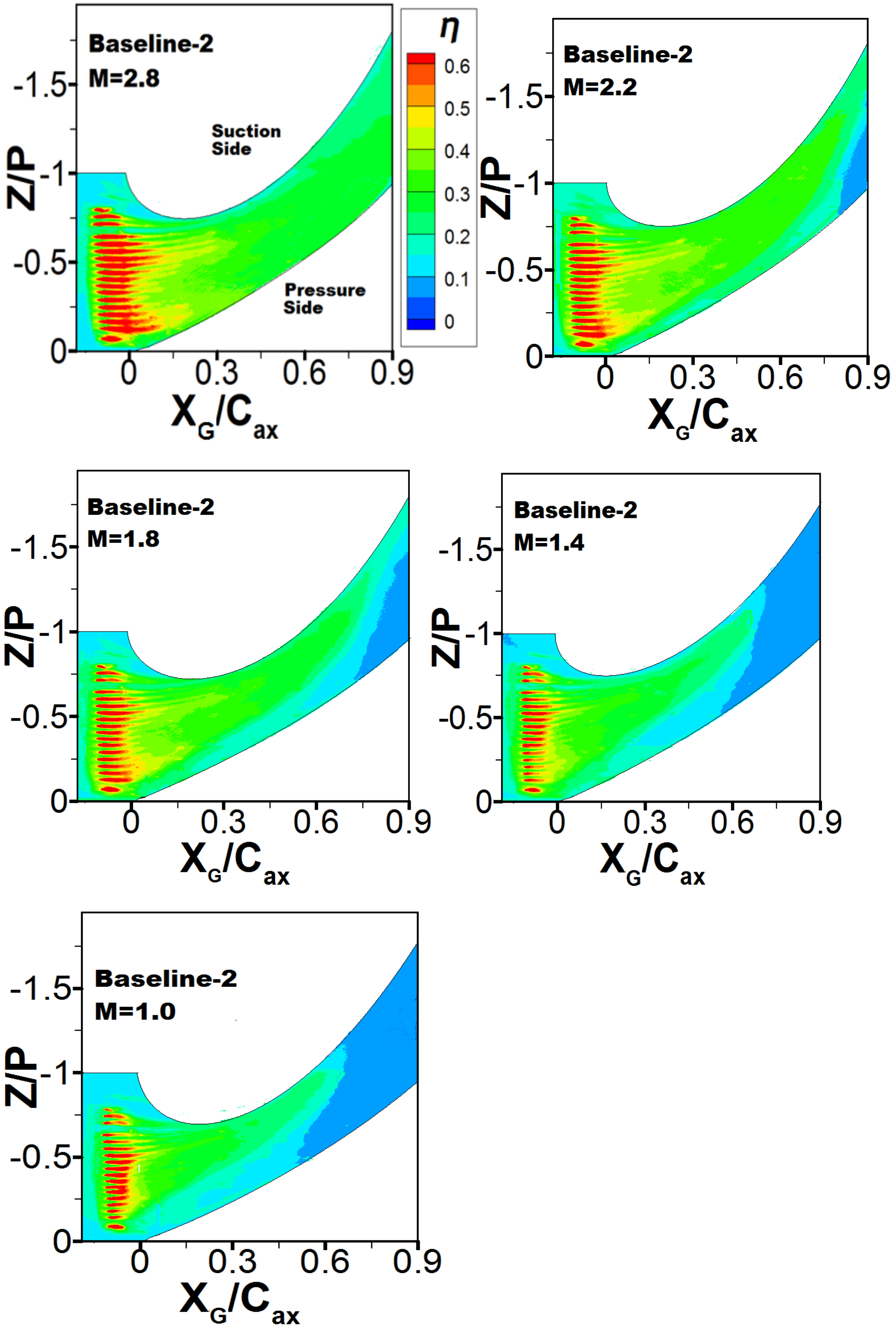

Figure 5-33: Endwall film cooling with bevelled holes geometry for Baseline-2

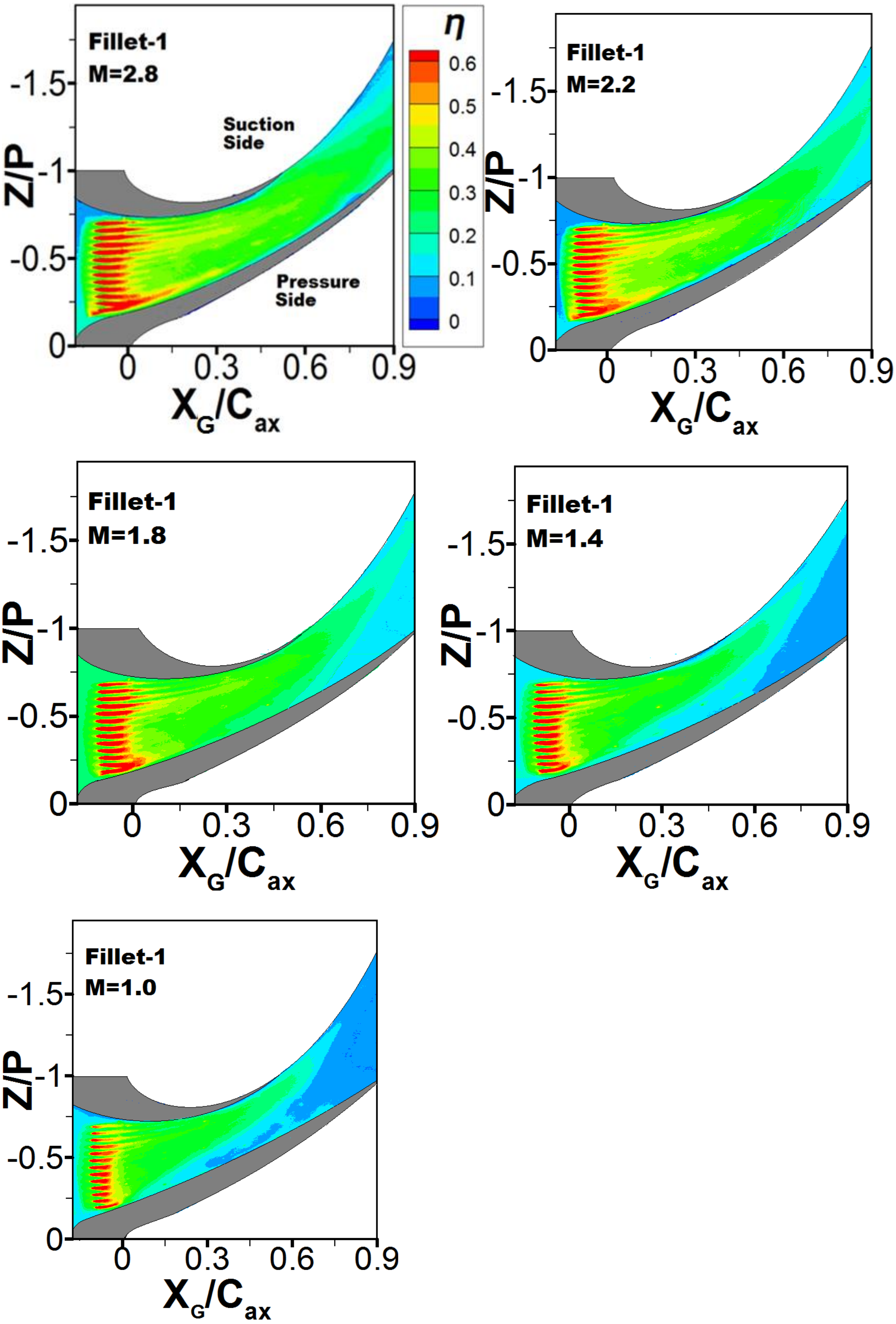

Figure 5-34: Endwall film cooling with bevelled holes geometry for Fillet-1

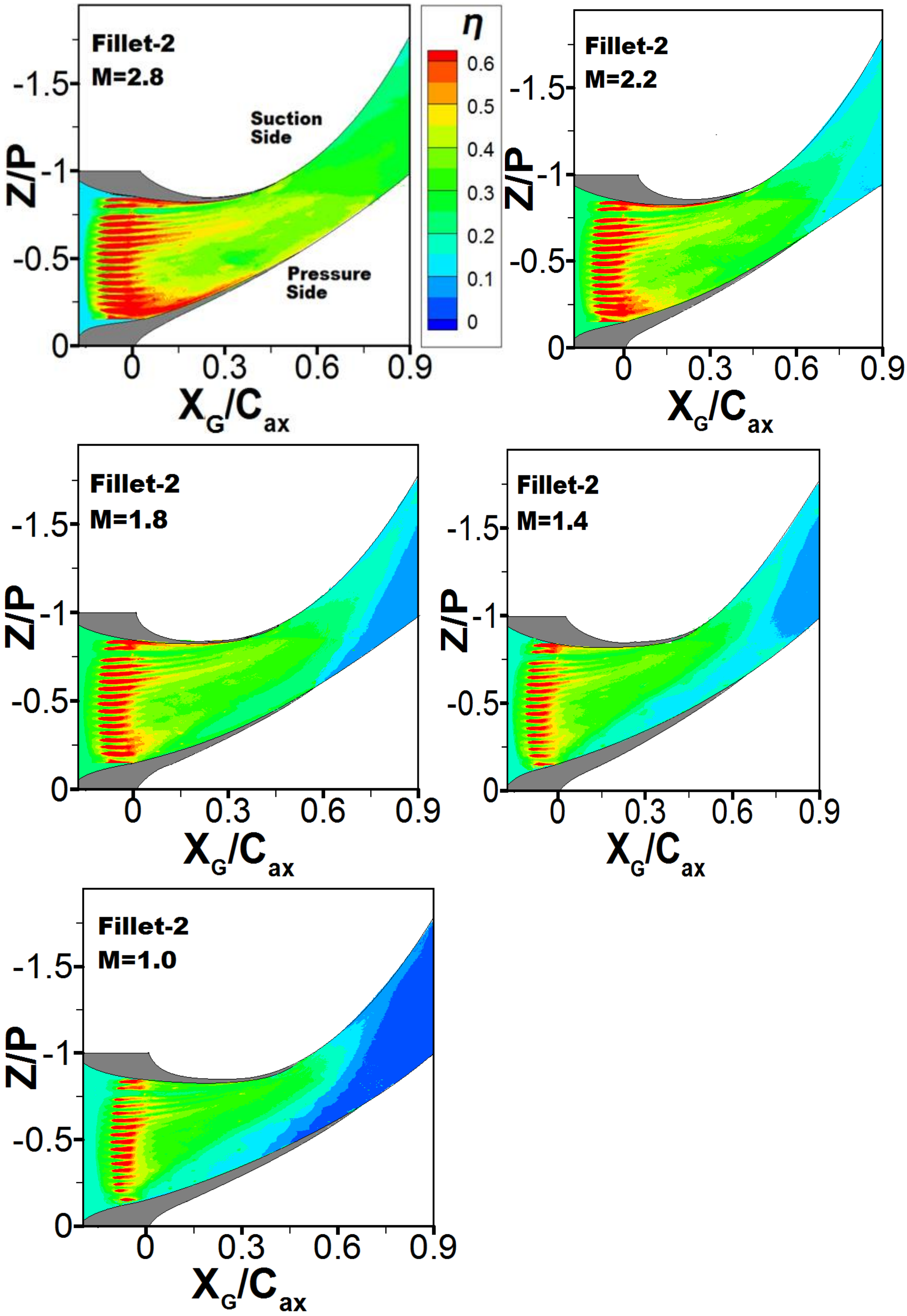

Figure 5-35: Endwall film cooling with bevelled holes geometry for Fillet-2

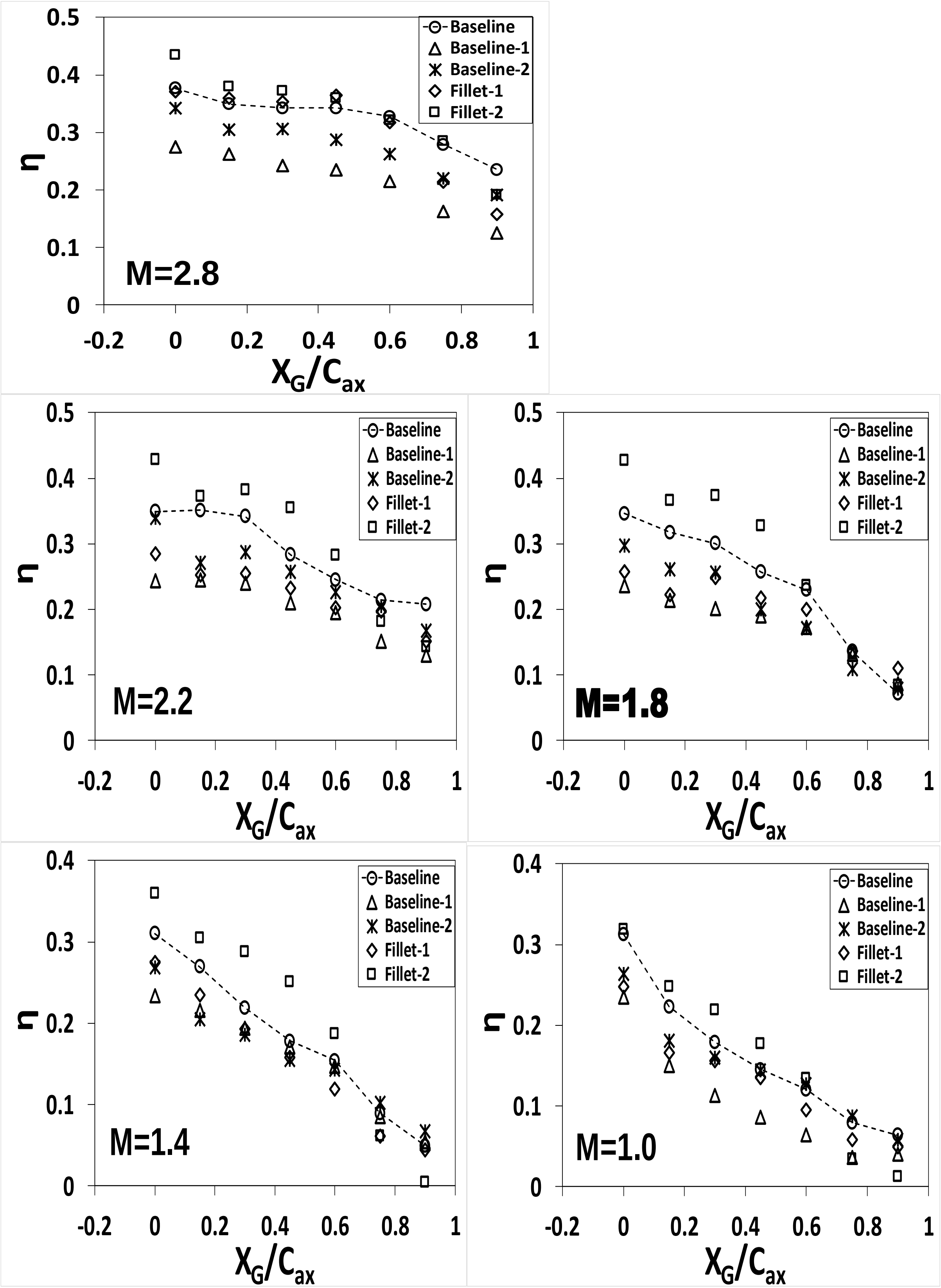

Figure 5-36: Pitchwise averaged of Adiabatic Effectiveness (η) Distribution at the Endwall, Y_G/S = 0.0 for Discrete Holes FC at M=1.0, 1.4, 1.8, 2.2 and 2.8

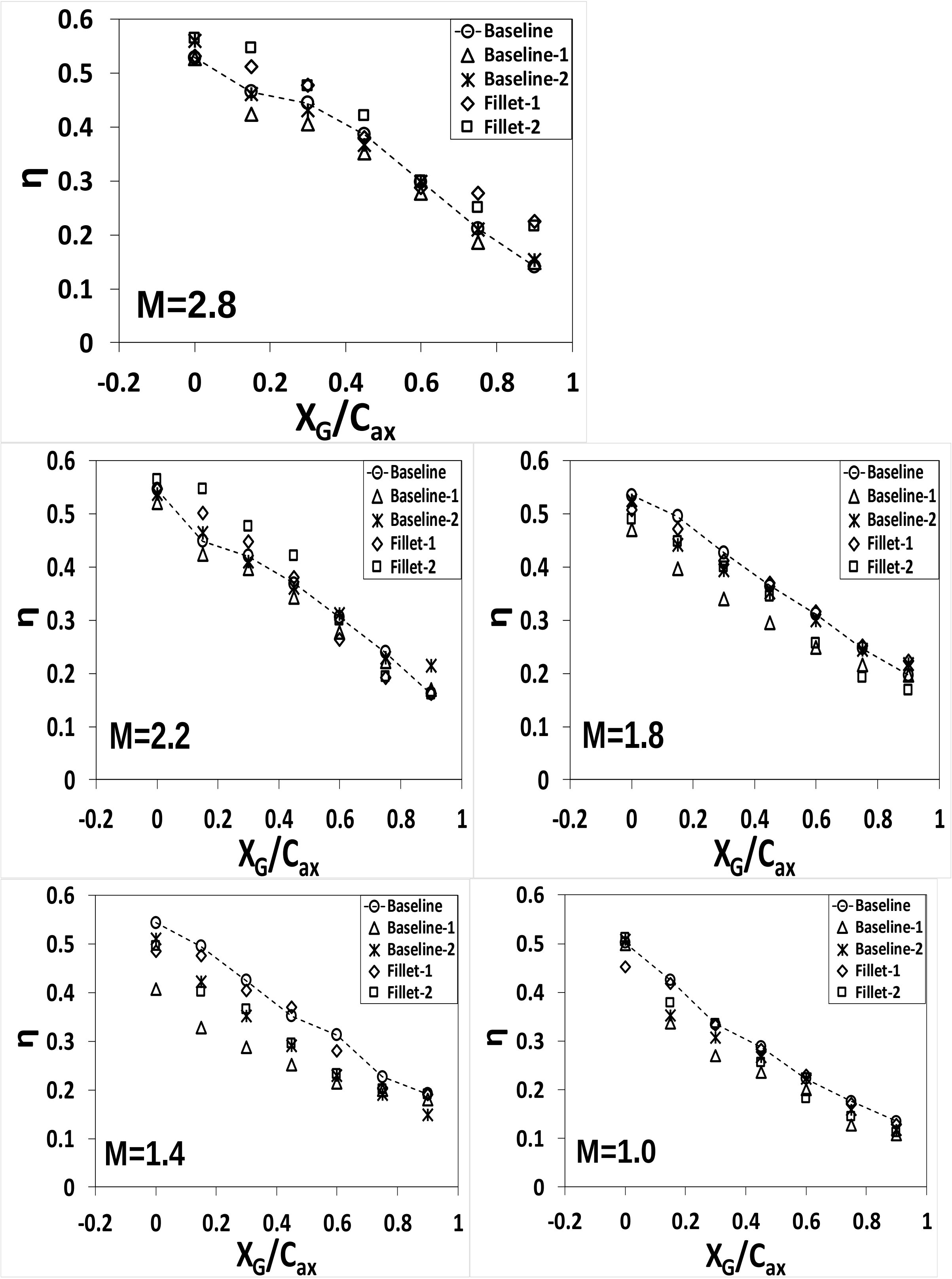

Figure 5-37: Pitchwise averaged of Adiabatic Effectiveness (η) Distribution at the Endwall, $Y_G/S = 0.0$ for Slot-Discrete Holes FC at M=1.0, 1.4, 1.8, 2.2 and 2.8

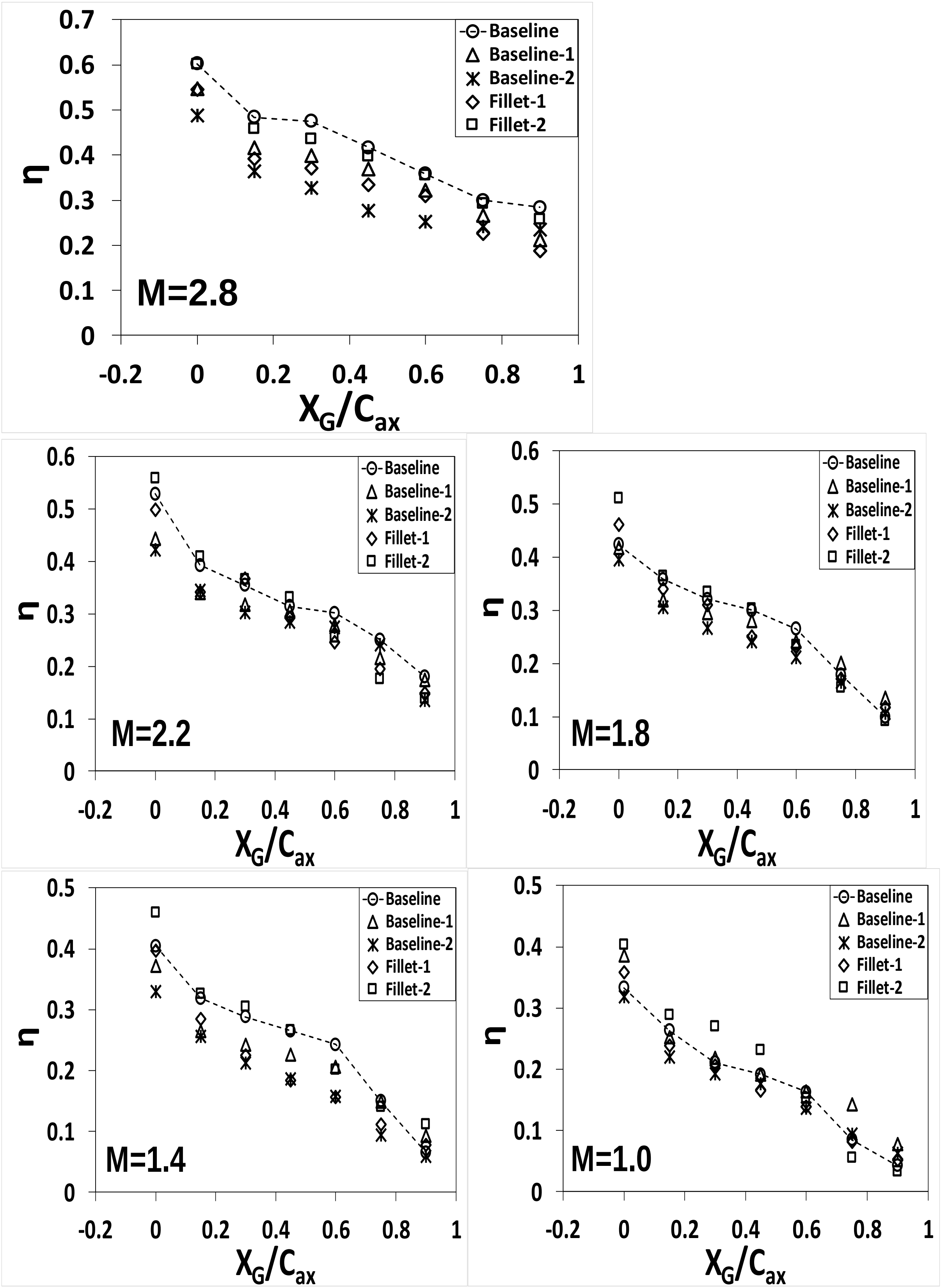

Figure 5-38: Pitchwise averaged of Adiabatic Effectiveness (η) Distribution at the Endwall, Y_G/S = 0.0 for Bevelled Holes FC at M=1.0, 1.4, 1.8, 2.2 and 2.8

6. CHAPTER 6: SYNOPSIS AND CONCLUDING REMARKS

6.1 Synopsis

A well designed turbine parts and components should be able to withstand very wide temperature and pressure fluctuations within the passage for a very long time. This research centres on provisions of reliable quantitative and qualitative data to turbine designers on the improvement of the endwall heat transfer particularly near the endwall region of the first stage vane passage.

Computations are carried out using StarCCM+^{TM} 8.06 to bench mark the baseline (without film cooling flow) and filleted case using Fillet-1. The reference flow conditions in the cascade are matched with the simulation to obtain valid results. Results are presented at the mid-span, endwall and Plane-4 for validation.

The experimental test section housing the seven GEE^3 linear blade profile was put together from scratch starting from design stage to the final commissioning of the test section. Measurements are taken between blade 5 and blade 3. National Instrument and the DAQ system are used extensively for the data logging due to their reliability and accuracy of measurement. The test section is powered by two serially connected suction blowers (7.5kW and 15kW). Reference properties are taken at 2.5C_{ax} upstream of the leading-edge of the cascade. Turbulent grid is also placed at 4C_{ax} upstream of the reference region. Five-hole probe calibration slot is located at 9.8C_{ax} from the leading-edge. At the top endwall, four slots are created for time-resolved data scanning and flow analyses within the vane passage.

Various modifications and configurations are considered at the endwall region. These modifications include the use of two distinct linear profile fillets at the endwall. Fillet-1 extends upstream by 0.3C_{ax}, and a spanwise height of 0.1S. On the pressure side, it varies linearly all the way to the trailing-edge while on the suction side, it terminates at the throat region. Fillet-2 is extending upstream by 0.2C_{ax} with a spanwise height of 0.08S. The profile varies linearly and ends at the throat region on both the pressure and suction sides.

Four unique leading-edge film cooling plates are also considered to determine the efficacies of each along with the endwall modifications. The adiabatic effectiveness and spread of the film cooling at the endwall is of paramount importance to prolong the life of the turbine system and components. At -0.079Cax location from the leading-edge, film cooling plates are located. The film chilling unit is designed to produce 'secondary' flows into the cascade arena. The chilling circuit is connected at the bottom endwall to supply film cooling jets into the cascade. The flow through the channel is metered by an orifice. Five blowing ratios (M=1.0, 1.4, 1.8, 2.2 and 2.8) are considered respectively for each of the four film cooling plates experimentation. The first plate consists of four flush slots linearly arranged at the cascade leading-edge. The longer slots are placed directly at the centre of the leading-edge while the other two are spaced at the centre of the passage. Film chilling Plate-2 consists of slots and discrete holes. Eleven discrete holes are strategically arranged on the leading-edge. Similar to Plate-1, the two slots are also spaced centrally upstream of the passage region. In Plate-3, the two central slots in Plate-2 are being replaced by fourteen discrete holes (Ø10mm) equi-spaced centrally upstream of the passage inlet. Plate-4 is just having twenty four linear curved/bevelled holes all through the entire leading-edge region. Thereafter, four windows are created on the top endwall for the IR camera capturing of the bottom endwall. The camera is positioned directly upright to view the bottom endwall through the Zinc Selenide glass window that is flushed with the inside passage. Four temperature fields are taken respectively from the four windows created. These IR temperature fields are calibrated and combined to form a full passage coverage of the film cooling effectiveness after averaging the area of overlap on the endwall.

Heating plate is designed and installed on the endwall to supply a constant heat flux from a suitable power supply. The endwall is heated at uniform heat flux through a suitable power supply. Data of the endwall heat transfer are taken without film cooling flow (M = 0). The enwall is also modified with the installation of the fillets and data taken for comparison after application of appropriate calibration. Forty five thermocouples are embedded on the endwall heater for IR temperature field calibration. Similar to the film cooling calibration, the temperature is also applied and converted to Nusselt number.

6.2 Conclusions

In general, the conclusions and the recommendations drawn are as follows:

(a) The velocity and thermal boundary layers conform to what is obtainable in the actual turbine inlet conditions. These boundary layers measured were useful in the design of Fillet-1 and Fillet-2. There is no significant change in the static pressure at the mid-span with the use of the fillet. This validates the design of the fillets as the fillets are not adding any pressure on the blade at the mid-span.

(b) A turbine passage was modelled for computation using StarCCM+^{TM}. Mass averaged increases gradually from the inlet to the passage exit. The computational result of the baseline static pressure on the endwall matches that of the experiment particularly at the region upstream of the throat region. Baseline total pressure also matches substantially that of the computation. This shows that the computational result conforms with experimental results. The employment of the Fillet-1 shows reduced turning at the leading-edge. The relocation of the reattachment line is apparent from the use of Fillet-1 close to the endwall. The $\tau_x/(0.5\rho U^2)$ values of Fillet-1 is higher than for baseline due to the flow separation within the passage and yaw angle. The computational model shows that the designed fillet is viable for further investigations in the cascade experimental facility.

(c) The aerodynamic influence of the flush slots of the film cooling at Plane-4 was examined at blowing ratios M = 1.0, 1.4, 1.8, 2.2 and 2.8. The result shows that as the blowing ratio increases the passage vortex is reduced in magnitude and size. The highest blowing ratio produces best results in terms of the reduction and relocation of the passage vortex. However, it is also discovered that the boundary layer increases within the passage as the film cooling flux increases. The introduction of Fillet-1 and Fillet-2 produce good results particularly towards the near endwall as regards vortices reduction. The fillets helped in the reduction of the complex turning and fluctuation of the cross-flow towards the suction side. Fillet-2 produces better result compared with Fillet-1. It is also worth mentioning that at blowing ratio $M \geq 2.2$, two distinct bulges as passage vortices are observed at Plane-4. Film cooling flows from endwall slots at cascade inlet and blade-endwall junction fillet employed in the experiments weaken secondary flows on endwall and total pressure losses across the vane cascade. The combination of the slot film cooling and fillet then also further reduce both the endwall secondary flows and total pressure losses. The secondary flows are the primary contributor to the local high heat transfer on the endwall in the turbine passage. Total pressure losses contribute to the loads of the gas turbine compressor.

(d) The heat transfer results for the baseline case without fillet ($M = 0$) established that the region downstream of the throat area has high Nusselt number. Installation of fillets shows that heat transfer at the throat region is being reduced. The fillet reduces the cross-flow and the complex turning which prevent the film cooling from fair penetration down-stream of the endwall. At the mid-passage region, Fillet-2 has lowest Nu which is favourable for film cooling at the endwall. The leading edge fillet at the blade-endwall junction can reduce the heat transfer between the mainstream flow and endwall. The fillet also creates favourable conditions for better distribution of the slot film cooling flows on the cascade endwall.

(e) The non-dimensional temperature shows that Fillet-1 and Fillet-2 are aiding the endwall cooling at region $Y/S < 0.1$, $X_G/C_{ax} = 0.58$ at blowing ratios $M = 1.0$ to 2.2. However, Fillet-2 shows better cooling at the leading-edge region. This is due to the reduction impact of the fillets on the pitchwise pressure gradient from the pressure side to the suction side to form passage vortex. In general, the installation of the fillets provide better cooling of the endwall region at higher blowing ratio except for Plane-1 where Fillet-1 is having highest magnitude close to the endwall. This could be attributed to the fluctuations caused by the profile of the fillet at the upstream region of the passage. Large fillet and high film cooling mass flux help in controlling of the activities of the secondary flows that are responsible for high heat transfer near the endwall thereby increasing the cooling at the endwall.

(f) For all the three plates examined for the film cooling of the endwall, the results show that the higher the flux jets, the better the adiabatic effectiveness. However, at blowing ratio ≤ 2.2, the film cooling is seen to be influenced by the main flow. Downstream of the passage region, the flow is directed towards the suction side for all the configurations. The film cooling adiabatic effectiveness spread is much better in the discrete hole and curved holes configurations than the other configurations. At the highest blowing ratio (M = 2.8), the cooling flux and effectiveness has a very strong effect on the pressure side. The effectiveness is seen to be very high on the pressure side for all configurations. With the slot-discrete holes configuration, high effectiveness is seen to concentrate at the slot region and disperse along the passage. The effectiveness increases along the passage as the flux increases in the passage. The use of the fillet is seen to be aiding the cooling at the endwall. The use of the fillet with the curved holes seems to produce uniform spread along the endwall. More uniform spread of the effectiveness at the endwall can be achieved with multiple cooling holes strategically arranged at the endwall.

REFERENCES

Acharya, S. & Mahmood, G. I. 2007. 3-D Aerodynamics. *The Gas Turbine Handbook,National Energy Technology Laboratory (NETL)-DOE,*, Vol. 1.0**,** Chap. 4.3.

Arnachellan, K. 2017. *Aerodynamic Loss Reduction in a Vane Cascade With Leading-Edge Fillet and Upstream Endwall Film-Cooling.* Master Thesis, University of Pretoria.

Aunapu, N. V., Volino, R. J., Flack, K. A. & Stoddard, R. M. 2000. Secondary Flow Measurements in a Turbine Passage With Endwall Flow Modification. *Journal of Turbomachinery,* 122**,** 651-658.

Barringer, M. D., Richard, O. T., Walter, J. P., Stitzel, S. M. & Thole, K. A. 2002. Flow Field Simulations of a Gas Turbine Combustor. *Journal of Turbomachinery,* 124**,** 508-516.

Barringer, M. D., Thole, K. A. & Polanka, M. D. 2007. Experimental Evaluation of an Inlet Profile Generator for High-Pressure Turbine Tests. *Journal of Turbomachinery,* 129**,** 382-393.

Barringer, M. D., Thole, K. A. & Polanka, M. D. 2009a. An Experimental Study of Combustor Exit Profile Shapes on Endwall Heat Transfer in High Pressure Turbine Vanes. *Journal of Turbomachinery,* 131**,** 021009-021009-10.

Barringer, M. D., Thole, K. A., Polanka, M. D., Clark, J. P. & Koch, P. J. 2009b. Migration of Combustor Exit Profiles Through High Pressure Turbine Vanes. *Journal of Turbomachinery,* 131**,** 021010-021010-10.

Bear, P., Wolff, M., Gross, A., Marks, C. R. & Sondergaard, R. 2018. Experimental Investigation of Total Pressure Loss Development in a Highly Loaded Low-Pressure Turbine Cascade. *Journal of Turbomachinery,* 140**,** 031003-9.

Becz, S., Majewski, M. S. & Langston, L. S. Leading Edge Modification Effects on Turbine Cascade Endwall Loss. Proc. ASME Turbo Expo, 2003. pp. 359-367.

Becz, S., Majewski, M. S. & Langston, L. S. An Experimental Investigation of Contoured Leading Edges for Secondary Flow Loss Reduction. Proc. ASME Turbo Expo, 2004. ASME, pp. 1407-1415.

Cardwell, N. D., Sundaram, N. & Thole, K. A. 2006. Effect of midpassage gap, endwall misalignment, and roughness on endwall film-cooling. *Journal of Turbomachinery,* 128**,** 62-70.

Cardwell, N. D., Sundaram, N. & Thole, K. A. 2007. The effects of varying the combustor-turbine gap. *Journal of Turbomachinery,* 129**,** 756-764.

Cardwell, N. D., Thole, K. A. & Burd, S. W. 2010. Investigation of Sand Blocking Within Impingement and Film-Cooling Holes. *Journal of Turbomachinery,* 132**,** 021020-021020-10.

Carullo, J. S., Nasir, S., Cress, R. D., Ng, W. F., Thole, K. A., Zhang, L. J. & Moon, H. K. 2011. The Effects of Freestream Turbulence, Turbulence Length Scale, and Exit Reynolds Number on Turbine Blade Heat Transfer in a Transonic Cascade. *Journal of Turbomachinery,* 133**,** 011030-011030-11.

CD-adapco 2013. STAR-CCM+ User Guide Version 8.06. Melville, New York, USA.

Colban, W. & Thole, K. 2007. Influence of hole shape on the performance of a turbine vane endwall film-cooling scheme. *International Journal of Heat and Fluid Flow,* 28**,** 341-356.

Colban, W., Thole, K. A. & Haendler, M. 2007. Experimental and Computational Comparisons of Fan-Shaped Film Cooling on a Turbine Vane Surface. *Journal of Turbomachinery,* 129**,** 23-31.

Colban, W., Thole, K. A. & Haendler, M. 2008. A comparison of cylindrical and fan-shaped film-cooling holes on a vane endwall at low and high freestream turbulence levels. *Journal of Turbomachinery,* 130.

Colban, W. F., Lethander, A. T., Thole, K. A. & Zess, G. 2003. Combustor turbine interface studies - Part 2: Flow and thermal field measurements. *Journal of Turbomachinery,* 125**,** 203-209.

Eberly, M. K. & Thole, K. A. 2014. Time-Resolved Film-Cooling Flows at High and Low Density Ratios. *Journal of Turbomachinery,* 136**,** 061003-061003-11.

Friedrichs, S., Hodson, H. P. & Dawes, W. N. 1997. Aerodynamic Aspects of Endwall Film-Cooling. *Journal of Turbomachinery, ASME,* 119**,** 786-793.

Friedrichs, S., Hodson, H. P. & Dawes, W. N. 1999. The Design of an Improved Endwall FilmCooling Configuration. *Journal of Turbomachinery,* 121**,** 772-780.

Hada, S. & Thole, K. A. 2011. Computational Study of a Midpassage Gap and Upstream Slot on Vane Endwall Film-Cooling. *Journal of Turbomachinery,* 133**,** 011024-011024-9.

Han, S. & Goldstein, R. J. 2008. The heat/mass transfer analogy for a simulated turbine blade. *International Journal of Heat and Mass Transfer,* 51**,** 5209-5225.

Harmanson, K., Kern, S., Picker, G. & Parneix, S. 2002. Predictions of External Heat Transfer for Turbine Vanes and Blades with Secondary Flow Fileds. *Proc. ASME Turbo Expo,,* Paper No. GT-2002-30206,.

Harrington, M. K., McWaters, M. A., Bogard, D. G., Lemmon, C. A. & Thole, K. A. 2001. Full-coverage film cooling with short normal injection holes. *Journal of Turbomachinery,* 123**,** 798-805.

Hermanson, K. S. & Thole, K. A. 2002. Effect of Nonuniform Inlet Conditions on Endwall Secondary Flows. *Journal of Turbomachinery,* 124**,** 623-631.

Kang, M. B., Kohli, A. & Thole, K. A. 1999. Heat Transfer and Flowfield Measurements in the Leading Edge Region of a Stator Vane Endwall. *Journal of Turbomachinery,* 121**,** 558-568.

Kang, M. B. & Thole, K. A. 2000. Flowfield Measurements in the Endwall Region of a Stator Vane. *Journal of Turbomachinery,* 122**,** 458-466.

Knost, D. G. & Thole, K. A. 2005. Adiabatic Effectiveness Measurements of Endwall Film-Cooling for a First-Stage Vane. *Journal of Turbomachinery,* 127**,** 297-305.

Laveau, B., Abhari, R. S., Crawford, M. & Lutum, E. 2015. High Resolution Heat Transfer Measurements on the Stator Endwall of an Axial Turbine. *journal of Turbomachinery,* 137**,** 041005-11.

Lawson, S. A., Lynch, S. P. & Thole, K. A. 2013. Simulations of Multiphase Particle Deposition on a Nonaxisymmetric Contoured Endwall With Film-Cooling. *Journal of Turbomachinery,* 135**,** 031032-031032-11.

Lawson, S. A. & Thole, K. A. 2012a. Simulations of Multiphase Particle Deposition on Endwall Film-Cooling. *Journal of Turbomachinery,* 134**,** 011003-011003-11.

Lawson, S. A. & Thole, K. A. 2012b. Simulations of Multiphase Particle Deposition on Endwall Film-Cooling Holes in Transverse Trenches. *Journal of Turbomachinery,* 134**,** 051040-051040-10.

Lawson, S. A., Thole, K. A., Okita, Y. & Nakamata, C. 2012. Simulations of Multiphase Particle Deposition on a Showerhead With Staggered Film-Cooling Holes. *Journal of Turbomachinery,* 134**,** 051041-051041-12.

Ligrani, P. M., Singer, B. A. & Baun, L. R. 1989a. Miniature Five-hole Pressure Probe for Measurement of Three Mean Velocity Components in Low-Speed Flows. *J. Phys. E,* 22**,** pp. 868–876.

Ligrani, P. M., Singer, B. A. & Baun, L. R. 1989b. Spatial Resolution and Downwash Velocity Corrections for Multiple-Hole Pressure Probes in Complex Flows. *Exp. Fluids,* 7**,** pp. 424–426.

Lynch, S. P., Sundaram, N., Thole, K. A., Kohli, A. & Lehane, C. 2011a. Heat Transfer for a Turbine Blade With Nonaxisymmetric Endwall Contouring. *Journal of Turbomachinery,* 133**,** 011019-011019-9.

Lynch, S. P. & Thole, K. A. 2008. The effect of combustor-turbine interface gap leakage on the endwall heat transfer for a nozzle guide vane. *Journal of Turbomachinery,* 130**,** 041019-10.

Lynch, S. P. & Thole, K. A. 2011. The Effect of the Combustor-Turbine Slot and Midpassage Gap on Vane Endwall Heat Transfer. *Journal of Turbomachinery,* 133**,** 041002-041002-9.

Lynch, S. P., Thole, K. A., Kohli, A. & Lehane, C. 2011b. Computational Predictions of Heat Transfer and Film-Cooling for a Turbine Blade With Nonaxisymmetric Endwall Contouring. *Journal of Turbomachinery,* 133**,** 041003-041003-10.

Mahmood, G. I. & Acharya, S. 2007. Experimental investigation of secondary flow structure in a blade passage with and without leading edge fillets. *Journal of Fluids Engineering,* 129**,** 253-262.

Mahmood, G. I., Gustafson, R. & Acharya, S. 2005. Experimental Investigation of Flow Structure and Nusselt Number in a Low-Speed Linear Blade Passage With and Without Leading-Edge Fillets. *Journal of Heat Transfer,* 127**,** 499-512.

Mensch, A. & Thole, K. 2015a. Simulations of Multiphase Particle Deposition on a Gas Turbine Endwall With Impingement and Film Cooling. *Journal of Turbomachinery,* 137**,** 111002-111002-8.

Mensch, A. & Thole, K. A. 2015b. Conjugate heat transfer analysis of the effects of impingement channel height for a turbine blade endwall. *International Journal of Heat and Mass Transfer,* 82**,** 66-77.

Mensch, A., Thole, K. A. & Craven, B. A. 2014. Conjugate heat transfer measurements and predictions of a blade endwall with a thermal barrier coating. *Journal of Turbomachinery,* 136**,** 121003-11.

Moffat, R. J. 1988. Describing the uncertainties in experimental results. *Experimental thermal and fluid science,* 1**,** 3-17.

Nasir, S., Carullo, J. S., Ng, W.-F., Thole, K. A., Wu, H., Zhang, L. J. & Moon, H. K. 2009. Effects of Large Scale High Freestream Turbulence and Exit Reynolds Number on Turbine Vane Heat Transfer in a Transonic Cascade. *Journal of Turbomachinery,* 131**,** 021021-021021-11.

Radomsky, R. W. & Thole, K. A. 2002. Detailed Boundary Layer Measurements on a Turbine Stator Vane at Elevated Freestream Turbulence Levels. *Journal of Turbomachinery,* 124**,** 107-118.

Radomsky, R. W. & Thole, K. A. 2000. Measurements and predictions of a highly turbulent flowfield in a turbine vane passage. *Journal of Fluids Engineering, ASME Trans.,,* 122**,** 666-676.

Ranson, W. W., Thole, K. A. & Cunha, F. J. 2005. Adiabatic Effectiveness Measurements and Predictions of Leakage Flows Along a Blade Endwall. *Journal of Turbomachinery,* 127**,** 609-618.

Saha, A. K. & Acharya, S. 2008. Computations of Turbulent Flow and Heat Transfer Through a Three-Dimensional Nonaxisymmetric Blade Passage. *Journal of Turbomachinery,* 130**,** 031008-031008-10.

Sangston, K., Little, J., Lyall, M. E. & Sondergaard, R. 2014. End Wall Loss Reduction of High Lift Low pressures Turbine Airfoils Using Profile Contouring-Part II: Validation. *Journal of Turbomachinery,* 134**,** 1 -10.

Sargent, S. R., Hedlund, C. R. & Ligrani, P. M. 1998. An infrared thermography imaging system for convective heat transfer measurements in complex flows. *Meas. Sci. Technol,* Vol. 9**,** pp. 1974-1981.

Shih, T. I. P. & Lin, Y. L. 2003. Controlling Secondary-Flow Structure by Leading-Edge Airfoil Fillet and Inlet Swirl to Reduce Aerodynamic Loss and Surface Heat Transfer. *Journal of Turbomachinery,* 125**,** 48-56.

Stitzel, S. & Thole, K. A. 2004. Flow Field Computations of Combustor-Turbine Interactions Relevant to a Gas Turbine Engine. *Journal of Turbomachinery,* 126**,** 122-129.

Sundaram, N., Barringer, M. D. & Thole, K. A. 2008. Effects of Deposits on Film Cooling of a Vane Endwall Along the Pressure Side. *Journal of Turbomachinery,* 130**,** 041006-041006-8.

Sundaram, N. & Thole, K. A. 2007. Effects of surface deposition, hole blockage, and thermal barrier coating spallation on vane endwall film cooling. *Journal of Turbomachinery,* 129**,** 599-607.

Sundaram, N. & Thole, K. A. 2008. Bump and Trench Modifications to Film-Cooling Holes at the Vane-Endwall Junction. *Journal of Turbomachinery,* 130**,** 041013-041013-9.

Sundaram, N. & Thole, K. A. 2009. Film-Cooling Flowfields With Trenched Holes on an Endwall. *Journal of Turbomachinery,* 131**,** 041007-041007-10.

Thole, K. A. & Knost, D. G. 2005. Heat transfer and film-cooling for the endwall of a first stage turbine vane. *International Journal of Heat and Mass Transfer,* 48**,** 5255-5269.

Thole, K. A., Radomsky, R. W., Kang, M. B. & Kohli, A. 2002. Elevated freestream turbulence effects on heat transfer for a gas turbine vane. *International Journal of Heat and Fluid Flow,* 23**,** 137-147.

Thrift, A., Thole, K. & Hada, S. 2013. Impact of the Combustor-Turbine Interface Slot Orientation on the Durability of a Nozzle Guide Vane Endwall. *Journal of Turbomachinery,* 135**,** 041019-041019-10.

Thrift, A. A. & Thole, K. A. 2012. Influence of flow injection angle on a leading-edge horseshoe vortex. *International Journal of Heat and Mass Transfer,* 55**,** 4651-4664.

Thrift, A. A., Thole, K. A. & Hada, S. 2011a. Effects of an Axisymmetric Contoured Endwall on a Nozzle Guide Vane: Adiabatic Effectiveness Measurements. *Journal of Turbomachinery,* 133**,** 041007-041007-10.

Thrift, A. A., Thole, K. A. & Hada, S. 2011b. Effects of an Axisymmetric Contoured Endwall on a Nozzle Guide Vane: Convective Heat Transfer Measurements. *Journal of Turbomachinery,* 133**,** 041008-041008-10.

Thrift, A. A., Thole, K. A. & Hada, S. 2012. Effects of Orientation and Position of the Combustor-Turbine Interface on the Cooling of a Vane Endwall. *Journal of Turbomachinery,* 134**,** 061019-061019-10.

Timko, L. P. 1990. Energy Efficient Engine High Pressure Turbine Component Test Performance Report. *Contract Report for NASA.*

Torre, D., Vázquez, R., de la Rosa Blanco, E. & Hodson, H. P. 2010. A New Alternative for Reduction in Secondary Flows in Low Pressure Turbines. *Journal of Turbomachinery*, 133**,** pp. 011029-011029.

Vakil, S. S. & Thole, K. A. 2005. Flow and thermal field measurements in a combustor simulator relevant to a gas turbine aeroengine. *Journal of Engineering for Gas Turbines and Power,* 127**,** 257-267.

Whitfield, C. A., Schroeder, R. P., Thole, K. A. & Lewis, S. D. 2015. Blockage effects from simulated thermal barrier coatings for cylindrical and shaped cooling holes. *Journal of Turbomachinery,* 137**,** 091004-091004 -10.

Zess, G. A. & Thole, K. A. 2002. Computational Design and Experimental Evaluation of Using a Leading Edge Fillet on a Gas Turbine Vane. *Journal of Turbomachinery*, 124**,** 167-175.

APPENDICES

Appendix A

Pressure Transducer Calibration

A total of nine differential transducers are used independently for data acquisition. Five transducers are connected with five-hole probe, two individual transducers are also connected with pitot-static tube, one is connected with the plenum box of the film-cooling to determine the inlet pressure of the cooling jet(s) and the last one is connected across the orifice plate to determine the flow rate. Each transducer is uniquely calibrated according to the manufacturers' specified pressure range. Setra Micro-Cal^{TM} calibrator is used to calibrate all the transducers one by one. It is capable of pressure range of 0 – 3500Pa with an accuracy of 1.42pa. The calibration equations are presented in Table D-1. These equations are used for all the data conversions from voltage to pressure after deducting the offset or no flow condition voltage.

Table A- 1: Pressure Transducer Calibration

S/N	Transducer Name	Pressure Rage (Pa)	Calibration Equation
1	Siemens SITRANS	0 – 496	$P1_{5H} = 106.18(v_1 - v_{1\text{-offset}}) - 6.140$
2	Omega PX653	0 - 1242	$P2_{5H} = 306.68(v_2 - v_{2\text{-offset}}) - 2.803$
3	Omega PX653	0 - 1242	$P3_{5H} = 308.96(v_3 - v_{3\text{-offset}}) - 4.516$
4	Omega PX653	0 - 1242	$P4_{5H} = 306.49(v_4 - v_{4\text{-offset}}) - 2.117$
5	Omega PX653	0 - 1242	$P5_{5H} = 308.31(v_5 - v_{5\text{-offset}}) - 2.584$
6	Omega PX2650	0 - 124	$P6_{tot} = 24.88(v_6 - v_{6\text{-offset}}) - 3.726$
7	Omega PX2650	0 - 496	$P7_{stat} = 98.094(v_7 - v_{7\text{-offset}}) - 0.765$
8	Omega PX2650	0 - 1242	$P8_{plm} = 165.82(v_8 - v_{8\text{-offset}}) - 4.803$
9	Omega PX164	0 - 1242	$P9_{orf} = 169.94(v_9 - v_{9\text{-offset}}) - 6.323$

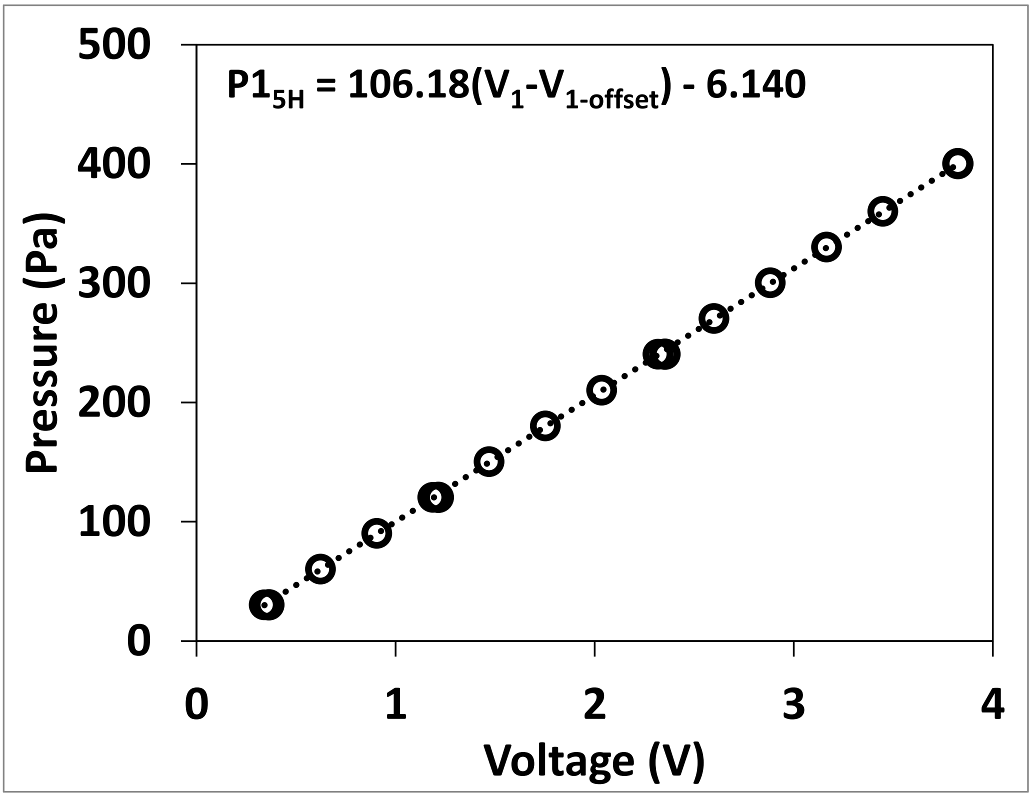

Figure A- 1: Siemens transducer calibration - Five hole probe port-1($P1_{5H}$)

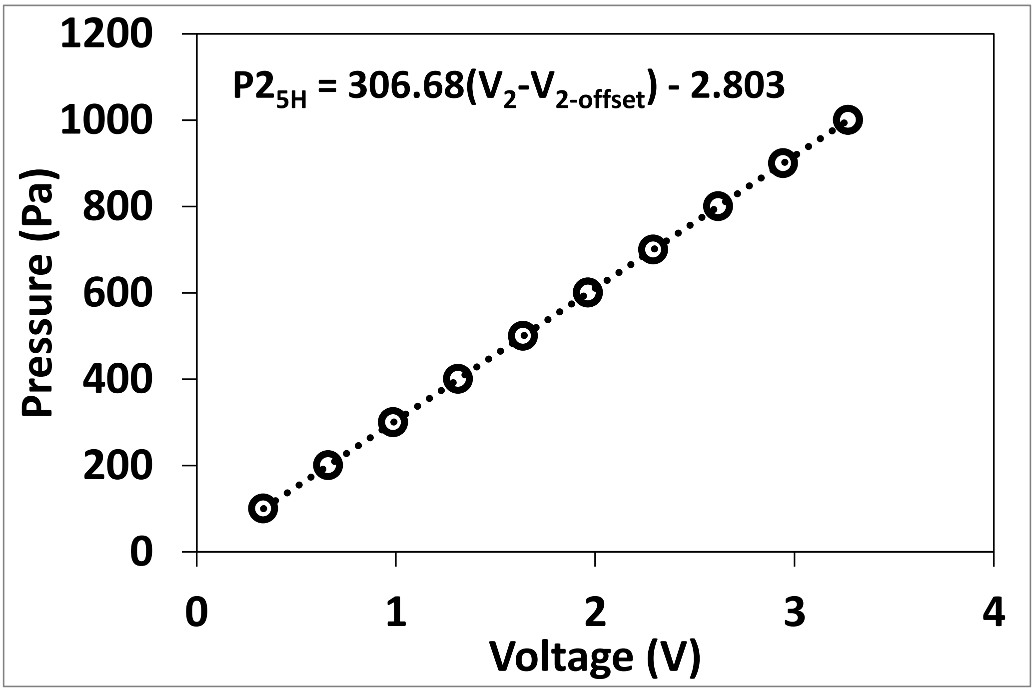

Figure A- 2: Omega PX653 transducer calibration - Five hole probe port-2($P2_{5H}$)

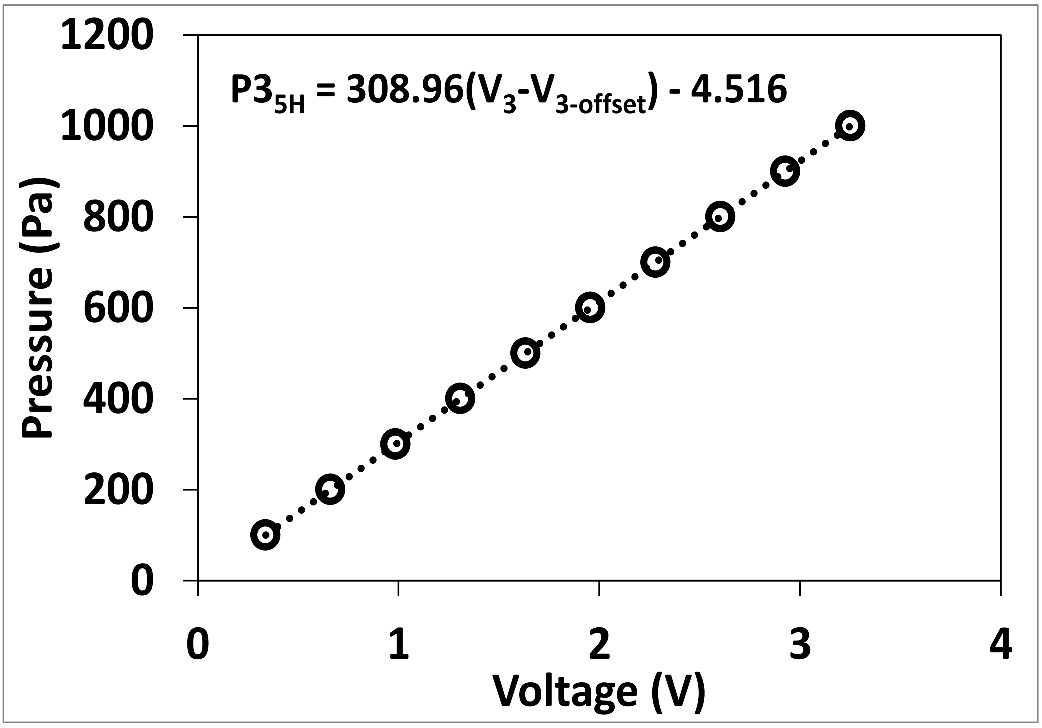

Figure A- 3: Omega PX653 transducer calibration - Five hole probe port-3($P3_{5H}$)

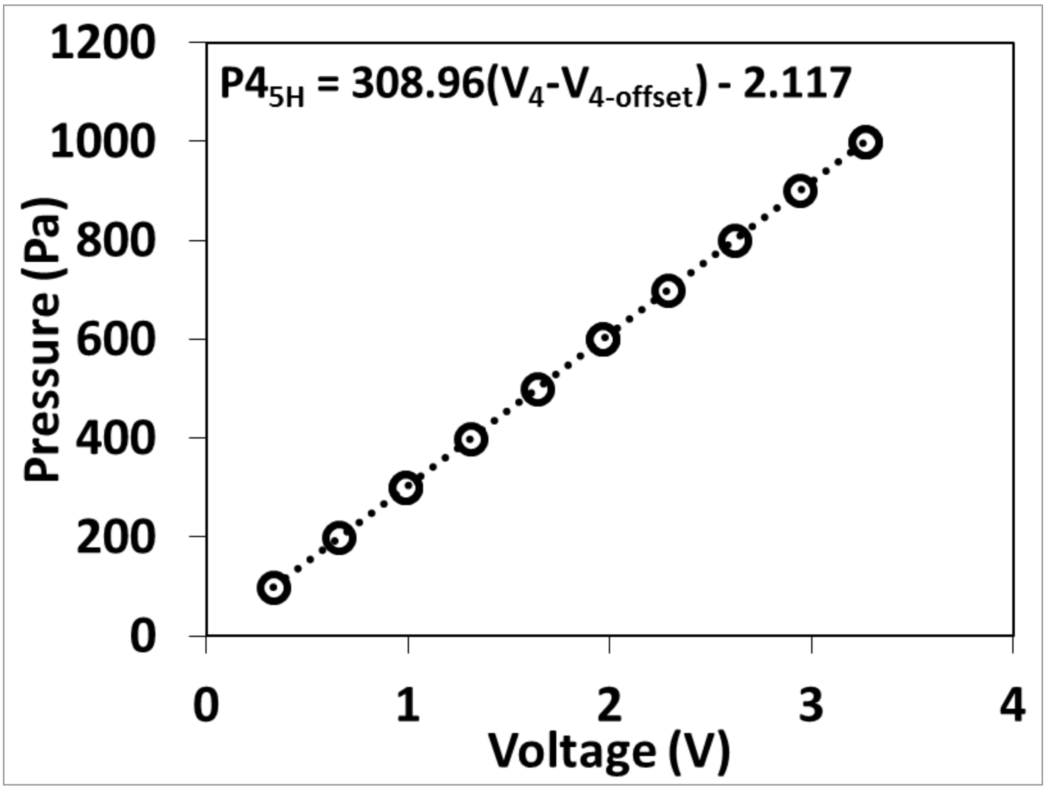

Figure A- 4: Omega PX653 transducer calibration - Five hole probe port-4($P4_{5H}$)

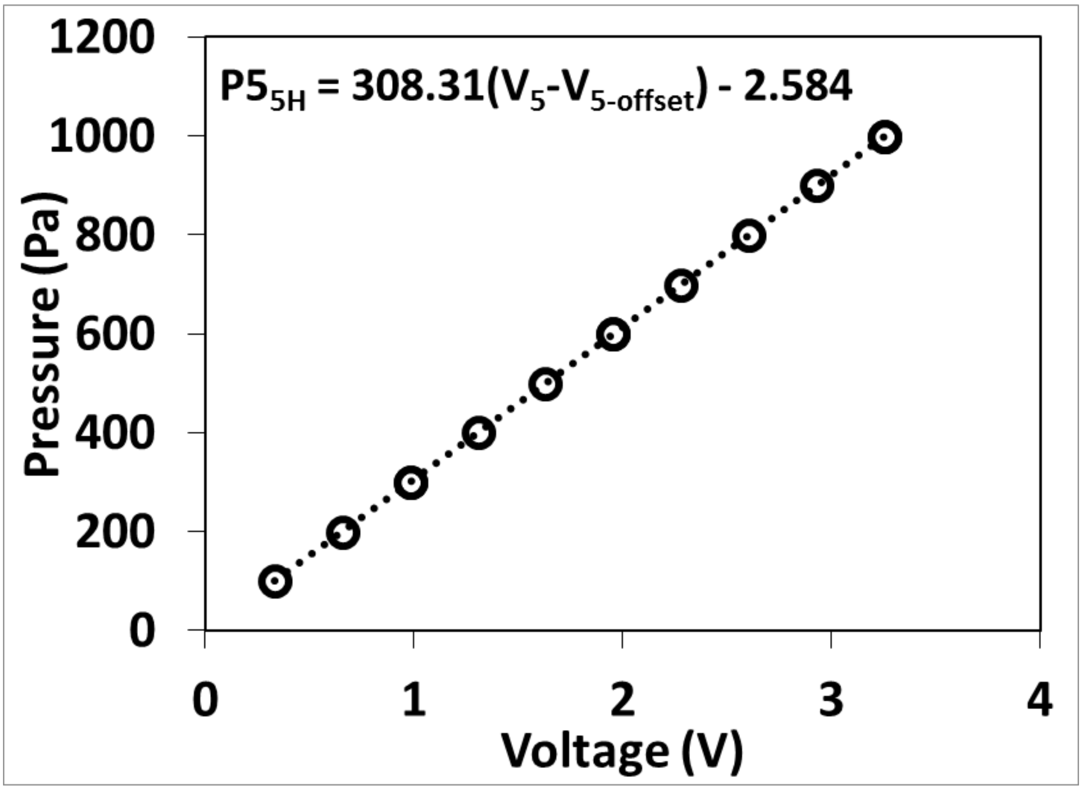

Figure A- 5: Omega PX653 transducer calibration – Five hole probe port-5(P5$_{5H}$)

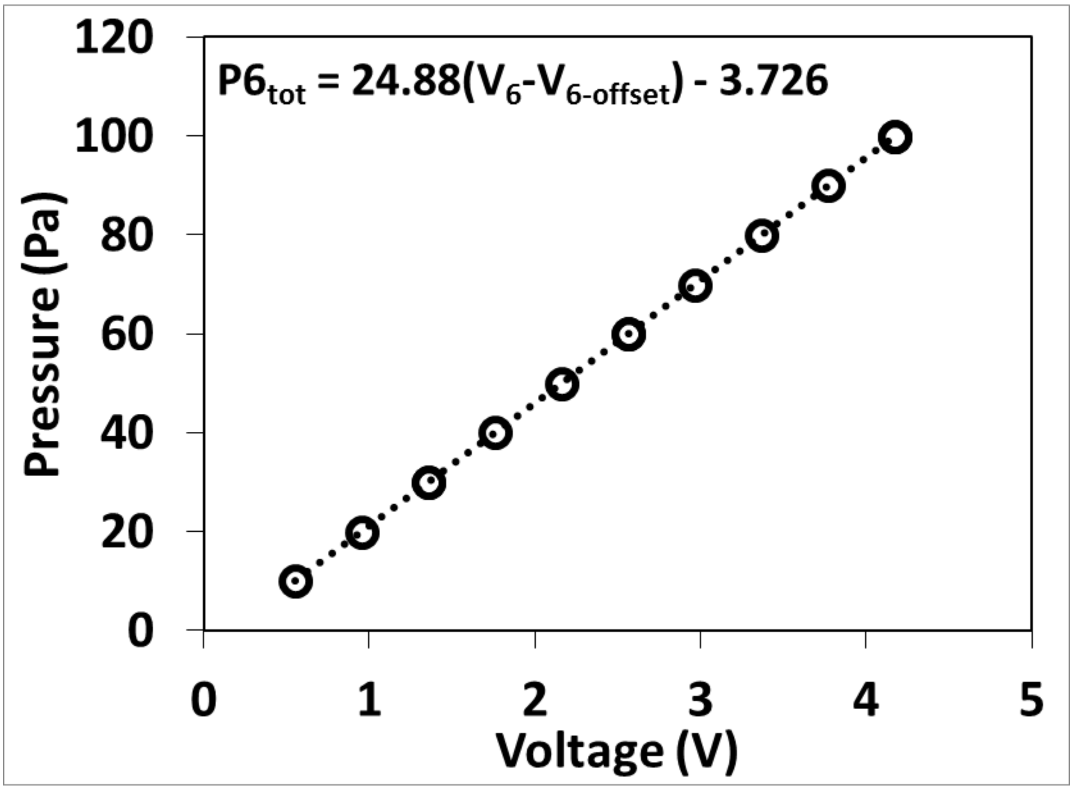

Figure A- 6: Omega PX2650 transducer calibration – Pitot probe (total)

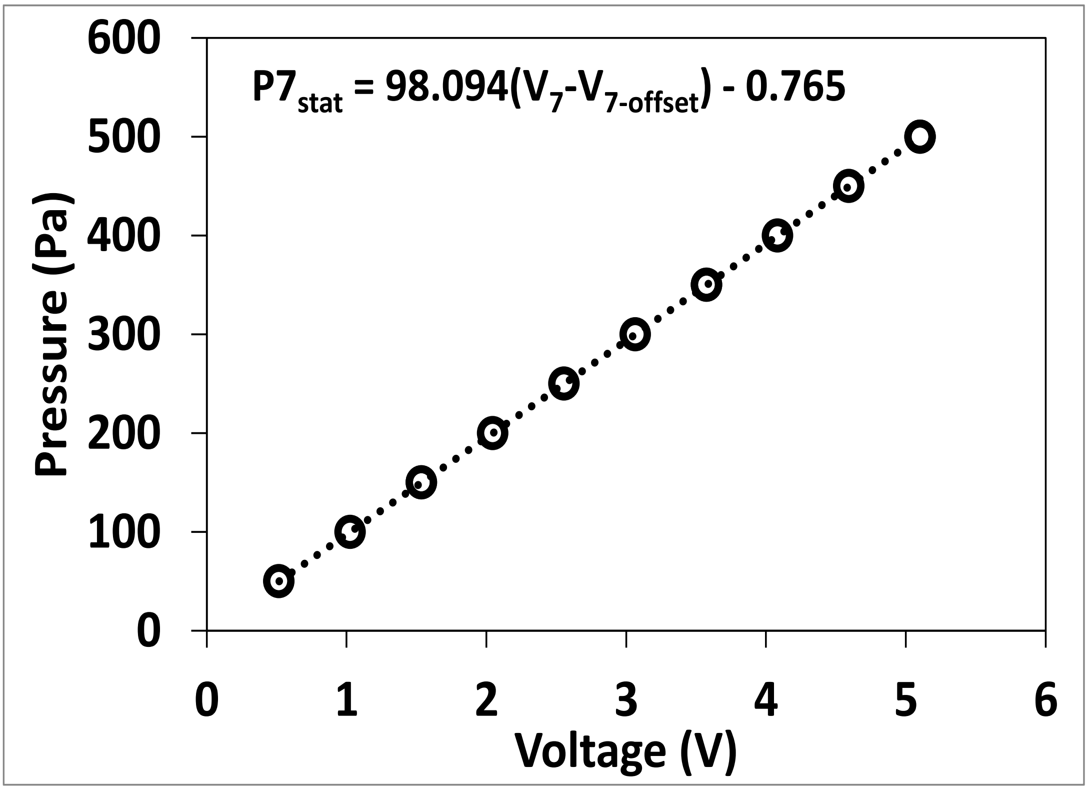

Figure A- 7: Omega PX2650 transducer calibration – Pitot probe (static)

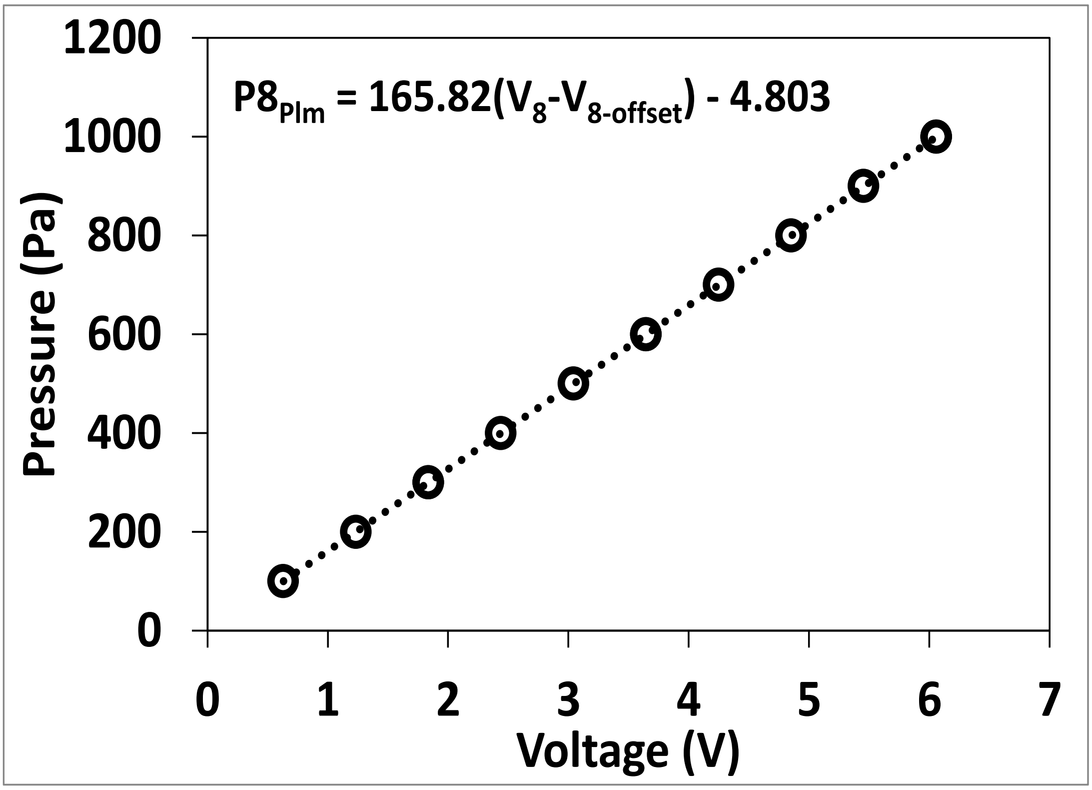

Figure A- 8: Omega PX2650 transducer calibration – Plenum box

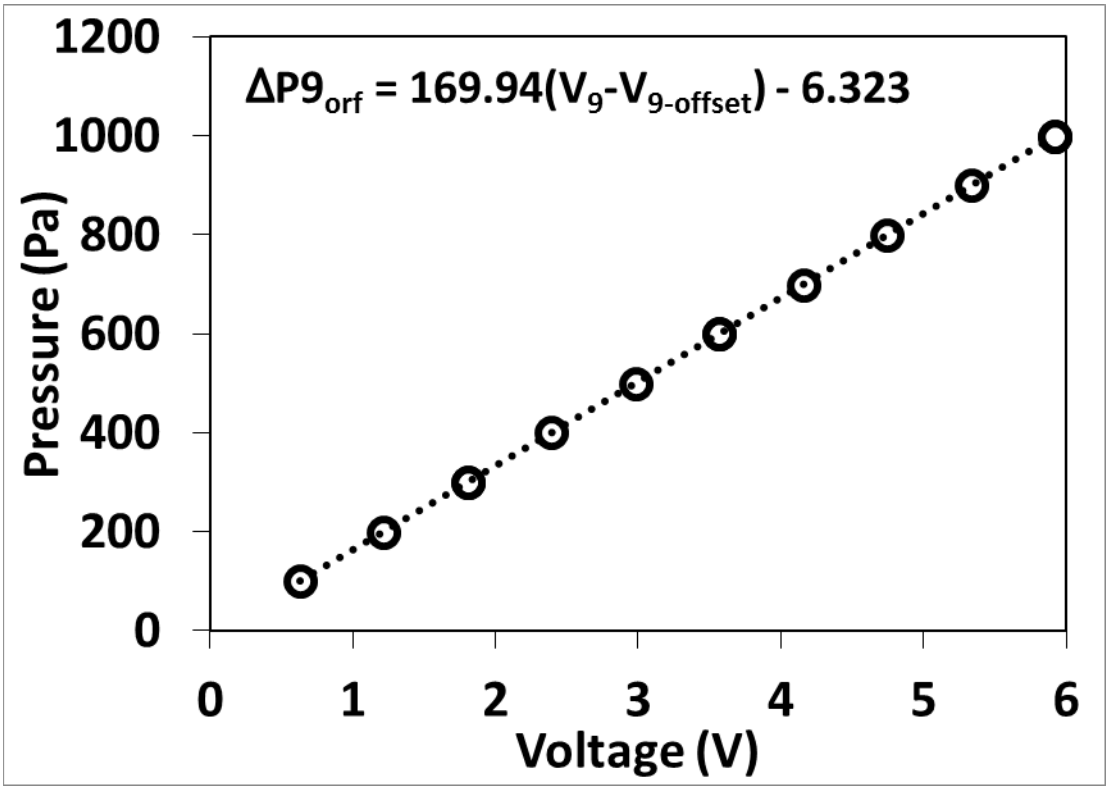

Figure A- 9: Omega PX164 transducer calibration – Orifice differential pressure

Appendix B

The five hole probe calibration was done at 9.8C_{ax} upstream of the leading edge of the cascade area where the free stream velocity is 10.7m/s. The yaw and the pitch traverses are fixed and the probe is mounted and secured on the traverse rig at zero yaw and zero pitch for probe pressure ports balancing. Thereafter, at a fixed yaw angle, the probe is manually rotated at an interval of 5° over a range of -30° to 30° for pitch angles. The yaw angle is also changed through 5° interval and the manual changing of the pitch is repeated until the whole -30° to 30° are exhausted. The calibrations (Figs. F-1 to F-5) conform with (Ligrani et al., 1989a).

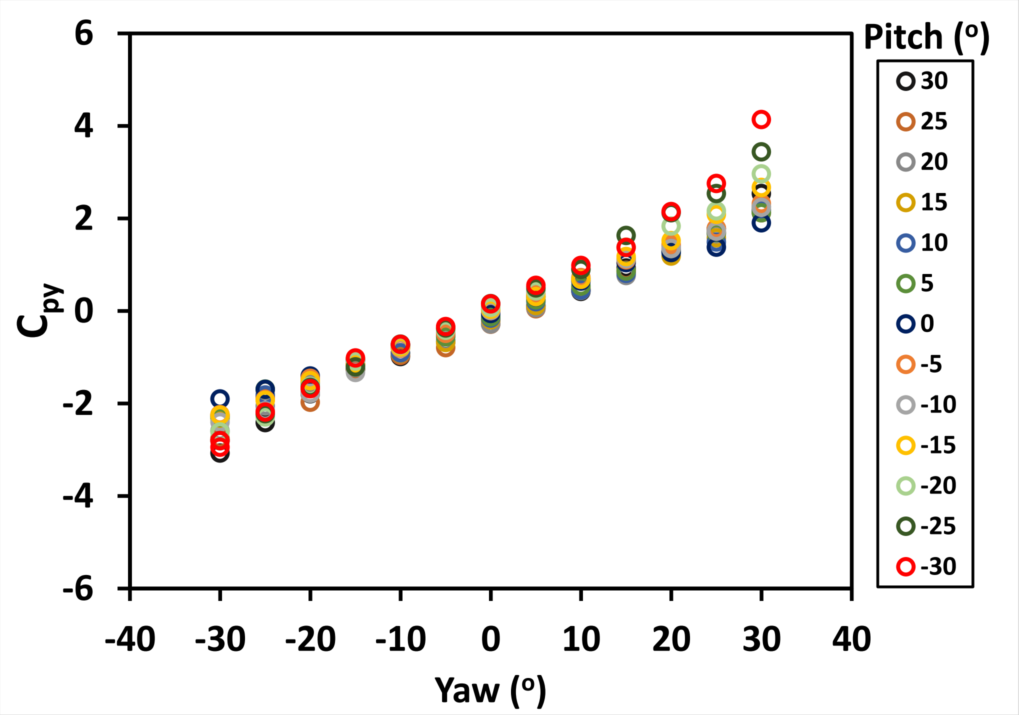

Figure B- 10: Coefficient C_{py} with yaw and pitch angles

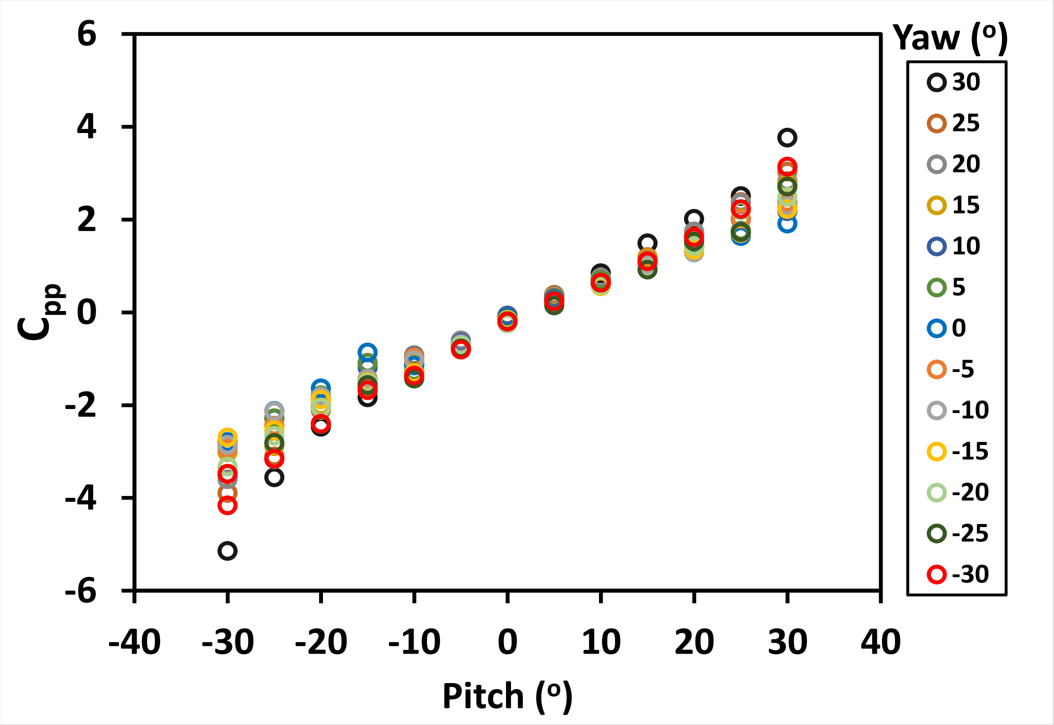

Figure B- 11: Coefficient C_{pp} with pitch and yaw angles

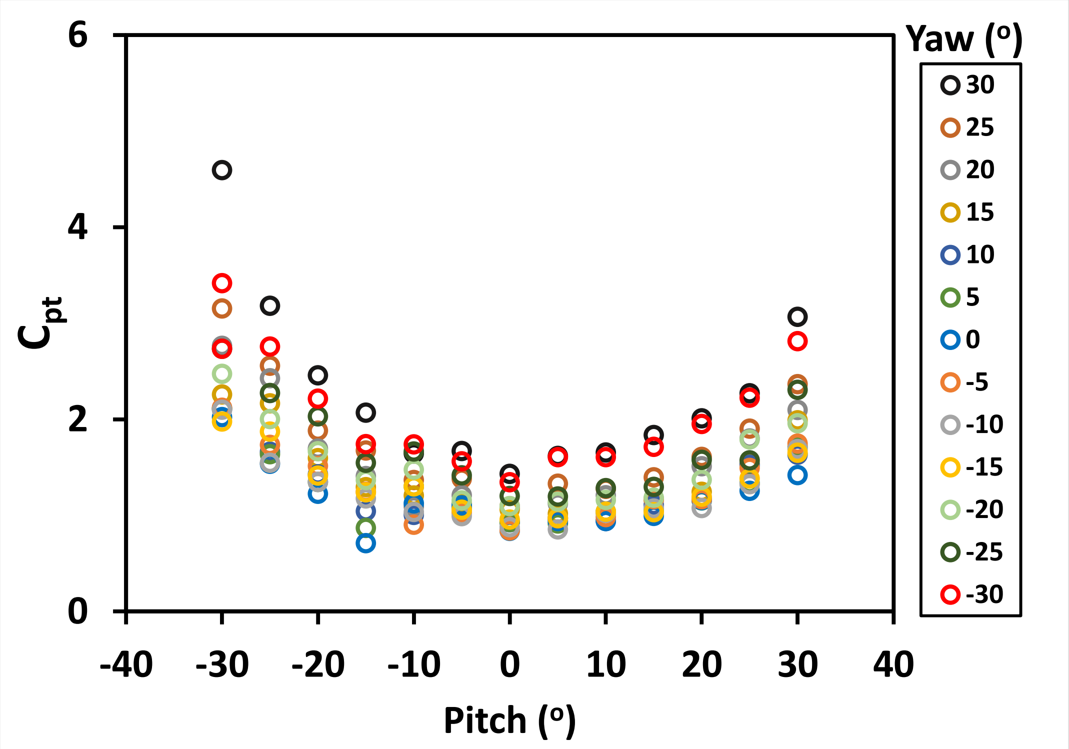

Figure B- 12: Coefficient C_{pt} with pitch and yaw angles

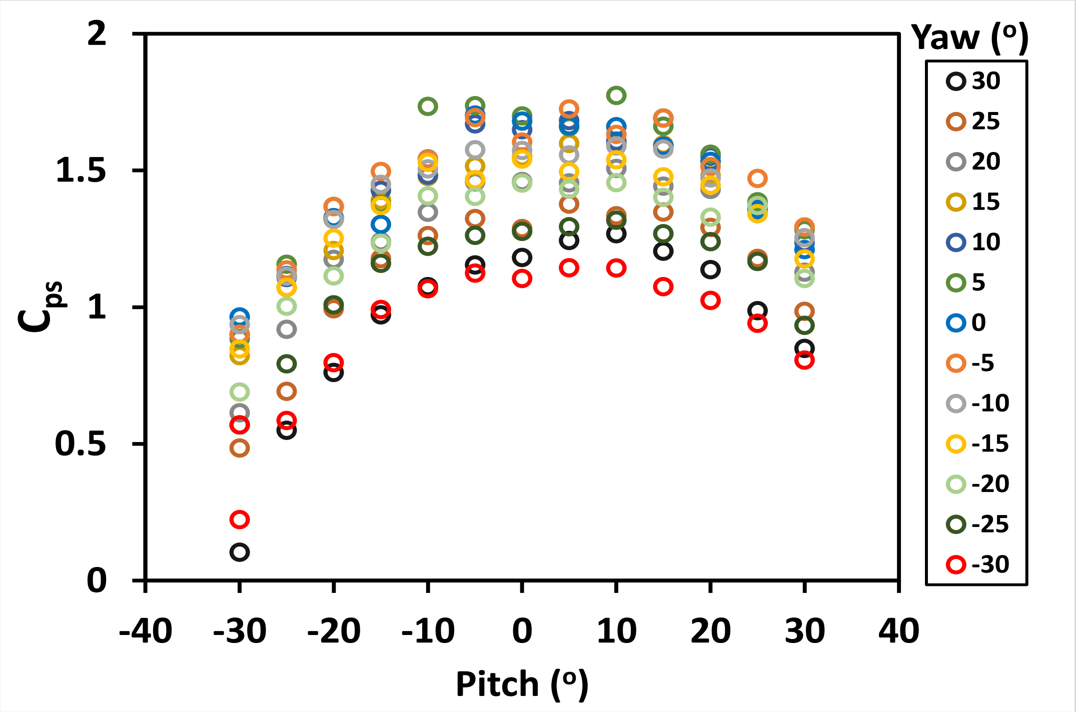

Figure B- 13: Coefficient C_{ps} with pitch and yaw angles

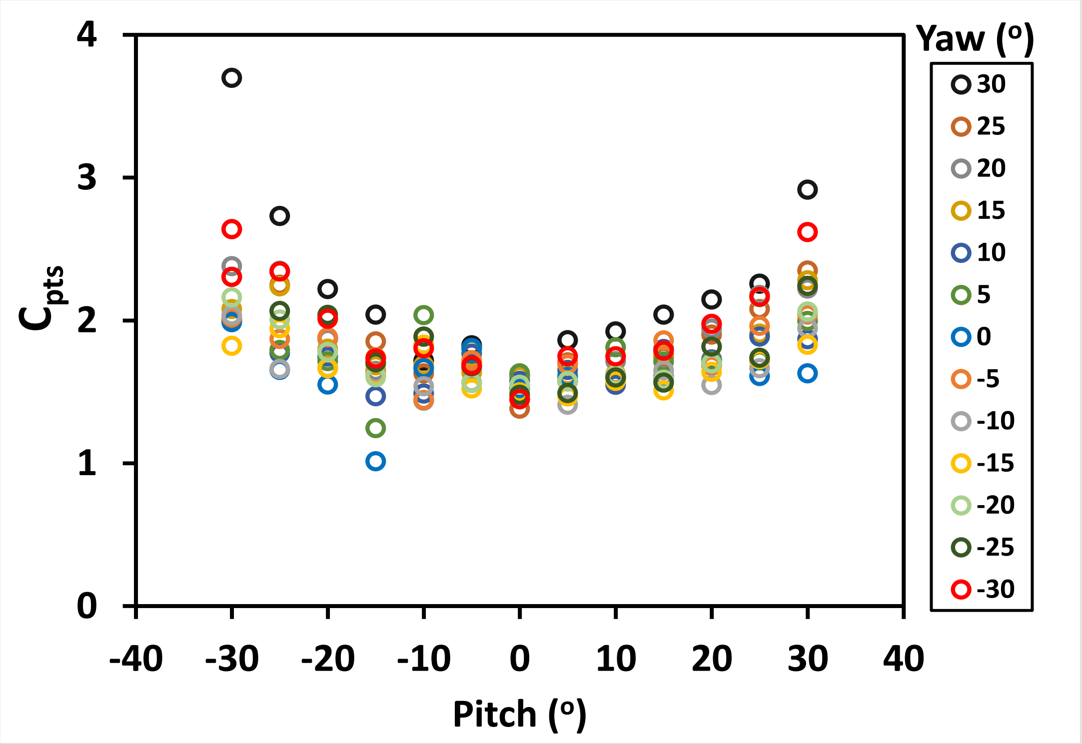

Figure B- 14: Coefficient C_{pts} with pitch and yaw angles

Appendix C

For Fillet-1:

$$y_{Fillet-1,\, a-b} = 0.2323x_{a-b}^{2} + 6.4887x_{a-b} + 11.384 \quad \text{(C-1)}$$

$$y_{Fillet-1,\, b-c} = 0.0005x_{b-c}^{4} + 0.035x_{b-c}^{3} + 0.9987x_{b-c}^{2} + 13.256x_{b-c} + 32.562 \quad \text{(C-2)}$$

$$y_{Fillet-1,\, c-d} = 0.0949x_{c-d}^{3} + 6.42x_{c-d}^{2} + 145.11x_{c-d} + 1130.1 \quad \text{(C-3)}$$

$$y_{Fillet-1,\, d-e} = -0.0514x_{d-e}^{4} - 4.8116x_{d-e}^{3} - 168.75x_{d-e}^{2} - 2628x_{d-e} - 315352 \quad \text{(C-4)}$$

$$y_{Fillet-1,\, e-f} = 0.0336x_{e-f}^{2} + 2.0558x_{e-f} + 4.9797 \quad \text{(C-5)}$$

$$y_{Fillet-1,\, f-g} = 0.0197x_{f-g}^{2} + 1.5481x_{f-g} + 0.4393 \quad \text{(C-6)}$$

For Fillet-2:

$$y_{Fillet-2,\, a-b} = 0.0017x_{a-b}^{3} + 0.184x_{a-b}^{2} + 4.72x_{a-b} + 1.0042 \quad \text{(C-7)}$$

$$y_{Fillet-2,\, b-c} = 0.0015x_{b-c}^{3} + 0.0965x_{b-c}^{2} + 2.8079x_{b-c} + 3.4434 \quad \text{(C-8)}$$

Appendix D

Uncertainty Estimation

Uncertainty or accuracy in the experimentation is a measure of dispersion of values from an acquired data and/or calculated results. It is thus a measure of reliability of experimental data set. A theoretical quantification of the experimental data are presented here. All variables and instrumentation that are involved are taken into consideration. There are two types of errors which are identifiable in experimental measurement. These are bias and precision accuracies. The bias accuracies is usually specified by the manufacturer of the instrumentation from its imperfection and calibration. Precision error is error due to measured data. The precision error is error due to measured data. The precision error is error due to measured data. The precision error is usually estimated within 95% confidence interval or probability of it occurrence. It is computed from the standard deviation of measured distribution of quantities. The overall precision uncertainty is calculated using Eqn. D-1 (Moffat, 1988).

$$\delta(\,) = \sqrt{B_i^2 + P_i^2} \qquad \text{(D-1)}$$

Where B_i is the bias and P_i is the precision error. Sensitivity describes how the estimate would be affected by a change in observation x_i . . . . . x_n. It is represented as the derivation of the result (R) given in Eqn. D-2.

$$\delta R_{x_i} = \frac{\partial R}{\partial x_i}\delta x_i \qquad \text{(D-2)}$$

Therefore, the overall uncertainty in a measurement is given as root sum square by Eqn, D-3

$$\delta R = \sqrt{\left(\frac{\partial R}{\partial x_1}\delta x_1\right)^2 + \left(\frac{\partial R}{\partial x_2}\delta x_2\right)^2 + \cdots\cdots + \left(\frac{\partial R}{\partial x_n}\delta x_n\right)^2} \qquad \text{(D-3)}$$

The actual uncertainty is expressed as a percentage (%) of the average of the observation. These incompleteness in experimental data and the use of instruments for measurement are expressed as uncertainties.

The uncertainties for the linear calibration of all the transducers used are presented in Table D-1.

Table D- 2: Uncertainties of Pressure transducers (Arnachellan, 2017)

S/N	Transducer Name	Bias Error (Pa)	Precision Error (Pa)	Overall Uncertainty (Pa)	Overall Uncertainty (%)
1	Siemens SITRANS	1.0	2.67	3.18	1.83
2	Omega PX653	3.105	1.08	3.58	0.78
3	Omega PX653	3.105	1.69	3.812	0.83
4	Omega PX653	3.105	0.867	3.523	0.79
5	Omega PX653	3.105	0.66	3.47	0.76
6	Omega PX2650	0.31	1.279	1.936	4.23
7	Omega PX2650	1.24	0.506	1.953	1.05
8	Omega PX2650	3.1	2.57	3.93	0.75
9	Omega PX2650	3.0	4.77	5.81	1.04

Reference Velocity Uncertainty

$$2\Delta P_{ref} = \rho_{air} U_{ref}^2 \tag{D-4}$$

$$U_{ref} = \left(\frac{2\left(P_{t,ref} - P_{s,ref}\right)}{\rho_{air}} \right)^{0.5} \tag{D-5}$$

Bias error (from the manufacturer) from total pressure transducer is 1.936Pa. The overall uncertainty for U$_{ref}$ is the summation of uncertainty from the total static pressure from reference.

$$\delta U_{ref} = \sqrt{\left(\delta P_{t,ref} \frac{\partial U_{ref}}{\partial P_{t,ref}} \right)^2 + \left(\delta P_{s,ref} \frac{\partial U_{ref}}{\partial P_{t,ref}} \right)^2}$$

And

i) $$\frac{\partial U_{ref}}{\partial U_{t,ref}} = \frac{\sqrt{2}}{2} \left(\frac{1}{\rho_{air} (P_{t,ref} - P_{s,ref})} \right)^{0.5}$$

ii) $$\frac{\partial U_{ref}}{\partial U_{t,ref}} = \frac{-\sqrt{2}}{2}\left(\frac{1}{\rho_{air}(P_{t,ref} - P_{s,ref})}\right)^{0.5}$$

Standard deviation for thirty data points is 0.208165, at $t_{v,95\%}$ = 2.045, P_{atm} @ 654mmHg = 86990.8Pa, ρ = 1.005kg/m^3 and T = 273.15K.

$$\delta P_{t,ref} = \sqrt{B^2_{t,ref\,(B)} + P^2_{t,ref\,(P)}}$$

$$\delta P_{t,ref} = \sqrt{1.936^2 + 0.426^2}$$

$$\delta P_{t,ref} \mp 1.982 Pa$$

This is the uncertainty for $\overline{P_{t,ref}} = 20.54Pa$.

Similarly, for static pressure,

$$\delta P_{s,ref} \mp 2.244 Pa$$

This is the uncertainty for $\overline{P_{s,ref}} = 77.05Pa$

Therefore,

$$\frac{\partial U_{ref}}{\partial U_{t,ref}} = \frac{\sqrt{2}}{2}\left(\frac{1}{1.005(77.05 - 20.54)}\right)^{0.5} = 0.012445$$

Also, $$\frac{\partial U_{ref}}{\partial U_{t,ref}} = \frac{-\sqrt{2}}{2}\left(\frac{1}{1.005(77.05 - 20.54)}\right)^{0.5} = 2.14732$$

$$\delta U_{ref} = \mp 0.27$$

$$\%\,\delta U_{ref} = \frac{0.27}{10.7} * 100 = 2.61\%$$

This is the uncertainty (2.61%) for average reference velocity of 10.7m/s.

Coefficient of Static Pressure Uncertainty

$$C_{p,static} = \frac{\left(p_{s,ref} - p_{e,x}\right)}{0.5\rho_{air} U^2} = \frac{P_{s,ref} - P_{loc}}{P_{s,ref} - P_{t,ref}}$$

The overall uncertainty for the static pressure is given by:

$$\delta C_{p,s} = \sqrt{\left(\delta P_{s,ref}\frac{\partial C_{p,s}}{\partial P_{s,ref}}\right)^2 + \left(\delta P_{t,ref}\frac{\partial C_{p,s}}{\partial P_{t,ref}}\right)^2 + \left(\delta P_{loc}\frac{\partial C_{p,s}}{\partial P_{loc}}\right)^2}$$

i) $\frac{\partial C_{p,s}}{\partial P_{s,ref}} = \frac{(P_{s,ref} - P_{t,ref}) + (P_{loc} - P_{s,ref})}{(P_{s,ref} - P_{t,ref})^2}$

ii) $\frac{\partial C_{p,s}}{\partial P_{t,ref}} = \frac{(P_{s,ref} - P_{loc})}{(P_{s,ref} - P_{t,ref})^2}$

iii) $\frac{\partial C_{p,s}}{\partial P_{t,ref}} = \frac{1}{(P_{t,ref} - P_{s,ref})}$

$$\frac{\partial C_{p,s}}{\partial P_{s,ref}} = \frac{(61.228-18.54)+(481.56-18.54)}{(61.228-18.84)^2} = 0.254$$

$$\frac{\partial C_{p,s}}{\partial P_{t,ref}} = \frac{(61.22-481.56)}{(61.228-18.54)^2} = -0.2306$$

$$\frac{\partial C_{p,s}}{\partial P_{t,ref}} = \frac{1}{(18.54-61.228)} - 0.0234 =$$

$$\delta C_{p,s} = \sqrt{(1.408 * 0.254)^2 + (-0.2306 * 0.5799)^2 + (3.7909 * -0.0234)^2}$$

$$\delta C_{p,s} = 0.3921$$

For nominal value of $C_{p,s}$ = 9.879Pa,

$$\%\delta C_{p,s} = 3.969\%$$

This is the overall uncertainty for the $C_{p,s}$ data.

Blowing Ratio Uncertainty

$$M = \left(\frac{P_{plm} - P_{s,ref}}{P_{t,ref} - P_{s,ref}}\right)^{\frac{1}{2}} = \left(\frac{P_{plm} + P_{s,ref}}{P_{s,ref} - P_{t,ref}}\right)^{0.5}$$

Global uncertainty for the blowing ratio of say M=2.8 is computed by:

$$\delta M = \sqrt{\left(\delta P_{s,ref}\frac{\partial M}{\partial P_{s,ref}}\right)^2 + \left(\delta P_{t,ref}\frac{\partial M}{\partial P_{t,ref}}\right)^2 + \left(\delta P_{loc}\frac{\partial M}{\partial P_{loc}}\right)^2}$$

i) $$\frac{\partial M}{\partial P_{s,ref}} = \frac{\left(\frac{1}{P_{s,ref} - P_{t,ref}}\right) - \left(\frac{P_{plm} - P_{s,ref}}{P\left(_{s,ref} - P_{t,ref}\right)^2}\right)}{2\left(\frac{P_{plm} - P_{s,ref}}{P_{s,ref} - P_{t,ref}}\right)^{0.5}}$$

ii) $$\frac{\partial M}{\partial P_{t,ref}} = \frac{\left(P_{plm} - P_{s,ref}\right)}{2\sqrt{\left(\frac{P_{plm} + P_{s,ref}}{P_{s,ref} - P_{t,ref}}\right)}\left(P_{s,ref} - P_{t,ref}\right)^2}$$

iii) $$\frac{\partial M}{\partial P_{t,ref}} = 2^{-1}\left[\left(P_{plm} - P_{s,ref}\right)\left(P_{s,ref} - P_{t,ref}\right)\right]^{-0.5}$$

$$\frac{\partial M}{\partial P_{s,ref}} = 0.0287$$

$$\frac{\partial M}{\partial P_{t,ref}} = 0.02361$$

$$\frac{\partial M}{\partial P_{plm}} = 0.003316$$

The overall uncertainty for M = 2.8 blowing ratio for slot film cooling with all the slots opened without fillet is given by

$$\delta M = \left((2.2244 * 0.0287)^2 + (1.98225 * 0.023611)^2 + (3.2463 * 0.003316)^2\right)^{0.5}$$
$$\delta M = 0.1305$$

For $\overline{M} = 2.8$ average value,

$$\% \delta M = 0.0466 * 100 = 4.66\%$$

Film cooling Flow Rate Uncertainty

The flow rate is computed using the notation with a β = 0.7 and coefficient of discharge, C_d of 0.6:

$$\dot{m}_{cool} = \rho C_d \left(\frac{\Pi}{4} D^2_{orifice}\right)\left(\frac{2\Delta P_{orifice}}{\rho\left(1 - \beta^4\right)}\right)^{0.5}$$

$$\delta \dot{m}_{cool} = \sqrt{\left(\delta \Delta P_{orifice} \frac{\partial \dot{M}_{cool}}{\partial \Delta P_{orifice}} \right)^2}$$

$$\frac{\partial \dot{m}_{cool}}{\partial \Delta P_{orifice}} = 2^{-1} \rho C_d \left(\frac{\pi}{4} D_{orifice}^2 \right) \left(\frac{2}{\rho\left(1-\beta^4\right)} \right)^{0.5} \left(\Delta P_{orifice} \right)^{-\frac{1}{2}}$$

$$\frac{\partial \dot{m}_{cool}}{\partial \Delta P_{orifice}} = 0.000733$$

The overall uncertainty for the film cooling is given by:

$$\delta \dot{m}_{cool} = \sqrt{(0.000733 * 3.6886)^2}$$

For nominal value of the film cooling flow value $\overline{\dot{m}_{cool}} = 0.072682 kg/s$ average value,

$$\%\delta \dot{m}_{cool} = \frac{0.002703}{0.072682} * 100 = 3.718\%$$

Therefore, 3.718% is the overall uncertainty for the film cooling flow of 0.072682kg/s.

Coefficient of Total Pressure Uncertainty

$C_{pt,loss} = \dfrac{\left(p_{t,ref} - p_{t,x}\right)}{0.5 \rho_{air} U_{ref}^2} = \dfrac{P_{t,ref} - P_{t,5-hole}}{P_{t,ref} - P_{s,ref}} \equiv \dfrac{P_{t,5-hole} - P_{t,ref}}{P_{s,ref} - P_{t,ref}}$ (Negative due to suction test section)

$$\delta C_{pt,loss} = \left(\left(\delta P_{s,ref} \frac{\partial C_{pt,olss}}{\partial P_{s,ref}} \right)^2 + \left(\delta P_{t,ref} \frac{\partial C_{pt,loss}}{\partial P_{t,ref}} \right)^2 + \left(\delta P_{t,5-hole} \frac{\partial C_{pt,loss}}{\partial P_{t,5-hole}} \right) \right)^{0.5}$$

i) $\dfrac{\partial C_{pt,loss}}{\partial P_{s,ref}} = \left(P_{t,ref} - P_{t,5-hole}\right)\left(P_{s,ref} - P_{t,ref}\right)^{-2}$

ii) $\dfrac{\partial C_{pt,loss}}{\partial P_{t,ref}} = -\left(\left(P_{s,ref} - P_{t,ref}\right)^{-1} + \dfrac{\left(P_{t,ref} - P_{t,5-hole}\right)}{\left(P_{s,ref} - P_{t,ref}\right)^2} \right)$

iii) $\dfrac{\partial C_{pt,loss}}{\partial P_{s,ref}} = \left(P_{s,ref} - P_{t,ref}\right)^{-1}$

$$\frac{\partial C_{pt,loss}}{\partial P_{s,ref}} = \text{-}0.01421$$

$$\frac{\partial C_{pt,loss}}{\partial P_{t,ref}} = -0.00349$$

$$\frac{\partial C_{pt,loss}}{\partial P_{s,ref}} = 0.017696$$

$\overline{P_{t,5-hole}} = 58.82Pa$ $\quad \overline{P_{t,ref}} = 20.562Pa$ $\quad \overline{P_{s,ref}} = 76.68Pa$

$\delta P_{t,5-hole} = \pm 2.338$ $\quad \delta P_{t,ref} = \pm 1.982$ $\quad \delta P_{s,ref} = \pm 2.4164$

$\delta C_{pt,loss} = \pm 0.04997$

$\%\delta C_{pt,loss} = 7.3\%$

For norminal value of the Cpt,loss = 0.682, the uncertainty is 7.3%.

Turbulent Intensity Uncertainty (Tu)

$$Tu = U_{rms} \bullet U_{ref}^{-1}$$

$$\delta Tu = \left(\left(\delta U_{rms} \frac{\partial Tu}{\partial U_{rms}} \right)^2 + \left(\delta U_{ref} \frac{\partial Tu}{\partial U_{ref}} \right)^2 \right)^{0.5}$$

i) $\frac{\partial Tu}{\partial U_{rms}} = \mathrm{U}_{ref}^{-1}$

ii) $\frac{\partial Tu}{\partial U_{ref}} = -U * \mathrm{U}_{ref}^{-2}$

$$\frac{\partial Tu}{\partial U_{rms}} = \mathrm{U}_{ref}^{-1} = 0.088261$$

$$\frac{\partial Tu}{\partial U_{ref}} = 0.002323$$

$\overline{U_{ref}} = 11.36m/s$ $\quad \overline{U_{rms}} = 0.3m/s$

$\delta U_{ref} = 0.116023m/s$ $\quad \delta U_{rms} = 0.014m/s$

$$\delta Tu = \left((0.014 * 0.08826)^2 + (0.116 * 0.002323)^2 \right)^{0.5}$$

$$\delta Tu = \pm 0.00126$$

For nominal value of $Tu = \frac{0.3}{11.36} = 0.026$

$$\%\delta Tu = \frac{0.00126}{0.026} * 100 = 4.8\%$$

Non-dimensional temperature Uncertainty

$$\theta = \frac{T_{loc} - T_{plm}}{T_{ref} - T_{plm}}$$

Global uncertainty for the Non-dimensional temperature is computed by:

$$\delta\theta = \sqrt{\left(\delta T_{ref} \frac{\partial\theta}{\partial T_{ref}}\right)^2 + \left(\delta T_{plm} \frac{\partial\theta}{\partial T_{plm}}\right)^2 + \left(\delta T_{loc} \frac{\partial\theta}{\partial T_{loc}}\right)^2}$$

i) $\frac{\partial\theta}{\partial T_{ref}} = \left(T_{plm} - T_{loc}\right)\left(T_{ref} - T_{plm}\right)^{-2}$

ii) $\frac{\partial\theta}{\partial T_{plm}} = -\left[\left(T_{ref} - T_{plm}\right)^{-1} + \frac{\left(T_{plm} - T_{loc}\right)}{\left(T_{ref} - T_{plm}\right)^2}\right]$

iii) $\frac{\partial\theta}{\partial T_{loc}} = \left(T_{ref} - T_{plm}\right)^{-1}$

$\overline{T_{loc}} = 19.83^o C$ $\overline{T_{plm}} = 16.1^o C$ $\overline{T_{ref}} = 21.19^o C$

$\delta T_{loc} = \pm 0.64$ $\delta T_{plm} = \pm 0.097$ $\delta T_{ref} = \pm 0.077$

$$\delta\theta = \left(\left(0.0768 * -0.145\right)^2 + \left(0.097 * -0.0544\right)^2 + \left(0.264 * 0.199\right)^2\right)^{0.5}$$

$$\delta\theta = \pm 0.0542$$

For nominal non-dimensional temperature (ϴ) value of 0.7028,

$$\%\delta\theta = \frac{0.0542}{0.7028} * 100 = 7.15\%$$

Endwall Adiabatic Effectiveness Uncertainty

$$\eta = \frac{T_{ref} - T_{ew}}{T_{ref} - T_{cool}}$$

Overall uncertainty for the Non-dimensional temperature is computed by:

$$\delta\eta = \sqrt{\left(\delta T_{ref} \frac{\partial\eta}{\partial T_{ref}}\right)^2 + \left(\delta T_{ew} \frac{\partial\eta}{\partial T_{ew}}\right)^2 + \left(\delta T_{cool} \frac{\partial\eta}{\partial T_{cool}}\right)^2}$$

i) $\dfrac{\partial \eta}{\partial T_{ref}} = \dfrac{(T_{ew} - T_{cool})}{(T_{ref} - T_{cool})^2}$

ii) $\dfrac{\partial \eta}{\partial T_{ew}} = \dfrac{(T_{cool} - T_{ref})}{(T_{ref} - T_{cool})^2}$

iii) $\dfrac{\partial \eta}{\partial T_{cool}} = \dfrac{(T_{ref} - T_{ew})}{(T_{ref} - T_{cool})^2}$

$\overline{T_{ref}} = 20.858^oC$ $\overline{T_{ew}} = 10.58^oC$ $\overline{T_{cool}} = 3.9^oC$

$\delta T_{ref} = \pm 0.1420$ $\delta T_{plm} = \pm 0.4237$ $\delta T_{cool} = \pm 0.1437$

$$\delta\eta = \left((0.142 * -0.023347)^2 + (0.4237 * -0.059)^2 + (0.1437 * 0.03567)^2\right)^{0.5}$$

$$\delta\eta = \pm 0.02574$$

For nominal value of η = 0.6066,

$$\%\delta\eta = 4.2\%$$

Endwall Nusselt Number Uncertainty

$$Q_{cond} = \frac{k_{ins} A_{pass} (T_{av1} - T_{av2})}{\Delta_{th}} = \frac{0.037 * 0.054 (T_{av2} - T_{av1})}{0.025}$$

$$Q_{conv} = IV - Q_{cond}$$

$$q_{flux} = \frac{Q_{conv}}{A_{heater}} = \frac{Q_{conv}}{0.054}$$

$$Nu = \frac{q_{flux} * 0.3545}{(T_{wall} - T_{ref}) * 0.026}$$

And $Q_{conv} = 8.9 * 23.9 - Q_{cond}$

$$Nu = \frac{53707.698 - 20.179 (T_{av2} - T_{av1})}{(T_{wall} - T_{ref})}$$

$$Nu = \frac{53707.698}{(T_{wall} - T_{ref})} - \frac{20.179 (T_{av2} - T_{av1})}{(T_{wall} - T_{ref})}$$

$$\delta Nu = \sqrt{\left(\delta T_{av1} \frac{\partial Nu}{\partial T_{av1}}\right)^2 + \left(\delta T_{av2} \frac{\partial Nu}{\partial T_{av2}}\right)^2 + \left(\delta T_{wall} \frac{\partial Nu}{\partial T_{wall}}\right)^2 + \left(\delta T_{wall} \frac{\partial Nu}{\partial T_{wall}}\right)^2}$$

i) $\dfrac{\partial Nu}{\partial T_{av2}} = \dfrac{-20.179}{\left(T_{wall} - T_{ref}\right)} = -0.74082$

ii) $\dfrac{\partial Nu}{\partial T_{av1}} = \dfrac{20.179}{\left(T_{wall} - T_{ref}\right)} = 0.74082$

iii) $\dfrac{\partial Nu}{\partial T_{wall}} = \dfrac{-53707.698}{\left(T_{wall} - T_{ref}\right)^2} + \dfrac{20.179\left(T_{av2} - T_{avi}\right)}{\left(T_{wall} - T_{ref}\right)^2} = -72.6928$

iv) $\dfrac{\partial Nu}{\partial T_{ref}} = \dfrac{53707.698}{\left(T_{wall} - T_{ref}\right)^2} - \dfrac{20.179\left(T_{av2} - T_{avi}\right)}{\left(T_{wall} - T_{ref}\right)^2} = 71.6928$

$\overline{T_{wall}} = 59.975^o C$ $\overline{T_{av1}} = 29.503^o C$ $\overline{T_{av2}} = 58.015^o C$ $\overline{T_{ref}} = 28^o C$

$\delta T_{wall} = \pm 0.22518$ $\delta T_{av1} = \pm 0.5823$ $\delta T_{av2} = \pm 1.05699$ $\delta T_{ref} = \pm 0.27368$

$$\delta Nu = \sqrt{(-0.7408 * 0.5823)^2 + (0.7408 * 1.05699)^2 + (-71.6928 * 0.225175)^2 + (71.6928 * 0.2737)^2}$$

$\delta Nu = 25.4239$

For nominal value of Nusselt Number = 2,363.666

Therefore, $\%\delta Nu = 1.068\%$

This is the uncertainty of 2,363.666 of Nu.

Appendix E

The second order gradient flux *G_f* is given by Eqn. (C-1) with δV_j^n as the swept volume for each cell face. The second order transient term is dropped out due to the steady-state. Eqns. (C-2)-(C-5) provide the second-order upwind scheme of discretization of the convective term. The terms $(\nabla\phi)_{r,0}$ and $(\nabla\phi)_{r,1}$ are the gradients in cell 0 and 1(CD-adapco, 2013).

$$G_f = \frac{(3\delta V_j^n - \delta V_j^{n-1})}{2\Delta t} \tag{E-1}$$

$$[\rho\phi(v.a - G)]_f = \begin{cases} \dot{m}_f \phi_{f,0} & for\ \dot{m}_f \geq 0 \\ \dot{m}_f \phi_{f,1} & for\ \dot{m}_f < 0 \end{cases} \tag{E-2}$$

$$\phi_{f,0} = \phi_0 + s_0 .(\nabla\phi)_{r,0} \tag{E-2}$$

$$\phi_{f,1} = \phi_0 + s_1 .(\nabla\phi)_{r,1} \tag{E-3}$$

$$s_0 = x_f - x_0 \tag{E-4}$$

$$s_1 = x_f - x_1 \tag{E-5}$$

Appendix F

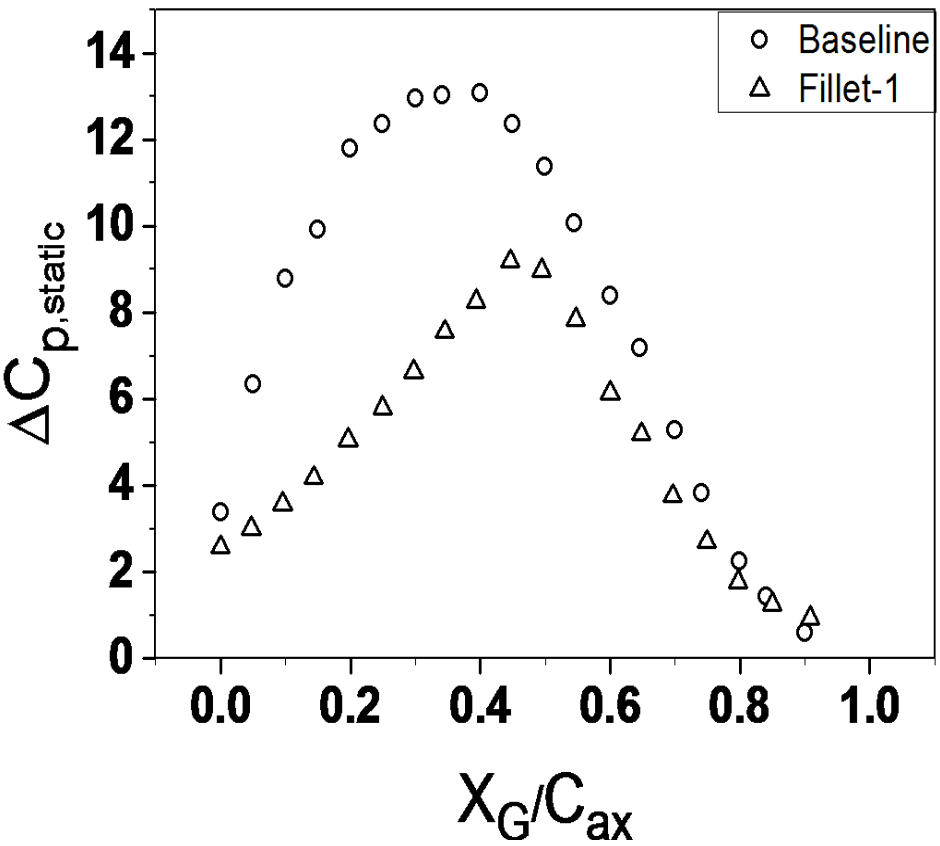

Figure F- 15: $\Delta C_{p,static}$ pitchwise difference for Baseline and Fillet-1 computations

Appendix G

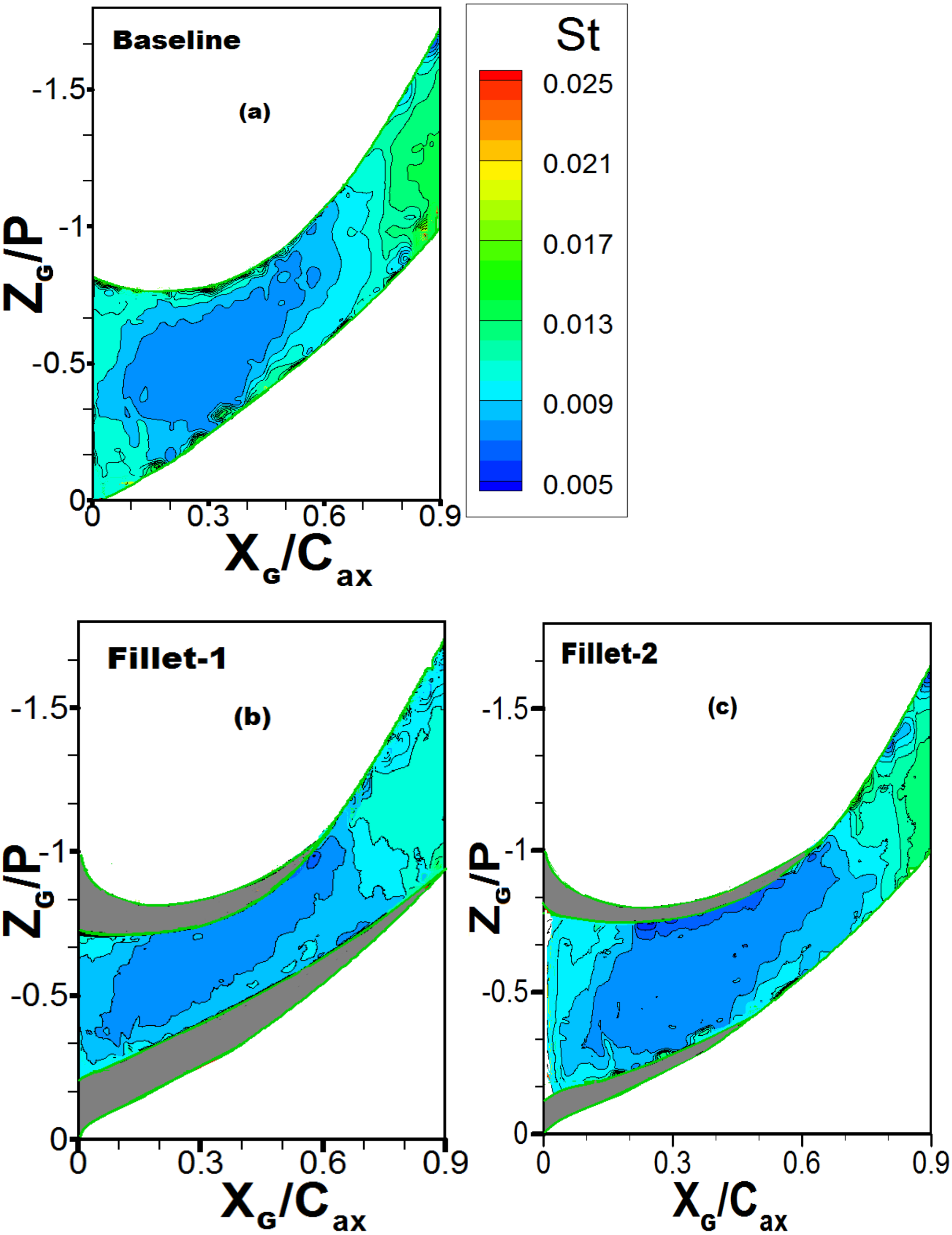

Figure G- 16: Stanton number distribution at the endwall for M = 0 with and without fillets (a) Baseline (b) Fillet-1 and (c) Fillet-2

Appendix H

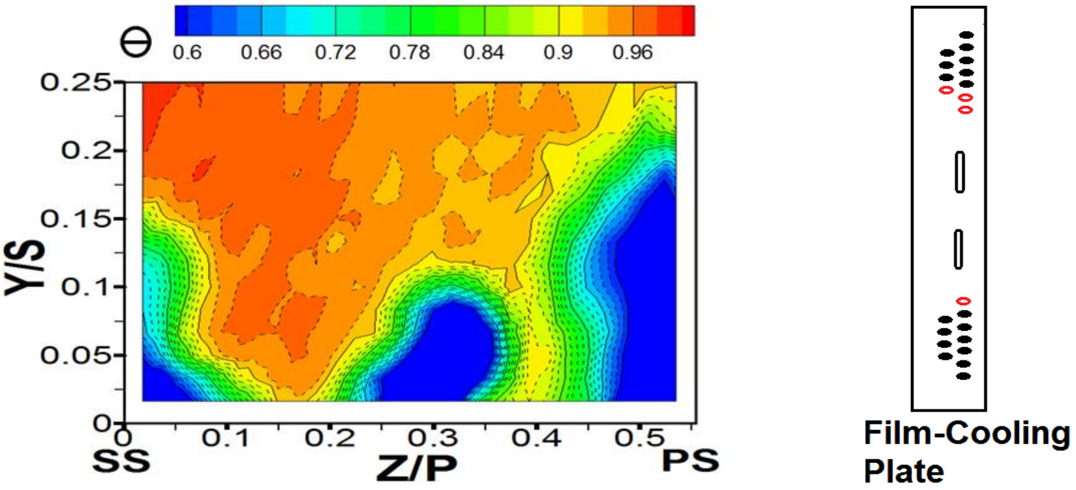

Baseline

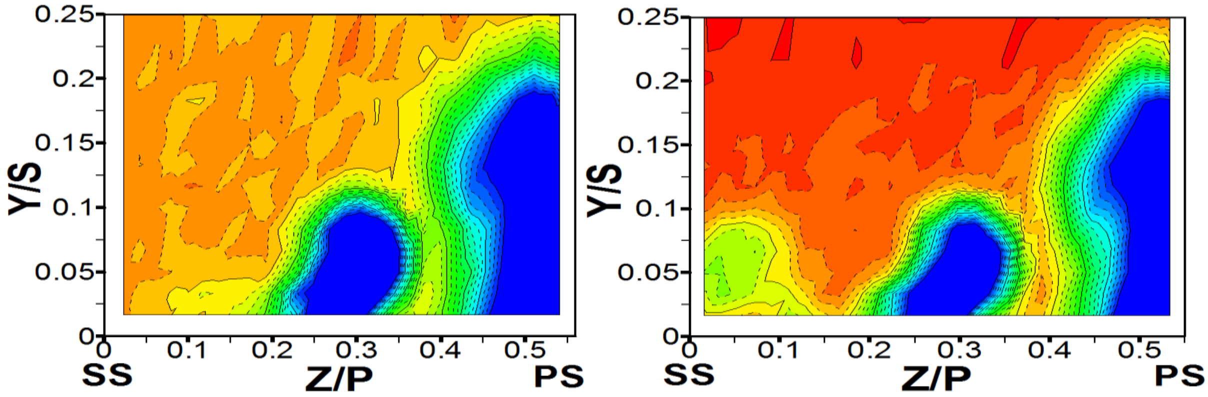

Baseline-1 **Baseline-2**

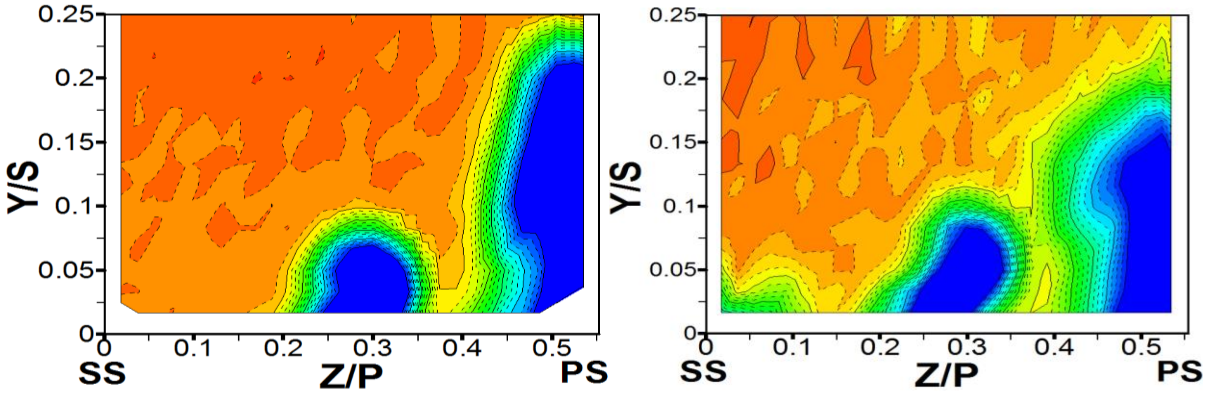

Fillet-1 **Fillet-2**

Figure H- 17: Contours of non-dimensional temperature (θ) distribution in Plane-3 at X_G/C_{ax} = 0.58 for M=2.8

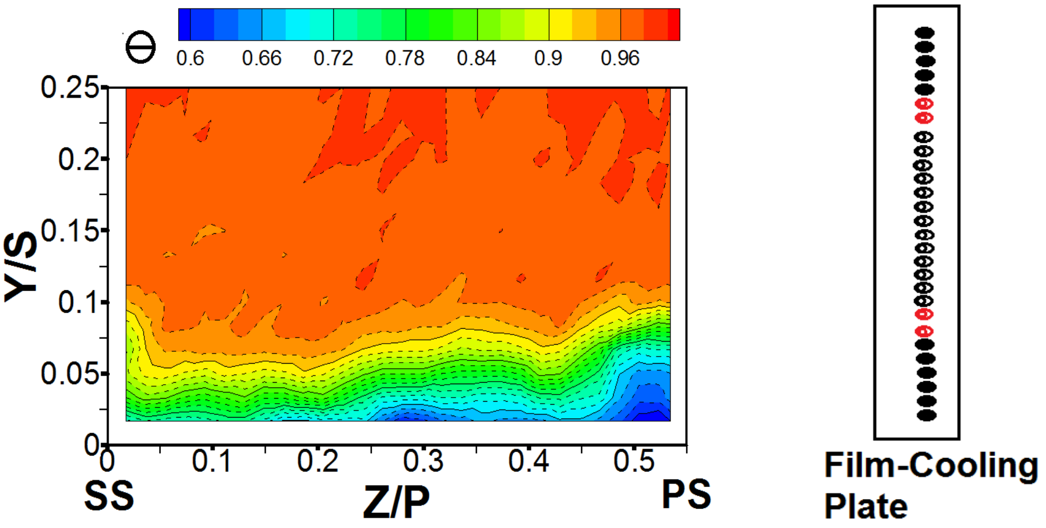

Film-Cooling Plate

Baseline

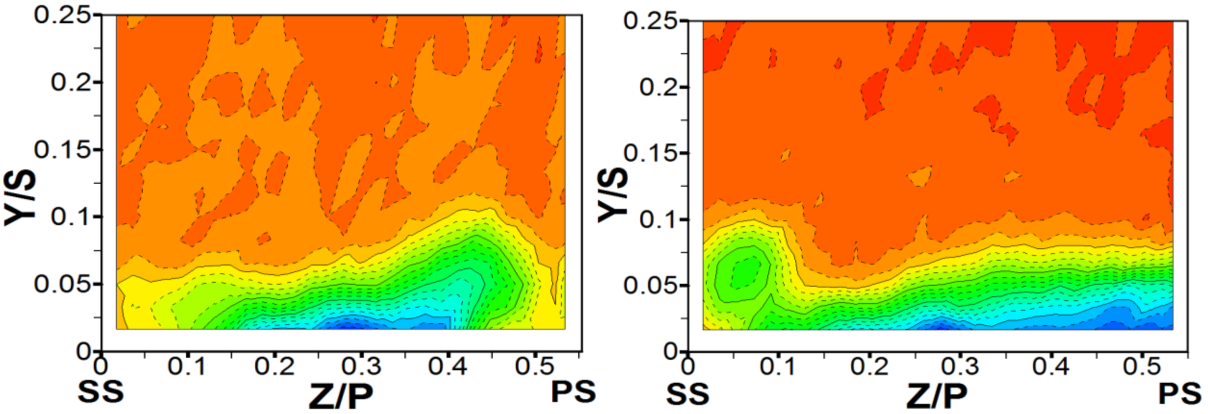

Baseline-1 Baseline-2

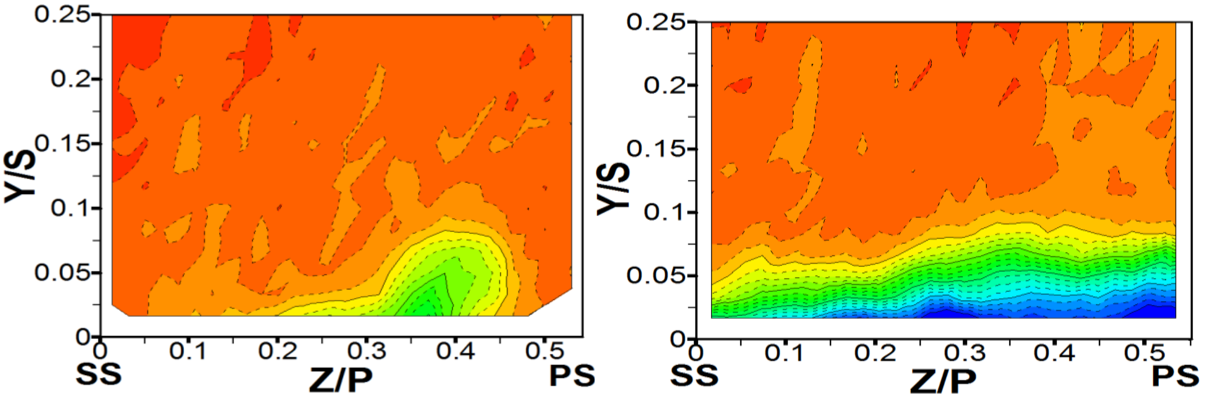

Fillet-1 Fillet-2

Figure H- 18: Contours of non-dimensional temperature (θ) distribution in Plane-3 at X_G/C_{ax} = 0.58 for M=2.8

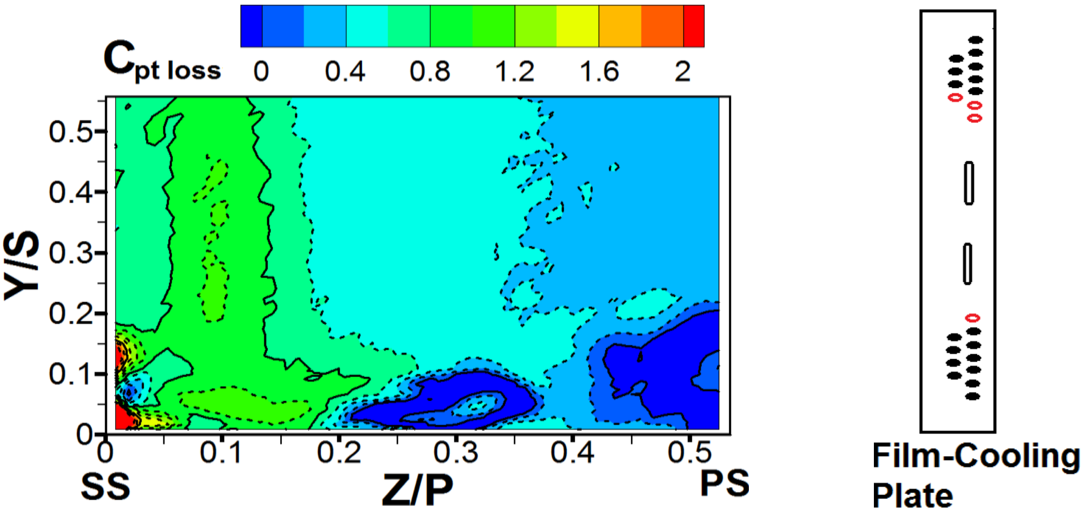

Baseline

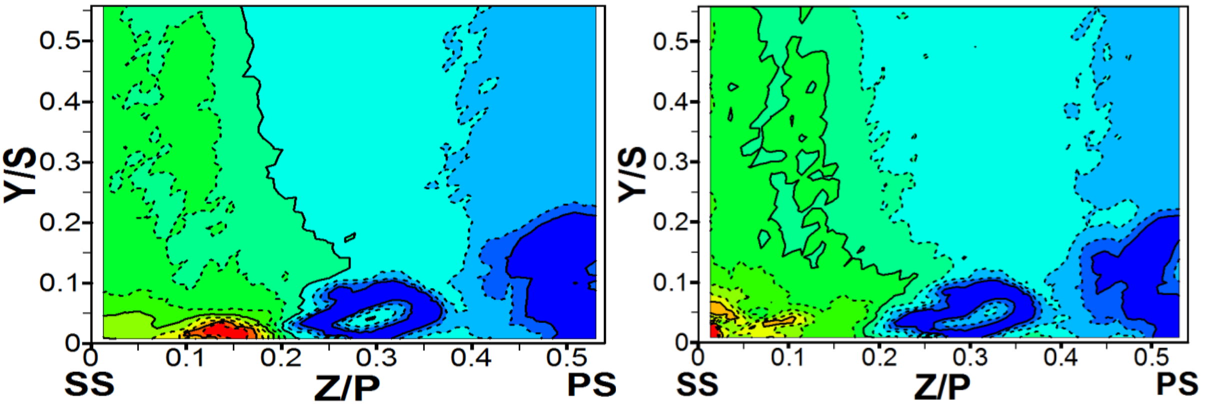

Baseline-1

Baseline-2

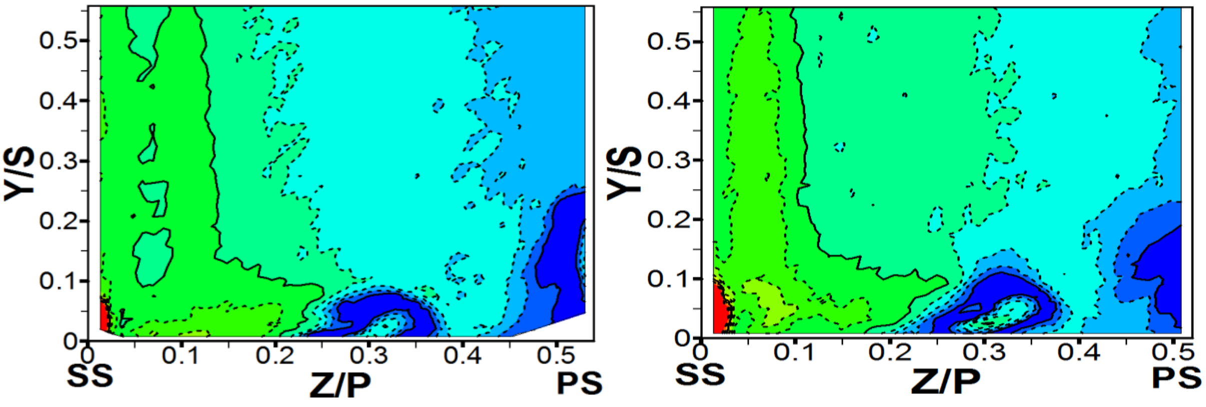

Fillet-1

Fillet-2

Figure H- 19: Contours of total pressure loss coefficient, $C_{pt,loss}$ distribution in Plane-3 at X_G/C_{ax} = 0.58 for M=2.8

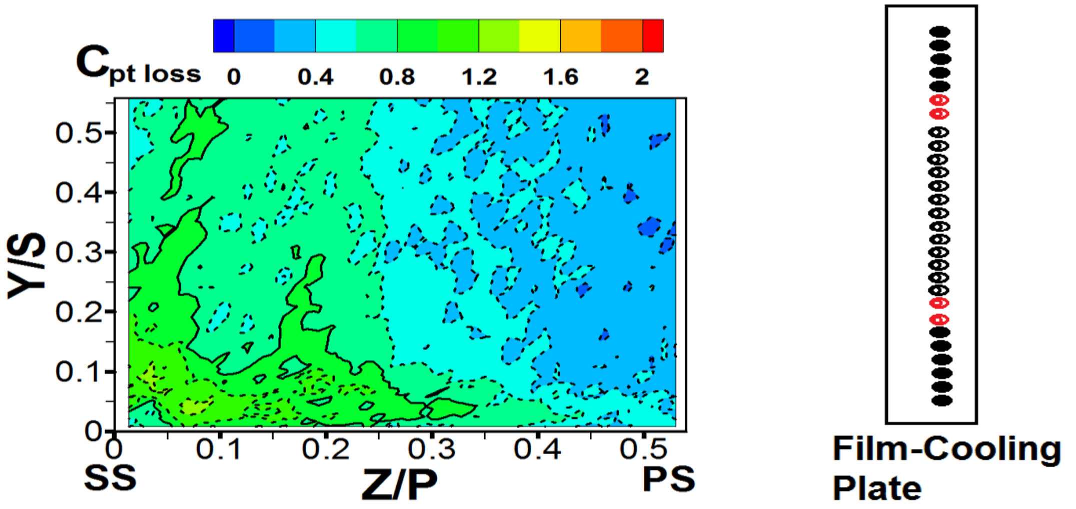

Baseline

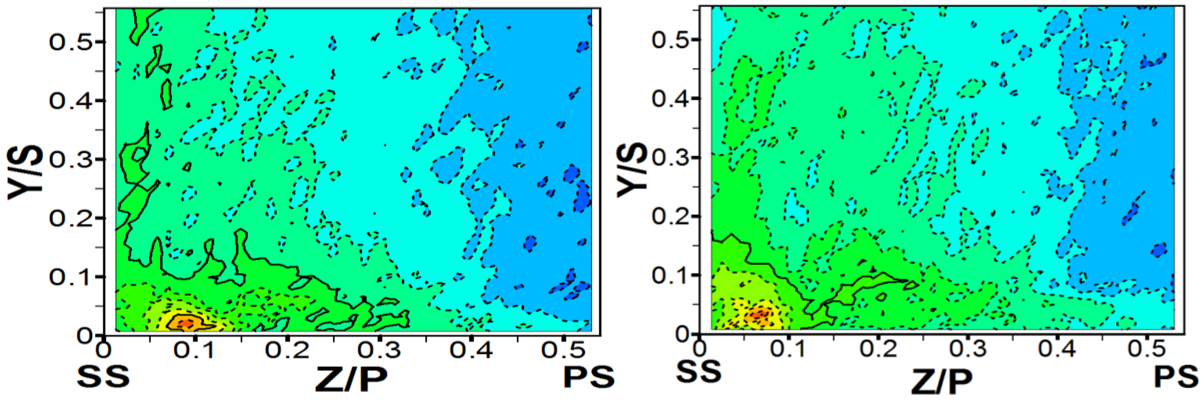

Baseline-1 **Baseline-2**

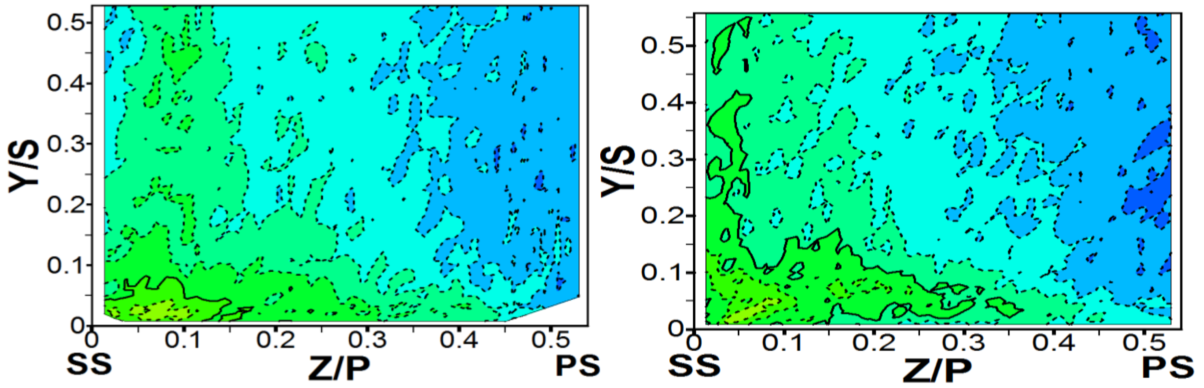

Fillet-1 **Fillet-2**

Figure H- 20: Contours of total pressure loss coefficient, $C_{pt,loss}$ distribution in Plane-3 at X_G/C_{ax} = 0.58 for M=2.8

Appendix I

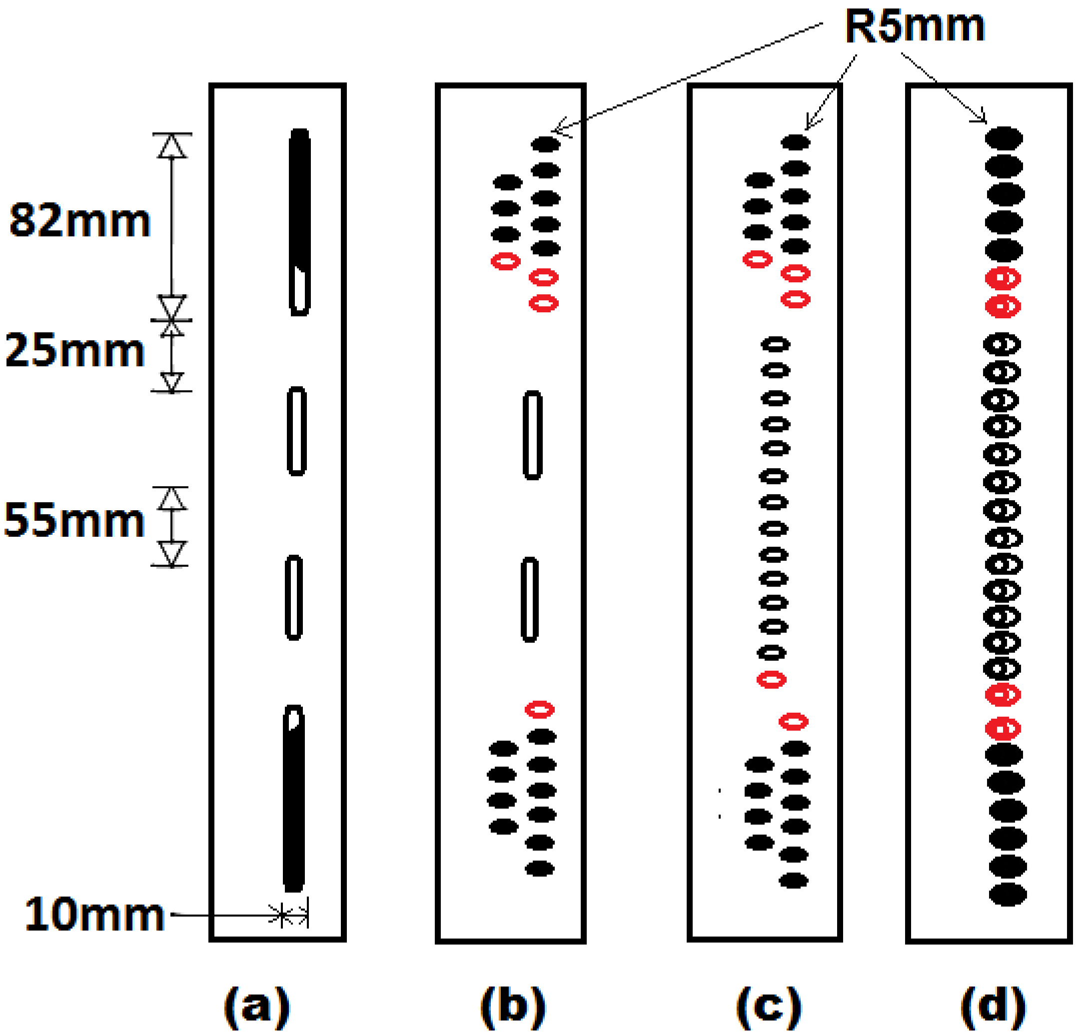

Figure I- 21: Leading-Edge film cooling slot and hole configurations